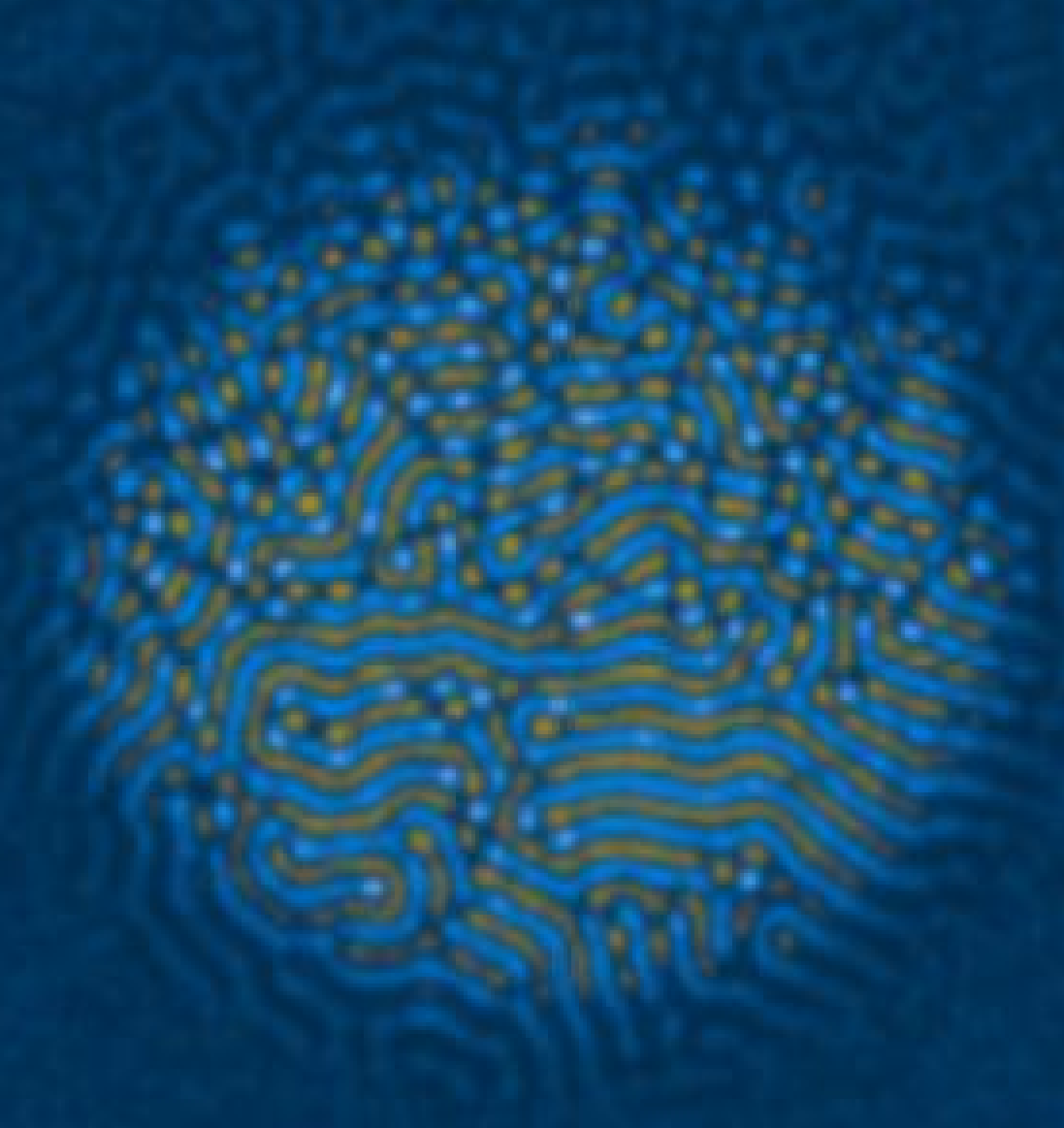# QUANTUM FLUCTUATIONS IN NONLINEAR OPTICAL SYSTEMS

Roberta Zambrini

QUANTUM FLUCTUATIONS
IN NONLINEAR OPTICAL SYSTEMS

PhD Thesis of Roberta Zambrini.
Supervisor: Maxi San Miguel.
University of Balearic Islands.

The picture on the cover represents the transverse profile of the signal field in a type I OPO (see Ch.4).

This is an example of a noise sustained stripe structure in the convective regime.

Acknowledgements

Contents

Chapter 1

Introduction

"Todo lo que mi mente puede imaginar es real."

Pablo Picasso

1.1 Motivation and Context

The subject of quantum structures in nonlinear optics is a quite recent interdisciplinary field. It deals with the quantum properties of electromagnetic radiation in self-organized spatial structures. Until the decade of 1980 the areas of quantum optics and self-organized patterns were investigated by two different communities:

- Most of the literature about pattern formation was concerned with classical features of the phenomenon [Haken, Cross & Hohenberg]. The *effects* of fluctuations in the process of pattern formation have been analyzed at length [García-Ojalvo & Sancho, San Miguel & Toral]. In fact, fluctuations allow for the exploration of several states, even producing new states, absent in a deterministic scenario (noise-induced states). However, there are only few studies about classical correlations functions and long-range spatial correlations in patterns. In addition, the possibility of quantum *correlations* in pattern formation was not investigated in detail.

- Theoretical and experimental results concerning quantum phenomena in optics were obtained neglecting the spatial effects associated with the transverse profile of light beams [Walls & Milburn, Mandel & Wolf]. Only a spatial mode of the electromagnetic field at a frequency was generally considered (*single-mode field*). These models describe the experimental situation in which the whole light beam is detected with a single photodetector. *Temporal* fluctuations were mostly investigated, neglecting any spatial effects in the transverse area of the light beam.

The investigation of quantum fluctuations and correlations in transverse spatial structures opened a new research area (see Refs. [Lugiato & al. (95), Kolobov, Quantum Structures (98), Lugiato & al. (99), Quantum Structures (03)]). The fundamental question in this context is to which extent the quantum phenomena previously investigated in single-mode systems can be found in spatial –instead of temporal– modes of the field. In other words, are quantum effects and correlations present when local portions of the transverse profile of the fields interacting with nonlinear media are detected?

Interesting spatial quantum effects had been found in the process of *parametric down-conversion* [Klyshko (88)], arising when a monochromatic laser interacts with a quadratic nonlinear medium, that is a medium in which its polarization is a quadratic function of the electromagnetic field. Local detections of the output beam in proper spatial far field regions allow for the identification of an entangled state of photons, largely studied in literature in the context of fundamental tests in Quantum Mechanics [Zeilinger]. This is a spatial phenomenon in the area of transverse quantum optics, but it is not related to any self-organized spatial structure. Moreover, it is observed in a regime of small rate of photon pairs production, in which the density of photons detected locally is very low.

In this work we go beyond such quantum spatial phenomena: we are concerned with **macroscopic** quantum phenomena in self-organized spatial structures [Haken, Nicolis & Prigogine]. We consider optical cavities filled with nonlinear media and driven by laser beams. The resonant cavity allows for the production of macroscopic fields, i.e. intense or multi-photon fields, that in single-mode configurations are known to lead to strong *non-classical* effects. Above some threshold, the homogeneous transverse profile of the electromagnetic field breaks spontaneously the transverse translational symmetry and shows a transition to a *spatial* structure, through a self-organization process [Arecchi & al.]. The investigation of the specific features of **quantum fluctuations in these self-organized spatial structures** constitutes an interesting and recent subject of research, almost not explored till end of the decade of 1990 [Lugiato & al. (99)]. Effects such as "quantum images" have been studied by Lugiato and coworkers (Sect.1.4) [Lugiato & al. (95)]. These phenomena occur below the threshold of pattern formation. Very few results had been obtained so far *above* the threshold for the formation of macroscopic spatial structures. This Thesis falls within this context: we study the quantum properties of the fluctuations in the transverse modes of the field in different regimes, characterized by several 'macroscopically' populated spatial modes. Our general goal is the investigation of quantum effects in unexplored regimes, above threshold, that in some cases are highly nonlinear, involving large fluctuations, and/or coupling between many spatial modes. Besides the spatial aspects, also the investigation of the role played by the vectorial character of the field (polarization state) is an interesting subject. We consider this degree of freedom in some of the spatial problems discussed in this work.

The investigation of quantum fluctuations in self-organized spatial structures is also a methodological challenge. There are no general methods valid to study the rich variety of nonlinear regimes appearing in spatial quantum optics. Different problems must be addressed considering the specific features of the system and looking for suitable approximations. Providing answers to these methodological questions is also a general goal of this work.

The interest in spatial aspects of quantum fluctuations is not only fundamental: the spatial degree of freedom gives an interesting new opportunity in the field of quantum information, allowing for quantum

parallel processing and multi-channel operation. Also, the importance of spatial quantum correlations has been considered in the context of parametric imaging. The importance of a quadratic crystal to up-convert [Firester] and to parametrically amplify [Fainman & al.] infrared images was noted long ago, but only recently the possibility of amplification [Kolobov & Lugiato] and duplication [Gatti & al. (99)b] of a faint coherent image has been considered focusing on the level of the quantum fluctuations. Parametric down-conversion allows for noiseless amplification of optical images, that is a phase sensitive amplification in which the signal-to-noise ratio is preserved. Experimental evidence of this phenomenon has been recently achieved [Choi & al.]. Another recent experiment in this context, is the measure of small displacements of a light beam below the standard quantum limit employing non-classical multimode states [Treps & al.]. Possible applications exploiting the spatial aspects of optical quantum fluctuations have been recently reviewed in Ref.[Gatti & al. (00)a], under the name of **Quantum Imaging**.

In the remaining part of this introductory Chapter some general background material is summarized. The historical considerations about the development of the interdisciplinary field of spatial quantum structures suggest a natural scheme for this introduction: we start considering quantum optical phenomena in single-mode treatments (Sect.1.2). We continue reviewing some basic features of pattern formation (Sect.1.3), and finally we link these two areas of investigation, discussing quantum features of self-organized spatial structures of light (Sect.1.4).

More in detail, in Sect.1.2 we focus on some non-classical phenomena in optics and on the principal *methods* of quantum optics of interest for this work. In Sect.1.2.1, we review quantum effects, such as squeezing, antibunching, and sub-Poissonian statistics, focusing on the nonlinear optical devices required to generate such quantum states and on the case of macroscopic fields. In Sect.1.2.2 we briefly review the formalism to describe intracavity dynamics, with emphasis on the non-classical features surviving when there is dissipation due to the losses of an optical cavity. We finally discuss the possibility of direct calculations with the operator Heisenberg equations and with the techniques based on phase space distributions, focusing on the problems appearing in strongly nonlinear regimes (Sect.1.2.3).

In Sect.1.3 we discuss pattern formation in general, and in particular in optical devices. In Sect.1.3.1 we review the model equations used to describe optical resonators filled with nonlinear media. The role of classical noise is discussed in the process of optical pattern formation: in Sect.1.3.2 we describe phenomena such as noisy precursors and noise sustained structures.

In Sect.1.4 we review some important quantum features of self-organized spatial structures of light. We first introduce a suitable formalism to treat spatial problems, generalizing to the space-time domain the definitions of quantum effects introduced for single-mode light in Sect.1.2.1. In Sect.1.4.1 we consider quantum effects in the intensity correlations, focusing on the specific features of different multi-photon generation processes. Previous literature was mainly concerned with *two photons* processes, in which the creation of a photon is always accompanied by the simultaneous creation of a twin photon (Sect.1.4.1.a). In Sect.1.4.1.b we discuss general multi-photon processes considering both few modes approximations and continuous models. In Sect.1.4.2 we review some quantum features appearing in the quadratures of the fields.

In Sect.1.5 we discuss the specific objectives of this work and we outline the contents of the remaining Chapters.

1.2   Quantum optics

Non-classical states of the electromagnetic field [Selected papers (Mandel & Wolf)] are produced by interaction between light and matter. We can identify two fundamental mechanisms: the emission of atom radiation by *resonant interaction*, and the interaction of light with a nonlinear medium in a *non resonant process*. For resonant interactions a system can be active or passive, depending on the population of the resonant atomic levels. Active systems, as the lasers, operate with population inversion of the atomic levels. A non-classical phenomenon in quantum optics was predicted by [Carmichael & Walls] in 1975 for the light generated in resonance fluorescence from a single atom driven by a monochromatic light field, that is a resonant process. In contrast with thermal light, that is bunched, i.e. with photons that tend to arrive in pairs [Hanbury Brown & Twiss], the fluorescence radiation was predicted to be antibunched, with photon arrivals spread in time. This phenomenon was observed by [Kimble & al.], giving a first experimental demonstration of a quantum optical effect. In this work we consider the second type of phenomena, i.e. **non resonant** processes, described in Sect.1.2.1.

An important common aspect of the processes we consider in this work, is the **macroscopic** number of photons involved. Historically, the first effects giving differences between quantized and classical electrodynamics were measured in regimes of low intensities, involving just one particle per detector ([Kimble & al.]). However, it is well-known that non-classical states of the electromagnetic field can be obtained for a macroscopic number of photons: in this regime the intensities are **continuous** variables. Some examples of macroscopic quantum states are discussed in the next Section. Here we point out that there is a recent interest to perform also in this regime fundamental tests on quantum mechanics (as Bell's inequalities tests) [Drummond (83), Kuzmich & al., Reid & al.]. So far these questions had been experimentally investigated in the microscopic single photon regime [Weihs & al., Rowe & al.]. Also, applications of continuous variables have been proposed in quantum communications [Leuchs & al.], quantum information [Lloyd & Braunstein], mapping from light to atomic media [Hald & al.], and quantum teleportation [Furusawa & al.].

The identification of quantum effects is often given by comparison with the statistical properties of the **coherent states**. In fact, coherent states mark the separation between classical and non-classical states of light [Mandel & Wolf]. An intuitive image of a coherent state is the superposition of a classical sinusoidal electromagnetic field and the zero-point noise. Such a state $|\alpha\rangle$ is the eigenvector of the destruction operator $\hat{a}$ [Glauber]:

$$\hat{a}|\alpha\rangle = \alpha|\alpha\rangle. \tag{1.1}$$

An important property of these states is that they approximate classical solutions of the harmonic oscillator problem, in the limit $\hbar \to 0$. In fact, the $\hbar$ vanishing condition does not always guarantee the transition from quantum to classical mechanics. For example, in the harmonic oscillator, the asymptotic probability to find the particle in a position x for the eigenenergy states in the limit $\hbar \to 0$ is really far from

the classical probability. The classical limit is properly obtained considering the coherent states, instead of the eigenfunctions of the energy of the harmonic oscillator. For coherent states, the expectation values of position and momentum follow the classical dynamics, and the uncertainties in these variables are well distributed, do not vary in time, and vanish for $\hbar \to 0$ [Gardiner & Zoller]. The properties of the coherent states are reviewed, for instance, in [Gardiner & Zoller, Ch.4] and [Barnett & Radmore, Ch.3].

Another important class of states of the electromagnetic field is given by the **number** or **Fock states** $|n\rangle$, defined as the eigenstates of the number operator $\hat{n} = a^\dagger \hat{a}$ with eigenvalue $n \, (= 0, 1, 2 \ldots)$ [Walls & Milburn]:

$$\hat{n}|n\rangle = n|n\rangle. \tag{1.2}$$

These states are the eigenenergy states for the Hamiltonian operator of the harmonic oscillator.

1.2.1 Nonlinear media and non-classical states of light

In this Section we describe some fundamental quantum effects appearing in nonlinear optical phenomena [Boyd]. Nonlinear optical phenomena occur when the optical properties of a medium are modified by the interaction with an intense light field. Generally, the intensity of a laser source is necessary to reach observable nonlinear effects [Franken & Ward]. Nonlinear media are characterized by the expansion of the polarization vector $\vec{P}$ in powers of the electric field

$$\vec{P} = \chi^{(1)}\vec{E} + \chi^{(2)}\vec{E}^2 + \chi^{(3)}\vec{E}^3 + ... \tag{1.3}$$

where $\chi^{(n)}$ are the coefficients of the susceptibility at different orders [1]. When quadratic and higher order terms in the expansion (1.3) can be neglected, the response of the medium to the light is linear (linear optics). In the more general case the presence of a nonlinear (quadratic or cubic) polarization allows for the generation of new frequencies of the field. A quadratic polarization term appears in noncentrosymmetric crystals, in which the inversion symmetry is broken. The first experiments in nonlinear optics date from the early 60's, and describe the **generation of the second harmonic (SHG)** of a laser through non-resonant interaction with crystalline quartz [Franken & al., Giordmaine]. The quadratic polarization of the medium is at the origin of the coupling between two pump modes at frequency ω, leading to a field with the sum frequency 2ω. The reverse mechanism, occurring also for quadratic polarization ($\chi^{(2)}$), is **parametric down-conversion (PDC)**, in which the pump mode at frequency ω_1 leads to two modes at frequencies ω_2 and ω_3, respectively, where $\omega_1 = \omega_2 + \omega_3$. In the case of frequency degeneracy ($\omega_1 = \omega_2$) this phenomenon is named degenerate PDC. If the quadratic medium is placed inside an optical resonator, the fields at ω_2 and ω_3 can build up to large photon numbers. Such a device is known as an **optical parametric oscillator (OPO)**, in which the process of PDC is highly increased above a threshold value of the intensity of the pump field. Materials such that $\vec{P} = \chi^{(1)}\vec{E} + \chi^{(3)}\vec{E}^3$ are known as Kerr media. The cubic term of the polarization allows for four wave

---

[1]Here we consider the simpler case of scalar susceptibility. In Ch.3 we will consider the vectorial character of the electromagnetic field in the case of a Kerr medium, in which the third order susceptibility becomes a third order rank tensor.

mixing [Boyd]. In these materials third order harmonics can be generated. In Ch.3 we will consider the appearance of nonlinear refractive index in the interaction of a monochromatic field with a Kerr medium.

In the 1960s and early 1970 the driving force behind the development of devices based on nonlinear materials was their ability to generate or amplify coherent light, tunable over a wide wavelength range, and also their ability to frequency up-convert light. The possibilities of these materials to generate important quantum effects attracted later the attention of the quantum optics community [Klyshko (88), Walls & Milburn]. We now discuss these possibilities.

The quantum description of nonlinear optical interactions generally involve atomic and field variables. However, for non resonant interactions and for a fast response of the medium to the applied field, the atomic variables can be adiabatically eliminated from the description. Therefore, the effect of the medium on the radiation is described by a polarization vector, as in the classical theory, and optical interactions between the field modes are described by a Hamiltonian operator [Hillery & Mlodinow]:

$$\hat{H} = f(\hat{a}_0, \hat{a}_0^\dagger, \hat{a}_1, \hat{a}_1^\dagger, ...) \tag{1.4}$$

where $\hat{a}_j, \hat{a}_j^\dagger$ ($j = 0, 1, 2...$) are the annihilation and creation operators at different frequencies. The propagation of the field and the coupling between modes determine the form of f. This function is quadratic in the creation and destruction operators for free fields, and in general when it describes linear processes. Light in nonlinear media is described by cubic or higher order functions f, depending on the susceptibility terms $\chi^{(n)}$ ($n \geq 2$).

As an example of nonlinear device showing quantum phenomena, we consider a quadratic crystal ($\chi^{(2)}$) used in the degenerate PDC process, in which a photon at frequency 2ω decays into two photons at frequency ω. The corresponding Hamiltonian in the interaction picture is:

$$\hat{H} = -\frac{i}{2}\chi^{(2)}\hbar(\hat{a}^2\hat{b}^\dagger - \hat{a}^{\dagger 2}\hat{b}), \tag{1.5}$$

with $\hat{b}$ being the annihilation operator of the pump mode at frequency 2ω, and $\hat{a}$ the annihilation operator of the down-converted field. In this example we observe that a $\chi^{(2)}$ medium leads to cubic Hamiltonians, while cubic polarizations leads to fourth order Hamiltonians (see Ch.3) [Hillery & Mlodinow]. In regimes in which the depletion and the fluctuations of the pump can be neglected, the pump field operator can be replaced by a classical c-number field, leading to approximated Hamiltonians of lower orders. In the case of the degenerate PDC the approximated Hamiltonian is

$$\hat{H} = -i\hbar\frac{g}{2}(\hat{a}^2 - \hat{a}^{\dagger 2}) \tag{1.6}$$

where g is proportional to the second order susceptibility and to the pump field [2].

Quantum fluctuations of light fields interacting with nonlinear media were extensively investigated since 1970, showing the possibility of quantum phenomena such as photon antibunching, sub-Poissonian statistics, squeezing and, in general, violations of classical inequalities, as we will see next. In particular we will show that squeezing arises naturally in PDC.

---

[2]The fact that the quadratic Hamiltonian gives a linear dynamics of the down-converted field must not be misinterpreted. The fundamental issue is that the interaction process between modes of the field (leading to this linear dynamics in one of the modes) is **nonlinear**.

Intensity photon correlation experiments can give results that cannot be explained classically [Walls (79), Loudon (83)]. One example is **photon antibunching**, mentioned previously. This phenomenon is defined in terms of the second-order temporal coherence function [Mandel & Wolf]

$$g^{(2)}(\tau) = \frac{\langle : \hat{I}(t)\hat{I}(t+\tau) : \rangle}{\langle \hat{I}(t) \rangle^2}, \tag{1.7}$$

with $\hat{I}(t) \propto \hat{a}^\dagger(t)\hat{a}(t)$. The symbol :: indicate the *normal ordering* of operators, corresponding to creation operators placed to the left (for instance $: (\hat{a}^\dagger \hat{a})^2 := (\hat{a}^\dagger)^2 \hat{a}^2$). The physical importance of such normal ordering prescription is related to the absorption processes at the basis of photodetection: in fact, photo-detectors do not measure vacuum fluctuations, but instead they measure normal ordered quantities [Glauber]. The second-order temporal coherence function $g^{(2)}(\tau)$ describes whether the photons in a single-mode beam tend to group together or to stay apart in time. In classical electrodynamics the field operator $\hat{a}(t)$ could be replaced by a stochastic c-number $\alpha(t)$, leading to $g^{(2)}(\tau) = \frac{\langle I(t)I(t+\tau)\rangle}{\langle I(t)\rangle^2}$, with a stochastic classical intensity $I(t) \propto \alpha^*(t)\alpha(t)$. Given the stationary random process I, it follows from the Cauchy-Schwarz inequality that $g^{(2)}(\tau) \leq g^{(2)}(0)$, i.e. the $g^{(2)}$ function is maximum for time delay $\tau = 0$. The violation of this inequality, i.e.

$$g^{(2)}(\tau) \geq g^{(2)}(0), \tag{1.8}$$

is a signature of non-classical behavior describing the photon number fluctuations [3]. Physically this means that the probability of detecting the second photon –instead of decreasing– increases with the time delay. Some authors [Davidovich, Kolobov, Orszag, Zou & Mandel] identify the phenomenon of antibunching with the inequality (1.8). For other authors [Walls & Milburn, Loudon (80), Paul], the phenomenon of photon antibunching arises when $g^{(2)}(0) \leq 1$: this is equivalent to (1.8) in the limit of an infinite long time delay, when the probability of joint detection coincides with the probability of independent detection (uncorrelated events) and $g^{(2)}(\tau \to \infty) = 1$. A good candidate to generate photon antibunching is the nonlinear process of SHG. In fact, in SHG, pairs of photons are annihilated in the pump beam at the fundamental frequency, to generate the second harmonic photons. Therefore, in the pump beam coincidences of two photons are unlikely and photons are spread in time, leading to photon antibunching (see the review in [Paul, Sect.IV]).

Another non-classical effect, related to intensity correlation properties, is the **sub-Poissonian photon statistics**, reviewed, for instance, by [Davidovich]. We have mentioned that coherent states $|\alpha\rangle$ mark the separation between classical and quantum states of light. Such states have a photon statistics characterized by the Poissonian distribution

$$p(n) = |\langle n|\alpha\rangle|^2 = e^{-\langle n\rangle}\frac{\langle n\rangle^n}{n!}. \tag{1.9}$$

Photon statistics for any state can be characterized by the Q parameter introduced by [Mandel(79)]

$$Q = \frac{\langle (\Delta n)^2 \rangle}{\langle n \rangle}. \tag{1.10}$$

---

[3]In Ref.[Reid & Walls] the violation of such inequalities is compared with Bell's inequalities: even if both distinguish between the predictions of classical and quantum theory, the second ones are known to be stronger.
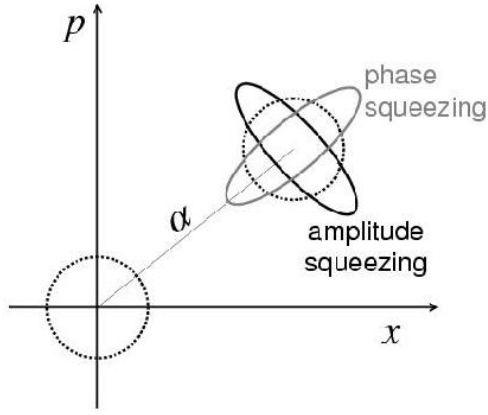
Figure 1.1: Uncertainties of coherent states $|0\rangle$ and $|\alpha\rangle$ (dotted lines) and squeezed states (continuous line) in the complex plane ($\alpha = x + ip$).
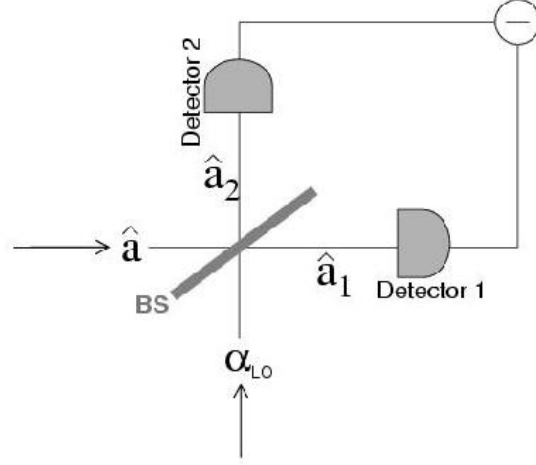
Figure 1.2: Balanced homodyne detector: the squeezed signal â interferes with a coherent local oscillator α_{LO} at a $50/50$ beam-splitter (BS). The output beams â$_1$ and â$_2$ are detected and are differenced to provide the *balanced-detector* output.

For coherent states this parameter vanishes and it is positive for classical states (super-Poissonian photon statistics). A sub-Poissonian distribution is a quantum effect characterized by $-1 \leq Q \leq 0$, being $Q = -1$ realized for Fock or number states $|n\rangle$. The first experimental observation of sub-Poissonian statistics dates from 1983. It was obtained in photoelectric counting experiments on atom fluorescence [Short & Mandel]. This phenomenon has been demonstrated for nonlinear media in type II OPO [Mertz & al.] [4]. In this process, described more in detail in Ch.5, the down-converted photons, generally called signal and idler, are distinguished by their orthogonal polarizations. Due to the simultaneous creation of such pairs of twin photons, the photon-number (or intensity) noise in the difference of the intensities of the signal and idler beams is smaller than the noise in each beam. Taking this difference the pair events are eliminated, and the fluctuations of the resulting intensity difference are reduced below the classical limit. A sub-Poissonian distribution is obtained [Reynaud, Reynaud & al. (87)], and the strong correlations between the signal and idler beams cannot be described in the classical electrodynamics context, as reviewed in Ref.[Walls & Milburn, Ch.V.2].

Next we consider a third quantum phenomenon, in which the fluctuations in one quadrature of the field are below the shot noise level (corresponding to the level fluctuations of a coherent state). A quadrature of the field $\hat{X}^{\theta}$ is defined by

$$\hat{X}^{\theta} = \hat{a}e^{i\theta} + \hat{a}^{\dagger}e^{-i\theta}. \tag{1.11}$$

Real and imaginary quadratures are obtained for $\theta = 0$ and $\theta = \pi/2$, respectively. The quadrature (1.11) has a variance equal to 1, independently of the value of θ, for any coherent state. Therefore,

---

[4]For a definition of type I and type II phase matching see Appendix B.

a field is squeezed in the quadrature θ if the variance of this quadrature is smaller than 1 [Stoler]. Fig.1.1 shows a phase space plot of the uncertainties of coherent and squeezed states in the complex plane [5]. The dotted lines represent the $|0\rangle$ and $|\alpha\rangle$ coherent states, with the same uncertainty in all the quadratures (circular shapes). The two ellipses represent two orthogonal squeezed states: we observe that one squeezed state shows less fluctuations than a coherent state in the angular phase (phase squeezing), while the other state shows less fluctuations in the direction of α (amplitude or intensity squeezing). Phase squeezed states have a super-Poissonian statistics, while amplitude squeezed states, for $|\alpha|$ sufficiently large, are an example of sub-Poissonian distribution [Mandel(82)]. The **squeezing effect** is reviewed, for instance, in Refs.[Walls (83), Kimble, Fabre, Teich & Saleh]. A squeezed state is generated mathematically by the action of a squeezing operator

$$\hat{S}(\zeta) = e^{-\frac{\zeta}{2}\hat{a}^{\dagger 2} + \frac{\zeta^*}{2}\hat{a}^2} \tag{1.12}$$

on a coherent or vacuum state, with squeezing parameter ζ. As shown by [Yuen], the quadratic term $\hat{a}^{\dagger 2}$ is related to a two-photon creation process: for this reason he defined the squeezed states as "two-photon coherent states". The relation with PDC is evident: the temporal evolution operator $\hat{U} = e^{-\frac{i}{\hbar}\hat{H}t}$ for the PDC shows exactly the quadratic dependence leading to squeezing (compare with Eq. (1.12)). Therefore, from this example, we see that the nonlinearity of the medium provides a natural way to generate squeezed states through the coupling of the modes of the field.

The quadratic nonlinearity gives a phase sensitive temporal dynamics of the field. Because there are certain values of the phase where the electric field uncertainty becomes small, a phase-sensitive form of detection (homodyning) is used for the detection of quadrature-squeezed light [Teich & Saleh]. *Homodyne detection* is used to extract the quadrature of the field with reduced fluctuations. In the single-ended configuration (only detector 1 in Fig.1.2), the squeezed light is combined at an unequal beam-splitter with coherent light from a laser local oscillator (LO). If the LO phase is chosen properly the superposition field will be photon-number squeezed, resulting in a sub-shot-noise spectrum. A problem with single-ended homodyne detection is that a very strong local oscillator is required to achieve the optimal conditions, and fluctuations in the power of the local oscillator (excess noise) increase the noise in the superposition beam, masking squeezing. A few years ago [Yuen & Chan] suggested a modification of the single-ended configuration, where a squeezed field signal â and a coherent local oscillator α_{LO} are incident on a $50/50$ beam-splitter. As shown in Fig.1.2, after the two beams $\hat{a}_1$ and $\hat{a}_2$ of both output ports are detected, they are subtracted to provide the *balanced-detector* output, and the squeezed uncertainty is recovered with no quantum or excess noise contributed by the local oscillator. The first observation of squeezing was achieved in 1985 by [Slusher & al.] in an experiment of parametric generation involving four-wave mixing in sodium vapor. This was followed by observations in PDC processes [Wu & al.] and in optical fibers [Shelby & al.]. Fig.1.3 summarizes some experimental results on squeezing obtained till 1998 in different optical devices.

In conclusion, coupling between field modes due to interaction with **nonlinear media** provides a

---

[5]The diagrams for different states represented in Fig.1.1 can be obtained as cuts of proper quasi-probabilities distributions in the complex plane. In Sect.1.2.3.b we will detail the relation between the operators $\hat{a}$ and the c-numbers $\alpha = x + ip$.

natural way to observe the non-classical features summarized in this Section. This coupling mecha-nism can be interpreted at a *microscopic* level in terms of processes of **creation and annihilation of photons**: in the example of the PDC we have seen that the process of creation of two photons from the annihilated pump photon is at the root of quantum phenomena, like squeezing or sub-Poissonian statistics. All these effects were initially studied in a single-mode approximation, neglecting spatial ef-fects in the transverse profile of the electromagnetic field. In Sect.1.4 we will generalize these concepts considering the *transverse* spatial modes of the field.

1.2.2 Open quantum systems

In an isolated system the time evolution is described by the total Hamiltonian; however, many quantum optical experiments involve the use of *optical cavities* to enhance fields strengths, as in most of the sys-tems we study in this work. The importance of the use of the cavity in the generation of quantum states can be illustrated considering parametric down-conversion. In order to generate an intense squeezed state one should increase the nonlinear effects, responsible for the creation of photon pairs. The non-linearity can be enhanced by making the process resonant, so that the pump field induces a transition between two atomic levels. This has, however, the disadvantage of producing a large population of the excited level, which may decay spontaneously, thus generating noise which spoils effects such as squeezing [Slusher & al.]. On the other hand, if the nonlinear medium is placed inside a high-Q cavity, the down-converted photons *stimulate* the process thus enhancing the nonlinear coupling, even though second-order susceptibilities might be still very small.

A system in an optical cavity is not isolated, because of the mirrors that couple the cavity modes with the environment. This coupling is responsible for the leaking of energy from the cavity and also for the introduction of environmental fluctuations into the cavity, which can have a profound effect on the quantum dynamics. On the other hand, this coupling is typically weak compared with couplings within the system of interest. Hence, it turns out that the effects of dissipation associated with the coupling through the optical mirrors do not, in general, depend on the precise form of the system nor
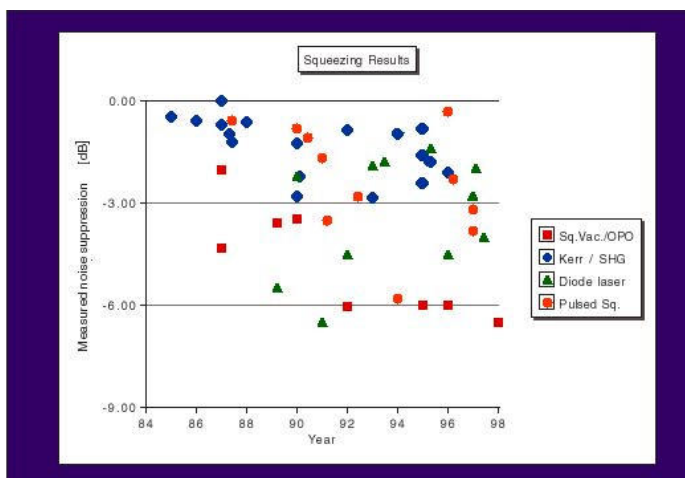

Figure 1.3: Experimental squeezing results obtained from 1984 till 1998. Taken from the web-page http://photonics.anu.edu.au/qoptics/people/bachor/book.html of Prof. Hans -A. Bachor.
Remember:
$1dB = 10\log_{10}(P_2/P_1)$ with P_i powers.

on the details of the coupling. Therefore a general formalism can be obtained to describe these open quantum systems.

Let us consider the total system (cavity + environment or system + bath): generally we have only statistical information about the state of the environment, so that instead of the total wave-function we use the total density matrix $\hat{\rho}_{tot}$ [Huang]. In the Schrödinger picture the evolution of $\hat{\rho}_{tot}$ is described by the von Neumann equation:

$$\frac{\partial \hat{\rho}_{tot}}{\partial t} = \frac{1}{i\hbar}[\hat{H}_{tot}, \hat{\rho}_{tot}], \tag{1.13}$$

with $\hat{H}_{tot}$ being the Hamiltonian describing the cavity, the environment and their interactions, and the symbol $[,]$ indicating the commutator. We are interested in the properties of the system alone, so we need only the evolution equation for the reduced density matrix $\hat{\rho}$ of the intracavity fields, obtained by taking the trace over the degrees of freedom of the environment. For a detailed derivation of the dynamical equation for the reduced density matrix in presence of dissipation see, for instance, [Carmichael] or [Barnett & Radmore]. The intracavity dynamics is described by a **Master equation** for the reduced density operator $\hat{\rho}$:

$$\frac{\partial \hat{\rho}}{\partial t} = \frac{1}{i\hbar}[\hat{H}, \hat{\rho}] + \Lambda\hat{\rho}, \tag{1.14}$$

with $\hat{H}$ being the Hamiltonian of the intracavity fields. The Liouvillian Λ is the super-operator accounting for dissipation (with strength γ) through the partially reflecting cavity mirror [6]:

$$\Lambda\rho = \gamma \left\{ [\hat{a}, \hat{\rho}\hat{a}^\dagger] + [\hat{a}\hat{\rho}, \hat{a}^\dagger] \right\} . \tag{1.15}$$

The Master equation has two terms: a strong coupling term having the same form as in the absence of dissipation, and the dissipative term having the same form it would have in the absence of the strong Hamiltonian coupling [Barnett & Radmore]. The most important assumption done to obtain Eq. (1.14) is the Markov approximation. In this approximation we assume that there are two different time scales in the total system: one is given by the decay time scale of the (intracavity) system and the other one by the decay time scale of the environment. When the environment and the system evolve in the same time scales, the Markovian approximation is not valid and we cannot obtain a Master equation. When there is a fast evolution of the environment we can neglect the time needed for the equilibration of the environment and we then obtain Eqs. (1.14-1.15).

An equivalent treatment of dissipation can be given considering the Heisenberg picture: in this case a set of Heisenberg equations of motion for the creation and annihilation operators are obtained, describing the intracavity dynamics. The damping appears through the action of proper Langevin operators [Barnett & Radmore, Kimble, Gardiner & Zoller]. We will describe this formalism in Sect.1.2.3.a.

New developments on quantum open systems have recently taken place in connection with the theory of decoherence, as reviewed, for example, in the book "Decoherence and the Appearance of a Classical World in Quantum Theory" [Giulini & al.]. In particular the phenomenon of decoherence through the interaction with the environment is discussed by E. Joos [Giulini & al., Ch.3]. Generally the decoherence effects caused by the environment are discussed in relation with superpositions of

---

[6]We assume that only one of the mirrors has reflection coefficient different from 1 and that the reservoir is in thermal equilibrium, with $\hbar\omega \ll K_B T$ (ω input frequency, K_B Boltzmann constant, and T temperature).

radiation states, for instance $|\alpha\rangle + |-\alpha\rangle$ ("Schrödinger cat states") [Zurek]. [El-Orany, Peřina & al.] describe quantum properties in a single-mode dissipative amplifier when the signal and idler are initially prepared in Schroedinger cat states, showing how the interaction with the environment and pump decay produce decoherence in the system. The subject of the manipulation of the bath has also attracted some attention. Several authors have shown how feedback effects and other mechanisms could control effects of decoherence (see [Agarwal] and Refs. therein). In this work we will not consider this kind of problems.

The effects of the losses of the cavity have been extensively studied also in relation to squeezed states and twin beams phenomena. Generally, the cavity losses decrease the quantum effects present inside the cavity. In Sect.1.4.1.a we will see that quantum correlations between twin beams in the non-degenerate PDC are perfect when there are no losses. These correlations are reduced in a lossy cavity [Graham]. The important point is how to link the intracavity results with the observable external cavity fields: 20 years ago [Collett & Gardiner] developed an **input/output** formalism for optical cavities in order to obtain the behavior of the fields outside the cavity, given the fields inside the cavity. In the case of a one port cavity (one mirror with non-vanishing transmittivity), the field immediately outside the cavity $\hat{a}^{out}$ is related to the intracavity field $\hat{a}$, and to the reflected input field $\hat{a}^{in}$ by:

$$\hat{a}^{out}(\vec{x}, t) = \sqrt{2\gamma}\hat{a}(\vec{x}, t) - \hat{a}^{in}(\vec{x}, t) \, , \tag{1.16}$$

where γ is the damping coefficient which depends on the transmittivity of the mirror. This relation allows for the evaluation of correlation functions of the output fields. In the problem of PDC, correlations between twin beams calculated inside the cavity are shown to be reduced with respect to their value when there are no losses. However, it is shown that perfect twin beams correlations are recovered for the output fields, if measured integrating over long times [Walls & Milburn, Ch.7]. Therefore, perfect correlations between twin beams are obtained when the detector collects all the photons pairs simultaneously generated in the medium and escaping independently from the cavity. The time of integration must be longer than the cavity lifetime [Heidmann].

1.2.3   Methods in quantum optics

In Sect.1.2.1 we have seen that nonlinear optical devices are often characterized by Hamiltonians which are not quadratic functions of the creation and destruction operators (Eq. (1.4)). Hence the Heisenberg equations describing the fields dynamics are a set of coupled nonlinear operator equations that usually defies analysis. In Sect.1.2.3.a we describe the Heisenberg picture and the conditions under which it is useful for analytical calculations.

In Sect.1.2.3.b we present one of the most powerful instruments in quantum optics: the phase space description of fields operators [Schleich]. In this description, the quantum state of the field is characterized by a quasiprobability distribution, defined in the basis of the coherent states [Glauber, Sudarshan]. The quasi-probabilities are similar to classical phase space probability distributions for the fields amplitudes. Averages of products of creation and destruction operators are calculated evaluating an integral weighted by the quasi-probability distribution. However, quasi-probabilities describing

optical systems are not always positive. Hence the phase space techniques are a practically useful formalism only in particular cases, as, for instance, in the case of linear fields dynamics. In Sect.1.2.3.b we review the techniques and the limits of such method.

A more complete discussion of the methods used in quantum optics can be found in the book *"Methods in Theoretical Quantum Optics"* [Barnett & Radmore], and in general books of quantum optics [Gardiner & Zoller, Walls & Milburn].

1.2.3.a   Heisenberg equations

An alternative description to the Shrödinger picture introduced in Sect.1.2.2 is the Heisenberg picture (see for instance [Barnett & Radmore]) in which the state remains unchanged, while the operators satisfy the Heisenberg equation

$$\frac{d}{dt}\hat{a}_j(t) = \frac{i}{\hbar}[\hat{H}, \hat{a}_j(t)] + \frac{\partial}{\partial t}\hat{a}(t), \tag{1.17}$$

where the partial derivative vanishes if the modes $\hat{a}_j$ do not depend explicitly on time. When there are dissipative contributions the dynamics of the intracavity fields is described by

$$\frac{d}{dt}\hat{a}_j(t) = \frac{i}{\hbar}[\hat{H}, \hat{a}_j(t)] - \gamma\hat{a}_j(t) + \sqrt{2\gamma}\hat{a}_{j,in}(t) \tag{1.18}$$

where the Langevin force $\hat{a}_{j,in}$ is the input field, and $\hat{H}$ is the intracavity Hamiltonian.

For Hamiltonians (1.4) of order higher than the quadratic one, this formalism is not particularly useful: in this case the commutators $[\hat{H}, \hat{a}_j(t)]$ result in nonlinear functions of the operators $\hat{a}_j$. Hence any attempt to evaluate the evolution of the fields moments gives rise to a *hierarchy of coupled equations* very difficult to handle. Therefore this method is generally of limited practical use to describe nonlinear systems.

However, in particular cases, the Hamiltonian can be *approximated* by a quadratic form in the fields operators. For instance, we have already discussed the case of the PDC in which only the quantum fluctuations of the signal are considered, while the pump fluctuations are neglected. In this approximation the cubic Hamiltonian reduces to a quadratic operator. In general, for an average value of the signal fields, showing "small" fluctuations $\delta\hat{a}_j = \hat{a}_j - \langle\hat{a}_j\rangle$, it is possible to reduce the exact Hamiltonian to an approximated one, quadratic in the fluctuation variables $\delta\hat{a}_j$.

Any quadratic Hamiltonian leads to a **linear** dynamics of the fields operators. In this case, the Heisenberg equations are

$$\frac{d}{dt}\hat{\mathbf{a}}(t) = A\hat{\mathbf{a}}(t) - \gamma\hat{\mathbf{a}}(t) + \sqrt{2\gamma}\hat{\mathbf{a}}_{in}(t) \tag{1.19}$$

where we have introduced the vector $\hat{\mathbf{a}} = [\hat{a}_0, \hat{a}_0^\dagger, \hat{a}_1, \hat{a}_1^\dagger, ...]$ and equivalently $\hat{\mathbf{a}}_{in}$; A is a matrix related the commutator terms in Eq.(1.18). Considering the Fourier modes, we obtain a set of linear algebraic operator equations giving $\hat{\mathbf{a}}(\omega)$ as a function of $\hat{\mathbf{a}}_{in}(\omega)$. Finally, the input-output relations Eq. (1.16) allow for a direct relation between the fields at the output $\hat{\mathbf{a}}_{out}(\omega)$ and at the input $\hat{\mathbf{a}}_{in}(\omega)$ of the cavity. In this way the output moments can be calculated as a function of the input moments. This procedure is reviewed, for instance, in [Walls & Milburn, Ch.7] and will be used in Ch.5 to study a type II OPO below threshold.

1.2.3.b Phase space methods

The Master equation (1.14) is an equation for operators that generally cannot be solved; moreover the density operator $\hat{\rho}$ is a rather abstract object, and it is hard to read off its properties clearly. A widely used representation of quantum mechanics to study a rich variety of systems is the phase space description in terms of quasiprobability distributions. It is well known that the uncertainty principle makes the concept of phase space in quantum mechanics problematic: a particle cannot simultaneously have a well defined position $\hat{q}$ and momentum $\hat{p}$. Therefore there is no true phase space probability distribution for a quantum mechanical particle. Nonetheless, quasiprobability distribution functions allow to express quantum mechanical averages in a form which is very similar to that of classical averages. Let us consider a classical probability in phase space $P_{cl}(q, p)$ for a particle and an observable $A(q, p)$. Then, the classical average is

$$< A >_{cl} = \int dq \int dp A(q, p) P_{cl}(q, p). \tag{1.20}$$

The analog quantum mechanical problem is described by $\hat{\rho}$ and the quantum average is

$$< \hat{A} >_q = Tr(\hat{A}\hat{\rho}). \tag{1.21}$$

The use of a quasiprobability distribution, P_q, allows to express the quantum mechanical average as

$$< \hat{A} >_q = \int dp \int dq A(q, p) P_q(q, p), \tag{1.22}$$

where the function $A(q, p)$ is derived from the operator $\hat{A}(\hat{q}, \hat{p})$ by a well defined correspondence rule which includes the operator ordering. The operators $\hat{q}, \hat{p}$ are associated with field operators $\hat{a}, \hat{a}^{\dagger}$ by the relations

$$\hat{q} \propto (\hat{a} + \hat{a}^{\dagger}), \qquad \hat{p} \propto (\hat{a} - \hat{a}^{\dagger}). \tag{1.23}$$

Comparing with Eq.(1.11) we see that $\hat{q}, \hat{p}$ are proportional to the real and imaginary quadratures, for this reason also known as position and momentum quadratures of the field. In quantum optics a number of quasiprobability distributions have been introduced, depending on the ordering of creation and destruction operators. The *normal ordering* corresponds to creation operators placed to the left $(\hat{a}^{\dagger})^m \hat{a}^n$. The *antinormal ordering* corresponds to creation operators placed to the right $\hat{a}^n (\hat{a}^{\dagger})^m$. An intermediate situation is given by the *symmetric ordering* in which all the possible orderings are averaged: for example when $m = n = 1$ we have $(\hat{a}\hat{a}^{\dagger} + \hat{a}^{\dagger}\hat{a})/2$. For any ordering a well defined quasiprobability is defined: the P distribution gives averages of normal ordered expressions, the Q distribution gives averages of the antinormal ones, and the Wigner distribution W gives averages of the symmetrically ordered ones.

The quasi-probability distributions can be used as an alternative to the density operator to describe the dynamics of an optical system. Using a well defined correspondence, Eq.(1.14) – or Eq.(1.13) if the system is isolated – is converted into an equation of motion for quasiprobability distributions in the classical phase-space of the system. This is the complex plane with axis $Re(\alpha)$ and $Im(\alpha)$, with the c-number α associated with the eigenvalue of $\hat{a}$ for a coherent state $|\alpha\rangle$ in (1.1). We report here the

quantum classical correspondence, referring for instance to Refs.[Gardiner & Zoller, Carmichael, Barnett & Radmore] for the derivation:

$$
\begin{aligned}
\rho\hat{a}^\dagger &\iff \left(\alpha^* + \frac{1-s}{2}\frac{\partial}{\partial\alpha}\right)\mathcal{W}_s(\alpha,\alpha^*) \\
\hat{a}^\dagger\rho &\iff \left(\alpha^* - \frac{1+s}{2}\frac{\partial}{\partial\alpha}\right)\mathcal{W}_s(\alpha,\alpha^*) \\
\rho\hat{a} &\iff \left(\alpha - \frac{1+s}{2}\frac{\partial}{\partial\alpha^*}\right)\mathcal{W}_s(\alpha,\alpha^*) \\
\hat{a}\rho &\iff \left(\alpha + \frac{1-s}{2}\frac{\partial}{\partial\alpha^*}\right)\mathcal{W}_s(\alpha,\alpha^*) \,.
\end{aligned}
\tag{1.24}
$$

Here we have introduced the notation $\mathcal{W}_s$ for the quasiprobability P_q. The parameter $1 \geq s \geq -1$ defines the choice of the representation; namely, $s = +1$ corresponds to the Glauber-Sudarshan (P) distribution; $s = 0$ to the Wigner W distribution, and $s = -1$ to the Husimi Q distribution. These formalisms have been unified by [Cahill & Glauber] who defined an s-parametrized ordering for the annihilation and creation operators.

In order to obtain the dynamical evolution equation for $\mathcal{W}_s$, it is enough to formally substitute products of field operators and the density operator in the Master equation (1.14) by suitable operations over the distribution, following the mapping (1.24). This procedure allows for a description of the dynamics of the state of the system in terms of a partial differential equation of the type:

$$
\begin{aligned}
\frac{\partial}{\partial t}\mathcal{W}_s &= -\frac{\partial}{\partial\alpha}A_\alpha\mathcal{W}_s - \frac{\partial}{\partial\alpha^*}A_{\alpha^*}\mathcal{W}_s + \frac{1}{2}\frac{\partial^2}{\partial\alpha^2}D_{\alpha\alpha}\mathcal{W}_s + \frac{1}{2}\frac{\partial^2}{\partial\alpha^{*2}}D_{\alpha^*\alpha^*}\mathcal{W}_s + \frac{\partial^2}{\partial\alpha\partial\alpha^*}D_{\alpha\alpha^*}\mathcal{W}_s \\
&\quad + \frac{\partial^3}{\partial\alpha^3}\Theta_{\alpha\alpha\alpha}\mathcal{W}_s + \frac{\partial^3}{\partial\alpha^2\partial\alpha^*}\Theta_{\alpha\alpha\alpha^*}\mathcal{W}_s + ...
\end{aligned}
\tag{1.25}
$$

with D_{ij} and Θ_{ijl} functions of α and α^*. This equation has the same form of the Kramers-Moyal expansion of a classical Master equation [Gardiner], and it is equivalent to the initial quantum Master equation (1.14).

Let us consider the case in which Eq.(1.25), for some s, reduces to

$$
\frac{\partial}{\partial t}\mathcal{W}_s = -\frac{\partial}{\partial\alpha}A_\alpha\mathcal{W}_s - \frac{\partial}{\partial\alpha^*}A_{\alpha^*}\mathcal{W}_s + \frac{1}{2}\frac{\partial^2}{\partial\alpha^2}D_{\alpha\alpha}\mathcal{W}_s + \frac{1}{2}\frac{\partial^2}{\partial\alpha^{*2}}D_{\alpha^*\alpha^*}\mathcal{W}_s + \frac{\partial^2}{\partial\alpha\partial\alpha^*}D_{\alpha\alpha^*}\mathcal{W}_s
\tag{1.26}
$$

with a positive definite matrix D. This is a **Fokker-Planck equation (FPE)** [Risken]: the first derivative terms are called drift terms and A is the drift vector. The second derivative terms are the diffusion terms and D is called diffusion matrix. In general the drift determines the mean or deterministic evolution of the field, $\langle\alpha\rangle$, and the diffusion (with the drift) enters in the dynamics of the correlations. The solution of a FPE is a positive function [Pawula]. Therefore it can be associated with a well defined probability distribution in α-space. Different methods are known to find solutions of a FPE [Gardiner]: in particular the solution is a Gaussian in the cases of linear drift and constant diffusion. In some quantum optics problems the knowledge of the stationary solution is sufficient. It can be found, if particular 'potential conditions' involving the drift and the diffusion are satisfied [Walls & Milburn, Ch.6]. An important property of the FPE is its relation to **stochastic differential equations** [Gardiner]. Any FPE can be

mapped in a set of equivalent Langevin equations,

$$\frac{\partial \alpha}{\partial t} = B_\alpha + C_{\alpha\alpha} f_\alpha(t) + C_{\alpha\alpha^*} f_{\alpha^*}(t) \tag{1.27}$$

$$\frac{\partial \alpha^*}{\partial t} = B_{\alpha^*} + C_{\alpha^*\alpha^*} f_{\alpha^*}(t) + C_{\alpha^*\alpha} f_\alpha(t), \tag{1.28}$$

driven by white Gaussian noise terms f_i. A more detailed description of the relation of Eq. (1.26) with Eqs.(1.27)-(1.28) is given in Appendix A. The importance of the Langevin equations lies in the possibility of performing numerical simulation of these stochastic equations for general complicated drift and diffusion terms. In fact this method is used in most parts of this Thesis.

An important problem is that, in general, only for linear problems Eq.(1.25) reduces to a FPE (in the Wigner representation) through the mapping (1.24). Demanding nonlinear optical regimes are described by Eq.(1.25), that in general has

- third or higher order derivatives ($\Theta \neq 0$), leading to a so called "generalized" FPE,

- non-positive definite matrix D, leading to a so called "pseudo" or "quantum" FPE.

Third or higher order derivatives imply non positive definite solutions $\mathcal{W}_s$ [Pawula]. This means that $\mathcal{W}_s$ can not be interpreted as a well defined probability distribution. In some cases, this non positiveness is a signature of the non-classical behavior of the system. Given generalized or pseudo FPE it is not generally possible to describe the dynamics of the system through stochastic differential equations of the form (1.27)-(1.28). Some *approximations* are needed to reduce the exact Eq. (1.25) to a FPE (1.26). The approximation most used in the literature is probably the system size expansion [Carmichael] leading to a FPE with linear drift and constant diffusion, and removing higher order derivatives in Eq. (1.25). Equivalently, one can approximate the Hamiltonian by a quadratic function of the operators describing the fluctuations of the fields ($\delta \hat{a}_j = \hat{a}_j - \langle \hat{a}_j \rangle$), neglecting higher order terms. These approximations are based on the assumption of "small noise" around the mean trajectory in phase space, and in fact they imply a *linearization* of the dynamics.

We can summarize the procedure here presented in three steps:

1. Derivation of the Master equation (for open systems) in terms of the Hamiltonian describing the fields.

2. Mapping through (1.24) the equation for the density operator into the dynamical equation (1.25) for a quasi-probability function.

3. When Eq. (1.25) is a FPE, or can be approximated by a FPE, formulation of an equivalent stochastic description for the c-numbers variables, associated with the fields operators.

In this work we present different approximated and exact methods, that lead to a FPE and, therefore, allow for a stochastic description of nonlinear optical phenomena. In regimes characterized by small fluctuations, we use the linearization approximation mentioned above (Ch.3 and Ch.5). In order to describe regimes in which the fluctuations are macroscopic and a nonlinear treatment is needed, we

will consider different methods. In Ch.2 we use a method based on a doubling phase space technique to treat the anharmonic oscillator, while in Ch.4 we discuss two different phase space approximations to describe the convective regime, introduced in Sect.1.3.2.

In the following we review some properties of different phase space quasi-probability distributions in relation to their dynamics for optical problems, referring to Refs.[Schleich, Hillery & al., Gardiner & Zoller, Barnett & Radmore, Walls & Milburn] for a more detailed description.

1.2.3.b.1 Glauber-Sudarshan and positive P representations: The simpler definition of the P representation [Glauber, Sudarshan] is

$$\hat{\rho} = \int d^2\alpha P(\alpha, \alpha^*)|\alpha\rangle\langle\alpha|, \tag{1.29}$$

in which the quasi-probability $P(\alpha, \alpha^*)$ appears as the "weight" function of the diagonal representation in coherent states of the density operator $\hat{\rho}$. From this definition we obtain

$$
\begin{aligned}
\langle : \hat{a}^n(\hat{a}^\dagger)^m : \rangle &= \langle (\hat{a}^\dagger)^m \hat{a}^n \rangle = Tr(\hat{a}^n \hat{\rho}(\hat{a}^\dagger)^m) = \int d^2\alpha P(\alpha, \alpha^*)(\alpha^*)^m \alpha^n Tr(|\alpha\rangle\langle\alpha|) \\
&= \int d^2\alpha P(\alpha, \alpha^*)(\alpha^*)^m \alpha^n.
\end{aligned}
\tag{1.30}
$$

This Equation is known in the literature as the 'optical equivalence theorem', affirming the equivalence between the quantum mechanical average and the average over the P distribution. Therefore, normal ordered moments can be calculated through a c-number integral weighted by the P distribution, through the correspondence $(\hat{a}^\dagger)^m \hat{a}^n \to (\alpha^*)^m \alpha^n$.

As examples of the P representation we consider a coherent state $|\alpha_0\rangle$, for which

$$P(\alpha, \alpha^*) = \delta^{(2)}(\alpha - \alpha_0), \tag{1.31}$$

a number or Fock state $|n\rangle$, for which

$$P(\alpha, \alpha^*) = \frac{e^{|\alpha|^2}}{n!} \frac{\partial^{2n}}{\partial\alpha^n \partial\alpha^{*n}} \delta^2(\alpha), \tag{1.32}$$

and a field at thermal equilibrium, for which

$$P(\alpha, \alpha^*) = \frac{1}{\pi\bar{n}} e^{-|\alpha|^2/\bar{n}}, \tag{1.33}$$

where $\bar{n}$ is the mean photon number. We have seen how the 'optical equivalence theorem' establishes an equivalence between quantum and classical statistical theories of the electromagnetic field, when the P representation has the properties of a probability distribution. This happens for instance for thermal states. However, the P representation is not always well behaved, being negative and highly singular for several states of interest as, for instance, for Fock states. For such singular behaviors, even though Eq. (1.30) remains formally valid, there is no longer such a simple correspondence between quantum and classical theories. Therefore the behavior of the P representation identifies the boundaries between the worlds of classical statistical and quantum statistical physics [Kimble]. In the rest of this work we refer as **"non-classical states"** to states leading to a negative P representation. In the

following we will present other representations of the density operator in coherent states that are useful (being positive and regular) also for non-classical states. The singularity of the P representation for nonlinear problems is evident by the form of the corresponding dynamical equation, that far from being a Fokker-Planck equation, can show negative diffusion or higher than second order derivatives.

A generally invoked procedure in nonlinear optical problems presenting *negative diffusion* is a doubling space technique leading to a class of generalized P representations [Gardiner & Zoller]; the most used is the **positive P representation**, P_+:

$$\hat{\rho} = \int d^2\alpha d^2\beta P_+(\alpha, \alpha^*, \beta, \beta^*) \frac{|\alpha\rangle\langle\beta^*|}{\langle\beta^*|\alpha\rangle}, \tag{1.34}$$

This definition includes all diagonal and off-diagonal coherent state components of the density matrix. It can be demonstrated [Gardiner & Zoller] that a positive function exists even for highly non classical fields. The P_+ representation is generally governed by a genuine Fokker-Planck equation with positive diffusion. However, in some systems this doubling phase-space technique presents technical problems such as divergent trajectories, associated with large excursions of the variables α, β in the complex plane [Gilchrist & al., Gardiner & Zoller]. This behavior has been generally associated with relatively large nonlinearities. An example is the case of the anharmonic oscillator, treated in Ch.2 and analyzed in Ref. [Gardiner & Zoller, Ch.6.7].

When the dynamical equation for P has *derivatives of higher order* than the second, other techniques are needed: in some regimes scaling arguments can be used [Carmichael] allowing to neglect the terms with these higher order derivatives. Recently, another approximated method has been proposed for the case in which Eq.(1.25) has only up to third order derivatives, consisting in a mapping of this partial differential equation into stochastic difference equations [Olsen & Plimak].

1.2.3.b.2 Husimi Q representation: An interesting alternative to the Glauber-Sudarshan P representation is the Q representation, corresponding to anti-normal ordering of field operators [Husimi]

$$\langle\hat{a}^n(\hat{a}^\dagger)^m\rangle = \int d^2\alpha Q(\alpha, \alpha^*)\alpha^n(\alpha^*)^m. \tag{1.35}$$

The most important property of this representation is that it satisfies the requirements for a true probability distribution. In fact the Q representation may be defined by the diagonal matrix elements of the density operator in the space of coherent states

$$Q(\alpha, \alpha^*) = \frac{1}{\pi} < \alpha|\hat{\rho}|\alpha > \tag{1.36}$$

and it is both positive and bounded [Gardiner & Zoller]:

$$\int d^2\alpha Q(\alpha, \alpha^*) = 1. \tag{1.37}$$

We point out that the definition (1.36) uniquely determines the density operator $\hat{\rho}$, even if only the diagonal elements in the coherent states are provided, because of the over completeness of the coherent states. A way to see the regularity of this representation is through its relation with the P function:

$$Q(\alpha, \alpha^*) = \int d^2\beta P(\beta, \beta^*)e^{-|\alpha-\beta|^2}, \tag{1.38}$$

i.e. the Q function results from a Gaussian convolution of the P representation. Hence a coherent state corresponds to a Gaussian Q distribution, as it is immediately seen from Eq.(1.31). Physically the regularity of the Q representation is due to the fact that it corresponds to simultaneous measurements of orthogonal quadratures, as limited by the Heisenberg principle, in a eight-port homodyne detector (see [Leonhardt, Ch.VI] and references therein).

The dynamical equation for the Q distribution for nonlinear problems of interest is often a pseudo FPE, with a non-positive diffusion matrix. On the other hand, we have seen that the Q function is always positive. The apparent contradiction is solved considering that not all mathematical forms for the Q function correspond to physical states: the selection of a restricted number of initial conditions for the dynamical equation leads to positive solutions of the FPE with nonpositive definite diffusion matrix [Gardiner & Zoller]. In any case, the problem of a FPE with non-positive diffusion matrix is the impossibility of a direct mapping into a set of equivalent Langevin equations. Some years ago [Yuen & Tombesi] proposed a method to convert the evolution equation for the Q quasi-probability into a pair of spatial differential equations, with a doubling space phase technique similar to that of the P_+ representation. This technique is described and applied in the case of the anharmonic oscillator in Ch.2. In a recent paper [de Oliveira] generalizes the doubling phase space techniques to generic distributions, defining *positive non diagonal quasiprobabilities* for any s ordering.

1.2.3.b.3 Wigner representation: Historically, the first quasiprobability function was introduced by [Wigner] in 1932. The Wigner (W) function corresponds to symmetrical ordering of field operators. We can define this distribution in terms of the characteristic function

$$\chi_W(\lambda, \lambda^*) = Tr\{\hat{\rho}\, e^{\lambda \hat{a}^\dagger - \lambda^* \hat{a}}\} \tag{1.39}$$

as

$$W(\alpha, \alpha^*) = \frac{1}{\pi^2} \int d\lambda^2 e^{-\lambda \alpha^* + \lambda^* \alpha} \chi_W(\lambda, \lambda^*). \tag{1.40}$$

An exciting problem explored recently is the experimental determination of the Wigner function of a single light mode. It was first shown theoretically [Vogel & Risken (89)b] that quadrature amplitude distributions measured in homodyne detection can be used to perform a complete reconstruction of the Wigner function. This method, called quantum tomography, was successfully realized in a series of experiments [Leonhardt]. The quantity recorded in the quantum tomography experiments was the statistics of the count difference of photodetectors facing the signal field superimposed to a strong coherent field (see for instance [Breitenbach & al.] and reference therein). The Wigner function was reconstructed from these data using numerical algorithms of the inverse Radon transform. An experimental reconstruction of the Wigner function of the squeezed vacuum state is represented in Fig.1.4. The corresponding analytical expression

$$W(p, q) = \frac{1}{\pi} \exp(-e^{2\zeta} q^2 - e^{-2\zeta} p^2) \tag{1.41}$$

is a Gaussian with squeezed width in the p direction, where p and q are related to the real and imaginary parts of α. The Gaussian shape, squeezed in the p direction, can be recognized in the reconstruction
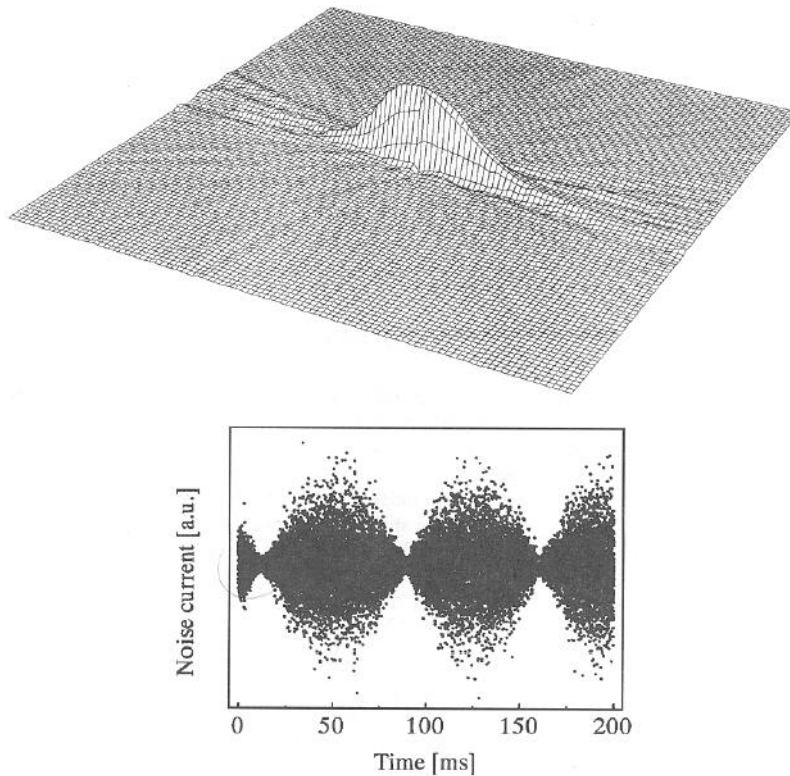
Figure 1.4: Wigner function (top) and quadrature fluctuations (bottom) for a squeezed vacuum. We see clearly a remarkable squeezing in phase space and the corresponding breathing of the quadrature noise. The noise trace shows a part of the experimental data used to reconstruct the depicted Wigner function via optical homodyne tomography. Taken from Ref. [Leonhardt].

in Fig.1.4 (top). The phase of the state is almost 'fixed', while strong fluctuations are evident in the amplitude (Fig.1.4 (bottom)).

Different equivalent definitions have been given for the Wigner function: in 1977 [Royer] defined W as the expectation value of a parity operator. In connection with this definition, alternative measurement of this quasi-probability have been proposed recently. These measurements are based on photocounting of even or odd photon numbers coincidences [Wallentowitz & Vogel, Banaszek & Wódkiewicz (96)]. Novel operational meanings of the W and also of the Q distribution functions have been proposed in Bell's tests of quantum non locality [Banaszek & Wódkiewicz (99)].

The W function obeys a well defined FPE for quadratic Hamiltonians, or equivalently when linearization approximations are used. For more general systems of interest in quantum nonlinear optics, the W function often obeys generalized FPE's, with derivatives of higher than second order. It is not generally known how to treat these higher order terms within a stochastic formalism. The usual approach is to simply drop these terms to produce a genuine FPE and the so called "stochastic electrodynamics" [Marshall]. It has been shown, however, that this frequently used approximation does not correctly reproduce higher-order correlations such as those predicted to occur in parametric oscillators

[Drummond & Kinsler, Kinsler, Chaturvedi & Drummond, Pope & al.]. The W distribution will be used in Ch.3 and Ch.4.

1.3   Optical pattern formation

Pattern formation is a **self-organization** phenomenon, due to the interplay between the nonlinear dynamics of a field and the coupling between different points in space in an extended system [Haken, Nicolis & Prigogine, Cross & Hohenberg]. When the system is driven away from equilibrium by an energy input, the response of an initially uniform system can show space or time structure above a certain threshold for the input. Non equilibrium spatial structures have been investigated in hydrodynamics, chemistry, biology, granular materials, optics, etc [Cross & Hohenberg, Gollub & Langer]. Depending on the system under consideration the spatial coupling can be due to the diffraction of the fields (for example in optical devices) or to diffusion (in fluids dynamics or chemical reactions) or to non-local interaction (in presence of feed-back [Ramazza & al.]).

A most interesting aspect of pattern formation is that, in spite of the many different systems in which patterns appear, there is a fundamental **universal** character, allowing for a unified approach to the problem. Characteristics such as the number of degrees of freedom, symmetries, the type of nonlinearity and of coupling terms (gradients, diffusion, diffraction...) overcome the importance of the specificity of the optical, chemical, acoustical or fluid system. For example a rich variety of phenomena near the instability threshold can be universally described in terms of amplitude and phase equations. These are theoretical powerful instruments to approach the problem of pattern formation [Walgraef].

In this Section we discuss pattern formation in the context of Optics. **Optical Pattern Formation** refers to the spatial or spatio-temporal phenomena that arise in the structure of the electromagnetic field in the plane orthogonal to the direction of propagation, when the field is interacting with a nonlinear medium. Pattern formation in optical systems shows peculiar features with respect to other systems, such as chemical reactions or hydrodynamics: as already mentioned, the spatial coupling is due to the diffraction of the field, that is a conservative term, at difference to the diffusive dissipative coupling appearing in other systems. Also, optical systems are very fast, opening the possibility to use spatial structures in applications, such as multichannel communication and parallel optical information processing. Both from the theoretical and technological points of view, optical systems are interesting also in relation to the extra degree of freedom given by the vectorial character of the fields: in fact the polarization state of the electric field is often involved in the pattern formation process. Finally, as will be discussed in Sect.1.4, optical structures display interesting macroscopic quantum effects, even at room temperature [Lugiato & al. (99)].

First transverse optical phenomena were not discussed in the context of optical pattern formation. In such earlier works the transverse degree of freedom of the fields was considered, but not studying the possibility of self-organized spatial structures. As an example in this line of research, we refer to the experiments of up-conversion of infrared images, started in 1970s [Midwinter, Firester] and the more recent parametric amplification of images [Fainman & al.]. In these experiments, devices based

on quadratic nonlinearities allow to transfer or amplify a "copy" of the input image in an output signal[7]. This phenomenon lies in the area of **transverse optics**, even though it is conceptually different from the spatial instability phenomena that we will consider in the following, in which the emerging spatial profile in the output field arises spontaneously instead of being injected in the system.

Among the **instability phenomena** first studied in transverse nonlinear optics, leading to modifications of the transverse profile of the propagating field, we mention self-focusing, filamentation and solitons in single pass systems [Abraham & Firth, Arecchi & al.]. Most of these spatial effects do *not* appear above some *threshold* of the input intensity. As an example, in Fig.1.5 we show the experimental observation of filamentation of a laser beam passing through a cell of sodium vapor [Bennink & al.] (Fig.1.5a). The filamentation process is the formation of spots with diameters small compared with the diameter of the laser beam [Arecchi & al.]. This instability appears for any laser intensity: in other words this process has no thresh-

Figure 1.5: (a) Experimental setup; patterns were recorded both in the near and far fields. Typical conditions were input power, $150mW$; input beam diameter, $160\mu m$; laser frequency, $2GHz$ blue-detuned from the sodium D2 line; cell length, 7 cm. (b) Example of pattern formation as observed in the near field (left) and far field (right). Taken from Ref.[Bennink & al.].

old. In Fig.1.5b a three-filament near-field pattern is shown. The far-field pattern consists of the coherent superposition of the diffraction pattern from each of the three beams and thus has the form of a honeycomb pattern. The far field is the Fourier transform of the near-field pattern.

The study of spatial structures in transverse nonlinear optics beyond some threshold is a relatively recent subject of investigation: In 1987 [Lugiato & Lefever] showed theoretically that a cavity filled with a Kerr medium and driven by a plane-wave laser beam allows for the spontaneous formation of a stationary pattern in the transverse profile of the field, above a threshold value of the input field. The predicted structure is a stripe pattern with a periodicity determined by the detuning between the cavity and the pump beam frequencies. In the last years, many systems and configurations have been theoretically and experimentally studied. Among them we mention cavities filled by a nonlinear medium pumped by a laser field, nonlinear media pumped by counter-propagating beams, single mirror configurations (with the medium injected by the laser input and by the reflected field) and laser devices. Specific review papers and Special Issues discussing optical pattern formation in these devices are [Abraham & al., Abraham & Firth, Lugiato, Lugiato & al. (95), Lugiato & al. (99), Arecchi & al.]).

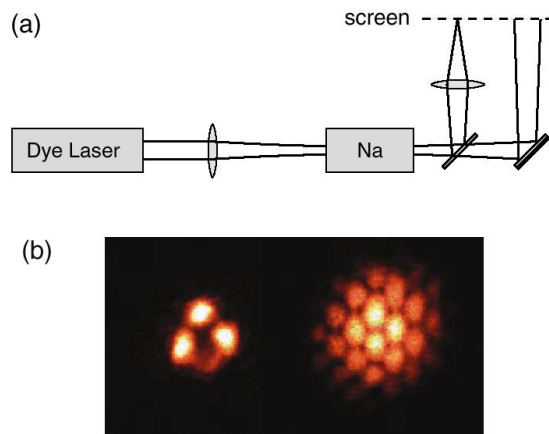[7]A more recent overview on classical image parametric amplification and its applications can be found in [Lantz & Devaux]. Some recent developments on image amplification and the interest of this phenomenon in the context of quantum optics will be discussed in sect.1.4.

Several types of spatial structures have been predicted and observed in these systems: we mention stripes, squares and hexagonal patterns, localized structures and disordered structures. Fig.1.6 shows transverse patterns observed by [Aumann & al.] in a single mirror configuration. This is device similar to that shown in Fig.1.5a), but with optical feed-back coming from a mirror. [Aumann & al.] found square patterns for linear polarized input laser beam, while changing the polarization to be slightly elliptical instead of linear, hexagons instead of squares arise at the threshold power for pattern formation. Fig.1.6 shows the transition to hexagons and squares patterns, in the two circular polarization components of the beam, changing the polarization state of the input laser.
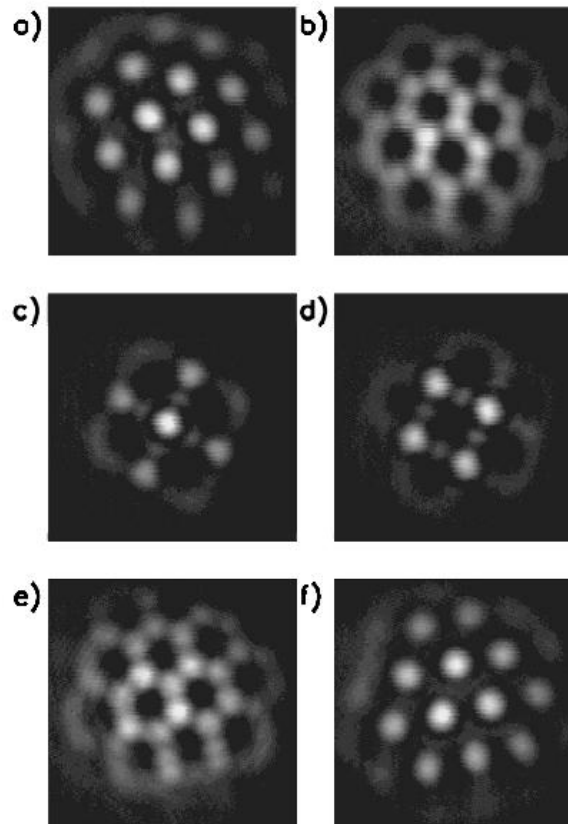
Figure 1.6: Transition from positive to negative hexagons via squares in the circular polarization components of the beam (left-hand column, left circular polarization; right-hand column, right circular polarization) induced by a change of sign of the input polarization ellipticity. The transverse size of the images is $2.6mm$. Taken from Ref.[Aumann & al.].

In Fig.1.7 we show an example of experimental patterns observed in a nonlinear resonator, a type II OPO. This is one of the devices that we will consider in this work. The near field Fig.1.7a and Fig.1.7b shows a spatial modulation, in form of rings, where the circular symmetry is dictated by the geometry
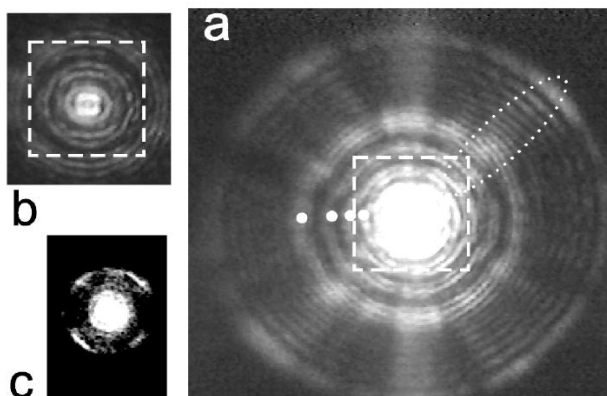
Figure 1.7: Transverse structure observed in the signal field: (a) near field with a saturated center, wide rings, and thin fringes (see, for example, inside the dotted ellipse); (b) detail of the central part of the near field (the intensity is reduced by a grey filter); and (c) far field configuration with a saturated center and a bright ring. (Taken form Ref.[Vaupel & al.]).

of the cavity [Vaupel & al.].

Another interesting phenomenon is the possibility of optical systems to support localized and spatially disordered structures. When there are two or more homogeneous stable solutions, the system is bistable or multistable, respectively. In the case of bistability, the spatial dependence of the transverse profiles of the fields allows for an interesting scenario: different solutions can be selected in different spatial regions, separated by domain walls. In two transverse spatial dimensions, these domain walls typically evolve reducing their curvature. In some cases (see Ref.[Gomila & al. (02)]) this phenomenon leads to the formation of localized structures. In other cases the domain walls are modulationally unstable and labirintyne patterns arise [Gallego & al., Gomila & al. (01)]. If only one transverse dimension is considered, domain walls lock at different distances, forming a disordered structure. This structure is an example of frozen chaos [Coullet & al.] and it is discussed in Ch.4.

1.3.1   Nonlinear media in optical resonators

In this work we consider passive optical devices, such as Optical Parametric Oscillators (OPO's) (Ch.4-5) and Kerr resonators (Ch.3). The specific features of these systems –different regimes, type of patterns, thresholds– are reviewed in the corresponding Chapters. Here we focus on the *model* equations common to the description of these systems. Let us consider a monochromatic linearly polarized laser field

$$Ee^{i(k_z z - \omega_0 t)} \tag{1.42}$$

pumping a cavity filled with a nonlinear medium with atomic frequencies far from ω_0. The input field amplitude E is a control parameter, leading to instabilities when its modulus is increased above some threshold value. Also the cavity detuning – the difference between the frequency ω_0 and the nearest cavity frequency – is a control parameter.

The cavity consists on two parallel mirrors (Fabry-Perot) or three or four mirrors (ring cavity as in the Fig.1.8) confining the input electromagnetic wave. In this work we consider ring cavities with planar mirrors.

The description of these resonators features electromagnetic fields, which depend on the four coordinates (x, y, z, t), and subject to appropriate boundary conditions due to the cavity mirrors. The nonlinearity of the system
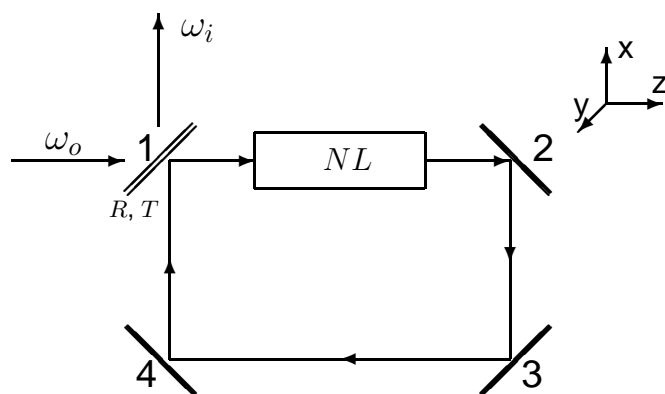

Figure 1.8: Ring cavity with a nonlinear (NL) medium. Mirror 1 partially transmits the input beam with frequency ω_0. The output fields in the more general case are at different frequencies ω_i, with i =0,1,2,.... Mirrors 2,3 and 4 are completely reflecting.

comes from the nonlinear polarization of the medium. Some approximations are needed to deal with

these problems, due to their complexity. The optical **models** we consider in this work are derived under the standard conditions of slowly varying envelopes, mean-field, and single longitudinal mode. In the following we focus on the qualitative meaning of these approximations; a detailed analysis can be found in [Lugiato & al. (99), Arecchi & al.]. Under the condition of atomic frequency bandwidth much smaller that the free spectral range of the cavity[8], only one longitudinal mode of the cavity is relevant. Also, the use of lasers as driving sources (see Eq.(1.42)) restricts the time dependence of the fields to a quasi-monochromatic behavior. Therefore the fields are of the type

$$f(x, y, z, t)e^{i(k_z z - \omega_0 t)} \tag{1.43}$$

where the exponential term accounts for a plane wave moving along the direction z of the cavity axis, and the dependence of f on z and t is slow:

$$\left|\frac{\partial f}{\partial z}\right| \ll k_z|f|, \qquad \left|\frac{\partial f}{\partial t}\right| \ll \omega_0|f|. \tag{1.44}$$

This is the slowly varying envelope approximation (SVEA). It is also assumed that the fields propagate in the cavity forming small angles with the cavity propagation axis z: this is the paraxial approximation, valid whenever the transverse wave-vectors components of the field ($\vec{k}_\perp = (k_x, k_y)$) are small with respect to the longitudinal component k_z.

We will consider optical cavities characterized by a small transmittivity $T \ll 1$ of the input/output mirror 1: most of the intracavity field is reflected by the mirror 1, so that the cavity photon lifetime is long. Hence the field bounces in the cavity and interacts with the nonlinear medium for a long time, allowing for significant nonlinear effects, even if the effects are small in a single round-trip. The mean field limit [Bonifacio & Lugiato] assumes that the variation of the field in the longitudinal coordinate z during a cavity round-trip can be neglected. Hence the propagation and cavity boundary condition effects can be averaged along the z direction, leading to fields envelopes depending only on the transverse coordinate (x, y) and on time. For a discussion of the validity of the mean field approximation see Refs. [Oppo & al. (01), Tlidi & al., Le Berre & al.(99)].

The Equations obtained for the field envelopes under the approximations mentioned above have the general form:

$$\frac{\partial}{\partial t}A_j = -\gamma_j(1 + i\Delta_j)A_j + E_j + ia_j\nabla_\perp^2 A_j + g_j(A_0, A_1, \dots). \tag{1.45}$$

A_j are envelops corresponding to different fundamental frequencies or polarization components of the field vectors. The coefficients γ_j, Δ_j and a_j describe the losses, the cavity detunings and the diffraction lengths, respectively. Generally the input field E_j is not vanishing only for one particular component j'. The nonlinear functions $g_j(A_0, A_1, \dots)$ describes the coupling between modes, as determined by the polarization $\vec{P}(\vec{E})$ of the medium. For $\chi^{(2)}$ media the nonlinear function is quadratic, and for $\chi^{(3)}$ media the nonlinear function is cubic in the fields.

For small input intensities $|E_j|^2$, or, equivalently, for large cavity detuning, the field modes in the cavity are homogeneous in the transverse direction, the steady state solutions A_j^s being proportional to

---

[8]The free spectral range $c/\mathcal{L}$ is the separation between the resonant frequencies of the cavity, where $\mathcal{L}$ is the cavity length.

the input or vanishing. In Second Harmonic Generation, notwithstanding the smallness of the input, the nonlinear effects allows the emission of a field at the second harmonic frequency for any pump intensity, beside the field at the pump frequency. Hence both the steady pump and second harmonic intensities depend upon the input energy and are transversely homogeneous. Further increasing the pump intensity, above some *threshold*, this state becomes *unstable* allowing for new solutions. In general systems described by Eq.(1.45), new solutions exist above a threshold value of the pump and they can appear at a different temporal frequency or in a polarization component not injected by the pump. For instance, in the OPO there is a threshold for the down-conversion process: above the threshold, beside the pump mode a signal mode at half the frequency is emitted. The new stable state can be another homogeneous solution, or can show a transverse spatial structure. In the example of the OPO, under proper conditions, the signal emitted at threshold has the form of a stripe pattern [Oppo & al. (94)]. This instability, leading to a stationary pattern from a spatially homogeneous state is known as **Turing instability**. It has been studied by [Turing] in nonlinear chemical systems, characterized by reaction and diffusion. Above the threshold for the Turing instability any perturbation of the steady spatially homogeneous solution would grow in time, allowing the system to evolve into a stable stationary pattern [Aguado & al.].

Below the threshold of optical pattern formation any perturbation of the homogeneous state is damped and decays. At threshold, the perturbations at some wave-number are linearly undamped. Generally this transverse wave-number is determined by the cavity detuning Δ_j. More precisely, a slight cavity detuning Δ_j allows for off-axis emission. In fact, the lack of cavity resonance of the axis modes can be improved by emission of tilted modes such that

$$k_\perp = |\vec{k}_\perp| = \sqrt{\Delta_j}. \tag{1.46}$$

This mechanism was described in Ref.[Oppo & al. (94)] for a type I OPO. Recently [Bortolozzo & al.] showed experimentally the evidence of the influence of cavity detuning in determining the periodicity of the pattern selected in an optical oscillator with one transverse spatial dimension.

Above threshold, a pattern is selected. The shape of the pattern can be visualized in the far field which is the Fourier transform of the near field. For instance, the far field of the signal field in the OPO above consists of two intense spots. These spots correspond to the transverse non-vanishing wave-vectors, $\vec{k}_+$ and $\vec{k}_-$, that interfere producing the near field stripe pattern. The wave-number $|\vec{k}_\pm|$ is linearly selected at threshold, but the shape of the spatial structure (stripes instead of hexagons or squares) is determined by a nonlinear selection process [Cross & Hohenberg].

1.3.2 Noise effects in pattern formation

Noise in spatially extended systems has important consequences (see Refs. [San Miguel & Toral, García-Ojalvo & Sancho]). In the previous section we mentioned that a perturbation of an **unstable** state grows taking the system to a new stable configuration. Generally, noise sources are at the basis of such perturbations. Noise effects are also observed in homogeneous as well as in pattern **stable** solutions, respectively below and above the threshold of optical pattern formation. In this Section we
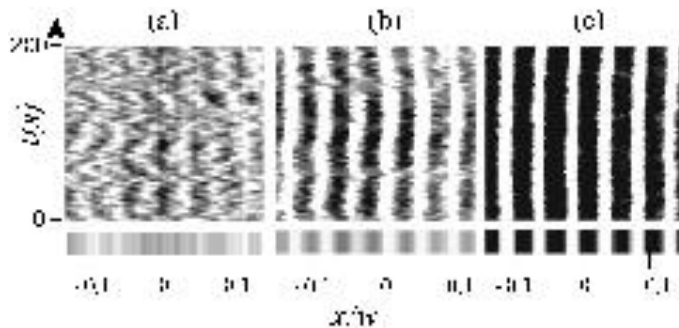
Figure 1.9: Evolution of the roll patterns in the near threshold region for different values of the incident intensity. Vertical axis, time; horizontal axis, space. The lower rectangles represent averages over 500 s. (a) and (b): noisy precursors below threshold; (c) stable pattern above threshold. Taken from [Agez & al., Fig.2].

discuss these two regimes. Then we introduce a more striking manifestation of noise: noise sustained patterns.

Below the threshold of pattern formation an interesting phenomenon is the one of **noisy precursors** (see Fig.1.9). This phenomenon corresponds to the anticipation below threshold of some temporal (frequency) [Jeffries & Weisenfeld] or spatial (wavenumber) characteristics of the state appearing above threshold. Below threshold the homogeneous state is stable: in fact any spatial perturbation relaxes, as represented in Fig.1.10a. However, perturbations at different wavenumbers are not attenuated at the same rate. Noise continuously perturb the stable state at all wavenumbers and perturbations at the critical wavenumber –selected at threshold– are *less damped*. A far field image below the threshold of pattern formation is dominated by an intense circle, with radius given by the critical wavenumber. This weakly damped modes are the noisy precursors. In Fig.1.9 we show the noisy pattern precursors observed experimentally in a Kerr-like slice subjected to one-dimensional optical feedback (for a description of the device see Ref.[Agez & al.]). These precursors are rolls with an undefined spatial phase which wander erratically and lock spatially when crossing the threshold. In Sect.1.4 we will introduce the strictly related phenomenon of quantum images.

Above the threshold of pattern formation, when the pattern is stable, noise also influences the system. In Ch.3 the role of noise is discussed in connection with the breaking of continuous space translation symmetry by pattern formation. We show that the fluctuations are dominated by the Goldstone mode, that tends to restore the translational symmetry broken by the appearance of a modulated structure. Another important effect of noise is the excitation of long wavelength modes that are weakly damped (soft modes) [Foster]. These soft modes are responsible of the local deformations of the fluctuating pattern and are known to destroy long range order in 1D systems [Viñals & al.].

So far we have discussed situations in which fluctuations are not amplified. A different situation is observed in presence of unstable states. In 1985 [Deissler] investigated the effects of a group *velocity* term in the context of Poiseuille flows. He showed that when the system is not Galilean invariant, a new regime of amplification of the perturbations appears, in which small fluctuations grow macroscopically as they move spatially. In Fig.1.10b we show the perturbation at two different times: we observe that –although the perturbation locally decreases– it is growing when it travels in the system. In fact, the perturbation grows but the advection velocity overwhelms the speed of spreading in the direction of the advection. An instantaneous perturbation at a time t is advected by the system, that is ultimately
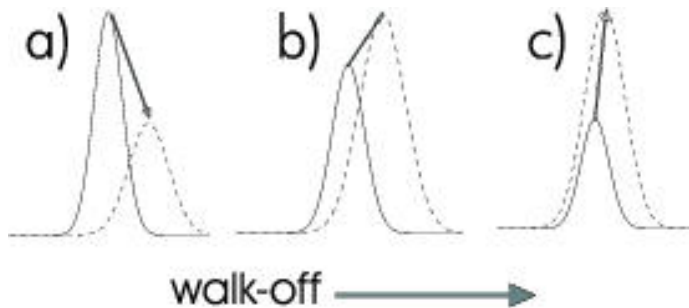
Figure 1.10: Evolution of a perturbation of an homogeneous state. The continuous line is the initial perturbation at time t. The dashed line represents the perturbation at time $t'\rangle t$. a) the homogeneous state is stable; b) the homogeneous state is convectively unstable; c) the homogeneous state is absolutely unstable

left undisturbed. This is the convective unstable regime [Infeld & Rowlands, Ch.3]. On the other hand, in the absolutely unstable regime, the perturbation grows in time at any fixed position, as shown in Fig.1.10c. Therefore, in the absolutely unstable regime, the perturbation grows taking the system from the unstable state to a new state.

The importance of the convective unstable regime is evident in presence of a continuous perturbation, such as a source of noise. Perturbations grow continuously and create a noise-sustained state. The patterns observed in this regime are due to the self-organization of the fluctuations and are called **noise sustained structures**. These noise sustained patterns are observed only when noise is present: If the noise is switched off, the pattern travels in the system, and finally an homogeneous state is reached. The difference with the absolutely unstable regime is evident: noise is needed only to reach a pattern configuration from an unstable state, but, if noise is switched off, a traveling pattern survives in the absolutely unstable regime.

Convective instabilities have been experimentally demonstrated in fluid systems by [Babcock & al., Tsameret & Steinberg]. Any system with an advection term and not translational invariant will be convectively unstable sufficiently close to the onset of the instability [Deissler]. This type of instability has also been predicted in several optical systems subject to a transverse walk-off. [Santagiustina & al. (97)] showed noise sustained structures in a cavity filled with Kerr media, with the pump injected forming a small angle with the cavity axis. In this system noise sustained rolls appear, with amplification factors of the noise up to 10^5. Convective instability has also been demonstrated in type I [Santagiustina & al. (98)a, Santagiustina & al. (98)b, Santagiustina & al. (99)] and type II [Izús & al., Ward & al. (98)] Optical Parametric Oscillators: here the transverse walk-off is due to the misalignment of the Poynting vectors and it is related to the phase matching process (see appendix B).

Convective unstable regimes are characterized by **macroscopic amplified** fluctuations around the unstable reference homogeneous state. For comparison, we remind that noisy precursors are weakly damped fluctuations. The macroscopic fluctuations in the convective regime involve several spatial and temporal modes. In fact, this regime is characterized by broad spectra both in frequency (looking at the temporal behavior in a fixed point of the transverse field profile $\vec{x}$) and in wave-vectors (Far Field profile in a fixed instant t). The transition from the convectively unstable regime to the absolutely unstable regime is characterized by a sudden narrowing of the spectra. In Ch.4 we will discuss these features when the sources of noise are quantum fluctuations.

The convective regime appears near the onset of the spatial instability: in fact it can be considered

as the **precursor** of the absolutely unstable regime. This is a fundamental difference with respect to convective instability in systems such as parametric amplifiers. The latter have neither a threshold for the convective regime nor they show transition to the absolutely unstable regime.

1.4   Optical quantum structures

The subject of quantum optics in spatially extended systems is a wide area, including so different phenomena as spontaneous Parametric Down Conversion in a quadratic crystal –leading to spatially separated pairs of quantum correlated photons–, amplification of images –with reduced signal to noise ratio–, and quantum fluctuations in the process of pattern formation –generating quantum states of the macroscopic radiation field–. This work is concerned with the last class of problems, focusing on optical quantum structures. It describes quantum features associated with self-organized spatial structures in nonlinear optical systems.

An overview of the main ideas on this subject needs the basic concepts presented in the previous two Sections. The first step is the introduction of a proper formalism and the generalization of the quantum effects, presented in Sect.1.2, from the temporal domain to the spatial one. We are considering the spatial dependence of quantum fluctuations and the possibility of quantum effects in local portions of the transverse profile of the electromagnetic field. We assume paraxial fields with a narrow spectrum around the fundamental temporal frequency. These fields depend on the transverse space coordinate $\vec{x} = (x, y)$ and time t. The optical pattern formation process involves the dependence of the field on the coordinates $\vec{x}$ [9]. The spatial profile of the field in the transverse plane can be detected by means of a photodetection array or a CCD (charge-coupled-device) camera, whose pixels span the transverse plane of the beam. In this work we treat systems in which the fields resonate in a cavity. For field modes inside the cavity ($\hat{A}$) the equal time commutator is

$$\left[\hat{A}(\vec{x}, t), \hat{A}^\dagger(\vec{x}', t) \right] = \delta(\vec{x} - \vec{x}'), \tag{1.47}$$

while the commutator at different times depends on the intracavity dynamics [Barnett & Radmore, Barnett & al.]. Divergences due to the δ-functions appear because of the assumption of a continuous of modes in the quantization process, and are removed when spatial averages of the measure process are taken into account [Bohr & Rosenfeld].

In this context, the spatial dependent operator $\hat{A}$ replaces the $\hat{a}$ mode introduced in Sect.1.2. In the phase space treatment (Sect.1.2.3.b), a spatial dependent function $\alpha(\vec{x})$ replaces now the c-number α. Therefore the quasi-probabilities $\mathcal{W}_s$ are now distribution functionals of spatial dependent fields ($\mathcal{W}_s(\alpha(\vec{x}), \alpha^*(\vec{x}))$), and in the correspondence (1.24) the derivatives $\partial/\partial\alpha$ are replaced by functional derivatives $\delta/\delta\alpha(\vec{x})$ [Gatti & al. (97)1].

Using this formalism, the quantum effects described in Sect.1.2 can be generalized to spatial dependent fields. This spatial dependence adds a new degree of freedom, that opens new possibilities in

---

[9]We consider here the general case of a transverse plane. However, particular devices configurations and the identification of proper symmetries in the system allows for an approximated $1D$ descriptions (x). Both $2D$ and $1D$ treatments are presented in this work.

Figure 1.11: Single counts (○) and coincidence (●) measurements taken with a photodetector fixed and the other scanned in the vertical direction (along which are placed the slits). Due to the low rate of down-conversion, data are relative to (long) sampling times of $1000s$. Taken from Ref.[Nogueira & al.].
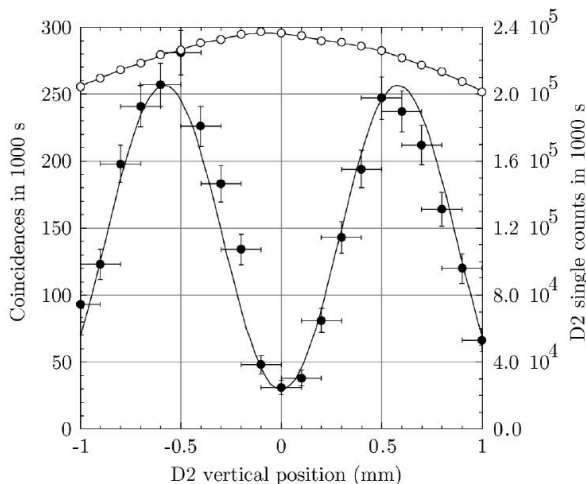
the investigation of quantum effects. The behavior of the fluctuations in local portions of the transverse profile of the field, and the correlations between the fluctuations in separated points can be investigated.

The temporal photon-antibunching (1.8) is generalized to the spatio-temporal photon-antibunching. This phenomenon is observed when

$$g^{(2)}(\vec{\xi}, \tau) \geq g^{(2)}(\vec{0}, 0),$$ (1.48)

where we have introduced the second-order *spatio-temporal* coherence function for homogeneous stationary fields

$$g^{(2)}(\vec{\xi}, \tau) = \frac{\langle : \hat{I}(\vec{x}, t)\hat{I}(\vec{x} + \vec{\xi}, t + \tau) : \rangle}{\langle \hat{I}(\vec{x}, t)\rangle^2}.$$ (1.49)

The **spatial photon-antibunching** is the effect due to non-classical correlations between different points [Le Berre & al.(79)] characterized by

$$g^{(2)}(\vec{\xi}, 0) \geq g^{(2)}(\vec{0}, 0).$$ (1.50)

It has been recently observed by [Nogueira & al.] in an interference experiment: the light down-converted by a type II quadratic crystal is passed through a birefringent double slit. The experimental curves for the photon single counts and for the coincidences are shown in Fig.1.11: we observe that the photon single counts are almost uniform (slit separation much greater than the transverse coherence length of the beam), while the coincidence rate is minimum for photons detected in the same point, increasing for detections in separated points. This is the spatial antibunching effect.

Also squeezing and sub-Poissonian statistics have been described considering different spatial modes of light. To clarify the nature of these phenomena, we point out that, for a coherent state the photons are randomly distributed not only in time, but also in the transverse profile of the beam. Hence, a detection in a small portion of the beam leads to fluctuations at the shot noise level, while different portions of the beam are not correlated [Fabre & al.]. In Sect.1.2.1 we defined the squeezing in a single-mode field. In that case, the detection in a small area immediately degrades the squeezing
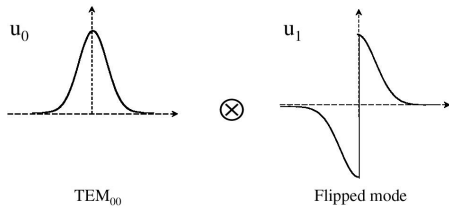
Figure 1.12: Electric field profile of the two constituent modes used to form the nonclassical multimode beam. Taken from Ref.[Treps & al.].
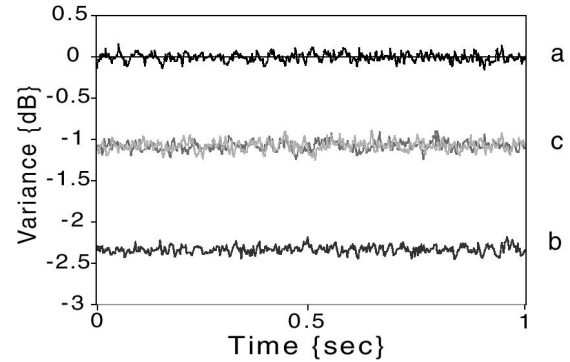

Figure 1.13: Noise spectral density at $4.5MHz$ of the photocurrents as a function of time. (a) Sum of the two photocurrents. (b) Difference between the photocurrents. (c) Noise on each detector. Taken from Ref.[Treps & al.].

measured, because a portion of a mode necessarily involves higher order modes, in which squeezing is absent [Fabre & al., Leonhardt]. [Kolobov & Sokolov] showed that when considering a paraxial field, propagating in a quadratic crystal, squeezing appears in a bandwidth of spatial transverse modes ($\vec{q}$): this phenomenon is named **spatially multimode squeezing**. The existence of spatial and frequency bandwidths of squeezed modes allows for the observation of quantum effects in local measurements, provided that the detection is performed on a photodetection area S and on a time interval T large enough. The minimum intervals S and T are fixed by the inverse of the spatial and frequency bandwidths [Kolobov]. Spatially multimode squeezing has been predicted in Optical Parametric Amplifier (OPA) [Kolobov & Sokolov] and in OPO below and at threshold [Gatti & Lugiato]. In Sect.1.2.1 we have mentioned the relation between amplitude squeezing in intense fields and sub-Poissonian statistics. The phenomenon of spatial sub-Poissonian statistics is equivalent to intensity squeezing in particular spatial modes.

Recently [Treps & al.] gave the first experimental evidence of spatially multimode intensity squeezing in a state obtained by the superposition of a squeezed vacuum mode and an intense flipped mode (see Fig.1.12). Photocourrent measurements, on the total transverse profile and on two symmetric portions, lead to the results shown in Fig.1.13: noise measured on the sum of the two spatial halves of the beam (Fig.1.13a) , i.e. on the total beam, coincides with the shot noise level, hence the whole beam is in a classical state. On the other hand, noise measured on each individual spatial half (Fig.1.13c) is reduced by $1.08dB$ below the quantum noise limit, demonstrating the multimode squeezing effect. Fig.1.13b gives the noise on the intensity difference between the two halves at $2.34dB$ below the quantum limit, suggesting that the beam is made of two strongly quantum correlated parts.

The state of Fig.1.12 has been proposed [Fabre & al.] to be useful for the measurement of displacement of a light beam with a precision below the standard quantum limit. The experimental realization of this proposal is one of the successful applications in the field of imaging of the quantum properties of the light fluctuations [Treps & al.]. Other possible applications include the detection of weak phase

and amplitude objects beyond the standard quantum limit, noiseless amplification of images, entangled two-photon microscopy, quantum lithography and quantum teleportation of optical images. A description of these applications and of the experimental achievements in this field are given in the papers *"The spatial behavior of nonclassical light"*, [Kolobov], and *"Quantum imaging"*, [Lugiato & al. (02)].

In this work we are concerned with the analysis of processes of *generation* of multimode quantum states and, in general, with the behavior of fluctuations in the context of transverse pattern formation in optical devices. We will show that "the quantum aspects are not a cosmetic addition to the classical picture but lie, rather, at the very root of optical pattern formation" (from Ref.[Lugiato & Oppo]). To this end we consider different regimes, in which the fluctuations continuously influence and are influenced by the pattern formation process in different ways. The characterization of the fluctuations is pursued by the analysis of the correlation functions between different quantities, as intensities or polarization Stokes parameters (see Sect.1.4.1), or the quadratures of the field modes (see Sect.1.4.2).

1.4.1   Intensity correlations

In this Section we consider the properties of intensity correlations among different spatial modes in the context of optical pattern formation. We will distinguish two classes of interaction processes that can be described as twin or multi-photon processes, respectively. **Twin photons** processes are a well known phenomenon investigated in different optical problems. In the Sect.1.4.1.a we describe the importance of this phenomenon in explaining some simple scenarios in pattern formation. More generally, different competing processes of creation and destruction of photons are involved in the formation of a spatial pattern. These **multi-photon** processes can lead to complex correlations between modes, as discussed in Sect.1.4.1.b.

1.4.1.a   Twin photons processes

In this section we first consider PDC as the prototype mechanism leading to simultaneous creation of pairs of photons. We continue our discussion considering the effects of a resonant cavity to generate macroscopic twin beams in an OPO. By including diffraction effects, spatial twin beams are predicted in cavity resonators at the threshold for pattern formation leading to stripe patterns. We describe twin photons processes in pattern formation in the two examples of an OPO and of a Kerr resonator. We conclude this Section discussing spatial twin beams in the regime of quantum images, which involves a continuous of spatial modes.

In Sect.1.2 we introduced the process of parametric down-conversion (PDC): in the non-degenerate configuration a photon at frequency ω_0, interacting with a $\chi^{(2)}$ crystal, decays into two highly correlated *twin* photons at lower frequencies ω_1, ω_2. In the PDC -without losses-, the photon number difference between the down-converted fields,

$$\hat{N}_D = \hat{N}_1 - \hat{N}_2, \tag{1.51}$$

is a constant of motion (Manley-Rowe relations [Manley & Rowe, Boyd]): at each time the pump creates a photon at ω_1 it must also create a photon at ω_2. Experiments of simultaneous measurement of the

twin photons pairs started in de decade of 1970 [Burnham & Weinberg, Friberg & al.]. The generation of photons in pairs is a necessary consequence of energy conservation, that therefore dictates the nature of the non-linear term coupling different operators modes:

$$\hat{H} = i\hbar g(\hat{a}_{\omega_0}\hat{a}^{\dagger}_{\omega_1}\hat{a}^{\dagger}_{\omega_2} - h.c.). \tag{1.52}$$

Taking signal (ω_1) and idler (ω_2) in the vacuum state as initial condition, the variance of the intensity difference vanishes at all times $\Delta^2\hat{N}_D(t) = 0$. In other words, there is total noise suppression in $\hat{N}_D$. However, the total mean intensity of the down-converted field increases in time. Therefore we obtain two intense fields with total noise suppression in their difference. This is a quantum effect of sub-Poissonian statistics, as it becomes clear considering the normal ordered variance:

$$: \Delta^2\hat{N}_D(t) := \Delta^2\hat{N}_D(t) - \langle\hat{N}_1(t) + \hat{N}_2(t)\rangle = -\langle\hat{N}_1(t) + \hat{N}_2(t)\rangle. \tag{1.53}$$

The negativity of this quantity is a signature of a non-classical sub-Poissonian statistics.

Eq.(1.53) describes the perfect and non-classical character of the correlation in photon number in PDC when there are no losses (Eq.(1.53)). If losses are taken into account in generic parametric processes, it can be shown [Graham] that in the *steady* state the mean value of $\hat{N}_D$ vanishes, and the variance is:

$$: \Delta^2\hat{N}_D := -\frac{1}{2}\langle\hat{N}_1 + \hat{N}_2\rangle. \tag{1.54}$$

Hence the two beams have the same intensity and the quantum effect of sub-Poissonian statistics in the intensity difference is still present, even if reduced to a 50% with respect to the level obtained in a system without losses.

In 1987 [Reynaud] suggested the use of the OPO in order to generate macroscopic non-classical states, instead of single photons pairs with very small probability as in PDC. The presence of the cavity increases the gain, concentrating the output energy only in a couple of modes. Above some threshold this yields two **intense laser-like twin beams**, that can be distinguished by their polarization (type-II phase matching) or by frequency (non degenerate OPO). Inside the cavity the result obtained by [Graham] (Eq.(1.54)) still applies, and a 50% of reduction of fluctuations with respect to the level of coherent states is predicted in the steady state value of $\hat{N}_D$. In [Reynaud & al. (87)] a perfect quantum noise suppression is predicted in the difference between the intensity of the two out-coming beams, counting the photons in a time interval large enough compared with the cavity lifetime. Non-classical statistics have been measured in continuous [Heidmann, Porzio & al.] and pulsed experiments [Aytür & Kumar], with a maximum of 88% of reduction of fluctuations in $\hat{N}_D$ below the shot noise limit [Gao & al.].

We now turn to situations of pattern formation. We consider a type I OPO *at threshold* of the signal generation, including the effect of diffraction of the fields. Under proper detuning conditions the signal emitted shows a *stripe* pattern in the transverse plane with critical wave-number k_c. This pattern is the result of the interference of a pair of modes with opposite transverse wavevectors ($\pm\vec{k}_c$). These modes are visualized in the far field, where two intense opposite spots appear. At a microscopic level,

we identify the process represented in Fig.1.14: a photon of the homogeneous pump (frequency 2ω and transverse wavevector $\vec{k}_\perp = 0$) is down converted in two tilted signal photons (frequency ω and $\vec{k}_\perp = \pm\vec{k}_c$). This process can be described by a Hamiltonian similar to Eq.(1.52), with the two down-con

verted photons distinguished by their transverse momentum

[Castelli & Lugiato]:

$$\hat{H} = i\hbar g \left[\hat{a}_{0,\vec{0}} \hat{a}^\dagger_{1,\vec{k}_c} \hat{a}^\dagger_{1,-\vec{k}_c} - h.c. \right].$$ (1.55)

The tilted beams are an example of twin beams. Due to the presence of the cavity these are macroscopic twin beams. Moreover, we mentioned before that these beams are measured by local detection in the far field plane, being opposite far field modes. Therefore they are spatial components of the signal beam. They are known as **spatial twin beams** [Lugiato & Castelli]. The intensity difference of the two down-converted beams is proportional to the total transverse momentum, that is conserved in the process. Since the photons entering in the medium have 0

Figure 1.14: Microscopic processes in an OPO at threshold: a photon of the homogeneous pump decay in two off-axis signal photons.

transverse momentum, then the total transverse momentum for the down-converted pairs $\hbar k_c \hat{N}_D$ must vanish, where $\hat{N}_D = \hat{N}_1(k_c) - \hat{N}_2(-k_c)$ [Grynberg & Lugiato].

Twin beams quantum correlations are common in devices showing stripe pattern formation at threshold. As another example we consider a Kerr resonator at threshold, with one transverse dimension [Lugiato & Castelli]. In this case the non-linear interaction of the plane wave pump with the cubic crystal leads to a four-wave mixing process, in which two pump photons are destroyed and two tilted photons appear, all with the same temporal frequency. This four-wave mixing is described by the Hamiltonian

$$\hat{H} = 2\hbar g \left[\hat{a}_{\vec{0}}^2 \hat{a}^\dagger_{\vec{k}_c} \hat{a}^\dagger_{-\vec{k}_c} - h.c. \right].$$ (1.56)

Even though the four-wave interaction Hamiltonian for the Kerr resonator at threshold is different from Eq.(1.55), both processes involve the simultaneous creation of two photons, with opposite wavevectors. Therefore, also in this device quantum correlations have been predicted between the pattern modes at $\pm k_c$, that are intense spatial twin beams [Lugiato & Castelli].

We have seen that the OPO and the Kerr resonator, at the instability threshold leading to a stripe pattern, can be described in terms of few spatial modes, whose interactions describe the process of twin photons creation. There are other situations which involve twin photons interactions: one of the most studied regimes, dominated by twin photon processes, is *below* the threshold of optical pattern formation. In this regime, there is generally a stable homogeneous solution, and quantum fluctuations around this state are small. They are distributed on a continuous of transverse spatial modes. This is the regime of **quantum images**, characterized by the "spatial structures manifested by the correlation functions" between the field at different points, and also by the "very noisy images" of the spatial fluctuations [Lugiato & al. (96)]. In Fig.1.15 we show a numerical simulation of the quantum images appearing
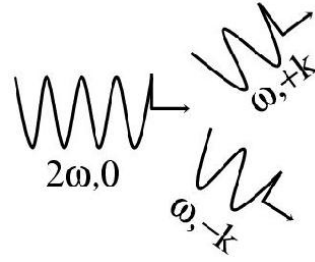
in the transverse profile of the near field (a) and of the far field (b) of a type I OPO below threshold. The quantum images are similar to the noisy precursors presented in the Sect.1.3.2: however in the quantum images noise has a quantum nature [Gatti & al. (97)2]. An extensive literature is devoted to the analysis of the quantum images generated by quantum fluctuations in several optical devices [Gatti & Lugiato, Lugiato & al. (96), Marzoli & al., Gatti & al. (97)1, Lugiato & al. (97), Gatti & al. (99)a, Lugiato & al. (99), Szwaj & al., Lodahl & Saffman, Bache & al.]. In these papers a description of this phenomenon is given taking into account the whole infinite set of transverse cavity modes (*continuous models*) in the fluctuation field operators, and linearizing the dynamics around the homogeneous steady states.

Most features of the intensity correlations between different spatial modes below the threshold of pattern formation are due to the microscopic process of generation of twin photons. For instance, in the case of the OPO with a flat pump, an approximated quadratic Hamiltonian can be introduced to describe the small fluctuations around the stable homogeneous solution. The fundamental interaction consists in the destruction of homogeneous pump photons, to create tilted signal photons, with *any* opposite transverse moments [Gatti & Lugiato, Gatti & al. (97)1, Szwaj & al.]. The linearized Hamiltonian in type I phase matching (see Appendix B) is

$$\hat{H} = i\frac{g}{2}A_0 \int d^2\vec{k} \left[\hat{A}_1^\dagger(\vec{k})\hat{A}_1^\dagger(-\vec{k}) - h.c. \right] \tag{1.57}$$

where A_0 is the homogeneous constant classical pump, and $\hat{A}_1(\vec{k})$ are the continuous of far field transverse modes in the down-converted beam. This Hamiltonian describes the simultaneous generation of photons pairs with opposite transverse momentum $\pm\vec{k}$, where $\vec{k}$ varies continuously in the far field plane. Hence twin beams correlations are found measuring the intensity difference in any symmetric portions of the far field (see two circles in Fig.1.15b). The less damped modes lie on the circle of radius k_c (precursors of the wavenumber that becomes unstable at threshold) and are more intense (Fig.1.15b). But the intensity difference of any two opposite modes show the same amount of noise reduction with respect to the shot noise level. An example of intensity correlations due to twin photons processes in the quantum images regime is presented in Ch.5.
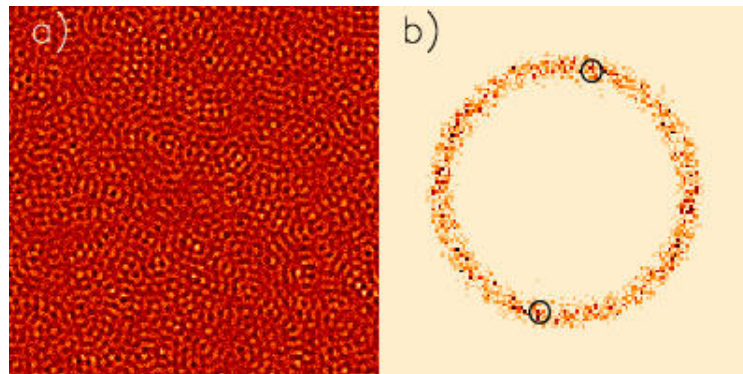

Figure 1.15: Near Field (a) and far field (b) of the down-converted field of a type I OPO, 2% below threshold. In (b) the two small circles correspond to symmetric regions.

1.4.1.b   Multi-photon processes

In the previous Section we have discussed situations which are dominated by the simultaneous creation of twin photons. In these cases the intensity correlations are determined by this fundamental microscopic process. However, only simple and approximated scenarios in optical pattern formation can be interpreted in terms of such processes, in which one or two pump photons decay in two off-axis photons of opposite transverse momentum. In general, as will become clear e.g. by the scheme in Fig.1.16, a mode of the electric field can be involved in different interactions: several steps, in which photons are created and destroyed, can occur in the process. We name "multi-photon processes" those processes in which there is coupling among several modes of the field, and in which the photons of the same mode are involved in different interactions.

Here we mention two examples of problems in which multi-photon processes are observed. As a first example we consider intracavity SHG with stripe pattern formation. This problem cannot be reduced to a scheme of twin photons processes, even below threshold. The second example we consider is the case of the Kerr resonator above threshold, where stable hexagonal patterns arise.

In Ref.[Bache & al.] quantum fluctuations in SHG with one transverse dimension are studied in the instability region of pattern formation. The microscopic processes shown in Fig.1.16 were identified in the threshold region, where stripe patterns appear in the fundamental and in the second harmonic field. The same diagram describes SHG in the regime of quantum images, below threshold, where the modes with the critical wave-number are weakly damped. In Fig.1.16 the six most intense modes are represented, and three different processes are identified. This interaction digram is more complicated that the simple mechanism identified in other systems below threshold for pattern formation, such as the Kerr resonator or both type I and type II OPO (see Fig.1.14). In the first step of the microscopic process identified in SHG (Fig.1.16(1)) two longitudinal photons at frequency ω are up-converted to give a longitudinal photon at frequency 2ω. The second step (Fig.1.16(2)) is the down-conversion of a second harmonic photon (2ω)
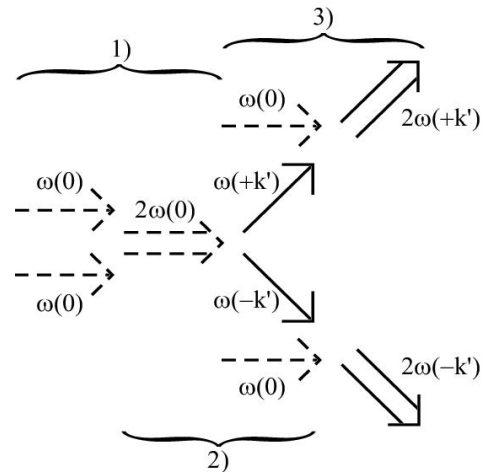
Figure 1.16: The basic picture of pattern formation at a microscopic level through SHG. The single arrows ($\rightarrow$) symbolize first harmonic photons, while double arrows ($\Rightarrow$) symbolize second harmonic photons. The dashed arrows are photons from the homogeneous background. Three fundamental processes are identified. The notation $\omega(k)$ is used to identify a photon with frequency ω and transverse momentum k [Bache & al.].

into two fundamental photons (ω) with opposite transverse momentum ($\pm k'$). This is the same process we have discussed in OPO at threshold (see Fig.1.14). In the last step (Fig.1.16(3)), off-axis second harmonic photons are obtained by combining the off-axis fundamental photon –created from step (2)– with a fundamental photon from the homogeneous background. Calculations identify twin-beams-like

correlations in SHG between opposite far field modes ($\pm k'$) at frequencies ω and 2ω. However in this case the correlation cannot be explained just in terms of twin photons emission. In particular the off-axis modes in the second harmonic field ($2\omega(\pm k')$) are generated in independent processes, which in principle are not correlated. Therefore no definite predictions are made for the correlations between opposite transverse modes, simply considering the microscopic processes represented in Fig.1.16. The microscopic scheme describes a rich intracavity dynamics and only the direct calculations of the spatial correlations can provide definitive answers.
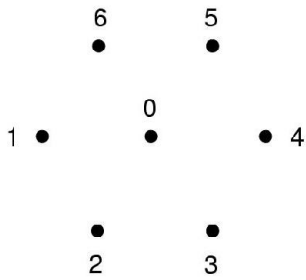

Figure 1.17: Seven modes far field of a hexagonal pattern. The numbers label photons with different transverse momentum.

A second example in which multi-photon interactions arise is a Kerr resonator at threshold. For self-focusing Kerr a hexagonal pattern is formed. This is the transverse two dimensional version of the system considered before: in that case the stripe pattern was stable in one transverse dimension. We now consider a transverse *plane*, were hexagons are stable structures. The properties of intensity quantum fluctuations in hexagons were studied in Ref.[Grynberg & Lugiato], neglecting losses and considering only six relevant far field modes (describing an hexagon) and the homogeneous pump mode, as shown in Fig.1.17. These modes interfere giving a regular extended hexagonal structure in the near field (see for instance Fig.1.18a). Considering this seven modes model, each photon is generated in two different

processes, both conserving transverse momentum: for instance the photon 1 in Fig.1.17 can be generated with the photon 4 in the twin photon process 0+0 $\Longleftrightarrow$ 1+4, but can also be generated in the process 2+6 $\Longleftrightarrow$ 0+1 [Grynberg & al.]. The second process would in principle destroy the twin beams correlations between modes 1 and 4. Therefore multiple microscopic processes do not give definitive indications on the important correlations between modes. In this complex multi-photon scenario, [Grynberg & Lugiato] calculated noise reduction in particular combinations of the intensity of four of the six modes (for instance $N_1 + N_2 - N_4 - N_5$, with N_i being the photons intensity at peak i). This result is obtained imposing the conservation of the transverse momentum of the filed. Recently this result, initially obtained neglecting losses, has been generalized including the losses of the intracavity dynamics [Gatti & Mancini]. Therefore, the existence of multiple microscopic process do not allow for the identification of the strong (quantum) correlations, because photons in the same macroscopic beam are generated in different processes. Nevertheless the identification of a conserved quantity (the transverse momentum) determines the squeezed quantities.

These few modes treatments suffer from an important limitation related to the subcritical instability mechanism through which hexagons appear. The hexagons arise with a large number of harmonics excited, as shown in Fig.1.18b and 1.18d. The results obtained approximating the hexagons by the interference of seven modes are not reliable to describe this regime. Classical correlations including the coupling with all the harmonics have been calculated, within a continuous model, by [Gomila & Colet], showing that the strongest correlations between the off-axis modes exist for hexagon modes separated by $120°$ angles (modes 1, 3 and 5 in Fig.1.17). These are correlations associated with the nonlinear
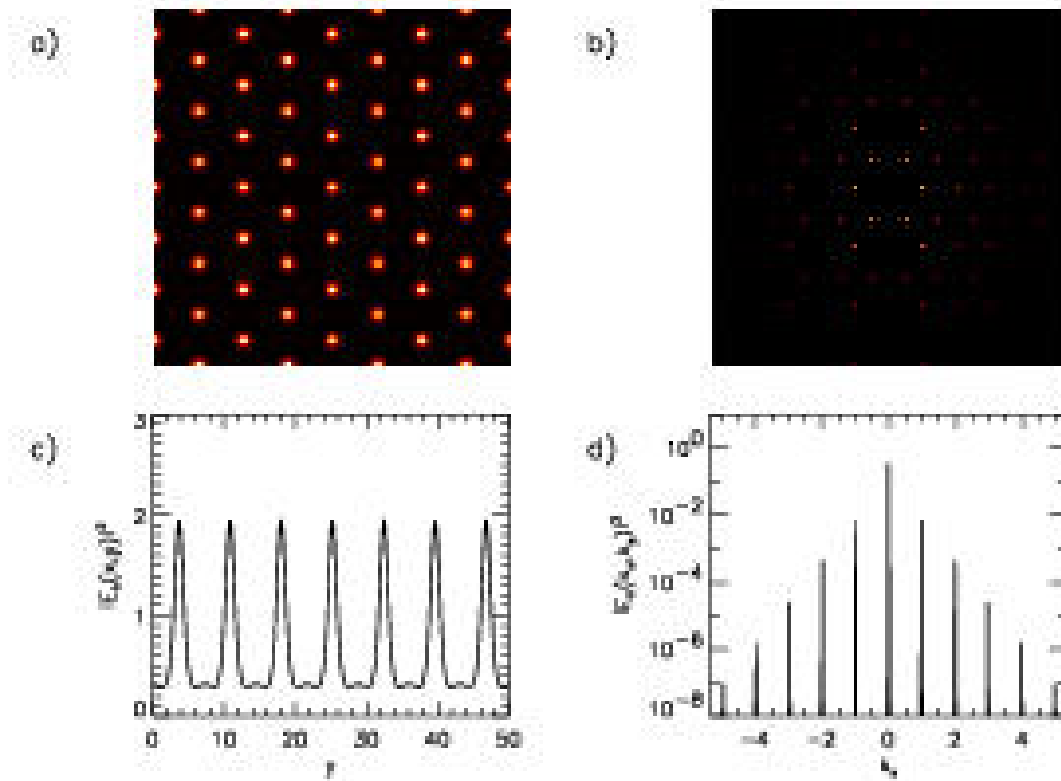
Figure 1.18: (a) Near field intensity $|E(x,y)|^2$ and (b) power spectrum (far field) $|E(\vec{k})|^2$ of a stationary hexagonal solution. Note the presence of high order harmonics in the far field. (c) shows a cross section along the x axis of the intensity pattern and (d) a cross section along the k_y axis of the power spectrum. Taken from Ref.[Gomila & Colet].

process of pattern selection.

In conclusion, few modes approximations are based on the identification of the most intense far field modes of a stable pattern [Lugiato & Castelli, Castelli & Lugiato, Grynberg & Lugiato, Hoyuelos & al. (99), Gatti & Mancini]: If only a twin photon process dominates the interactions, twin-beams-like correlations are obtained. In general, the microscopic process involves several interactions, so that the level of the macroscopic correlations cannot be inferred, and direct calculations are needed. The example of hexagonal patterns formation in Kerr resonators makes clear the limitation of few modes approximations and the need to deal with continuous models [Gomila & Colet]. In this work, we will see that, in some problems, the huge number of intense spectral modes does not allow for a few modes description and a consequent identification of a few relevant microscopic processes. A continuous description of the far field is needed. Several examples of multi-photon processes are discussed in Chs.3-5, in multimode patterns such as stripes with harmonics, in noisy sustained structures and in disordered structures. All these examples will be discussed with models including a continuous if spatial modes.

1.4.2 Quadrature correlations

In the previous Section we have discussed quantum effects associated with intensity correlations between spatial modes. The fluctuations of the electric field can show non-classical interesting effects also in other variables, such as the quadratures of the fields, that we now address. Spatial correlations in a type I OPO below threshold were studied in Ref.[Gatti & Lugiato]. The possibility to obtain spatial squeezing in this device is due to the quadratic form of the interaction, when pump fluctuations and depletion can be neglected (below threshold). In the plane immediately outside the cavity, the correlation function of a quadrature of the field detected in two points $\vec{x}$ and $\vec{x}'$, depends only on $\vec{x} - \vec{x}'$ (translation invariance) and shows a modulation at the critical wave vector of the pattern forming instability, with an amplitude decreasing exponentially. If a small bandwidth of points is considered ($|\vec{x} - \vec{x}'| \to 0$) the correlation function is non-classical: spatially multimode squeezing below the level of coherent states is found in the proper quadrature.

A new interest in the study of the correlations in quadratures has arisen in the context of the Einstein-Podolsky-Rosen (EPR) paradox [Einstein & al.]: in Ref.[Castelli & Lugiato] a type I OPO at threshold is considered in a three spatial modes approximation (Fig.1.14). In this device the opposite signal modes ($\pm k_c$) are highly correlated both in the intensity and in the phase quadratures. Therefore from a measurement of a quadrature in one of the modes, one can infer the corresponding value in the opposite mode, with a certain precision [10]. The same is true for the orthogonal non-commuting quadrature. The paradox is present when the precisions with which the inference is performed, give a product below the value fixed by the Heisenberg uncertainty principle. Spatial Einstein-Podolsky-Rosen paradox has also been theoretically demonstrated in the OPO below threshold [Gatti & al. (99)a].

In Ch.4 and Ch.5 we present results on quadratures squeezing and on EPR entanglement, both below and at threshold of optical pattern formation in type I and type II OPO.

1.5 Objectives and outline

In this work we have considered nonlinear optical devices in which transverse spatial self-organized structures appear. We have studied the possibility to observe quantum features in different regimes of these pattern formation processes. The study of some of these regimes needed new methodological tools. We can identify two different lines in this work: The first one is the **phenomenological** aspect, i.e. the study of quantum effects in the transverse profile of the light interacting with nonlinear resonators. In particular we have studied new unexplored regimes, with features such as macroscopic fluctuations, symmetry breaking effects and polarization entanglement. The second line of interest concerns the **methods** studied to treat nonlinear quantum fluctuations. These methods include doubling phase space techniques, input-output stochastic methods and the use of proper approximations to describe regimes with macroscopic nonlinear fluctuations.

The different methods and optical systems considered in this Thesis are briefly summarized in the scheme below.

---

[10]The precision is the variance of the difference of the quadratures in the opposite points
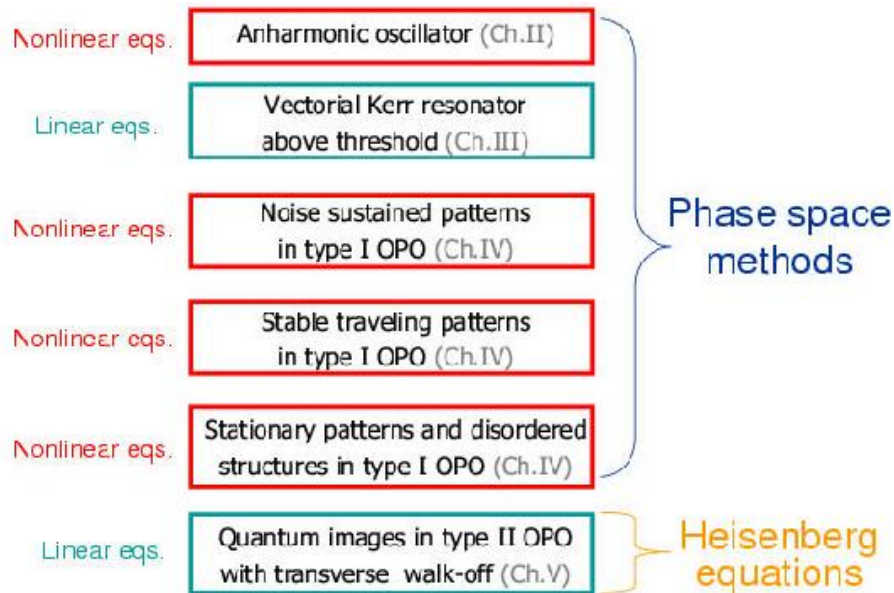
In the following we give a brief outline of the remaining chapters:

- In Ch.2 we discuss the methodological problems arising in the study of the quantum properties of nonlinear systems. In particular the possibility of a *stochastic description for a pseudo FPE with negative diffusion* is investigated, through a method proposed by [Yuen & Tombesi]. This method had been applied to a linear problem in calculations of squeezing properties. Our main objective has been to clarify the possibility of using this method for highly nonlinear dynamics. To this end we have considered the analytically soluble problem of the single-mode anharmonic oscillator [Zambrini & Barnett].

- In Ch.3 we consider a vectorial Kerr resonator, in which a linearly polarized pump leads to pattern formation in the orthogonal polarization component. We present the results of the first treatment of the spatial distribution of the quantum fluctuations of a *stable pattern* using a *continuous model*, i.e. considering the continuous of spatial transverse modes of the field. Previous studies were based on approximations in which only few modes were considered [Hoyuelos & al. (99)]. Our treatment allows to identify the *spatial* configuration of the fluctuations, which are dominated by the Goldstone mode. An approximated but general way to treat the problem of the realization of the output field through a stochastic numerical simulation is also presented [Zambrini & al. (00)].

- Ch.4 is devoted to the study of type I OPO. We discuss four major problems: the possibility of quantum correlations in the convective regime (see Sect.1.4.1.b), the behavior of the quantum critical correlations at threshold, the identification of the effects of the walk-off as a term breaking the reflection symmetry, and the possibility of twin photons correlations for spatially disor-

dered structures. The study of these *nonlinear* regimes needed the introduction of proper methods and approximations. In particular we present two new methods to describe these regimes in terms of classical stochastic equations, namely a time dependent parametric approximation and a stochastic representation of the Q-functional [Zambrini & al. (02), Zambrini & San Miguel, Zambrini & al. (03)1].

- In Ch.5 we study the properties of quantum fluctuations in the quantum images regime of type II OPO. In this device photons are emitted with orthogonal *polarization* states. Interesting quantum effects are observed –such as spatial EPR entanglement– which depend on the polarization state of the light; the properties of the polarization state of the field fluctuations are studied through the analysis of spatial dependent Stokes parameters and through their correlations [Zambrini & al. (03)2].

Chapter 2

Stochastic description of the quantum anharmonic oscillator

In this Chapter we discuss a phase space method to study the quantum properties of an isolated nonlinear system. The method was proposed by [Yuen & Tombesi] in 1986 to give a stochastic representation of pseudo Fokker-Planck equations with negative diffusion. It was successfully applied to a linear problem [Tombesi]. The aim of our work is to apply the proposal of Yuen and Tombesi to the analytically soluble problem of the single-mode anharmonic oscillator. This system presents interesting quantum features associated with the nonlinearity. We note that this chapter focuses on a system that differs from the rest of systems treated in this work, being a single-mode and closed system: the motivation of this Chapter is the discussion of a **method** that opens a new possibility to treat nonlinear quantum models, through a simulation of stochastic processes, even if in the phase space representation they are described by equations involving a not positive definite diffusion matrix. The results presented in this Chapter have been published in the Ref. [Zambrini & Barnett].

2.1   Introduction

The treatment of even quite simple quantum optical systems can present a significant technical challenge. As reviewed in Ch.1 the description of a problem involving optical field modes, can be mapped onto a partial differential equation for a quasi-probability distribution. In some cases it is possible to solve this equation. In Sect.1.2.3.b we have discussed when this equation can be mapped onto an equivalent stochastic process, that can be simulated numerically.

Mapping the quantum problem onto a stochastic system relies on a formal similarity between the partial differential equation, obtained from the master equation, and the Fokker-Planck equation associated with Brownian motion. The general form of the Fokker-Planck equation was discussed in

Sect.1.2.3.b [1]

$$\frac{\partial}{\partial t}\mathcal{W} = -\frac{\partial}{\partial \alpha}A_\alpha \mathcal{W} - \frac{\partial}{\partial \alpha^*}A_{\alpha^*}\mathcal{W} + \frac{1}{2}\frac{\partial^2}{\partial \alpha^2}D_{\alpha\alpha}\mathcal{W} + \frac{1}{2}\frac{\partial^2}{\partial \alpha^{*2}}D_{\alpha^*\alpha^*}\mathcal{W} + \frac{\partial^2}{\partial \alpha\partial \alpha^*}D_{\alpha\alpha^*}\mathcal{W},$$

This equation describes the dynamics of a single field mode or harmonic oscillator, where the complex variables α and α^* are associated with the mode [Barnett & Radmore, Gardiner & Zoller].

The requirement that $\mathcal{W}$ is a real-valued function imposes the conditions that $A_{\alpha^*}^* = A_\alpha$, $D_{\alpha^*\alpha^*} = D_{\alpha\alpha}^*$ and $D_{\alpha\alpha^*}$ is real. This equation can be mapped onto a pair of stochastic differential equations for the phase-space coordinates (also written as α and α^*) in the form

$$\dot{\alpha} \quad = \quad v_\alpha + \xi(t) \tag{2.1}$$

$$\dot{\alpha}^* \quad = \quad v_{\alpha^*} + \xi^*(t), \tag{2.2}$$

where v_α and v_{α^*} are functions of the drift and diffusion coefficients (A_i and D_{ij}) appearing in Eq. (2.1) and the dot denotes a derivative with respect to time. The terms $\xi(t)$ and $\xi^*(t)$ are stochastic fluctuating terms with correlation functions related to the diffusion coefficients. There is no unique stochastic representation of a given Fokker-Planck equation. We work with the Stratonovich form of the stochastic integral [Gardiner]. A brief discussion of this is given in Appendix A.

Unfortunately, not all problems of interest can be converted into the Fokker-Planck form (2.1). In Ch.1 we mentioned that systems of interest in quantum nonlinear optics often produce equations for the evolution of quasi-probabilities that have derivatives of higher than second order. A second, more subtle, problem is that even when we do obtain an equation of the form (2.1), it might still not be possible to map this onto stochastic differential equations of the form (2.1) and (2.2). The difficulty arises when we have negative diffusion, that is when $D_{\alpha\alpha^*} < |D_{\alpha\alpha}|$. With negative diffusion, we are led to stochastic differential equations in which ξ^* cannot be the complex conjugate of ξ and hence α^* will not be the complex conjugate of α. It was to resolve problems of this kind that the positive P representation was introduced [Gardiner & Zoller, Drummond & Gardiner, Drummond & al. (81), Gilchrist & al.].

In this Chapter we consider a proposal by Yuen and Tombesi to convert the evolution equation for the Q quasi-probability into a pair of stochastic differential equations [Yuen & Tombesi, Tombesi]. Their idea is that the correct averages should be obtained by *formal* application of the Langevin method by simply ignoring the presence of negative diffusion. These authors applied their method to squeezing calculations, obtaining the correct quadrature squeezing evolution.

In Ref. [Zambrini & Barnett] we apply the Yuen-Tombesi approach to the more demanding, but still analytically soluble problem of the undamped anharmonic oscillator [Milburn, Yurke, Tanas & al.]. This model is known to cause difficulties with stochastic simulations derived from the positive P representation [Gardiner & Zoller, Gilchrist & al., Plimak & al.]. We find that the Yuen-Tombesi method gives the correct results but that it cannot reliably be applied to numerical simulation of the problem. We trace the origin of this difficulty to the order in which stochastic averages and averages over the initial phase-space distribution have to be performed.

---

[1]Comparing with Eq.(1.26) here we omit the dependence on the index s of the function $\mathcal{W}$.

2.2   Method of Yuen and Tombesi

The method of Yuen and Tombesi was designed to deal with problems in which the evolution equation for the Q function displays negative diffusion. The Q function for a single field mode or oscillator has been introduced in Sect.1.2.3.b.2:

$$Q(\alpha, \alpha^*) = \frac{1}{\pi} \langle \alpha | \hat{\rho} | \alpha \rangle, \tag{2.3}$$

where $\hat{\rho}$ is the density operator for the mode [2]. This distribution can be used to obtain anti-normal ordered moments of the annihilation and creation operators by integration over the complex α plane:

$$\langle \hat{a}^n \hat{a}^{\dagger m} \rangle = \int d^2\alpha \, Q\alpha^n \alpha^{*m}. \tag{2.4}$$

We consider systems (such as the anharmonic oscillator) in which the evolution equation for the Q function is of the form given in Eq. (2.1), with *negative* diffusion. This leads to associated stochastic differential equations in which the stochastic variable $\alpha^*(t)$ is not the complex conjugate of $\alpha(t)$. As an example, consider an equation in which $D_{\alpha\alpha^*} = 0$. This necessarily implies negative diffusion associated with $D_{\alpha\alpha}$ and $D_{\alpha^*\alpha^*}$. We can follow the method outlined in Appendix A to obtain a pair of stochastic differential equations that are equivalent to our evolution equation for Q [3]:

$$\dot{\alpha} = A_\alpha - \frac{1}{4}\frac{\partial}{\partial\alpha}D_{\alpha\alpha} + \sqrt{D_{\alpha\alpha}}f_\alpha \tag{2.5}$$

$$\dot{\alpha}^* = A_\alpha^* - \frac{1}{4}\frac{\partial}{\partial\alpha^*}D_{\alpha^*\alpha^*} + \sqrt{D_{\alpha^*\alpha^*}}f_{\alpha^*}. \tag{2.6}$$

It might appear that these equations are mutual complex conjugates but this is not the case as the two Gaussian noise terms are *independent* and hence do not take complex conjugate values. It follows that we cannot interpret α and α^* as mutual complex conjugates. The situation is reminiscent of that found with the positive P representation and we employ the same notation by writing our stochastic variables as $\alpha(t)$ and $\alpha^+(t)$ [Drummond & Gardiner]. Anti-normal ordered expectation values should then correspond to stochastic averages of corresponding functions of α and α^+, with $\hat{a}(t)$ replaced by $\alpha(t)$ and $\hat{a}^\dagger(t)$ replaced by $\alpha^+(t)$.

We can introduce the variables α and α^+ more formally by means of the complex function

$$\tilde{Q}(\alpha, \alpha^+) = \frac{1}{\pi} \langle 0 | e^{\alpha^+ \hat{a}} \hat{\rho} e^{\alpha \hat{a}^\dagger} | 0 \rangle e^{-\alpha^+ \alpha}, \tag{2.7}$$

which is a function of α and α^+ but not of their complex conjugates. This reduces to the familiar Q function (2.3) when $\alpha^+ = \alpha^*$. We can convert our master equation for $\hat{\rho}$ into an evolution equation for

---

[2]This definition differs by a factor of π from that used by Milburn [Milburn].

[3]These are obtained from the equations given in Appendix A by the choosing $C_{\alpha\alpha^*} = 0 = C_{\alpha^*\alpha}$.

$\tilde{Q}$ by making the substitutions

$$
\begin{aligned}
\hat{\rho}\hat{a}^\dagger &\rightarrow \left(\alpha^+ + \frac{\partial}{\partial\alpha}\right)\tilde{Q} \\
\hat{a}^\dagger\hat{\rho} &\rightarrow \alpha^+\tilde{Q} \\
\hat{a}\hat{\rho} &\rightarrow \left(\alpha + \frac{\partial}{\partial\alpha^+}\right)\tilde{Q} \\
\hat{\rho}\hat{a} &\rightarrow \alpha\tilde{Q}.
\end{aligned}
\tag{2.8}
$$

The resulting equation for $\tilde{Q}$ will be of the same form as that for our Q function with α^* replaced by α^+.

2.3   Anharmonic Oscillator

The anharmonic oscillator is one of the simplest analytically solvable models in quantum optics. The Hamiltonian for this model can be written in the form

$$
\hat{H} = \omega\left(\hat{a}^\dagger\hat{a} + \frac{1}{2}\right) + \mu(\hat{a}^\dagger\hat{a})^2,
\tag{2.9}
$$

where ω is the natural angular frequency for the mode and we work with units in which $\hbar = 1$. The term proportional to μ is sometimes written in normal order as $\mu\hat{a}^\dagger\hat{a}^\dagger\hat{a}\hat{a}$. This is the same model but with the ω changed to $\omega + \mu$. It is convenient to remove the free evolution of the mode and this can be achieved by working in an interaction picture rotating at angular frequency ω. The interaction picture form of the Hamiltonian (2.9) is

$$
\hat{H}_I = \mu(\hat{a}^\dagger\hat{a})^2.
\tag{2.10}
$$

This Hamiltonian has been used in quantum optics as a model for the Kerr nonlinear refractive index. Despite its simplicity, it produces a number of nonclassical effects including squeezing [Tanas & al.] and Schrödinger cat states [Yurke], that is superpositions of coherent states. The accurate reproduction of these features, especially the cat states, presents a stiff challenge to a stochastic simulation method such as that proposed by Yuen and Tombesi [Yuen & Tombesi, Tombesi]. The fact that the model is analytically soluble means that we can compare the results of such simulations with exact analytical expressions. We will give an example of this comparison in the following section. In this section we present a brief review of some of the known features of the model.

It is clear from the form of the Hamiltonian that it commutes with the number operator $\hat{a}^\dagger\hat{a}$. It follows that the number of excitations (or photons) in the mode will be conserved and that the photon number states $|n\rangle$ will be the eigenstates of our interaction Hamiltonian

$$
\hat{H}_I|n\rangle = n^2\mu|n\rangle.
\tag{2.11}
$$

The corresponding time-evolution operator is

$$
\hat{U}(t) = \exp(-i\hat{H}_I t) = \sum_{n=0}^{\infty}|n\rangle\langle n|e^{-in^2\mu t}
\tag{2.12}
$$

Figure 2.1: Phase-space plot of the quantum Q function for initial circular Gaussian contour centered on $\alpha_0 = 2$: (a) $\nu = \pi/2$, (b) $\nu = \pi$, (c) $\nu = 3\pi/2$, (d) $\nu = 2\pi$. Taken from Ref.[Milburn]. In the notation of [Milburn] $\nu = 2\mu t$.
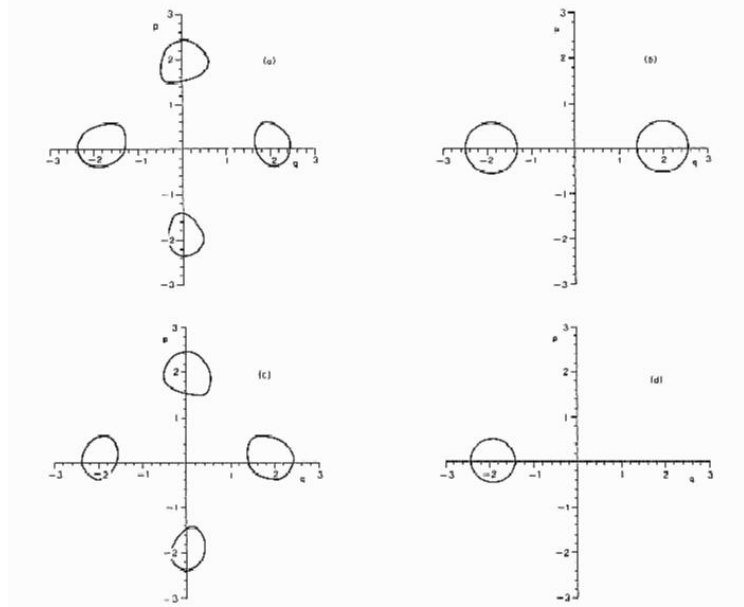
and it follows that the evolution of our oscillator will be periodic with period $2\pi/\mu$. If we can expand our initial state in terms of the number states, then we can use this result to solve for the time-evolved state in the Schrödinger picture. For example, an initial coherent state $|\alpha_0\rangle$ will evolve to the state

$$\hat{U}(t)|\alpha_0\rangle = e^{-|\alpha_0|^2} \sum_{n=0}^{\infty} \frac{\alpha_0^n}{\sqrt{n!}} e^{-in^2\mu t} |n\rangle. \tag{2.13}$$

This state has a rich structure that can be seen in pictures of the associated quasi-probability distributions [Milburn, Tanas & al.]. Fig.2.1 shows the distribution at different times, taking a coherent state ($\alpha_0 = 2$) as initial condition. This initial state (not represented in Fig.2.1) corresponds to a circular contour on the horizontal axis, centered in 2. For short times the initial circular contour rotates and stretches. However as the distribution is smeared out around the origin, separate peaks form on a fairly flat background. These peaks smear out, flatten and reemerge as the cycle proceeds, eventually yielding two identical Gaussian peaks on opposite sides of the origin (Fig.2.1b). The state (2.13) has a simple form at the quarter periods when it can be written as [Yurke]

$$\hat{U}[\pi/(2\mu)]|\alpha_0\rangle = \frac{1-i}{2}|\alpha_0\rangle + \frac{1+i}{2}|-\alpha_0\rangle$$

$$\hat{U}[\pi/\mu]|\alpha_0\rangle = |-\alpha_0\rangle$$

$$\hat{U}[3\pi/(2\mu)]|\alpha_0\rangle = \frac{1+i}{2}|\alpha_0\rangle + \frac{1-i}{2}|-\alpha_0\rangle. \tag{2.14}$$

At one quarter and three quarters of a period is a superposition of the coherent states $|\alpha_0\rangle$ and $|-\alpha_0\rangle$, as represented in Fig.2.1b. Such superposition states have interesting nonclassical properties and have been called Schrödinger cat states.

Our stochastic treatment is designed to produce expectation values of operators for the oscillator. These can also be calculated analytically, but this is most easily performed in the Heisenberg interaction

picture. The time-evolved annihilation and creation operators are

$$\hat{a}(t) = \hat{U}^\dagger(t)\hat{a}\hat{U}(t) = e^{-i\mu t}e^{-i2\mu t\hat{a}^\dagger\hat{a}}\hat{a} \tag{2.15}$$

$$\hat{a}^\dagger(t) = \hat{U}^\dagger(t)\hat{a}^\dagger\hat{U}(t) = e^{i\mu t}\hat{a}^\dagger e^{i2\mu t\hat{a}^\dagger\hat{a}}, \tag{2.16}$$

where we have written the initial operators as $\hat{a}$ and $\hat{a}^\dagger$. It is straightforward to use these expressions to calculate expectation values for functions of $\hat{a}(t)$ and $\hat{a}^\dagger(t)$. For example, the expectation value of the annihilation operator for the coherent state $|\alpha_0\rangle$ is

$$\langle\hat{a}(t)\rangle = e^{-i\mu t}\langle\alpha_0|e^{-i2\mu t\hat{a}^\dagger\hat{a}}\hat{a}|\alpha_0\rangle = e^{-i\mu t}\alpha_0\exp\left(|\alpha_0|^2(e^{-i2\mu t}-1)\right). \tag{2.17}$$

In this expression we have omitted the free-evolution in the form of a factor $e^{-i\omega t}$. This corresponds to working in a frame rotating at frequency ω, associated with our choice of interaction picture. All expressions in this Chapter will be given in this frame. The expectation value of $\hat{a}^\dagger(t)$ is the complex conjugate of Eq. (2.17) and higher order moments can also be calculated without difficulty.

The evolution equation for the Q function can be written in the form [Milburn]

$$\frac{\partial}{\partial t}Q = -i\mu\left[\frac{\partial}{\partial\alpha^*}(2|\alpha|^2-3)\alpha^*Q - \frac{\partial}{\partial\alpha}(2|\alpha|^2-3)\alpha Q + \frac{\partial^2}{\partial\alpha^{*2}}\alpha^{*2}Q - \frac{\partial^2}{\partial\alpha^2}\alpha^2 Q\right]. \tag{2.18}$$

Comparison with Eq. (2.1) reveals that this equation has negative diffusion ($D_{\alpha\alpha^*} = 0 < |D_{\alpha\alpha}| = 2|\mu\alpha^2|$) and hence is a good candidate with which to test the ideas of Yuen and Tombesi. We should emphasize that the partial differential Eq. (2.18) itself does not present any difficulties in spite of the negative diffusion [Vogel & Risken (89)a]. In fact [Milburn] solves this equation, obtaining the correct temporal dynamics of the Q function, represented for particular conditions in Fig.2.1.

2.4   Analytic stochastic treatment of the anharmonic oscillator

We can re-express the evolution of our Q function, given by Eq. (2.18) as an equivalent stochastic process using the method outlined in Appendix A. A simple and natural choice is to set $C_{\alpha\alpha^*} = 0 = C_{\alpha^*\alpha}$ so that $C_{\alpha\alpha} = \sqrt{i2\mu}\alpha$ and $C_{\alpha^*\alpha^*} = \sqrt{-i2\mu}\alpha^*$. The evolution equation for our Q function clearly displays negative diffusion and so we write our stochastic differential equations in terms of the variables α and α^+. For the choices described above, our equations become

$$\dot{\alpha} = -i\mu 2(\alpha^+\alpha-1)\alpha + \xi\alpha \tag{2.19}$$

$$\dot{\alpha}^+ = i\mu 2(\alpha^+\alpha-1)\alpha^+ + \xi^+\alpha^+, \tag{2.20}$$

where ξ and ξ^+ are complex, white Gaussian noises with the stochastic averages

$$\langle\xi(t)\xi(t')\rangle_S = 2i\mu\delta(t-t')$$

$$\langle\xi^+(t)\xi^+(t')\rangle_S = -2i\mu\delta(t-t')$$

$$\langle\xi^+(t)\xi(t')\rangle_S = 0. \tag{2.21}$$

We will require averages over both the stochastic noise realizations and also over the initial quasi-probability distribution. The subscript S identifies the fact that we have carried out the stochastic average. The stochastic averages (22) do not fully determine the forms of the noise terms. It is clear, however, that $\xi^+(t)$ cannot be the complex conjugate of $\xi(t)$. It has been suggested that the considerable freedom in choosing the forms of $\xi(t)$ and $\xi^+(t)$ can be used to suppress, although not completely remove, stochastic sampling errors in the analogous problem in the positive P representation. The analysis presented in this section is independent of this choice of Gaussian noise and hence the freedom to select the forms of $\xi(t)$ and $\xi^+(t)$ will not address the problem uncovered.

We require the solution of Eqs. (2.19) and (2.20) with the initial conditions $\alpha(0) = \beta$ and $\alpha^+(0) = \beta^*$. These mean that $\alpha^+(0) = \alpha^*(0)$ and allow us to use the initial Q_0 function to perform the average over the initial state. As already noted in Sect. 2.2, the form of the stochastic noise means that $\alpha^+(t)$ will not take the value $(\alpha^*(t))$ in any given realization. The full quantum average will only be obtained by performing an average over the Q_0 function for the initial state. For the coherent state $|\alpha_0\rangle$ this is

$$Q_0(\beta) = \frac{1}{\pi} e^{-|\beta - \alpha_0|^2}. \tag{2.22}$$

We denote the average obtained by integrating over β by the subscript Q_0:

$$\langle F\left(\alpha(t), \alpha^+(t)\right)\rangle_{Q_0} = \int_{-\infty}^{\infty} d^2\beta Q(\beta) F\left(\alpha(t), \alpha^+(t)\right).$$

Quantum expectation values should be obtained on performing both the stochastic average and the average over the this Q_0 function. In particular, the mean value of $\hat{a}$ at time t will be

$$\langle \hat{a}(t)\rangle = \langle\langle \alpha(t)\rangle_S\rangle_{Q_0}. \tag{2.23}$$

We have not yet given a prescription for the order, if any, in which these averages must be performed. We will see that this question is of some importance for the solution of the stochastic differential equations.

In this section we will calculate the expectation value of the annihilation operator at time t by solving the Eqs. (2.19) and (2.20). We start by noticing that the combination $\alpha^+\alpha$ satisfies the equation

$$\frac{d}{dt}\alpha^+\alpha = (\xi + \xi^+)\alpha^+\alpha. \tag{2.24}$$

The formal solution to this equation is

$$\alpha^+(t)\alpha(t) = \beta^*\beta e^{\int_0^t [\xi(t') + \xi^+(t')]dt'}. \tag{2.25}$$

This already suggests that the stochastic simulation of this problem may run into difficulties. We expect the average obtained from $\alpha^+(t)\alpha(t)$ will be $\langle \hat{a}(t)\hat{a}^\dagger(t)\rangle$, which should take the constant value $|\alpha_0|^2 + 1$. The solution (2.25), however, clearly shows that the stochastic noise will cause $\alpha^+(t)\alpha(t)$ to fluctuate away from its initial value in a single realization of the stochastic process. The average is constant but the corresponding variance increases in time. The presence of a complex driving force $\xi + \xi^+$ means that $\alpha^+(t)\alpha(t)$ can acquire any complex value. Nevertheless we can proceed by inserting our solution

(2.25) into our stochastic differential equations (2.19) and (2.20). We find that the resulting equations are linear. In particular, the equation for $\alpha(t)$ becomes

$$\dot{\alpha}(t) = \left[-i2\mu \left(|\beta|^2 e^{\int_0^t [\xi(t') + \xi^+(t')]dt'} - 1 \right) + \xi(t) \right] \alpha(t),$$

the solution of which is

$$\alpha(t) = \beta \exp \left\{ \int_0^t \left[-i2\mu \left(|\beta|^2 e^{\int_0^{t'} [\xi(t'') + \xi^+(t'')]dt''} - 1 \right) + \xi(t') \right] dt' \right\}. \tag{2.26}$$

Similar expressions have been given for the same model treated in the positive P representation [Plimak & al.]. The average of this quantity should be the expectation value of $\hat{a}(t)$. Let us start by performing the stochastic average. This can be achieved most readily by expanding the outer exponential in powers of $|\beta|^2$

$$\langle \alpha(t) \rangle_S = \beta e^{i2\mu t} \langle e^{\int_0^t \xi(t')dt'} \left[1 - i2\mu|\beta|^2 \int_0^t e^{\int_0^{t'} [\xi(t'') + \xi^+(t'')]dt''} dt' - \right.$$

$$\left. 2\mu^2 |\beta|^4 \int_0^t dt' \int_0^t dt'' e^{\int_0^{t'} [\xi(s) + \xi^+(s)]ds} e^{\int_0^{t''} [\xi(s') + \xi^+(s')]ds'} + \cdots \right] \rangle_S. \tag{2.27}$$

Here we have made explicit use of the Gaussian nature of our stochastic noise in evaluating the averages of exponential functions of the noise. We can evaluate the average of each term in turn. The order zero and order one terms are

$$\langle e^{\int_0^t \xi(t')dt'} \rangle_S = e^{i\mu t} \tag{2.28}$$

$$-i2\mu|\beta|^2 \langle \int_0^t dt' e^{\int_0^{t'} [2\xi(s) + \xi^+(s)]ds} e^{\int_{t'}^t \xi(s')ds'} \rangle_S = -i2\mu|\beta|^2 \int_0^t dt' e^{4i\mu t'} e^{-i\mu t'} e^{i\mu(t-t')}$$

$$= -|\beta|^2 e^{i\mu t} (e^{2i\mu t} - 1). \tag{2.29}$$

It is straightforward to show that the stochastic average of the term of order $|\beta|^{2n}$ is

$$(-1)^n |\beta|^{2n} e^{i\mu t} (e^{2i\mu t} - 1)^n / n!. \tag{2.30}$$

It is tempting to re-sum the series in Eq. (2.27) to give

$$\langle \alpha(t) \rangle_S = \beta e^{i3\mu t} \exp \left(|\beta|^2 (1 - e^{i2\mu t}) \right). \tag{2.31}$$

Let us see the consequences of this re-summing by completing our calculation of the expectation value of $\hat{a}(t)$ with the average over β. This procedure leads to the expression

$$\langle \langle \alpha(t) \rangle_S \rangle_{Q_0} = \frac{1}{\pi} \int d^2\beta e^{-|\beta - \alpha_0|^2} \beta e^{i3\mu t} \exp \left(|\beta|^2 (1 - e^{i2\mu t}) \right).$$

Inspection of the integrand reveals a problem. It is clear that the integrand is *unbounded* (and the integral *undefined*) for times t such that $\cos(2\mu t) \leq 0$. It is interesting to note that this includes the times, $\pi/(2\mu)$ and $3\pi/(2\mu)$, at which the anharmonic oscillator evolves into the Schrödinger cat states given in Eqs. (2.14). The problem is that we have assumed that it is acceptable to perform the stochastic average before performing the average over initial conditions. In fact this is not the case and we should

perform the Q_0 average first. We can see this by evaluating the average over the Q_0 function before re-summing the series in our stochastic average given in Eq. (2.27). This gives the final average value

$$
\begin{aligned}
\langle\langle\alpha(t)\rangle_{Q_0}\rangle_S &= e^{i3\mu t}\sum_{n=0}^{\infty}\frac{(1-e^{i2\mu t})^n}{n!}\int\frac{d^2\beta}{\pi}\beta^{n+1}\beta^{*n}e^{-|\beta-\alpha_0|^2} \\
&= e^{i3\mu t}\sum_{n=0}^{\infty}(1-e^{i2\mu t})^n\sum_{l=0}^{n}\frac{(n+1)!}{l!(l+1)!(n-l)!}\alpha_0^{l+1}\alpha_0^{*l} \\
&= e^{i3\mu t}\sum_{l=0}^{\infty}\frac{|\alpha_0|^{2l}}{(l+1)!}\sum_{n=l}^{\infty}(1-e^{i2\mu t})^n\frac{(n+1)!}{(n-l)!l!} \\
&= e^{-i\mu t}\alpha_0\exp\left(|\alpha_0|^2(e^{-i2\mu t}-1)\right),
\end{aligned}
\tag{2.32}
$$

which we recognize as the correct answer given in Eq. (2.17). Other moments can be obtained in the same manner.

We can see the origin of the incorrect stochastic average given in Eq. (2.31) by considering the form of the annihilation operator in the Heisenberg picture, Eq. (2.15), which we can also write in the form

$$
\hat{a}(t) = e^{3i\mu t}\hat{a}e^{-i2\mu t\hat{a}^\dagger\hat{a}} = e^{3i\mu t}\!\stackrel{..}{\hat{a}e^{(1-e^{i2\mu t})\hat{a}\hat{a}^\dagger}}\!
\tag{2.33}
$$

where $\stackrel{..}{\ }\stackrel{..}{\ }$ denotes antinormal ordering and we have used the antinormal ordering theorem for the exponential of $\hat{a}^\dagger\hat{a}$ [Barnett & Radmore]. We note that this becomes the expression (2.31) obtained by performing the stochastic average, if we identify $\hat{a}$ and $\hat{a}^\dagger$ with β and β^* respectively. We have written Eq. (2.33) in antinormal order because the Q function gives antinormally ordered moments. If we use this expression to calculate the expectation value of $\hat{a}(t)$, for our initial coherent state, then we find

$$
\langle\hat{a}(t)\rangle = e^{3i\mu t}\langle\alpha_0|\!\stackrel{..}{\hat{a}\exp\left((1-e^{i2\mu t})\hat{a}\hat{a}^\dagger\right)}\!|\alpha_0\rangle.
\tag{2.34}
$$

We can, of course, evaluate this expectation value by putting the operator into normal ordered form and using the fact that the coherent states are right-eigenstates of the annihilation operator. Our aim, however, is to investigate the problems with the stochastic average associated with simulations designed to reproduce antinormal ordered averages. We can work with the antinormal ordered form in Eq. (2.34) by expanding the exponential as a Taylor series and inserting the identity in the form of an integral over the coherent states $|\beta\rangle$ [Barnett & Radmore]:

$$
\begin{aligned}
\langle\hat{a}(t)\rangle &= e^{3i\mu t}\langle\alpha_0|\sum_{n=0}^{\infty}\frac{(1-e^{i2\mu t})^n}{n!}\hat{a}^{n+1}\int\frac{d^2\beta}{\pi}|\beta\rangle\langle\beta|\hat{a}^{\dagger n}|\alpha_0\rangle
\end{aligned}
\tag{2.35}
$$

$$
= e^{3i\mu t}\sum_{n=0}^{\infty}\frac{(1-e^{i2\mu t})^n}{n!}\int\frac{d^2\beta}{\pi}\beta|\beta|^{2n}e^{-|\beta-\alpha_0|^2}.
\tag{2.36}
$$

Clearly it would be wrong to evaluate the summation before carrying out the integral. Evaluating the integral first corresponds, in our stochastic treatment, to averaging over initial conditions before performing the stochastic average and gives the correct result.

Figure 2.2: Time evolution of the stochastic average $Re\langle\alpha(t)\rangle_S$, using 50000 trajectories and starting from $\beta = 0.001 + i0.1$. The diamonds represent numerical values. The continuous line represents the analytical result for $\langle\alpha(t)\rangle_S$. The dashed line represents $\langle\langle\alpha(t)\rangle_{Q_0}\rangle_S$ for the initial coherent state $|\alpha_0 >$ with $\alpha_0 = 0.001 + i0.1$.
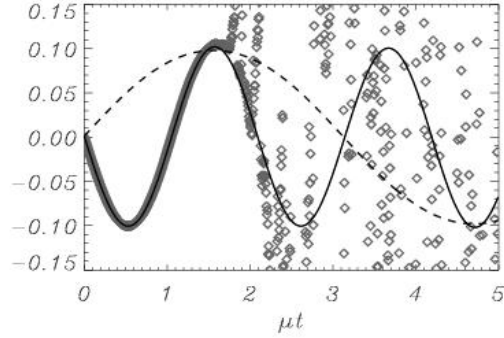
It is interesting to note that there is a strong similarity between the stochastic differential equations discussed here and those found for the anharmonic oscillator in the positive P representation. Indeed, if we write equations for $\alpha e^{-i\mu t}$ and $\alpha^+ e^{i\mu t}$, then we recover the equations discussed by Plimak *et al* [Plimak & al.]. An important difference, however, is that the diffusion for the positive P representation occurs with the opposite sign to that for the Q function. This means that the stochastic averages (2.21) have opposite signs when applied to the positive P representation. We can use the methods described in this section to obtain the expectation value of $\hat{a}(t)$ in the positive P representation. The stochastic average gives $\langle\alpha(t)\rangle_S = \beta e^{-i\mu t}\exp\left(|\beta|^2(e^{-i2\mu t} - 1)\right)$. Performing the average of this over a δ-function positive P distribution, peaked at $\beta = \alpha_0 = \beta^{+*}$, gives the correct result (2.17). The positive P representation is associated with operator moments in normal order and this seems to be the reason for the well-behaved form of the stochastic averages for initial coherent states.

2.5 Stochastic simulation of the anharmonic oscillator

In this section we present results of numerical simulations [Toral & al.] of the stochastic process $\alpha(t)$ given in Eq. (2.26). Our simulations were performed using two discrete Gaussian processes η_l, η_l^+ of the form

$$\eta_l = \int_{\Delta t} dt' \xi(t') , \qquad \eta_l^+ = \int_{\Delta t} dt' \xi^+(t') \tag{2.37}$$

where $t = l\Delta t$. In this way $< \eta_l\eta_{l'} >= 2i\mu\Delta t\delta_{ll'}$ and $< \eta_l^+\eta_{l'}^+ >= -2i\mu\Delta t\delta_{ll'}$. We note that the relations (2.21) do not completely specify the two independent *complex* white noises. As recently shown in [Plimak & al.] the degree of freedom in the choice of the noise could be used to improve the results of the numerical simulation by choosing the stochastic processes ξ and ξ^+ so as to inhibit (but not completely suppress) the fast growth of $\alpha(t)$. In this Chapter, however, we have considered only the forms $\xi = \sqrt{2i\mu}\phi$ and $\xi^+ = \sqrt{-2i\mu}\phi^+$ with ϕ and ϕ^+ being *real* white noises. Each stochastic realization must start from a single point in phase space. For this reason, the analysis of the preceding section leads us to conclude that diverging trajectories, exploring large values of $|\alpha|$ are inevitable. These divergences are responsible for the unbounded average obtained by performing the stochastic

Figure 2.3: Phase space plot of the numerical average $\langle\alpha(t)\rangle_S$, the real part of which is shown in Fig. 2.2. The points represent numerical values at different times. The circle represents the analytical result for $\langle\alpha(t)\rangle_S$.
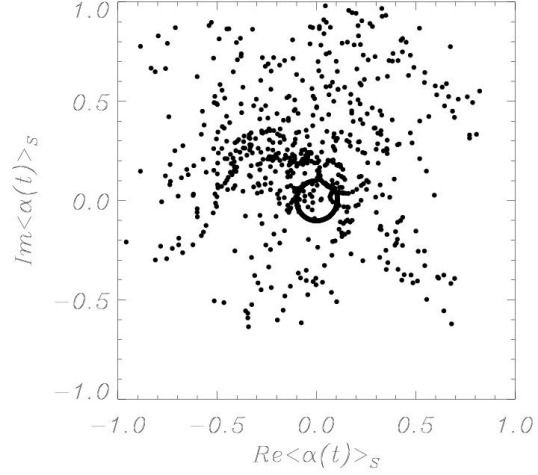
average before the average over the initial Q distribution. Each of our simulations starts with at a point $\alpha(0) = \alpha^{+*}(0) = \beta$. Naturally, the average over the initial Q distribution requires stochastic realizations for a range of values of β, weighted by the distribution (2.22). Consideration of a single value of β, however, suffices to illustrate the divergences associated with individual trajectories. We observe, in each case, a divergence after some time. We can see the origin of these divergences in the Eqs. (2.19) and (2.20); the complex variables α and α^+ are not constrained to be complex conjugate quantities and so, in any given realization, the combination $\alpha^+\alpha$ can acquire an imaginary part. This leads to exponential growth of α or α^+. The time at which this divergence appears varies between realizations and also depends on the initial conditions. In particular, the divergence appears earlier for larger values of $|\beta|^2$. This is because of the exponential dependence of $\alpha(t)$ on $|\beta|^2$ as seen in Eq. (2.26).

If we select a sufficiently small value of β and perform an average over a large number of trajectories then we find a result that is, for short times, in good agreement with the analytical average Eq. (2.31). In Fig. 2.2 we have plotted the time evolution of $Re\langle\alpha(t)\rangle_S$, obtained by considering 50000 trajectories, starting from the initial condition $\beta = 0.001 + i0.1$ (diamonds line). For comparison the analytical expression for the stochastic average is represented by a continuous line. At very short times, we observe a near perfect agreement between the numerical results and the analytical expression. At longer times, this agreement is lost because of the divergence induced by the independent stochastic noises.

The trajectories start from a single point in phase space. This corresponds to selecting, in each simulation, a δ function phase-space probability distribution. Such a narrow distribution for the Q_0 distribution does not correspond to any physically allowed state [Gardiner & Zoller]. Indeed, the evolution obtained from the Fokker-Planck equation for such an initial condition is highly singular. It is this behavior that is reflected in the divergent numerical simulations. Fig. 2.3 depicts the numerically obtained value of $\langle\alpha(t)\rangle_S$. We see that this average explores an extended region of the complex plane. The analytical average, Eq. (2.31), is represented by the small circle.

The relationship between the time at which trajectories diverge and the initial condition (β) means that an ensemble of trajectories starting from a range of different initial conditions will rapidly produce divergences. For this reason the analytical result (2.17) cannot be reproduced numerically in any straightforward manner.

2.6 Conclusion and outlook

In conclusion in this Chapter we have considered a proposal of [Yuen & Tombesi] to give a stochastic representation of a Fokker-Planck equation with negative diffusion for the Q distribution. We have shown that the correct analytical moments for an anharmonic oscillator (associated with a *nonlinear* $\chi^{(3)}$ process) can be obtained from the stochastic differential equations. These results, however, are highly sensitive to the order in which averages over the stochastic realizations and over the distribution of the initial conditions are performed. It is clear that more sophisticated techniques are required for stochastic simulation of the problem. Recent work suggests that the effects of divergences can be significantly suppressed but not yet eliminated [Plimak & al., Carusotto & al.].

The system studied in this Chapter is highly idealized. We could include the effects of loss and expect that these will improve the stability of the numerical results. Such an improvement has been noted in studies of the positive P [Gilchrist & al.]. It is possible, that there are other interesting systems that are less sensitive to the noise and for these, stochastic simulations using the Yuen-Tombesi method may prove to be a useful technique. Possible systems for study in quantum optics include the OPO and SHG, that can be successfully studied with this approach. In these systems the diffusion matrix in the equation for Q is negative for values of the pump mode twice above its threshold value. For input intensities not close to twice the threshold value this method can be used. The Q representation in pattern forming intracavity SHG is used in Ref.[Bache & al.]. The use of the Q representation in a type I OPO is further discussed in Ch.4.

Chapter 3

Vectorial Kerr resonator: Quantum fluctuations above threshold

In this Chapter we consider an optical cavity filled with a Kerr medium, pumped by a laser field (Kerr resonator). The basic nonlinear process in this device is the same cubic nonlinearity characterizing the anharmonic oscillator studied in the previous Chapter. However, the anharmonic oscillator is a crude approximation for the interaction between one mode of the field and a Kerr medium. In this chapter we consider a more realistic continuous model for the description of the light properties in a Kerr resonator. This is a *Kerr vectorial model* [Hoyuelos & al. (98)] in which the vectorial character of the field, i.e. the **polarization** state, is explicitly considered.

In Sect.3.1-3.2 we introduce the model and the corresponding temporal evolution of the Wigner distribution. We discuss under which conditions and in which approximations the dynamics of the Wigner distribution can be described in terms of partial stochastic differential equations. We propose two approximations, one consisting in a linearization around the pattern solution (Sect.3.2.1) and the other one obtained dropping the third order derivatives in the equation for the W functional (Sect.3.2.2). The equations presented in Sect.3.2.2 are used only to give a qualitative picture of the evolution of the total fields. Calculations of the quantum properties are performed using the linear equations (Sect.3.2.1). The classical features of this system have been studied by [Geddes & al., Hoyuelos & al. (98)] and are reviewed in Sect.3.3, where we calculate the classical stationary solutions, that constitute the reference state about which *linearization* is performed. We study the intracavity dynamics of the fluctuations and their spatial features in Sect.3.4. In Sect.3.5 we provide a dynamical description of the fluctuations at the **output** of the cavity. These output fluctuations are used to study the quantum correlations in Sect.3.6.

The analysis presented in this Chapter takes into account the whole set of transverse cavity modes in the field operators. This is the first analysis with a **continuous** model of quantum correlations between transversal spatial modes of the field, in a pattern **above threshold**. As mentioned in Sect.1.4, previous studies in situations above threshold were based on three-mode approximations

[Lugiato & Castelli, Lugiato & Grynberg, Castelli & Lugiato, Hoyuelos & al. (99)].

3.1   Phase space description

In this Section we describe the vectorial Kerr resonator in the quantum formalism: following the theoretical procedure presented in Ch.1, we obtain from the Master equation the equation for the Wigner (W) quasi-probability distribution.

We consider a one-directional ring cavity (see Fig.1.8 in Ch.1) with four flat mirrors, one of which has a high, but finite reflectivity, and the others are fully reflecting. Inside the cavity is placed a sample of an isotropic Kerr medium, characterized by a third order susceptibility tensor $\chi_{ijkl}^{(3)}$. The cavity is driven by a coherent, plane-wave, monochromatic and stationary field, with a uniform distribution in the transverse plane and frequency ω_0. The input field is linearly polarized, for definiteness along the x direction. The relations between linear (E_x, E_y) and circular (E_+, E_-) polarizations are

$$E_+ = \frac{E_x + iE_y}{\sqrt{2}}, \qquad E_- = \frac{E_x - iE_y}{\sqrt{2}} \tag{3.1}$$

In our case, the circularly polarized components of the pump are equal: $E_{0+} = E_{0-} = E_0$.

We assume the slowly varying envelope and paraxial approximations, and the cavity mean field limit, that allows to neglect the dependence of the field on the longitudinal coordinate z along the sample (see Sect.1.3.1). Under these conditions only one longitudinal cavity mode is relevant, precisely the one corresponding to the longitudinal cavity resonance ω_c closest to ω_0. We denote by $\hat{A}_+(\vec{x}, t)$ and $\hat{A}_-(\vec{x}, t)$ the intracavity field envelope operators corresponding to the right and left circularly polarized components. These operators depend on the transverse space coordinate $\vec{x} = (x, y)$ and time t, and obey the standard equal-time commutation relations introduced in Sect.1.4:

$$\left[\hat{A}_i(\vec{x}, t), \hat{A}_j^\dagger(\vec{x}', t) \right] = \delta_{ij} \delta(\vec{x} - \vec{x}') , \tag{3.2}$$

where the indexes i, j stand for $+, -$. By adopting a picture in which the fast oscillation at the carrier frequency ω_0 is eliminated, the reversible part of the dynamics of the intracavity field is described by the following Hamiltonian [Hoyuelos & al. (99)], that represents a generalization to the vectorial case of the one introduced in [Lugiato & Castelli] for a scalar Kerr medium:

$$\hat{H} = \hat{H}_0 + \hat{H}_{ext} + \hat{H}_{int} . \tag{3.3}$$

$\hat{H}_0$ describes the free propagation of the intracavity field in the paraxial approximation:

$$\hat{H}_0 = \hbar K \int d^2 \vec{x} [\hat{A}_+^\dagger(\vec{x})(\eta\theta - a\nabla^2)\hat{A}_+(\vec{x}) + \hat{A}_-^\dagger(\vec{x})(\eta\theta - a\nabla^2)\hat{A}_-(\vec{x})] , \tag{3.4}$$

where $K = cT/(2\mathcal{L})$ is the cavity linewidth, with c being the speed of light, T the transmittivity coefficient of the input/output mirror and $\mathcal{L}$ the total cavity length; $\eta\theta$ is the cavity detuning parameter; η is the sign of the Kerr nonlinearity ($\eta = 1$ for the self-focusing case and $\eta = -1$ for the self-defocusing case); ∇^2 is the two dimensional transverse Laplacian that models the effect of diffraction in the paraxial

approximation; the parameter a has the dimension of an area, so that $l_D = \sqrt{a} \approx \sqrt{\mathcal{L}\lambda/(2\pi T)}$, with λ being the wavelength, defines the length scale for transverse pattern formation.

$\hat{H}_{ext}$ models the coherent pumping by a classical plane-wave driving field of amplitude E_0:

$$\hat{H}_{ext} = i\hbar K E_0 \int d^2\vec{x}[\hat{A}_+^\dagger(\vec{x}) - \hat{A}_+(\vec{x}) + \hat{A}_-^\dagger(\vec{x}) - \hat{A}_-(\vec{x})]\,, \tag{3.5}$$

where, without any loss of generality, E_0 has been taken real.

$\hat{H}_{int}$ is the interaction Hamiltonian that describes the coupling due to the Kerr nonlinearity:

$$\hat{H}_{int} = -\eta\hbar K g \int d^2\vec{x} \left\{ \frac{\alpha}{2} \left[\hat{A}_+^{\dagger 2}(\vec{x})\hat{A}_+^2(\vec{x}) + \hat{A}_-^{\dagger 2}(\vec{x})A_-^2(\vec{x}) \right] + \beta \left[\hat{A}_+^\dagger(\vec{x})\hat{A}_-^\dagger(\vec{x})\hat{A}_+(\vec{x})\hat{A}_-(\vec{x}) \right] \right\}$$

where the coupling constant g is related to the element $\chi_{1111}^{(3)}$ of the susceptibility tensor. Constants α and β are also related to the susceptibility tensor components [Boyd]. For an isotropic medium they satisfy $\alpha + \beta = 2$. We will use typical values for a liquid Kerr medium: $\alpha = 1/4$ and $\beta = 7/4$ [Geddes & al., Hoyuelos & al. (98)].

We apply the quantum classical correspondence

$$\hat{\rho}\hat{A}_\pm^\dagger(\vec{x}) \iff \left(\alpha_\pm^*(\vec{x}) + \frac{1-s}{2} \frac{\delta}{\delta\alpha_\pm(\vec{x})} \right) W_s(\alpha_+, \alpha_+^*, \alpha_-, \alpha_-^*)$$

$$\hat{A}_\pm^\dagger(\vec{x})\hat{\rho} \iff \left(\alpha_\pm^*(\vec{x}) - \frac{1+s}{2} \frac{\delta}{\delta\alpha_\pm(\vec{x})} \right) W_s(\alpha_+, \alpha_+^*, \alpha_-, \alpha_-^*)$$

$$\hat{\rho}\hat{A}_\pm(\vec{x}) \iff \left(\alpha_\pm(\vec{x}) - \frac{1+s}{2} \frac{\delta}{\delta\alpha_\pm^*(\vec{x})} \right) W_s(\alpha_+, \alpha_+^*, \alpha_-, \alpha_-^*)$$

$$\hat{A}_\pm(\vec{x})\hat{\rho} \iff \left(\alpha_\pm(\vec{x}) + \frac{1-s}{2} \frac{\delta}{\delta\alpha_\pm^*(\vec{x})} \right) W_s(\alpha_+, \alpha_+^*, \alpha_-, \alpha_-^*)\,. \tag{3.6}$$

to the Maser equation (1.14) introduced in Ch.1, obtaining the evolution equation for any quasiprobability distributions:

$$\frac{\partial W_s(*)}{\partial t} = \int d^2\vec{x} K \left[-\sum_{i=1}^4 \left(\frac{\delta}{\delta z_i(\vec{x})} Q_i \right) + \frac{1}{2} \int d^2\vec{x}' \sum_{i,j=1}^4 \frac{\delta^2}{\delta z_i(\vec{x})\delta z_j(\vec{x}')} D_{ij}(\vec{x},\vec{x}') \right.$$

$$\left. + \frac{1}{6} \int d^2\vec{x}' \int d^2\vec{x}'' \sum_{i,j,l=1}^4 \frac{\delta^3}{\delta z_i(\vec{x})\delta z_j(\vec{x}')\delta z_l(\vec{x}'')} T_{ijl}(\vec{x},\vec{x}',\vec{x}'') \right] W_s(*), \tag{3.7}$$

where $(z_1, z_2, z_3, z_4) = (\alpha_+, \alpha_+^*, \alpha_-, \alpha_-^*)$, and $W_s(*) = W_s(z_1, z_2, z_3, z_4)$. The dependence on space and time of variables z_i is omitted to simplify the notation. The drift (Q_i), diffusion (D_{ij}) and third order derivative (T_{ijl}) terms are given in Appendix C.1.

Eq.(3.7) is not a bona-fide Fokker-Planck equation (FPE) for a probability distribution: in the Wigner representation ($s = 0$) third order derivatives appear, and in the P ($s = +1$) and Q ($s = -1$) representation the diffusion is negative. So, generally, the solution of Eq.(3.7) is not positive definite. Moreover, these peculiarities are actually at the origin of the most interesting quantum effects, being associated with negative values of the quasiprobabilities. For a well defined FPE there is an equivalent stochastic representation in terms of trajectories of a classical Langevin process [Gardiner]. The Langevin equations equivalent to the FPE are a powerful numerical instrument. As mentioned in Ch.1.2.3.b.1, a commonly used approach, to circumvent difficulties when quasiprobabilities do not obey a FPE, consists in

the use of the P_+ distribution [Drummond & al. (81)], considering a doubled phase space: increasing the number of variables of the problem it is possible to avoid negativity of the diffusion, obtaining a FPE in the doubled phase space. However the problem of the solution of functional equations, in presence of nonlinear coupling between modes, is still open: in fact also the P_+ distribution give divergence problems in the stochastic trajectories associated with the FPE in the doubled space [Gilchrist & al.]. In the previous Chapter we have seen similar problems extending the Q distribution to a doubled phase space. Moreover, doubling phase space techniques have the disadvantage to increase the number of equations to integrate. This is an important problem in the analysis of spatial dependent systems, that require huge integration times for numerical simulations.

In the next Section we discuss the possibilities to give a stochastic description of the Kerr resonator, based on the Wigner representation.

3.2   Stochastic description

Equation (3.7) is of little practical use, both from an analytical and computational point of view. In order to obtain a more useful equation we have to introduce some approximation (see Sect.1.2.3.b). In the Sect.3.2.1 we outline the linearization procedure, leading to a set of linear Langevin equations for the fields fluctuations. This is a good approximation in presence of stable reference states.

In Sect.3.2.2 another approximated set of non linear Langevin equations for the total fields is presented. The validity of this kind of approximation is a topic under investigation. It is known that the evaluation of higher order moments in this model is not always correct [Drummond & Kinsler, Kinsler]. For this reason this nonlinear Langevin equations will be used only in order to have a qualitative picture of the behavior of the pattern in presence of noise.

3.2.1   Linear Langevin equations

In this Section we will be interested in describing the dynamics of small quantum fluctuations around some classical mean value. This linearization procedure is independent of the particular type of average solution around which we are linearizing. Therefore we outline the procedure assuming to have an inhomogeneous reference state that is stable, so that fluctuations around this solution are small.

Rather than deriving this dynamics from the inverse system size expansion of Eq.(3.7), we will use an equivalent procedure, which amounts to expanding the master equation (1.14) in a power series of fluctuation operators. For this purpose we separate the field operators into two parts,

$$\hat{A}_\pm(\vec{x}, t) = F_\pm(\vec{x}) + \delta\hat{A}_\pm(\vec{x}, t)\,, \tag{3.8}$$

where $F_\pm(\vec{x})$ are c-number fields, representing macroscopic, classical stationary fields, and $\delta\hat{A}_\pm(\vec{x}, t)$ are fluctuation operators. Next, we expand both the Hamiltonian (3.3) and the Liouvillian operator (1.15)

in power series of the fluctuation operators $\delta\hat{A}_\pm(\vec{x}, t)$:

$$\hat{H} = \hat{H}^{(0)} + \hat{H}^{(1)} + \hat{H}^{(2)} + \dots \tag{3.9}$$

$$\Lambda = \Lambda^{(0)} + \Lambda^{(1)} + \Lambda^{(2)} \tag{3.10}$$

The zero-order terms $\hat{H}^{(0)}, \Lambda^{(0)}$ do not give any contribution to the dynamics; the first-order contributions give rise in the master equation to terms that vanish identically when the c-number fields $F_\pm(\vec{x})$ are taken as the steady-state solution of the classical time evolution equations [Geddes & al., Hoyuelos & al. (98)]

$$0 = -(1 + i\eta\theta)F_\pm + ia\nabla^2 F_\pm + E_0 + i\eta g[\alpha|F_\pm|^2 + \beta|F_\mp|^2]F_\pm. \tag{3.11}$$

The second-order term of the Hamiltonian is explicitly given by:

$$\hat{H}_0^{(2)} = \hbar K \int d^2\vec{x} \sum_{i=+,-} \delta\hat{A}_i^\dagger(\vec{x})(\eta\theta - a\nabla^2)\delta\hat{A}_i(\vec{x})$$

$$\hat{H}_{ext}^{(2)} = 0$$

$$\hat{H}_{int}^{(2)} = -\eta\hbar K g \int d^2\vec{x} \frac{\alpha}{2} \sum_{i=+,-} \left[\delta\hat{A}_i^2(\vec{x})F_i^{*2}(\vec{x}) + \delta\hat{A}_i^{\dagger 2}(\vec{x})F_i^2(\vec{x}) + 4|F_i(\vec{x})|^2\delta\hat{A}_i^\dagger(\vec{x})\delta\hat{A}_i(\vec{x}) \right]$$

$$+ \beta \left[F_+(\vec{x})F_-(\vec{x})\delta\hat{A}_+^\dagger(\vec{x})\delta\hat{A}_-^\dagger(\vec{x}) + F_+(\vec{x})F_-^*(\vec{x})\delta\hat{A}_+^\dagger(\vec{x})\delta\hat{A}_-(\vec{x}) + h.c. \right]$$

$$+ \beta \left[|F_+(\vec{x})|^2\delta\hat{A}_-^\dagger(\vec{x})\delta\hat{A}_-(\vec{x}) + |F_-(\vec{x})|^2\delta\hat{A}_+^\dagger(\vec{x})\delta\hat{A}_+(\vec{x}) \right].$$

Higher order terms in the Hamiltonian are neglected, on the basis of a small quantum noise approximation, which is valid for a macroscopic system, i.e. for large saturation photon number n_s, not too close to critical points. The expression for the Liouvillian $\Lambda^{(2)}$ is obtained by simply replacing $\hat{A}_\pm(\vec{x})$ by $\delta\hat{A}_\pm(\vec{x})$ in (1.15).

Next we apply to the approximated Master equation the correspondence relations (3.6), with the field operators replaced by the fluctuations operators. In the Wigner representation we obtain the following Fokker-Planck equation:

$$\frac{\partial W_0(z_1, z_2, z_3, z_4)}{\partial t} = \int d^2\vec{x} \left[-\sum_{i=1}^4 \left(\frac{\delta}{\delta z_i(\vec{x})} Q_i \right) \right. \tag{3.12}$$

$$\left. + \frac{1}{2} \int d^2\vec{x}' \sum_{i,j=1}^4 \frac{\delta^2}{\delta z_i(\vec{x})\delta z_j(\vec{x}')} D_{ij}(\vec{x}, \vec{x}') \right] W_0(z_1, z_2, z_3, z_4),$$

where now $(z_1, z_2, z_3, z_4) = (\Delta\alpha_+, \Delta\alpha_+^*, \Delta\alpha_-, \Delta\alpha_-^*)$ are the c-number fields corresponding to the fluctuation operators. The drift and diffusion terms are given in Appendix C.2.

As mentioned in Ch.1, for a quadratic Hamiltonian, the diffusion matrix of the Fokker-Planck equation in the Wigner representation is positive definite. This condition is not necessarily fulfilled in other representations. A positive definite diffusion matrix allows us to interpret $\Delta\alpha_+$ and $\Delta\alpha_-$ as classical stochastic processes, described by a set of Langevin equations [Gardiner], equivalent to (3.12), that

are given by:

$$\frac{\partial \Delta\alpha_\pm(\vec{x},t)}{\partial t} = \left\{ -(1+i\eta\theta) + i\nabla^2 + i\eta[2\alpha|F_\pm(\vec{x})|^2 + \beta|F_\mp(\vec{x})|^2] \right\} \Delta\alpha_\pm(\vec{x},t) + \tag{3.13}$$

$$i\eta \left[\alpha F_\pm^2(\vec{x})\Delta\alpha_\pm^*(\vec{x},t) + \beta F_\pm(\vec{x})F_\mp^*(\vec{x})\Delta\alpha_\mp(\vec{x},t) + \beta F_\pm(\vec{x})F_\mp(\vec{x})\Delta\alpha_\mp^*(\vec{x},t) \right] + \sqrt{2}\Delta\alpha_\pm^{in}(\vec{x},t).$$

where, in order to simplify the notation, we have introduced the scaled variables:

$$\begin{aligned}
\widetilde{x} &= x/\sqrt{a}, \\
\widetilde{t} &= Kt, \\
\widetilde{E}_0 &= \sqrt{g}E_0, \\
\widetilde{\Delta\alpha_j} &= \sqrt{a}\Delta\alpha_j, \\
\widetilde{F_\pm} &= \sqrt{g}F_\pm
\end{aligned} \tag{3.14}$$

and omitted the tildes.

The stochastic terms $\Delta\alpha_\pm^{in}(\vec{x},t)$ can be interpreted as quantum fluctuations entering the cavity through the coupling mirror [Reynaud & al. (92)], and are described by Gaussian white noise, with zero average and correlations given by:

$$\begin{aligned}
\langle \Delta\alpha_i^{in}(\vec{x},t)\,\Delta\alpha_j^{*\,in}(\vec{x}',t') \rangle &= \frac{1}{2}\delta_{ij}\delta(\vec{x}-\vec{x}')\delta(t-t'), \\
\langle \Delta\alpha_i^{in}(\vec{x},t)\,\Delta\alpha_j^{in}(\vec{x}',t') \rangle &= 0,
\end{aligned} \tag{3.15}$$

where the subindices i,j stand for the circularly polarized components $+,-$.

These equations will be used to calculate fluctuations correlations, while in order to visualize the full fields dynamics, in the next section, we propose a set of nonlinear Langevin equations in a different approximation.

3.2.2 Nonlinear Langevin equations

In our model the parameter g^{-1} plays the role of a scaling factor for the photon number; precisely $n_s = ag^{-1}$ represents the intracavity saturation photon number on the characteristic area a in the transverse plane, and typically is a very large number. By reformulating Eq. (3.7) in terms of scaled fields, $z_i \to \sqrt{g}z_i$ it is readily seen that the second order derivative terms scale as g, while the third order derivative terms scale as g^2. In the case of the Wigner representation it is possible to neglect the third order derivatives, resulting in a Fokker-Planck equation which has a positive definite diffusion matrix [Drummond (86)]. The drift Q_1, in terms of the scaled fields, takes the form $Q_1 = [-(1+i\eta\theta) + ig\eta(\alpha+\beta/2)(s-1) + ia\nabla^2]z_1 + E_o + i\eta[\alpha z_1 z_2 + \beta z_3 z_4]z_1$ where the term $ig\eta(\alpha+\beta/2)(s-1)$ is of higher order in g and can be neglected. Proceeding in a similar way for all the drift terms, the equivalent set of Langevin equations finally read:

$$\frac{\partial \alpha_\pm}{\partial t} = -(1+i\eta\theta)\alpha_\pm + i\nabla^2\alpha_\pm + E_0 + i\eta[\alpha|\alpha_\pm|^2 + \beta|\alpha_\mp|^2]\alpha_\pm + \sqrt{2}\xi_\pm(\vec{x},t), \tag{3.16}$$

where we have used the space and time scaling introduced in the previous section and for the total fields:

$$\widetilde{\alpha}_j = \sqrt{g}\alpha_j. \tag{3.17}$$

Here $\xi_{\pm}(\vec{x}, t)$ are complex Gaussian random variables of zero mean and variance given by:

$$\langle \xi_i(\vec{x}, t)\xi_j^*(\vec{x}', t')\rangle = \frac{1}{2n_s}\delta_{ij}\delta(\vec{x} - \vec{x}')\delta(t - t'), \tag{3.18}$$

$$\langle \xi_i(\vec{x}, t)\xi_j(\vec{x}', t')\rangle = 0 \tag{3.19}$$

By letting $n_s \to \infty$, and hence dropping the stochastic noise terms ξ_i, one recovers the classical time evolution equations of the model [Geddes & al., Hoyuelos & al. (98)], for the macroscopic fields $E_{\pm}(\vec{x}, t)$:

$$\frac{\partial E_{\pm}}{\partial t} = -(1 + i\eta\theta)E_{\pm} + i\nabla^2 E_{\pm} + E_0 + i\eta[\alpha|E_{\pm}|^2 + \beta|E_{\mp}|^2]E_{\pm}. \tag{3.20}$$

Equations (3.16) can be as well interpreted as the classical nonlinear equations of the model, with a Gaussian noise term added. The derivation of these equations from a quantum model adds to this picture a precise value of the strength of the Gaussian noise, and allows us for interpreting it as vacuum fluctuations entering the input/output cavity mirror. However, we have already mentioned that there are important limitations to this kind of approach, known as "stochastic electrodynamics".

3.3   Stationary pattern

In this Section we review the process of pattern formation in a Kerr cavity, described by the classical equations (3.20). In particular we refer to the papers of [Geddes & al., Hoyuelos & al. (98)] in which this system is considered including the polarization degree of freedom. In self-defocusing ($\eta = -1$) scalar models there are not stable patterns. For this reason initial investigations focused on the self-focusing case ($\eta = 1$), in which stripes (one transverse dimension) or stable hexagons patterns (two transverse dimensions) are predicted [Scroggie & al.]. However including the polarization degree of freedom (**vectorial Kerr model**) a polarization instability is predicted, producing patterns also in the self-defocusing case. Let us consider Eq.(3.20): we observe that for an input field x-polarized the equations are symmetric in the polarization field components. If we look for *homogeneous* stationary solutions of the classical equations (3.20), we can find *symmetric* solutions, such that

$$E_+^{st} = E_-^{st}, \tag{3.21}$$

but also *asymmetric* solutions, such that

$$E_+^{st} \neq E_-^{st}. \tag{3.22}$$

In the first case the solution has the same x-polarization of the pump so that a scalar model would be enough, while in the second case there is a finite intensity also in the polarization component not excited by the pump, so that the interaction with the medium changes the polarization of the field.
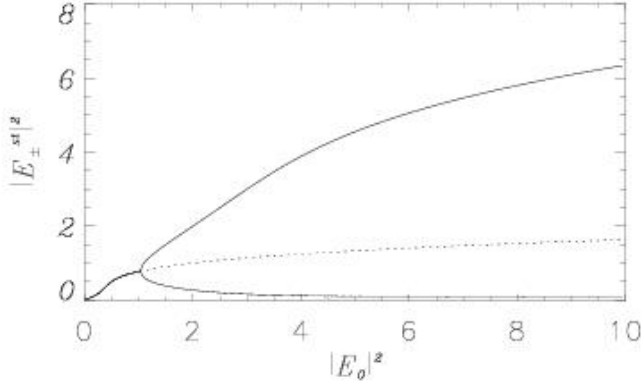
Figure 3.1: Symmetric (central line) and asymmetric homogeneous solutions (upper an lower lines) for $\eta = -1, \theta = 1, \alpha = \frac{1}{4}, \beta = \frac{7}{4}$. The stable solution is represented by a continuous line and the unstable one by a dotted line. The intersection point corresponds to the threshold (3.24).

The homogeneous stationary *symmetric* solution is given by:

$$E_+^{st} = E_-^{st} = E^{st} \qquad |E_0|^2 = |E^{st}|^2 [1 + (2|E^{st}|^2 - \theta)^2]. \tag{3.23}$$

This relation implies bistability, for values of $\theta > \sqrt{3}$: for some input intensities there are 2 stable values for the output intensity. In this work we consider $\theta < \sqrt{3}$.

On the other hand an homogeneous stationary *asymmetric* solution, breaking the symmetry $+ \leftrightarrow -$, appears for an input intensity $|E_0|^2$ such that the intensity of the symmetric solution is larger than

$$I_s'' = \frac{\theta(B-2) + \sqrt{\theta^2 B^2 + 4(B-1)}}{4(B-1)}. \tag{3.24}$$

where the correspondence with the notation used in [Geddes & al., Hoyuelos & al. (98)] is $\alpha = A$ and $\beta = A + B$. In this range of values of $|E_0|^2$ the solution (3.23) is unstable under asymmetric perturbations, and the stable output is elliptically polarized.

In Fig.3.1 the homogeneous stationary *symmetric* and *asymmetric* solutions are plotted as function of the input intensity: the continuous lines represent the stable solutions and the dotted line the unstable one -with respect to homogeneous perturbations-. We can observe how the symmetric solution stable for low pump is destabilized by an *asymmetric* solution ($E_+^{st} \neq E_-^{st}$), above the threshold given by Eq.(3.24).

Eq.(3.23) gives the symmetric *homogeneous* stationary solutions of the equations (3.20), corresponding to plane-wave solutions for the total field. The next step is to consider if such solutions are stable under spatially modulated perturbations. In the self-defocusing case $\eta = -1$, the steady state (3.23) becomes unstable when the pump intensity is increased to a value such that $|E^{st}|^2 > |E_c^{st}|^2 = 1/(\beta - \alpha) = 2/3$ [Geddes & al., Hoyuelos & al. (98)]. For an x-polarized pump field, and immediately above this instability threshold, a y-polarized stripe pattern emerges, characterized by the critical transverse wave-vector

$$k_c = \sqrt{\theta - \alpha/(1-\alpha)}, \tag{3.25}$$

while the x-component remains basically homogeneous. Increasing the pump, on top of the

homogeneous part, the x-polarized component of the stationary solution shows very small amplitude stripes with wavevector $2k_c$ [Hoyuelos & al. (98)]. This is usually called a **polarization pattern** since it emerges as a consequence of a polarization instability. In Fig. (3.2) we show the range of values of $I_{s+} = |E_{s+}|^2$ for which a pattern appears, destabilizing the symmetric solution ($I_{s+} < I_s''$) or the asymmetric solution ($I_{s+} > I_s''$). In this work we will consider an input intensity immediately above the pattern formation threshold, corresponding to the lowest region of the "island" plotted in Fig. (3.2).

The classical fields $F_\pm(\vec{x})$ describing these stripe patterns can be obtained by numerical integration of the dynamical equations (3.20). The numerical scheme used here is described in detail by [Montagne & al.]. The method is pseudo-spectral and second-order accurate in time, and is similar to the so-called two-step method. Lattices of size 128×128 were used with $\Delta x = 0.6012$ and $dt = 0.05$. The orientation of the stripes is selected by the initial condition. We choose an initial condition that favors the formation of vertical stripes. In Fig. (3.3) we show the stationary solution, in the x and y polarization components, where

$$F_\pm = \frac{F_x \pm iF_y}{\sqrt{2}}. \tag{3.26}$$

On the left column we plot the near field, and in the right one the far field intensities, corresponding to the Fourier transforms of the near field. In F_y a modulation at $k_x \sim k_c$ around the zero homogeneous
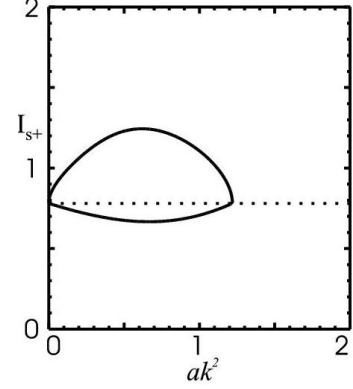
Figure 3.2: Marginal stability curve for $\eta = -1, \theta = 1, \alpha = \frac{1}{4}, \beta = \frac{7}{4}$, with respect to perturbations at k. $I_{s+} = |E_{s+}|^2$. The horizontal dotted line corresponds to I_s''.
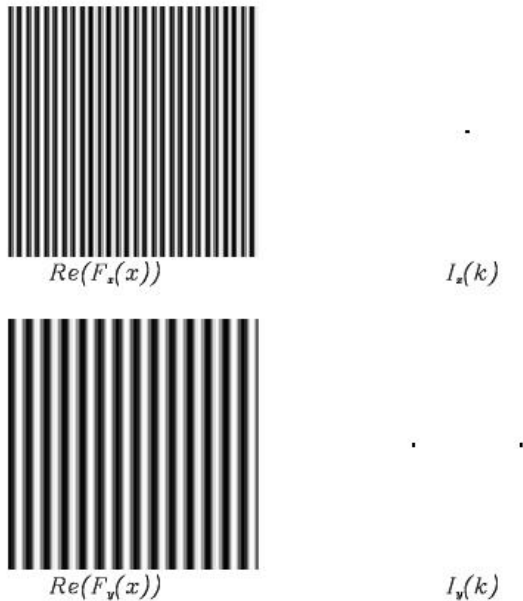
Figure 3.3: Real parts of the x and y components of the stationary solution, for $E_0 = 0.919, \theta = 1$. On the left are represented the near fields and n the right the far fields.

solution appears; while in F_x dominates the homogeneous component with a small modulation at $k_x \sim 2k_c$, due to the nonlinear coupling between x and y components. The predominance of the mode $F_x(\vec{0})$ is evident looking at the far field: the peaks $|F_x(\pm 2k_c, 0)|^2$ are negligible in comparison with $F_x(\vec{0})$. These fields obtained numerically enter as space-dependent coefficients in the linearized Langevin equations (3.13), that are studied in the next Chapter.

3.4 Fluctuations inside the cavity

In this Section we present the numerical results of the simulation of Eq.(3.13). These Langevin equations describe the linearized fluctuations dynamics around a fixed stationary solution, that, in the parameter regime we are considering, is an inhomogeneous solution, in form of a stripe pattern. Fluctuations are calculated from these stochastic equations, which are numerically integrated using a pseudo-spectral method in Fourier space with periodic boundary conditions. The method is first order accurate in time so that with respect to the case of the deterministic equations, we decrease the time steps to $dt = 0.005$. The Gaussian stochastic process $\Delta\alpha_i^{in}$, representing the input fluctuations is obtained using the random number generator proposed in [Toral & al.].

A main qualitative aspect of the fluctuations calculated numerically in this way can be observed in Fig.3.4. In a single stochastic realization of equations (3.13), the fluctuations of the x-polarized field component appear homogeneously distributed in space; this follows from the spatial homogeneity of the x-polarized component of the stationary classical solution. However, fluctuations in the y-polarized component tend to be distributed in space with a stripe structure, similar to that of the corresponding steady-state solution, but shifted to the left or to the right by a quarter-period, as shown in Fig. 3.5.

The spatial structure of the field fluctuations can be understood in terms of a **Goldstone mode** [Foster] as we explain in the following. Very generally, consider a
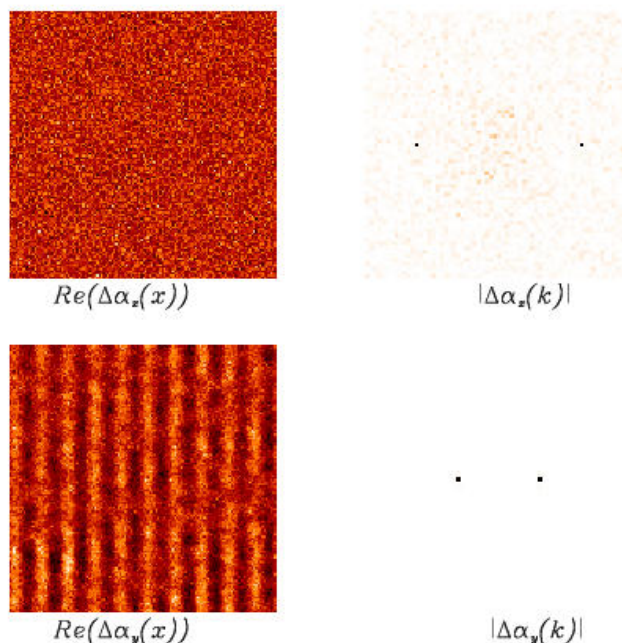

Figure 3.4: Fluctuations in the Near field and in the Far Field, with same parameters of Fig. (3.3)
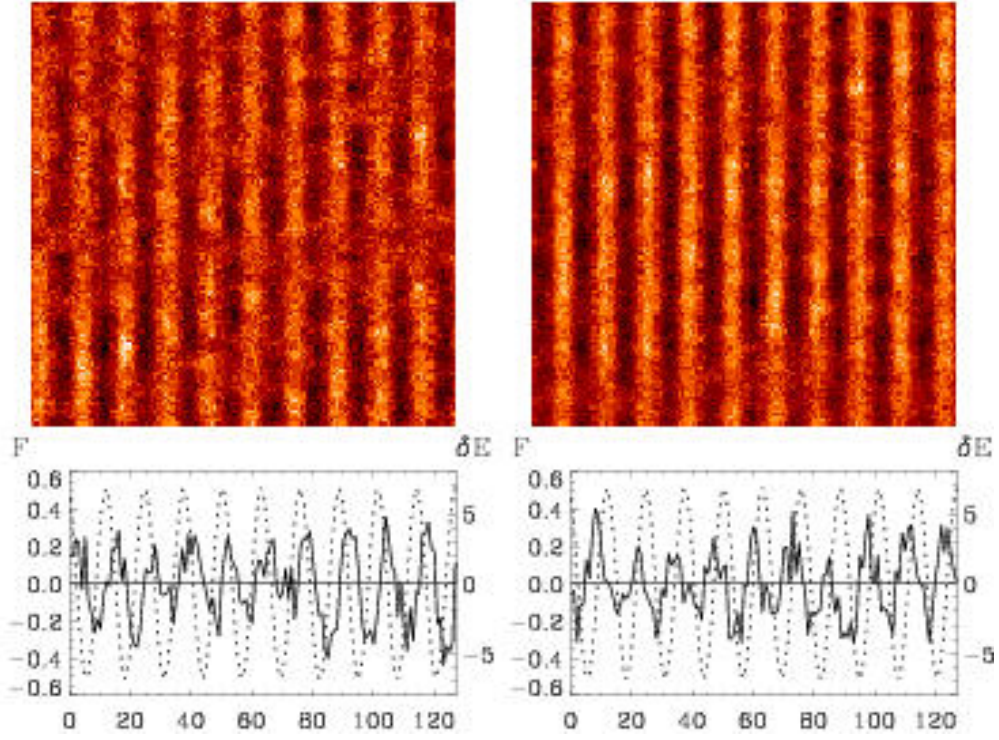
Figure 3.5: *Upper plots*: distribution in the transverse plane of the real part of the y-polarized fluctuations for two different realizations in a stationary regime ($Kt \sim 10^4$). For these two realizations the patterns of fluctuations are shifted half of the wavelength one with respect to the other. *Bottom plots*: The solid line shows the cross-section of the real part of the scaled y-polarized fluctuations at $y = 10$. For comparison, the dotted line shows the real part of the scaled y-polarized stationary solution. We note that, as explained in the text the scaling of the stationary solution and the fluctuations is different. The transverse system size is in scaled units $L = 128 \times \Delta x$ where the integration discretization is $\Delta x = 0.6012$. We have taken $\theta = 1$, $E_0 = 0.919 = 1.07 E_0^c$

set of fields $\psi_i(\vec{x}, t)$ which obey dynamical equations of the form

$$\frac{\partial \psi_i(\vec{x}, t)}{\partial t} = F_i(\nabla, \psi_1, ..., \psi_N), \tag{3.27}$$

where F_i is a general functional of ∇ and the fields $\psi_i(\vec{x}, t)$, and such that they admit a stationary configuration $\psi_i^0(\vec{x})$. The linear analysis of fluctuations around this stationary configuration is made by calculating the eigenvalues of the matrix operator

$$M_{lj} = \left[\frac{\delta F_l}{\delta \psi_j} \right]_{\psi_i = \psi_i^0}. \tag{3.28}$$

If the system is translationally invariant, $\psi_i^0(\vec{x} + \vec{x}_0)$ is also a stationary configuration for any fixed $\vec{x}_0$. From this condition, and in a system with spatial dimensionality D, it follows immediately that the D independent components of the vector $\nabla \psi_i^0(\vec{x})$ are eigenfunctions of M with zero eigenvalue. For example, in $D = 2$ these two eigenfunctions are $(\partial_x \psi_1^0, ..., \partial_x \psi_N^0)$ and $(\partial_y \psi_1^0, ..., \partial_y \psi_N^0)$. These neutrally stable modes of the linearized dynamics are the Goldstone modes. When noise is present, fluctuations
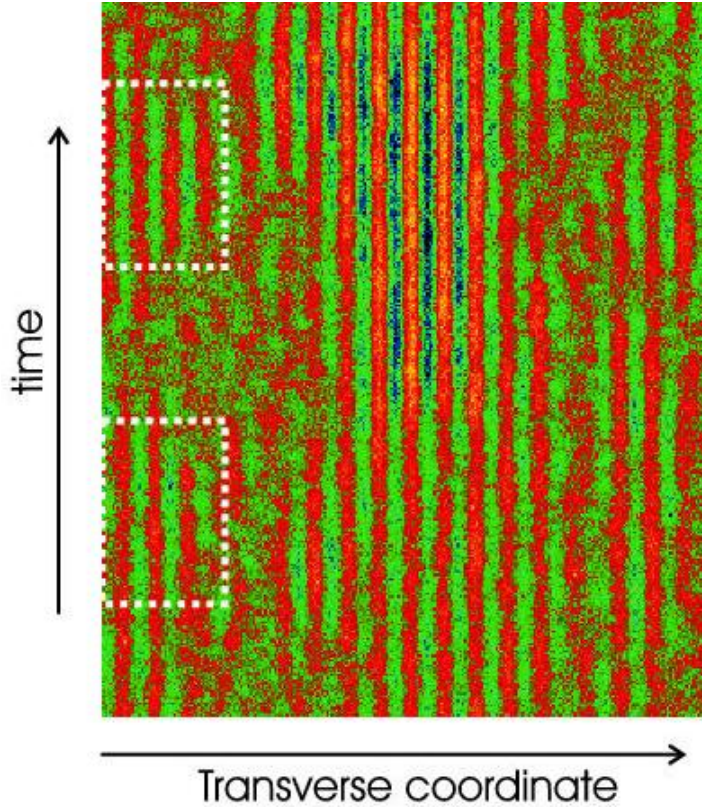
Figure 3.6: Fluctuations (y-polarized component) in a 1D system. Horizontal axis: transverse spatial coordinate; vertical axis: time. As time goes on a jump of half a period takes place in the position of the fluctuating stripes in the left side of the figure, as evidenced by the white frames. Parameters are: $E_0 = 0.919$, $\theta = 1$. The integration time is $Kt = 300$ (60000 integration time steps) and the transverse system size is $L = 256 \times \Delta x$.

around a stable stationary solution are damped, but Goldstone modes are excited without cost and they dominate the spatial structure of the fluctuations. For a stripe pattern the Goldstone mode is given by the spatial gradient of the stripe pattern. This is another stripe pattern shifted in space by a quarter of the spatial period. The Goldstone mode is associated with rigid spatial displacements of the stationary pattern in the direction perpendicular to the stripes. Such rigid displacements are generated by fluctuations that change the value of $\vec{x}_0$, that is, homogeneous fluctuations in a global and arbitrary phase of the stripe pattern. The spatial structure of the fluctuations observed in Fig.3.5 reflects a maximum of fluctuations corresponding to the Goldstone mode.

The stripe pattern of the fluctuations is shifted with respect to the underlying steady-state stripe pattern a quarter of the spatial period either to the right or to the left. Over large time scales, fluctuations in a region of the plane can in principle make a half-period spontaneous jump between those two configurations. This implies a spontaneous change in the direction of displacement of the steady-state pattern, to which fluctuations are associated. We have visualized this effect in a one dimensional (1D) system, described by the same dynamics. The 1D stationary pattern shows a regular modulation along the spatial coordinate, similar to a section of the two dimensional pattern perpendicular to the direction of the stripes. Again, the spatial structure of the fluctuations reflects the corresponding Goldstone mode with right or left displacements of the stationary pattern. We have plotted the time evolution of the spatial distribution of fluctuations in Fig.3.6. In this figure the two white frames evidence a portion
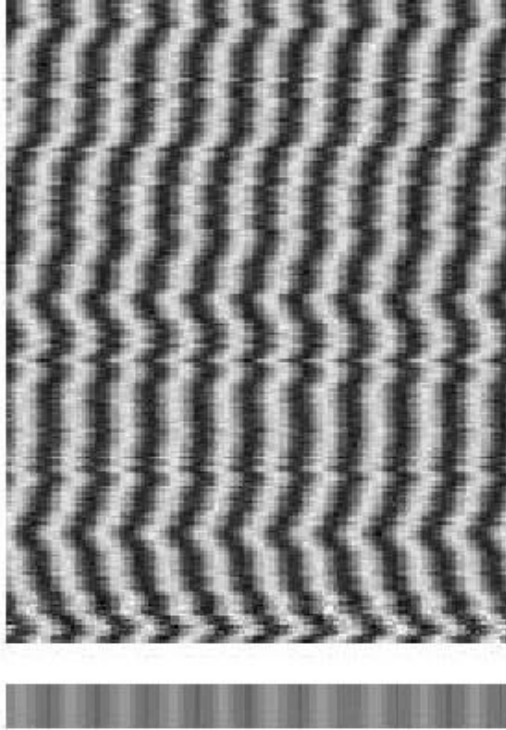
Figure 3.7: Spatiotemporal evolution of the real part of the y polarized component of the field, using the nonlinear Langevin equations (3.16) in a 1D system. Horizontal axis: spatial transverse coordinate; vertical axis: time. We show 2000 snapshots of the transverse field distribution, taken every 400 time units (80000 integration time steps), in a lattice of 128 points. The stripe on the bottom shows the time averaged pattern. The noise strength $(2n_s)^{-1/2}$ is 0.02, and the other parameters are as in Fig.3.5.

of the transverse section of the beam where, as time goes on, a phase jump takes place.

The random rigid motion of the stripe pattern in the 1D case can be shown explicitly by displaying the entire field instead of the fluctuations of the field. This can be obtained by numerically integrating the full nonlinear Langevin equations (3.16) for the field. Figure 3.7 shows a stochastic realization, from which it can be clearly seen that the location of the maxima and minima of the pattern move in space as time goes on. This is precisely the diffusive motion of the roll pattern predicted in [Lugiato & Grynberg]. The stripe on the bottom of Fig.3.7 shows the time average of the pattern, which confirms that the roll pattern is washed out by this motion, if the average is made over time intervals large with respect to the diffusion time. Fig.3.7 confirms also that the fluctuations associated with the Goldstone mode, and leading to rigid spatial displacements to the left and to the right randomly, are undamped. Being more precise, the motion of the patterns is not strictly rigid. The reason for this is that in a large continuous system there are long wavelength and weakly damped modes, connected with the Goldstone mode, that are easily excited by noise (soft modes) [Foster]. These continuous band of modes do not come into play when a continuous system is described in an approximation consisting of a few discrete modes. These soft modes are responsible of the local deformations of the fluctuating pattern. They are also known to destroy long range order in 1D systems in the limit of systems of infinite size [Ma]. An example of this decaying correlations in a prototype model (Swift-Hohenberg equations) of pattern formation is discussed in [Viñals & al.]. Our numerical simulations are made for rather large optical systems. Still they are far from the limit of infinite size considered from a Statistical Physics point of view. In order to see how long range order is destroyed, we need to consider a system with a size L

much larger than the correlation length l. To visualize this effect we show in Fig. 3.8 the result of a simulation for a system which is 64 times larger than the one of Fig.3.7. One observes domains of the system with a size given by the correlation length, $l \ll L$, in which the pattern drifts as a whole in a given direction, as it was the case in Fig.3.7. However, the pattern moves locally in different directions giving a local drifting in opposite directions for different regions of the system. The pattern is essentially coherent in domains of the size of l, but there is no long range order in the system as a whole.
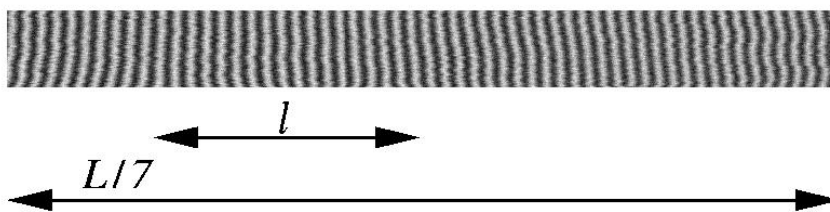

Figure 3.8: Spatiotemporal evolution of the real part of the y polarized component of the field, in a large 1D system. The total system size is $L = 8192 \times \Delta x$ and the total integration time is 10000. Only one seventh of the total system is shown here. The correlation length of the pattern l is indicated. Other parameters are as in Fig.3.7.

In 2D, and for relatively small systems, we observe stripes that can be understood as a set of strongly coupled 1D patterns. A zero wavenumber in the direction of the stripes is strongly dominant. The field fluctuations are still governed and patterned by the Goldstone mode as shown in Fig.3.5. However, phase jumps as the one described in Fig.3.6 are very unlikely during finite observations times. In addition, the soft modes associated with the Goldstone mode are known not to destroy long range order in spatial dimensions larger than 2. When excited by noise they soften the order parameter, but while long range order is completely lost in $d = 1$, $d = 2$ is the critical dimension with a logarithmic divergence such that the periodicity is not totally lost [Ma].

3.5 Fields outside the cavity

In this Section we use the standard input/output formalism for optical cavities introduced in Sect.1.2.2 [Collett & Gardiner] in order to obtain the behavior of the fields outside the cavity, given the fields inside the cavity. The intracavity fields, in the small fluctuations limit, result adding the stationary fields (Sect.3.3) and the fluctuations (Sect.3.4).

In the case of a one port cavity, the field immediately outside the cavity coupling mirror $\hat{A}_{\pm}^{out}$ is linked to the intracavity field, and to the reflected input field $\hat{A}_{\pm}^{in}$ by:

$$\hat{A}_{\pm}^{out}(\vec{x}, t) = \sqrt{2}\hat{A}_{\pm}(\vec{x}, t) - \hat{A}_{\pm}^{in}(\vec{x}, t) \, , \tag{3.29}$$

where scaling (see relations (3.14)) is such that $\langle \hat{A}_{\pm}^{out\,\dagger} \hat{A}_{\pm}^{out} \rangle$ $(\langle \hat{A}_{\pm}^{in\,\dagger} \hat{A}_{\pm}^{in} \rangle)$ represents the average number of photons crossing an area a in a time K^{-1}. Notice that the mean value of the input field is related to the pump amplitude introduced in (3.5) by $\langle \hat{A}_{\pm}^{in} \rangle = E_0/\sqrt{2}$. Hence, taking the mean value of

Eq.(3.29) we have

$$F_\pm^{out}(\vec{x}, t) = \sqrt{2} F_\pm(\vec{x}, t) - E_0/\sqrt{2}. \tag{3.30}$$

The same input-output relation (3.29) holds for the field fluctuation operators $\delta \hat{A}_\pm$.

In the quasiclassical description of quantum fluctuations [Reynaud & al. (92)], also c-number fluctuations $\Delta \alpha_\pm(\vec{x}, t)$ in the Wigner representation have similar input/output relations:

$$\Delta \alpha_\pm^{out}(\vec{x}, t) = \sqrt{2} \Delta \alpha_\pm(\vec{x}, t) - \Delta \alpha_\pm^{in}(\vec{x}, t), \tag{3.31}$$

where now $\Delta \alpha_\pm^{in}(\vec{x}, t)$ are Gaussian stochastic processes that represent input vacuum fluctuations, and have correlations given by (3.15).

Intracavity fluctuations $\Delta \alpha_\pm(\vec{x}, t)$ can be simulated by means of numerical integration of Eqs. (3.13). The problem arises with the input term $\Delta \alpha_i^{in}(\vec{x}, t)$, because it is a Gaussian white noise, δ-correlated in time, so that its instantaneous value is ill-defined. This implies that the instantaneous value of the input and output fields is ill-defined. A similar problem is encountered when calculating the instantaneous frequency during the switch-on of a laser using a semiclassical model which includes spontaneous emission white noise [Balle & al. (91)]. A way to give meaning to these fast fluctuating quantities is to average the fluctuations integrating in a time window [Balle & al. (91), Balle & al. (93)]. In numerical simulations, the divergence is strictly avoided due to the fact that the time is discretized. However, it is usually necessary to take very small time steps to preserve the accuracy, so that large fluctuations will still be present. This behavior can be regularized taking the average over several steps of integration which corresponds precisely to the integration of fluctuations in a time window.
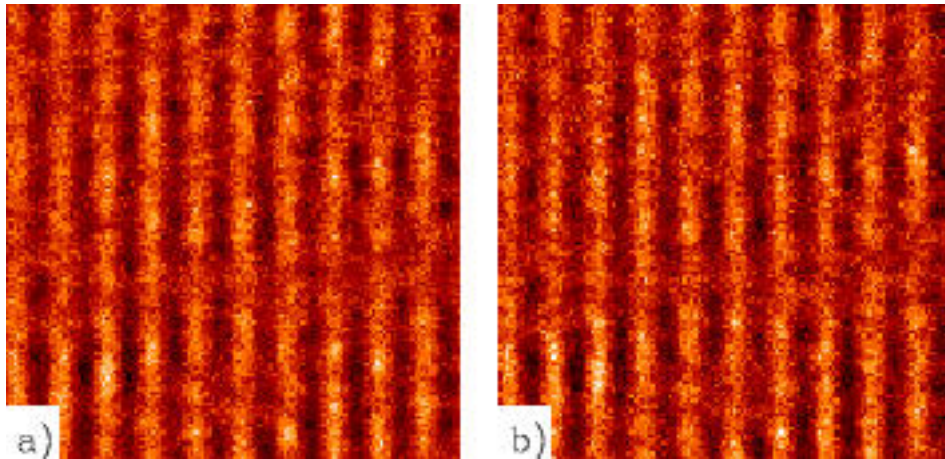

Figure 3.9: a) Distribution in the transverse plane of the y-polarized output field fluctuations (real part). The output field has been averaged over 0.5 time units, which corresponds to 100 integration time steps. For comparison, the instantaneous real part of the fluctuations of the field inside the cavity is shown in b). Parameters as in Fig.3.5.

We briefly discuss here how to perform a numerical realization of the output field. This requires the integration of equation (3.13) together with (3.31). We consider a discretized time $t = n\tau$, where

$\tau << 1$ is the time step for integration. From Eq.(3.31), the output field integrated over one time step, is

$$\Delta\alpha_{\pm,n}^{out}(\vec{x}) \cong \int_{n\tau}^{(n+1)\tau} \Delta\alpha_{\pm}^{out}(\vec{x},t)dt = \sqrt{2}\int_{n\tau}^{(n+1)\tau} \Delta\alpha_{\pm}(\vec{x},t)dt - \Delta\alpha_{\pm,n}^{in}(\vec{x}). \qquad (3.32)$$

Where $\Delta\alpha_{\pm,n}^{in}(\vec{x})$ are the input field fluctuations, integrated over one time step:

$$\Delta\alpha_{\pm,n}^{in}(\vec{x}) = \int_{n\tau}^{(n+1)\tau} \Delta\alpha_{\pm}^{in}(\vec{x},t)dt. \qquad (3.33)$$

These are Gaussian random numbers of zero mean and correlations

$$\langle \Delta\alpha_{i,n}^{in}(\vec{x})\Delta\alpha_{j,n'}^{*\ in}(\vec{x}')\rangle = \frac{\tau}{2}\delta_{i,j}\delta(\vec{x}-\vec{x}')\delta_{nn'} \qquad (i,j) = (+,-). \qquad (3.34)$$

From Eq.(3.13) we have

$$\Delta\alpha_{\pm}(\vec{x},n\tau+s) = \Delta\alpha_{\pm}(\vec{x},n\tau) + Q_{\pm}(n\tau)s + \sqrt{2}\int_{n\tau}^{n\tau+s} \Delta\alpha_{\pm}^{in}(\vec{x},t')dt' + \mathcal{O}(s^{\frac{3}{2}}), \qquad (3.35)$$

where Q_+ (Q_-) correspond to the expressions Q_1 (Q_3) (see Eq.(C.4)). Then, integrating both sides of Eq.(3.35) over a time step:

$$\int_{n\tau}^{(n+1)\tau} \Delta\alpha_{\pm}(\vec{x},t)dt \approx \Delta\alpha_{\pm}(\vec{x},n\tau)\tau + \frac{\tau^2}{2}Q_{\pm}(n\tau) + \sqrt{2}\int_{n\tau}^{(n+1)\tau} dt \int_{n\tau}^{t} \Delta\alpha_{\pm}^{in}(\vec{x},t')dt'. \qquad (3.36)$$

Substituting Eq.(3.36) in Eq.(3.32), we have

$$\frac{\Delta\alpha_{\pm,n}^{out}(\vec{x})}{\tau} = \sqrt{2}\Delta\alpha_{\pm,n}(\vec{x}) + \frac{\tau}{\sqrt{2}}Q_{\pm}(n\tau) + \frac{\eta_{\pm,n}(\vec{x})}{\tau}, \qquad (3.37)$$

where terms of order higher than τ have been neglected. $\eta_{\pm,n}(\vec{x})$ are defined as

$$\eta_{\pm,n}(\vec{x}) = 2\int_{n\tau}^{(n+1)\tau} dt \int_{n\tau}^{t} \Delta\alpha_{\pm}^{in}(\vec{x},t')dt' - \Delta\alpha_{\pm,n}^{in}(\vec{x}). \qquad (3.38)$$

As they are a linear combination of Gaussian process, $\eta_{\pm,n}$ are Gaussian random numbers with zero mean and correlations given by:

$$\langle \eta_{i,n}(\vec{x})\eta_{j,n'}^{*}(\vec{x}')\rangle = \left(\frac{2}{3}\tau^3 - \tau^2 + \frac{1}{2}\tau\right)\delta_{ij}\delta(\vec{x}-\vec{x}')\delta_{nn'}. \qquad (3.39)$$

The correlation between $\eta_{\pm,n}(\vec{x})$ and the input fluctuations is given by

$$\langle \eta_{i,n}(\vec{x})\Delta\alpha_{j,n'}^{*\ in}(\vec{x}')\rangle = \frac{\tau}{2}(\tau-1)\delta_{ij}\delta(\vec{x}-\vec{x}')\delta_{nn'}. \qquad (3.40)$$

In Fig.3.9 we show a realization of the output field fluctuations averaged over 100 integration time steps (this is $\frac{1}{100\tau}\sum_{n=1}^{100}\Delta\alpha_n^{out}$) which corresponds to a time window of 0.5 time units. The output fluctuations (Fig.3.9.a) are qualitatively very similar to the intracavity fluctuations (Fig.3.9.b) .

3.6 Quantum correlations

Quantum fluctuations in the presence of a stripe pattern in the y-polarized field have been already studied in a Kerr system using a three-mode approximation. In the following we make a comparison between the results of [Hoyuelos & al. (99)] and the ones obtained using the continuous model presented here. In Sect.3.6.1 we check the conditions for using the Kerr cavity as a quantum non-demolition (QND) measurement device, and in Sect.3.6.2 we consider the correlations between the two y-polarized tilted beams.

3.6.1 QND measurements

A quantum measurement usually perturbs the quantity which is measured adding "back-action noise" to the system under study. However, QND measurements can be performed, leaving the observed quantity unperturbed, while adding the back-action noise to another complementary observable. The key issue is to devise measurement schemes in which the back-action noise is kept entirely within unwanted observables, without being coupled back onto the quantity of interest. This quantity then remains uncontaminated by the measurement process, allowing repeated measurements to be performed with arbitrary high accuracy [Grangier, Braginsky].

Here we consider the Kerr cavity as a QND device: in fact the basic technique used for QND in quantum optical experiments couples a signal beam (to be measured) to a second beam, called the meter, through an optically nonlinear medium. We consider an x-polarized input field which carries a signal that has to be measured with the smallest possible perturbation. The idea is to take advantage of the correlations between the pattern fluctuations and the homogeneous mode fluctuations [Hoyuelos-Colet-San Miguel] to perform an indirect measurement of the signal fluctuations by measuring the fluctuations of the pattern modes $\vec{k}_c$ and $-\vec{k}_c$ [Hoyuelos & al. (99)], which work as a meter in the QND measurement. Here $k_c = 2\pi/\lambda_c$, where λ_c is the wavelength that characterizes the roll pattern near the instability threshold, and is given by (3.25). In the far field plane of the y-polarized field, these two modes give rise to an intensity distribution with two large maxima in symmetrical position. We identify the far field plane with the Fourier plane (k_x, k_y), and thus the field distribution in the far field plane is given by the spatial Fourier transform of the field immediately outside the cavity:

$$\hat{A}_j^{out}(\vec{k}, t) = \int \frac{d^2\vec{x}}{2\pi} e^{-i\vec{k}\cdot\vec{x}} \hat{A}_j^{out}(\vec{x}, t) \,. \tag{3.41}$$

We consider the operator

$$\hat{N}_{jR}^{out}(t) = \int_R d^2\vec{k} \hat{A}_j^{\dagger out}(\vec{k}, t) \hat{A}_j^{out}(\vec{k}, t) \,, \tag{3.42}$$

that represents the number of photons with polarization j per unit time over a region R of the far field. In general the polarization could be circular (right or left) or linear (x or y). As we did for the intra-cavity fields (3.8), we can separate the stationary mean field from the fluctuations in the output-cavity field,

$$\hat{A}_j^{out}(\vec{k}, t) = F_j^{out}(\vec{k}) + \delta\hat{A}_j^{out}(\vec{k}, t) \,, \tag{3.43}$$

where $F_\pm^{out}$ is given by Eq.(3.30). Neglecting second order terms in the field fluctuations

$$\langle \hat{A}_j^{\dagger out} \hat{A}_j^{out}\rangle = F_j^{*out}\delta\hat{A}_j^{out} + F_j^{out}\delta\hat{A}_j^{\dagger out} + \delta\hat{A}_j^{out}\delta\hat{A}_j^{\dagger out}\,, \tag{3.44}$$

we introduce the scaled photon fluctuations as,

$$\delta\hat{N}_{jR}^{out} = \frac{\int_R d^2\vec{k}\left[F_j^{*out}(\vec{k})\delta\hat{A}_j^{out}(\vec{k},t) + h.c.\right]}{\sqrt{\int_R d^2\vec{k}|F_j^{out}(\vec{k})|^2}}\,. \tag{3.45}$$

With this normalization, the squeezing spectra take the value 1 for the shot-noise level.

The far field intensity distributions are strongly peaked around $\vec{k} = 0$ (x-polarized component) and $\vec{k} = \vec{k}_{\pm c}$ (y-polarized component). We are going to consider three regions R_0, R_1 and R_2, around the homogeneous mode $\vec{k} = 0$ and the two pattern modes $\vec{k}_c$ and $-\vec{k}_c$, respectively. When the size of each region is on the the order of the diffraction length l_D the whole peak is enclosed. We consider the x-polarized photon fluctuations in the first region $\delta\hat{N}_{xR_0}^{out}$, which for simplicity we will call $\delta\hat{N}_0^{out}$. In regions R_1 and R_2 we consider the y-polarized photon fluctuations $\delta\hat{N}_1^{out} = \delta\hat{N}_{yR_1}^{out}$ and $\delta\hat{N}_2^{out} = \delta\hat{N}_{yR_2}^{out}$. Finally we also consider the y-polarized photon fluctuations in the region $R_1 + R_2$, $\delta\hat{N}_{1+2}^{out} = \delta\hat{N}_{yR_1+R_2}^{out}$. Notice that as $|F_j^{out}(\vec{k}_c)|^2 = |F_j^{out}(-\vec{k}_c)|^2$ then $\delta\hat{N}_{1+2}^{out} = \delta\hat{N}_1^{out} + \delta\hat{N}_2^{out}$. In the QND measurements, δN_0^{out} is the outgoing signal while we are going to use $\delta\hat{N}_{1+2}^{out}$ as the meter.

The expression of the squeezing spectrum of the fluctuations in any of these regions is [Holland & al., Sinatra & al.],

$$S_i(\omega) = \langle\delta\hat{N}_i^{out}\delta\hat{N}_i^{out}\rangle_\omega\,, \tag{3.46}$$

where the notation $\langle\rangle_\omega$ means Fourier transform of the symmetrized correlation, and it is defined, for some generic operators $\hat{W}$ and $\hat{Z}$, as,

$$\langle\hat{W}\hat{Z}\rangle_\omega = \int_{-\infty}^{\infty}\langle\hat{W}(t)\hat{Z}(0)\rangle_{symm}e^{-i\omega t}dt\,, \tag{3.47}$$

with

$$\langle\hat{W}(t)\hat{Z}(0)\rangle_{symm} = \langle\hat{W}(t)\hat{Z}(0) + \hat{Z}(0)\hat{W}(t)\rangle/2. \tag{3.48}$$

The conditional variance of $\hat{N}_0^{out}$ given a measurement on $\hat{N}_{1+2}^{out}$ is given by,

$$V(0|1+2) = S_0\left(1 - \frac{|\langle\delta\hat{N}_0^{out}\delta\hat{N}_{1+2}^{out}\rangle_\omega|^2}{S_0 S_{1+2}}\right). \tag{3.49}$$

This is a measure of the correlations between the outgoing signal $\hat{N}_0^{out}$ and the outgoing meter $\hat{N}_{1+2}^{out}$. Strong correlations correspond to small values of $V(0|1+2)$.

Additionally, we study how the fluctuations of the homogeneous mode are transferred from the input to the output of the cavity (the non-demolition character of the measurement), and also from the input to the pattern modes (accuracy of the measurement). This information is given by the following
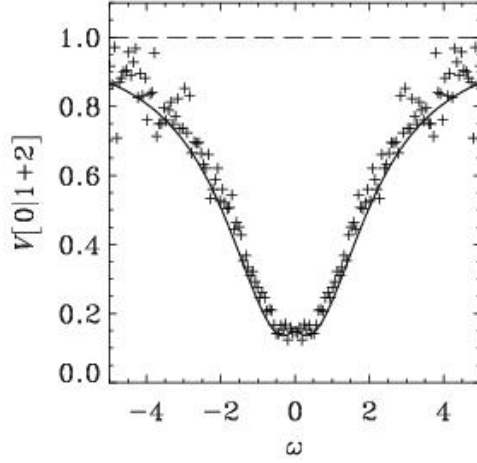
Figure 3.10: Conditional variance $V(0|1 + 2)$ given by Eq.(3.49). The solid line represents the three-mode model while the dots represent the continuous model. Parameters: $\eta = -1$ (self-defocusing case), $E_0 = 0.919$ and $\theta = 1.7$.

normalized correlations [Holland & al.],

$$C_s = \frac{|\langle \delta\hat{N}_0^{in}\delta\hat{N}_0^{out}\rangle_\omega|^2}{\langle \delta\hat{N}_0^{in}\delta\hat{N}_0^{in}\rangle_\omega \langle \delta\hat{N}_0^{out}\delta\hat{N}_0^{out}\rangle_\omega} \tag{3.50}$$

$$C_m = \frac{|\langle \delta\hat{N}_0^{in}\delta\hat{N}_{1+2}^{out}\rangle_\omega|^2}{\langle \delta\hat{N}_0^{in}\delta\hat{N}_0^{in}\rangle_\omega \langle \delta\hat{N}_{1+2}^{out}\delta\hat{N}_{1+2}^{out}\rangle_\omega}, \tag{3.51}$$

where the x-polarized input fluctuations are given by,

$$\delta\hat{N}_0^{in} = \frac{\int_{R_0} d^2\vec{k}\left[F_x^{*in}(\vec{k})\delta\hat{A}_x^{in}(\vec{k}, t) + h.c.\right]}{\sqrt{\int_{R_0} d^2\vec{k}|F_x^{in}(\vec{k})|^2}} = \delta\hat{A}_x^{in}(\vec{k} = 0, t) + h.c.. \tag{3.52}$$

The last equality comes from the fact that the input field mean value $F_x^{in}(\vec{k})$ has only contributions at $k = 0$. Since the input beam is in a coherent state, the fluctuations correspond to the shot noise level: $\langle \delta\hat{N}_0^{in}\delta\hat{N}_0^{in}\rangle_\omega = 1$.

In order to perform a QND measurement of the input field fluctuations $\delta\hat{N}_0^{in}$ using the pattern fluctuations $\delta\hat{N}_{1+2}^{out}$ as a meter it is required that $V(0|1+2) < 1$ and $C_s + C_m > 1$ [Holland & al., Braginsky]. We have evaluated the correlations and variances described above by numerically simulating Eq.(3.13) for a detuning $\theta = 1.7$. For this value of the detuning, the threshold for pattern formation is $E_0^c = 0.869$. At each time step, the fluctuations in the output field $\Delta\alpha_\pm^{out}$ have been numerically calculated using Eq. (3.37) and averaging over a time 0.5 which corresponds to 100 integration time steps. The c-numbers corresponding to the operators $\delta\hat{N}_{Rj}^{out}$ are calculated as in Eq.(3.45) substituting $\delta\hat{A}_j^{out}$ by $\Delta\alpha_j^{out}$. The two times symmetrized correlations (3.48) are then calculated using the corresponding c-numbers and averaging over time for a stochastic realization of the output field. In the results shown below averages has been performed over 20.000 time units. Finally, we fast Fourier transform these correlations to obtain the squeezing spectrum as well as the conditional variances.

In Fig.3.10 we show the results for the conditional variance $V(0|1 + 2)$ for a pump $E_0 = 0.919$, that is quite close to threshold. The symbols correspond to the results obtained from the continuous model

whereas the solid line represents the three modes approximation [Hoyuelos & al. (99)]. The correlation between the outgoing signal and the outgoing meter is well below the shot-noise level (shown as a dashed line). As predicted by the three modes model, we can use a vectorial self-defocusing Kerr medium to prepare a state of the homogeneous output with known fluctuations. Comparing both models, the three modes model predicts slightly larger correlations (smaller values for $V(0|1+2)$) than the continuous model. This fact can be explained taking into account that the correlation $\langle \delta \hat{N}_0^{out} \delta \hat{N}_{1+2}^{out} \rangle_\omega$ in Eq.(3.49) is smaller in the continuous case. This is so because part of the energy is translated to the higher order modes that were neglected in the three modes approximation.
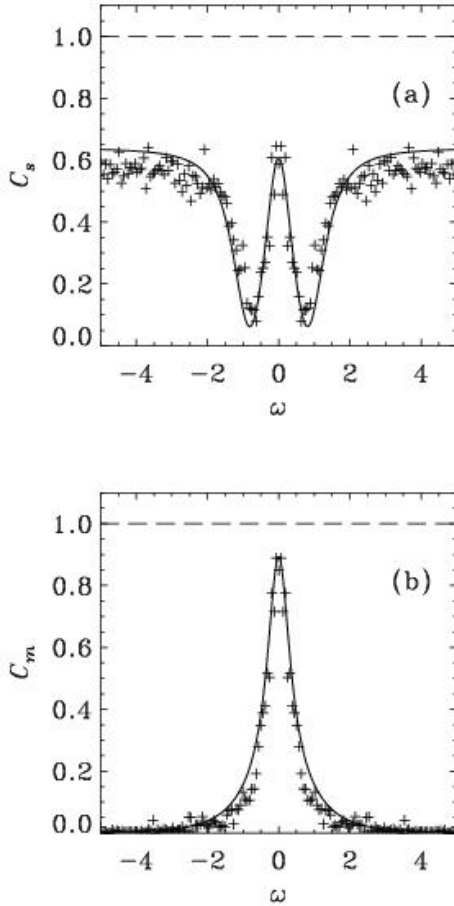
In Fig.3.11 we plot correlations C_s and C_m. As before, the solid line corresponds to results from the three modes model and the symbols to the continuous model. Again there is a small difference between the two models, which is more clearly seen in the correlation between the incoming and the outgoing signal, C_s, for high frequencies. Also the peak in the correlation between the incoming signal and the outgoing meter, C_m, is slightly narrower. Nevertheless, the fitting of the curves is good and demonstrates the validity of the three modes approximation close to the instability threshold. From the plots it can be seen that the condition $C_s + C_m > 1$ is fulfilled for a range of frequencies $|\omega| < 0.3$. In this range of frequencies all the conditions for a QND measurement of the x-polarized input fluctuations using the y-polarized pattern as a meter are satisfied.

Similar results can be obtained for other values of the detuning, provided we are below the limit of bistability for the homogeneous solution ($\theta < \sqrt{3}$). However, as the detuning is decreased the QND performance is degraded, as predicted by the three modes model [Hoyuelos & al. (99)].

Figure 3.11: Correlations C_s (a) and C_m (b) given by Eq.(3.51). The solid lines represent the three modes model while the dots represent the continuous model. Same parameters as in Fig.3.10.

3.6.2 Twin beams correlations

Another quantity of interest (not related with the QND conditions), which is able to show the quantum nature of fluctuations, is the correlation between the two opposite pattern modes $\vec{k}_c$ and $-\vec{k}_c$. As we discussed in Ch.1, the conservation of transverse momentum, in kerr resonators at threshold for stripes pattern formation, leads to the emission of correlated photons that propagate in symmetrical directions; this implies a high correlation between fluctuations in two
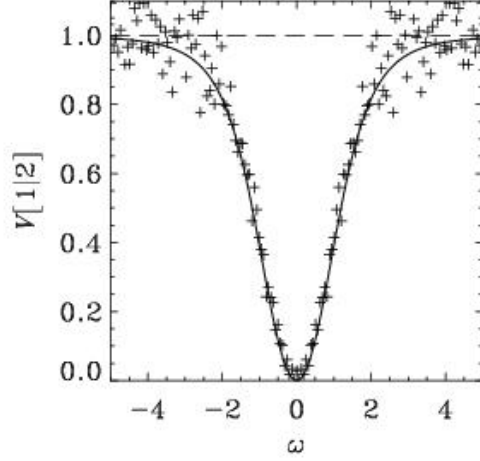
Figure 3.12: Conditional variance $V(1|2)$ given by Eq.(3.53). The solid line represents the three modes model while the dots represent the continuous model. Same parameters as in Fig.3.10.

symmetric portion of the beam cross section in the far field. These correlation has been studied with a semiclassical model [Hoyuelos-Colet-San Miguel]. The appropriate variable that gives us information about the quantum correlation of the pattern modes is the conditional variance of $\hat{N}_1^{out}$ given a measurement on $\hat{N}_2^{out}$,

$$V(1|2) = S_1 \left(1 - \frac{|\langle \delta \hat{N}_1^{out} \delta \hat{N}_2^{out} \rangle_\omega|^2}{S_1 S_2} \right). \tag{3.53}$$

If the correlation $\langle \delta \hat{N}_1^{out} \delta \hat{N}_2^{out} \rangle_\omega$ is big enough, we will have a variance below the shot noise level: $V(1|2) < 1$, which means a reduction of the fluctuations below the classical limit.

In Fig.3.12 we plot the conditional variance $V(1|2)$. The results of the two models coincide perfectly for small frequencies. As predicted by the three modes model, the conditional variance is dramatically reduced at low frequencies. In fact it goes to zero at zero frequency, showing the existence of strong quantum correlations between the two opposite pattern modes $\vec{k}_c$ and $-\vec{k}_c$. For larger frequencies, the results form the continuous model shows a large dispersion, although they basically coincide with the prediction from the three modes model. The large dispersion could be reduced increasing the statistics, that is, integrating over a longer stochastic realization.

It is interesting to observe that the reduction of fluctuations in the intensity difference $\delta \hat{N}_y(\vec{k}_c) - \delta \hat{N}_y(-\vec{k}_c)$, appears in a multimode interaction. In fact, in the regime that we have considered the spatial harmonics $\pm 2k_c$ are excited, even if with a small intensity compared with the three modes $0, \pm k_c$. As discussed in Sect.1.4, the argument of momentum conservation generally invoked [Lugiato & Grynberg], cannot give a constraint in the twin beams intensity difference in a multimode interaction. We will discuss further this point in Ch.4. Here we point out that, probably, the twin beams correlations are not reduced due to the low rate of other interactions leading to harmonics. Therefore very near to threshold the few modes process considered in [Hoyuelos & al. (99)] give a correct description of correlations.

3.7   Summary and conclusions

Our analysis, based on the classical-looking set of Langevin equations (3.13) in the Wigner representation, led to the following main results.

- The use of a continuous model in the transverse spatial modes allows to observe interesting features: The numerical solutions of the complete nonlinear Langevin equations in the 1D spatial case have confirmed that the stripe pattern undergoes locally rigid random translation to the left and to the right, as predicted by the three-mode model [Lugiato & Grynberg]. On the other hand, in 2D phase jumps of the entire pattern are extremely unlikely to occur during finite observation times. The underlying presence of such displacements is manifested, however, by the spatial configuration of the fluctuations, which is dominated by the Goldstone mode. Such mode is the eigenstate of the linearized problem with zero eigenvalue, and it is given by the spatial gradient of the underlying stationary stripe pattern. The Goldstone mode is always present in a system with broken translational symmetry, as the one that emerges in a pattern forming instability. It is excited at no cost by noise and leads to rigid translations of the pattern. In a continuous system there are also soft modes arbitrary close to the Goldstone mode which produce local deformations of the pattern and that would destroy long range order in 1D systems in the limit of very large system size.

- We have formulated a general description of the spatial configuration of the output field immediately beyond the input/output mirror, for an arbitrary size of the time window over which fluctuations are averaged. We have shown that the spatial configuration of the output field is closely similar to that of the intracavity field, provided that this time window is on the order of the cavity linewidth K^{-1}, which corresponds to select a spectral bandwidth of the output fluctuations on the same order as that of the intracavity fluctuations.

- We analyzed on the one side the anticorrelation between the quantum fluctuations of the intensity of the x-polarized pump field and the y-polarized pattern modes, and on the other the correlation between the intensity fluctuations of the two symmetrical components (twin beams) of the y-polarized field. It turns out that the predictions of the three-mode model are in good agreement with the results of the multimode model. In the case of the system analyzed here, this agreement persists also well beyond the instability threshold in all the regions where the roll pattern is found, because the amplitudes of the modes different from those of the three-mode model are negligible. We believe, however, that for other models such an agreement can be found, in general, only close to the instability threshold. Hence the conclusions concerning the validity of the QND scheme formulated in [Hoyuelos & al. (99)] are confirmed.

Chapter 4

Type I Optical Parametric Oscillator

In this Chapter we study spatial quantum fluctuations in degenerate type I OPO. In this OPO configuration the linearly polarized pump at frequency 2ω is down converted in a signal at frequency ω with polarization state orthogonal to that of the pump. The signal field is known to show quantum effects below [Gatti & Lugiato, Gatti & al. (97)1] and at [Castelli & Lugiato] threshold. Our aim is the investigation of quantum effects in **nonlinear and multimode** regimes in which a **continuous** set of transverse spatial modes has to be considered. In this continuous formalism we also discuss the effects of the **transverse walk-off**: this walk-off is due to the birefringence of the crystal (see Appendix B). This discussions, together with the one of Ch.5, are the first studies of walk-off effects in the quantum fluctuations in the OPO. The different regimes that we consider in type I OPO are described in Sect.4.1, where we review the spatial instabilities of interest in the rest of the Chapter, leading to noise sustained patterns, traveling and stationary stripe patterns and disordered structures.

These regimes present a common **methodological** problem due to the *nonlinear* interaction of the fields in the OPO, described by a cubic Hamiltonian in the field operators. The quantum formulation of the model is introduced in Sect.4.2, where we discuss the problems arising in the description of the OPO in different phase space descriptions (Sect.4.2.1). As mentioned in Ch.1, the analysis of the quantum dynamics cannot be performed without some approximations: In Sect.4.2.2 and Sect.4.2.3 we propose two **nonlinear approximations** that are suitable to deal with large fluctuations, in case in which standard linearization techniques can not be justified. The proposed methods use the Wigner and the Q representations, respectively. They give *stochastic* descriptions of the fields of the OPO in different regimes. In both approximations we obtain nonlinear Langevin equations describing the pump and signal fields dynamics. Our motivation to propose these two methods was the description of the convective regime caused by walk-off (see Sect.1.3.2): In this regime macroscopic multimode quantum fluctuations occur.

These nonlinear methods have been useful for the description of several interesting regimes appearing in the type I OPO. The results of our analysis are presented in three sections:

- When considering a *finite* transverse profile of the pump field, walk-off leads to a *convectively un-*

stable regime. In this regime macroscopic patterns are both initiated and sustained by quantum noise. The features of this regime in a semiclassical approximation are reviewed in Sect.4.1.1. In Sect.4.3 we have studied quantum effects in the **macroscopic quantum noise** characterizing the convective regime. The results presented in this Section [Zambrini & al. (02)] have been obtained applying the nonlinear approximation based on the use of the W distribution, presented in Sect.4.2.2.

- The inclusion of walk-off effect breaks the **reflection symmetry** in the transverse plane. The consequences of such symmetry breaking in the absolutely unstable regime are studied in Sect.4.4. In this regime a deterministic multimode pattern with several excited harmonics arises. We consider the region near to the threshold of pattern instability, applying the nonlinear approximation based on the use of the W distribution, presented in Sect.4.2.2. The results presented in this Section were published in Ref.[Zambrini & San Miguel].

- In Sect.4.5 we consider the OPO when the *walk-off vanishes*. We study the quantum correlations above the threshold of formation of a **multimode spatial structure** [Zambrini & al. (03)1]. We study quantum fluctuations in two different regimes: in a **periodic pattern** (Sect.4.5.2.a) and in a spatially **disordered structure** (Sect.4.5.2.b). The results presented in this Section have been obtained with the nonlinear approximation based on the use of the Q distribution, presented in Sect.4.2.3.

4.1 Spatial structures in type I OPO

In this Section we introduce the classical equations describing a **degenerate OPO (DOPO)**. In the type I phase matching the ordinary polarized pump beam is down-converted to an extraordinary polarized signal. In general, the extraordinary polarized signal walks off in the transverse direction relative to the ordinary polarized pump (see Appendix B). This transverse walk-off effect is described in the dynamical equations by a term which accounts for a *relative transverse velocity* between the pump and the down-converted field. In Sect.4.1 and 4.1.1 we discuss the instability of a DOPO, with and without transverse walk-off effects.

A detailed derivation of the classical equations of the OPO including diffraction and walk-off effects is presented in Ref.[Ward & al. (98), Ward], while linear and nonlinear stability analysis are discussed in Ref. [Santagiustina & al. (98)a, Ward & al. (00)]. The intracavity dynamics is described by two slowly varying complex field amplitudes $A_0(\vec{x}, t)$ (pump) and $A_1(\vec{x}, t)$ (signal), which depend on the transverse spatial coordinates $\vec{x} = (x, y)$ and the time t. Within the paraxial approximation (for propagation in the z direction), the mean field limit and for single longitudinal mode operation (see Sect.1.3.1) the dynamical equations become:

$$\partial_t A_0(\vec{x}, t) = -\gamma_0[1 + i\Delta_0 - ia_0\nabla^2]A_0(\vec{x}, t) - \frac{g}{2}A_1^2(\vec{x}, t) + E_0(\vec{x}) + \epsilon_0\xi_0(\vec{x}, t), \tag{4.1}$$

$$\partial_t A_1(\vec{x}, t) = -\gamma_1[1 + i\Delta_1 - ia_1\nabla^2 - v\partial_y]A_1(\vec{x}, t) + gA_0(\vec{x}, t)A_1^*(\vec{x}, t) + \epsilon_1\xi_1(\vec{x}, t). \tag{4.2}$$

Here ξ_i $(i = 0, 1)$ are additive Gaussian white sources of noise, with non-vanishing correlations of the form:

$$< \xi_i(\vec{x}, t)\xi_j^*(\vec{x}', t') > = \delta_{ij}\delta(\vec{x} - \vec{x}')\delta(t - t'). \tag{4.3}$$

The level of noise introduced is fixed by the parameters ϵ_0 and ϵ_1. Our fully quantum analysis will produce equations of similar form in which these parameters are fixed. E_0 is the amplitude of the driving field which we take to be real. The remaining parameters in these equations are the cavity decay rates γ_i, the cavity detunings Δ_i, the diffraction a_i, the walk-off v and the nonlinear coefficient g.

It is convenient to introduce scaled variables

$$t' = \gamma t , \quad \vec{x}' = \frac{\vec{x}}{\sqrt{a}} , \quad v' = \frac{v}{\sqrt{a}}, \tag{4.4}$$

$$A_i' = \frac{g}{\gamma}A_i , \quad E_0' = \frac{g}{\gamma^2}E_0 , \quad \epsilon_i' = \frac{g}{\gamma^{3/2}a^{D/4}}\epsilon_i,$$

where we have restricted the cavity decay rates and diffraction coefficients such that $\gamma = \gamma_0 = \gamma_1$ and $a = a_0 = a_1/2$. Our equations are valid either for one or two transverse spatial dimensions ($D = 1, 2$). On omitting the primes, our amplitude Eqs. (4.1) and (4.2) become

$$\partial_t A_0(\vec{x}, t) = -[1 + i\Delta_0 - i\nabla^2]A_0(\vec{x}, t) - \frac{1}{2}A_1^2(\vec{x}, t) + E_0(\vec{x}) + \epsilon_0\xi_0(\vec{x}, t), \tag{4.5}$$

$$\partial_t A_1(\vec{x}, t) = -[1 + i\Delta_1 - 2i\nabla^2 - v\partial_y]A_1(\vec{x}, t) + A_0(\vec{x}, t)A_1^*(\vec{x}, t) + \epsilon_1\xi_1(\vec{x}, t). \tag{4.6}$$

4.1.1 Walk-off effects: the convective regime

For a uniform driving field E_0, the equations (4.5) and (4.6) admit the *homogeneous stationary solution*

$$A_0^{st} = \frac{E_0}{1 + i\Delta_0} , \quad A_1^{st} = 0 . \tag{4.7}$$

The threshold for parametric oscillation can be determined by a linear stability analysis of this solution. The linearized equations for signal and pump fluctuations $\delta A_i(\vec{x}, t) = A_i(\vec{x}, t) - A_i^{st}$ $(i = 0, 1)$ are decoupled, and the fluctuations of the pump are always damped. For the signal, we consider perturbations of the form $e^{i\vec{k} \cdot \vec{x} + \lambda(\vec{k})t}$ and find the dispersion relation

$$\lambda_\pm(\vec{k}) = -1 + ivk_y \pm \sqrt{F^2 - (\Delta_1 + 2|\vec{k}|^2)^2}, \tag{4.8}$$

where we have introduced a scaled pump

$$F = \frac{E_0}{\sqrt{1 + \Delta_0^2}}. \tag{4.9}$$

We find that there is an instability at

$$F = 1, \tag{4.10}$$

i.e. $E_0 = \sqrt{1 + \Delta_0^2}$. For $F < 1$, $Re(\lambda_\pm) < 0$ and the solution (4.7) is **absolutely stable**. For $F > 1$, there is a positive growth rate of fluctuations ($Re(\lambda_+) > 0$) which takes a maximum value for

$$|\vec{k}_c| = \sqrt{-\Delta_1/2} \tag{4.11}$$

Figure 4.1: Stability diagram as a function of the signal detuning Δ_1. The different lines correspond to the threshold of absolute instability (F_c) for different values of the walk-off parameter: $v = 0.2$ (dotted line), $v = 0.42$ (continuous line), $v = 0.6$ (dashed line). When $F < 1$ the solution (4.7) is absolutely stable, while for $1 < F < F_c$ the solution is convectively unstable.
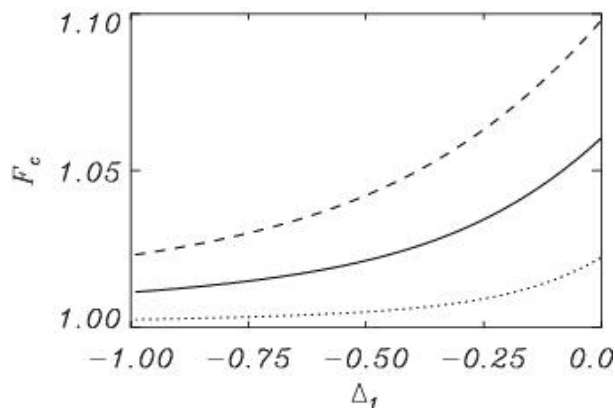
if the signal detuning is negative ($\Delta_1 < 0$), and for $k = 0$ if $\Delta_1 > 0$. In the following we are interested in the case of pattern formation and we restrict our analysis to the case $\Delta_1 < 0$. The instability at $F = 1$ when $v = 0$ is a Turing instability, in which a stationary pattern appears [Oppo & al. (94)] (see Sect.4.1.2). If $v \neq 0$ then the eigenvalue becomes complex and we find a Hopf bifurcation[1] in which a traveling pattern emerges [Santagiustina & al. (98)a].

The *direction of instability* is determined by the eigenfunctions $V_\pm(\vec{k}, -\vec{k})$ of the linear problem $\partial_t V_\pm(\vec{k}, -\vec{k}) = \lambda_\pm(\vec{k})V_\pm(\vec{k}, -\vec{k})$. Solving this gives

$$V_\pm(\vec{k}, -\vec{k}) = e^{i\Phi_\pm}\delta A_1(\vec{k}) \pm \delta A_1^*(-\vec{k}) \tag{4.12}$$

$$e^{i\Phi_\pm(\vec{k})} = \mp\frac{i\Delta_1 + 2i|\vec{k}|^2 \mp \sqrt{|A_0^{st}|^2 - (\Delta_1 + 2|\vec{k}|^2)^2}}{A_0^{st}}.$$

The solution $V_+(\vec{k}, -\vec{k})$ gives the direction of amplification of fluctuations, while fluctuations are damped for $V_-(\vec{k}, -\vec{k})$. In particular, for the critical wave-vector $|\vec{k}_c|$ and for a real pump E_0 and $\Delta_0 = 0$, we obtain $V_\pm(\vec{k}_c, -\vec{k}_c) = \delta A_1(\vec{k}_c) \pm \delta A_1^*(-\vec{k}_c)$. Therefore, in this case, the difference of real parts and the sum of imaginary parts of field in $\vec{k}_c$ and $-\vec{k}_c$ will show damped fluctuations at threshold. We also note that the instability direction is *independent of the walk-off term*.

Above the instability threshold ($F > 1$) the steady state (4.7) is **convectively unstable**: any perturbation grows while traveling in the direction fixed by the walk-off term and eventually leaves the system [Santagiustina & al. (98)a]. As discussed in Sect.1.3.2, in this regime a continuous perturbation such as a source of noise, gives rise to a *noise-sustained pattern* consisting in disordered traveling stripes in the signal. On increasing the pump a second threshold is reached at $F = F_c$. Beyond this threshold the pattern is sustained by the nonlinear dynamics, being also present in the absence of perturbations, once it is formed. The state (4.7) is **absolutely unstable** in this regime [Santagiustina & al. (98)a]. In Fig.4.1 we plot the result of the calculation of the absolute instability threshold as function of the signal detuning Δ_1, for different values of the walk-off parameter v.

Walk-off has three main effects in this process of pattern formation [Santagiustina & al. (99), Santagiustina & al. (98)a]. The first is the existence of the convective regime in which patterns are

---

[1]A Hopf bifurcation is characterized by an eigenvalue $\lambda_\pm(\vec{k}_c)$ at threshold with non vanishing imaginary part.

sustained by noise. Second is that it breaks the rotational symmetry, favoring the formation of stripes orthogonal to the walk-off direction and traveling in this direction. Thirdly the selected wave-vector, that is the most intense mode $\vec{k}_M$ of the pattern, depends on the walk-off parameter. An approximate expression for $\vec{k}_M$ can be obtained in the context of front propagation into an unstable state [Santagiustina & al. (98)b, Taki & al.].

There are two important characteristics of the noise sustained patterns that exist in the convective regime. The first one is a broad spectrum, both in frequency and in wave-vectors [2]. The second important characteristic is the **macroscopic amplified signal fluctuations around the unstable reference state** (4.7). These characteristics imply that the convective regime cannot be studied within a few-mode approximation, because many modes contribute significantly to the spectral properties. The existence of macroscopic fluctuations also invalidates approximations based on linearization schemes. These facts make a quantum formulation of the convective regime especially difficult. We face a situation in which nonlinearities determine the dynamics of fluctuations around the reference state, with fundamental quantum noise being amplified by several orders of magnitude to produce a macroscopic pattern in the signal. In Sect.4.2 we discuss possible descriptions of this regime through stochastic equations in the quantum formalism.

4.1.2   Pattern formation for vanishing walk-off

In this Section we consider the case of vanishing walk-off $v = 0$ in the Eqs.(4.5-4.6). The dispersion relation for the growth of the signal field perturbations with wave vector $\vec{k}$ given in Eq. (4.8) reduces to [Oppo & al. (94)]

$$\lambda_\pm(\vec{k}) = -1 \pm \sqrt{F^2 - (\Delta_1 + 2|\vec{k}|^2)}. \tag{4.13}$$

As mentioned in the previous Section, for *negative* signal detunings, the zero homogeneous solution becomes unstable at $F = 1$. The perturbations with maximum growth rate are those with wave number $|k_c| = \sqrt{-\Delta_1/2}$, and a pattern with this wave number is formed at threshold [Oppo & al. (94)]. For vanishing walk-off this pattern is **stationary** and **absolutely stable at threshold**.

For *positive* signal detunings the zero homogeneous solution is stable for

$$F < \sqrt{1 + \Delta_1^2}, \tag{4.14}$$

or equivalently $E_0 < \sqrt{(1 + \Delta_0^2)(1 + \Delta_1^2)}$. In this case the instability takes place at zero wave number leading to a non zero homogeneous solution [Trillo & al., Pettiaux & al., Drummond & al. (80)]

$$A_1^{st} = \pm\sqrt{\frac{E_0|A_1^{st}|^2}{(1 + i\Delta_0)(1 + i\Delta_1) + |A_1^{st}|^2}} \tag{4.15}$$

$$A_0^{st} = \frac{E_0(1 + i\Delta_1)}{(1 + i\Delta_0)(1 + i\Delta_1) + |A_1^{st}|^2} . \tag{4.16}$$

There are two equivalent solutions for the signal field with a π phase difference.

---

[2]This spectrum is sharply narrowed on passing into the absolutely unstable regime [Santagiustina & al. (98)a].

In the following we will consider the case of zero pump detuning ($\Delta_0 = 0$) and negative signal detuning ($\Delta_1 < 0$), in which *stripe pattern* arises at threshold ($F = 1$). In general, several spatial harmonics describe this stripe pattern, whose number increases with the distance from the threshold (see Sect.4.5.2.a).

Increasing further the pump the nonzero *homogeneous solutions* (4.15) become stable. We will show in Sect.4.5.2.b that homogeneous solutions are stable for pump values around $E_0 = 1.1$. This pump value is lower than the value at which the stripe pattern becomes linearly unstable [Etrich & al., Gomila & al. (02)]. Numerical studies in this regime find multistability between the stripe pattern, the two nonzero homogeneous solutions and several irregular spatially modulated solutions. The latter are formed by fronts with oscillatory tails connecting the two equivalent homogeneous solutions. In systems with two spatial dimensions, there are also coexisting labyrinthine patterns. In this case ($D = 2$) both the irregular spatially modulated solutions and the labyrinthine patterns cease to exist at the modulational instability of a flat front connecting the two homogeneous solutions [Gomila & al. (02), Gomila & al. (01)].

Here we consider systems with only *one transverse spatial dimension* for which such an instability does not exist. This means that the regime of multistability in parameter space is much larger. The irregular spatially modulated solutions found in this system are an example of **frozen chaos** as described in Ref.[Coullet & al.]. In that case the interaction of two distant fronts can be described by a potential with several wells which become progressively deeper as the distances between the fronts decreases. The OPO cannot be described in terms of such potentials, but numerical studies reveal equilibrium distances whenever the maxima (or the minima) of the local oscillations of the front overlap with each other [Etrich & al., Gomila & al. (02)]. We describe these spatial **disordered structures** in Sect.4.5.2.b.

4.2   Quantum formulation

In the quantum formulation of the DOPO the intracavity pump and signal fields are given by operators $\hat{A}_0(\vec{x}, t)$ and $\hat{A}_1(\vec{x}, t)$ that satisfy standard equal-time commutation relations [Gatti & al. (97)1]

$$\left[\hat{A}_i(\vec{x}, t), \hat{A}_j^\dagger(\vec{x}', t) \right] = \delta_{ij} \delta(\vec{x} - \vec{x}'), \tag{4.17}$$

where the indices i, j stand for $0, 1$. Following the techniques described in [Gatti & al. (97)1], we can introduce a model Hamiltonian for the device. This will include the effects of diffraction together with the driving by a real, classical external field, nonlinear interaction between the fields and cavity damping. Our model, however, also requires that we take account of the effects of walk-off. The resulting Hamiltonian gives, on making the usual Markov approximation, the coupled Heisenberg equations:

$$\partial_t \hat{A}_0(\vec{x}, t) = -\gamma_0[(1 + i\Delta_0) - ia_0\nabla^2]\hat{A}_0(\vec{x}, t) - \frac{g}{2}\hat{A}_1^2(\vec{x}, t) + E_0(\vec{x}) + \hat{F}_0 \tag{4.18}$$

$$\partial_t \hat{A}_1(\vec{x}, t) = -\gamma_1[(1 + i\Delta_1) - ia_1\nabla^2 - v\partial_y]\hat{A}_1(\vec{x}, t) + g\hat{A}_0(\vec{x}, t)\hat{A}_1^\dagger(\vec{x}, t) + \hat{F}_1 \tag{4.19}$$

Note that these are very similar in form to the semi-classical Eqs. (4.1) and (4.2). The Langevin operators $\hat{F}_i$ describe the quantum noise added as a consequence of the interaction with the bath of

external modes. These have the non-vanishing second order moments:

$$\langle \hat{F}_i(\vec{x}, t) \hat{F}_j^\dagger(\vec{x}', t') \rangle = 2\gamma_i \delta_{ij} \delta(\vec{x} - \vec{x}') \delta(t - t'). \tag{4.20}$$

We discuss in Sect.1.2.3.a that a direct solution of these nonlinear Langevin equations of operators is impractical, requiring the solution of an infinite hierarchy of equations for the evolution of all the products of operators that are coupled by the dynamics. A standard alternative approach to this Heisenberg picture is to consider the evolution equation of the reduced density operator $\hat{\rho}$ of the system in the Schrödinger picture and to use quasi-probability functionals. The intracavity dynamics is described by a master equation (Sect.1.2.2):

$$\frac{\partial \hat{\rho}}{\partial t} = \frac{1}{i\hbar}[\hat{H}, \hat{\rho}] + \Lambda \hat{\rho}, \tag{4.21}$$

where $\hat{H}$ is the Hamiltonian. The Hamiltonian operator, expressed as a function of fields operators $\hat{A}_0(\vec{x}, t)$ and $\hat{A}_1(\vec{x}, t)$, is [Gatti & al. (97)1]:

$$\hat{H} = \hat{H}_0 + \hat{H}_{int} + \hat{H}_{ext} \tag{4.22}$$

where

$$\hat{H}_0 = \hbar \int d^2\vec{x} \sum_{i=0,1} \left[\gamma_i \hat{A}_i^\dagger(\vec{x})(\Delta_i - a_i\nabla^2)\hat{A}_i(\vec{x}) + i\gamma_1 v \hat{A}_1^\dagger(\vec{x})\partial_y \hat{A}_1(\vec{x}) + \right] \tag{4.23}$$

describes free propagation of fields in the cavity and the linear walk-off effect,

$$\hat{H}_{ext} = i\hbar \int d^2\vec{x} E_0(\vec{x}) \left[\hat{A}_0^\dagger(\vec{x}) - \hat{A}_0(\vec{x}) \right] \tag{4.24}$$

is due to the interaction with the external pump E_0, which we choose to be real, and

$$\hat{H}_{int} = i\hbar \frac{g}{2} \int d^2\vec{x} \left[\hat{A}_0(\vec{x})\hat{A}_1^{\dagger 2}(\vec{x}) - \hat{A}_0^\dagger(\vec{x})\hat{A}_1^2(\vec{x}) \right] \tag{4.25}$$

is the interaction term between first and second harmonic. Here Δ_i and a_i are cavity detunings and diffraction parameters for the pump and signal expressed in units of the associated decay constants γ_i

The Liouvillian Λ accounts for dissipation through the partially reflecting plane mirror of the cavity and is given by

$$\Lambda \hat{\rho} = \sum_{j=0,1} \int d^2\vec{x} \gamma_j \left\{ [\hat{A}_j(\vec{x}), \hat{\rho}\hat{A}_j^\dagger(\vec{x})] + [\hat{A}_j(\vec{x})\hat{\rho}, \hat{A}_j^\dagger(\vec{x})] \right\}.$$

4.2.1 Problems of phase space descriptions

In this Section we discuss the problems associated with the use of phase space methods to describe nonlinear interactions in the OPO. In Sect.4.2.2 and 4.2.3 we propose two nonlinear approximations that are useful to describe the nonlinear dynamics of the fields.

Following the procedure presented in Sect.1.2.3.b, the master equation (4.21) can be mapped onto an equation of motion for a quasi-probability distributions in the phase-space of the system [Barnett & Radmore, Gardiner & Zoller, Carmichael]. These distributions are functionals of the c-number fields $\alpha_i(\vec{x})$ associated with the operators $\hat{A}_i(\vec{x})$. The evolution equations obtained in this way

for the distributions are functional partial differential equations. These are not in general of the Fokker-Planck type and they do not lead to well-behaved stochastic representations in terms of Langevin equations driven by Gaussian white noise. The offending term for the system of interest is $\hat{H}_{int}$, which gives a functional term of the form

$$[\hat{A}_0(\vec{x})\hat{A}_1^{\dagger^2}(\vec{x}) - h.c., \hat{\rho}] \Longleftrightarrow \left(s\alpha_0\frac{\delta^2}{\delta\alpha_1^2} + \frac{1-s^2}{4}\frac{\delta^3}{\delta\alpha_1^2\delta\alpha_0^*} + \frac{\delta}{\delta\alpha_0}\alpha_1^2 - 2\alpha_0\alpha_1^*\frac{\delta}{\delta\alpha_1} + c.c.\right)W_s \qquad (4.26)$$

where the parameter s depends on the ordering. These terms do not fulfill the requirements that guarantee a positive definite solution for W_s.

In the Wigner representation ($s = 0$) we find **third order derivatives**. In Ch.1 we discussed the problems of such "generalized FPE", and the limits of the "stochastic electrodynamics", obtained simply dropping these third order terms. If the classical solutions are stable and the fluctuations are small it is possible to linearize around these solutions, obtaining a FPE for the Wigner function in the fluctuations of the field (Sect.1.2.3.b). The linearization is allowed when the fluctuations around the solution are damped and therefore small: we have already mentioned the DOPO below the threshold of signal generation, in the regime of quantum images where linearization is possible (Sect.1.4.1.a). The same type of approximation is generally possible above threshold, linearizing around a pattern solution [Zambrini & al. (00)], when the fluctuations around the stable pattern are all damped. Above threshold great care has to be taken if the system is translational invariant (flat mirrors and homogeneous transversal pump profile). The pattern solution breaks the translational symmetry and therefore there is a Goldstone mode which is neutrally stable [Zambrini & al. (00)]. As we have seen in Ch.3 noise excites this mode, giving diffusion of the phase which fixes the position of the pattern [Zambrini & al. (00)]. Moments involving such big fluctuations cannot be correctly described within a linearized treatment in the fields amplitudes. In particular, such an approach leads to *unphysically divergent quadrature correlations*, although correct results can be obtained for the intensity correlations [Gomila & Colet].

For the P ($s = 1$) and Q ($s = -1$) representation third order derivatives disappear, but the diffusion matrix is **not positive definite** so that positive solutions are again not guaranteed, although the Q function retains positivity through having a minimum allowed width [Gardiner & Zoller]. Generally these problems have been avoided by using linearization schemes [Carmichael]. We have mentioned above some problems arising above threshold in a stable spatial structure, when neutrally stable modes are identified. In the following we stress that linearization schemes cannot be used in a convective regime as the reference state is unstable and the fluctuations, far from being small, are amplified. The alternative of the P positive representation [Gilchrist & al.] is not suitable for the same reason: the unstable reference state results in diverging trajectories.

Our aim is to find a method to describe the macroscopic quantum fluctuations of the convective regime. To illustrate the problems of this regime we compare the noise sustained structures (in the convective regime) with the quantum images (below threshold), introduced in Ch.1. Below threshold of signal generation, the stable solution is a homogeneous pump with an amplitude that depends on the coherent driving field. The signal field is zero on average, but its fluctuations show a level of self-organization that increases near the threshold. The quantum images reflect the presence of eigenmodes of the linearized equations, whose eigenvalues are such that their negative real part ap-

proaches zero at threshold. The fluctuations of these eigenmodes are the **least damped** ones and dominate the dynamics of the signal. The important point is that the intensity of such quantum images of the signal is of the order of quantum noise, while the pump has a macroscopic mean value. It is then possible to *linearize*, obtaining a well defined FPE for the Wigner distribution, that can be mapped in equivalent Langevin equations (Sect.1.2.3.b).

In this absolutely stable regime (below threshold) the quantum noise does not change drastically the solution with respect to the stable deterministic solution. This means that in the stochastic representation, fluctuations only induce the dynamical trajectory to visit a small region in phase space in the neighborhood of the classical deterministic solution. In the convective regime the classical deterministic solution is *unstable* and macroscopically different from the stochastic solution. In this regime quantum noise in the DOPO is **amplified**, destroying the zero-valued homogeneous deterministic solution for the down-converted field and driving the system into noise sustained states having a macroscopic number of photons. Neither linearization approximations nor the P_+ representation are useful.

Therefore a description of the macroscopic quantum fluctuations in the spatial structures of the OPO (such as noise sustained structures) needs specific nonlinear approximations. In the next Sects.4.2.2-4.2.3 we present two proposals of approximations based on the use of quasi-probabilities.

4.2.2 A first nonlinear approximation: Time dependent parametric approximation

In this Section we propose a nonlinear approximation to describe the quantum dynamics of the DOPO in the convective regime, based on the main physical features of this regime. Our aim is to be able to treat the macroscopic quantum fluctuations associated with the signal field.

In the convective regime there are large signal fluctuations around the unstable solution $A_1 = 0$. The coupling of signal and pump gives the nonlinear saturation for these amplified fluctuations. On the other hand, the pump field is always macroscopic and stable, with small damped fluctuations. This suggests the approximation of neglecting quantum noise in the pump and approximating it by a classical field $\mathcal{A}_0(\vec{x}, t)$. In this way we obtain a Hamiltonian that is quadratic in the operators describing the quantum dynamics of the signal field. For such quadratic Hamiltonians, the Wigner quasi-probability functional of the complex function $\alpha_1(\vec{x}, t)$ obeys the following FPE in which the classical pump field $\mathcal{A}_0(\vec{x}, t)$ appears parametrically:

$$\frac{\partial W(\alpha_1; \mathcal{A}_0)}{\partial t} = \left[-\left(\frac{\delta}{\delta \alpha_1} \gamma_1[(1 + i\Delta_1) - ia_1\nabla^2 - v\partial_y]\alpha_1(\vec{x}, t) + g\mathcal{A}_0(\vec{x}, t)\alpha_1^*(\vec{x}, t) + c.c. \right) \right.$$
$$\left. + \gamma_1 \frac{\delta^2}{\delta \alpha_1 \delta \alpha_1^*} \right] W(\alpha_1; \mathcal{A}_0)). \tag{4.27}$$

The associated Langevin equation that represents the stochastic dynamics of the signal field $\alpha_1(\vec{x}, t)$ is

$$\partial_t \alpha_1(\vec{x}, t) = -\gamma_1[(1 + i\Delta_1) - ia_1\nabla^2 - v\partial_y]\alpha_1(\vec{x}, t) + g\mathcal{A}_0(\vec{x}, t)\alpha_1^*(\vec{x}, t) + \sqrt{\gamma_1}\xi_1(\vec{x}, t), \tag{4.28}$$

where $\xi_1(\vec{x}, t)$ is a complex Gaussian white noise (see Eq.(4.3)). This noise term accurately represents the effects of vacuum fluctuations associated with cavity losses on the signal field. We note that treating the pump field classically in this way is a natural extension of the parametric approximation to three-mode interactions, which treats a strong mode classically and has been widely used in quantum optics for many years [Louisell & al.].

It is important to note that $\mathcal{A}_0(\vec{x}, t)$ cannot be replaced by an expectation value of $\langle \hat{A}_0 \rangle$ as would be possible in the regime of absolute stability (quantum images). Such an ansatz decorrelates the pump modes from the sub-harmonic ones and eliminates the saturation effect of the pump. In fact, with such an ansatz Eq. (4.28) becomes linear, giving a Gaussian probability distribution for the signal modes. This distribution would always be centered on zero, but with statistical moments that diverge above threshold because the signal modes are undamped in the convective regime. Therefore, the stochastic differential equation must be solved self-consistently with an equation defining the dynamics of the classical field $\mathcal{A}_0$. The equation we propose for $\mathcal{A}_0$ is suggested by the Heisenberg equation (4.18), with $\hat{A}_0$ replaced by a classical field $\mathcal{A}_0$. We first neglect the noise source in (4.18) since quantum fluctuations entering in the cavity are unimportant, as compared with the macroscopic fluctuations of the signal term $\hat{A}_1^2$. Secondly we replace the operator $\hat{A}_1^2$ by the c-number function α_1^2 associated with our stochastic representation of the signal. This replacement is independent of operator ordering and hence will be the same should be choose to use a different quasi-probability. This procedure gives a partial differential equation for the "classical" pump field driven by the c-number representation of the *quantum* signal field:

$$\partial_t \mathcal{A}_0(\vec{x}, t) = -\gamma_0[(1 + i\Delta_0) - ia_0\nabla^2]\mathcal{A}_0(\vec{x}, t) - \frac{g}{2}\alpha_1^2(\vec{x}, t) + E_0(\vec{x}) \qquad (4.29)$$

A justification for this equation is that its mean value coincides with the expectation value for $\hat{A}_0$ obtained from the operator equation (4.18). This procedure is reminiscent of the time dependent refinement of the parametric approximation described in some detail by [Kumar & Mehta] and [Barnett & Knight]. This approach allows for the quantum evolution of the weak fields to feed back and affect the classical strong field. In the approach of Kumar and Mehta, this feedback is via quantum expectation values of operators for the weak fields. Here, however, we are required to take explicit account of the noisy properties of the quantum sub-harmonic field. We do this by using the c-number representation of the quantum field, associated with our stochastic simulation of it, as a term in equation (4.29).

In summary, our **time dependent parametric approximation** is defined by stochastic classical equations in the Wigner representation for the fields $\mathcal{A}_0$ and α_1, which, with the scaling (4.4), are:

$$\partial_t \mathcal{A}_0(\vec{x}, t) = -[(1 + i\Delta_0) - i\nabla^2]\mathcal{A}_0(\vec{x}, t) - \frac{1}{2}\alpha_1^2(\vec{x}, t) + E_0(\vec{x}) \qquad (4.30)$$

$$\partial_t \alpha_1(\vec{x}, t) = -\left[(1 + i\Delta_1) - 2i\nabla^2 - v\partial_y\right]\alpha_1(\vec{x}, t) + \mathcal{A}_0(\vec{x}, t)\alpha_1^*(\vec{x}, t) + \frac{1}{a^{D/4}}\frac{g}{\gamma}\xi_1(\vec{x}, t). \qquad (4.31)$$

Stochastic averages of the c-number variable $\alpha_1(\vec{x}, t)$ will provide symmetrically ordered averages of the quantum fluctuations in the signal field as driven by the "classical" pump field. The classical pump field is driven by the macroscopic quantum fluctuations in the signal as represented by the c-number

representation $\alpha_1(\vec{x}, t)$. This time dependent parametric approximation appears useful not only in the convective regime (Sect.4.3) but also in situations in which there are large fluctuations of the signal that cannot be described by approximations based on linearization. An example is the instability region, near to the threshold of pattern formation, where critical fluctuations appear (Sect.4.4).

4.2.3 A second nonlinear approximation:
Langevin equations in Q representation

In this Section we employ the Q representation (see Sect.1.2.3.b) for the pump and signal fields:

$$Q(\alpha_0, \alpha_1) = \frac{1}{\pi} < \alpha_0, \alpha_1 | \hat{\rho} | \alpha_0, \alpha_1 > \tag{4.32}$$

The most important property of this representation is that it satisfies the requirements for a true probability distribution. From Eq. (4.26) (with $s = -1$) we observe that the Q representation suffers of negative diffusion. Unlike the Wigner function, however, the Q function is always positive and well-behaved, as we have seen in Sect.1.2.3.b. In Ch.2 we have seen that a Q representation with a doubled phase-space has been proposed in order to deal with negative diffusion [Yuen & Tombesi] and this has been shown to give good results in some nonlinear quantum systems [Zambrini & Barnett].

In this Chapter we investigate the possibility to use the Q representation for devices consisting on a cavity filled with a χ^2 medium, as in the OPO and SHG. The evolution equation of the functional Q for our model (described above) is:

$$\frac{\partial Q(\alpha_0, \alpha_1)}{\partial t} = \int d^2\vec{x} \left\{ - \left(\frac{\delta}{\delta\alpha_0(\vec{x})} V_0 + \frac{\delta}{\delta\alpha_1(\vec{x})} V_1 + c.c. \right) \right.$$
$$+ \int d^2\vec{x}' \left[2\gamma_0 \frac{\delta^2}{\delta\alpha_0(\vec{x})\delta\alpha_0^*(\vec{x}')} + 2\gamma_1 \frac{\delta^2}{\delta\alpha_1(\vec{x})\delta\alpha_1^*(\vec{x}')} + \right.$$
$$\left. \left. \frac{1}{2} \left(-g\alpha_0 \frac{\delta^2}{\delta\alpha_1(\vec{x})\delta\alpha_1(\vec{x}')} + c.c \right) \right] \right\} Q(\alpha_0, \alpha_1), \tag{4.33}$$

where the drift terms are

$$V_0 = -\gamma_0[(1 + i\Delta_0) - ia_0\nabla^2]\alpha_0(\vec{x}, t) - \frac{g}{2}\alpha_1^2(\vec{x}, t) + E_0$$
$$V_1 = -\gamma_1[(1 + i\Delta_1) - ia_1\nabla^2]\alpha_1(\vec{x}, t) + g\alpha_0(\vec{x}, t)\alpha_1^*(\vec{x}, t).$$

If the diffusion term is positive then our evolution equation is a bona-fide Fokker-Planck equation. In the other case this equation doesn't describe an ordinary diffusion process. For equation (4.33) the diffusion term is positive if

$$|\alpha_0(\vec{x}, t)| < \frac{2\gamma_1}{g}. \tag{4.34}$$

The modulus of the stationary field at threshold takes the value $|A_0^{thr}| = \gamma_1/g$ (see Sect. 4.1.2). This means that the condition (4.34) corresponds to pump trajectories taking values that are less than twice the threshold value. Staying in a region far from the limit (4.34) – we are considering $A_0^{st} \leq 1.5 A_0^{thr}$ – an extremely large fluctuation in a trajectory would be necessary in order to lose the positiveness of

the diffusion. Clearly these trajectories have a negligible probability to appear, and never appeared in our simulations. For these reasons, the approximation we propose in this section is to study Langevin equations related to the FPE given by (4.33) *and* (4.34), neglecting any trajectories that would make negative the diffusion term. Clearly the condition (4.34) does not depend on the frequency at which the system is pumped. For this reason the method is suitable, and has been already successfully used, to describe nonlinear fluctuations in stripe patterns in SHG in a regime of pump values limited by Eq. (4.34) [Bache & al.].

From Eqs.(4.33-4.34), with the scaling (4.4), we obtain the equations:

$$\partial_t \alpha_0(\vec{x},t) = -\left[(1+i\Delta_0) - i\nabla^2\right]\alpha_0(\vec{x},t) + E_0 - \frac{1}{2}\alpha_1^2(\vec{x},t) + \sqrt{\frac{2}{a}}\frac{g}{\gamma}\xi_0(\vec{x},t) \qquad (4.35)$$

$$\partial_t \alpha_1(\vec{x},t) = -\left[(1+i\Delta_1) - 2i\nabla^2\right]\alpha_1(\vec{x},t) + \alpha_0(\vec{x},t)\alpha_1^*(\vec{x},t) + \sqrt{\frac{2}{a}}\frac{g}{\gamma}\xi_1(\vec{x},t). \qquad (4.36)$$

The condition (4.34) in the new variables is

$$|\alpha_0(\vec{x},t)| < 2. \qquad (4.37)$$

We solve these Langevin equations by numerical simulation, neglecting any trajectories that do not satisfy the condition (4.37), should these occur. ξ_0 is a white Gaussian noise with non-vanishing moment:

$$\langle\xi_0(\vec{x},t)\xi_0^*(\vec{x}',t')\rangle = \delta(\vec{x}-\vec{x}')(t-t') \qquad (4.38)$$

The signal noise ξ_1 results to be *phase sensitive*, due to the diagonal terms in the diffusion matrix of Eq. (4.33). Moreover this noise is multiplicative, depending on the value of the pump field. However due to the form of $\hat{H}$ (quadratic in $\hat{A}_1$ and linear in $\hat{A}_0$), these equations have the same formal expression in the Ito or Stratonovich interpretations [Gardiner].

The phase sensitive multiplicative noise $\xi_1(x,t)$ can be written as

$$\xi_1(x,t) = \left[\frac{-\alpha_{0I}(x,t)}{2\sqrt{2+\alpha_{0R}(x,t)}} + \frac{i}{2}\sqrt{2+\alpha_{0R}(x,t)}\right]\phi(x,t) + \sqrt{\frac{1-\frac{|\alpha_0(x,t)|^2}{4}}{2+\alpha_{0R}(x,t)}}\psi(x,t) \qquad (4.39)$$

with $\alpha_0 = \alpha_{0R} + i\alpha_{0I}$ and ϕ,ψ uncorrelated real white noises in space and time, with variances one. Actually, the diffusion matrix of a Fokker-Plank equation fix only three of the four degrees of freedom in the choice of the real and imaginary parts of the noise term ξ_1; this depends on the multiplicity of Langevin processes associated with the same FPE [Gardiner]. Hence Eq.(4.39) corresponds to a particular choice among several possible representations.

The Langevin equations (4.35-4.36) based on the Q representation have two advantages with respect to the equations obtained within the time dependent approximation presented in the previous Section. First, they are useful in a larger domain of parameter values, providing a good description of the nonlinear quantum fields far from the threshold. Second, quantum fluctuations of the pump are also included. Nevertheless using Eqs.(4.35-4.36) the physical nature of the approximation is less clear, while in the case of Eqs.(4.30-4.31) there is a clear phenomenological basis for the time dependent parametric approximation, i.e. the smallness of the pump vacuum fluctuations in the signal dynamics in particular regimes.

4.3   Quantum fluctuations in the convective regime

In this Section we use the time dependent parametric approximation introduced in Sect.4.2.2 to describe the transition from the regime of quantum images to the one of noise sustained patterns and to the absolutely unstable regime. We also characterize in detail the nonclassical properties of the noise sustained patterns that appear in the convective regime.

4.3.1   Stochastic trajectories and Wigner distribution function

Numerical simulations of the stochastic trajectories associated with the Langevin equations (4.30) and (4.31) give a good intuitive understanding of the dynamical properties of the regime below threshold, the convective regime and the absolutely unstable regime. In this section we present such numerical simulations working with a single transverse dimension ($D = 1$):

$$\partial_t \mathcal{A}_0 = [-(1 + i\Delta_0) + i\partial_x^2]\mathcal{A}_0 - \frac{1}{2}\alpha_1^2 + E_0 \tag{4.40}$$

$$\partial_t \alpha_1 = \left[-(1 + i\Delta_1) + 2i\partial_x^2 + v\partial_x\right]\alpha_1 + \mathcal{A}_0\alpha_1^* + \xi(x, t).$$

Numerical simulation are performed using the same pseudo-spectral method and Gaussian random number generator [Toral & al.] of Ch.3.

Fig.4.2 is a space-time plot of the near-field for the signal in the below-threshold, convective and absolutely unstable regimes. Fig.4.3 gives the far-fields associated with the same simulations. In the
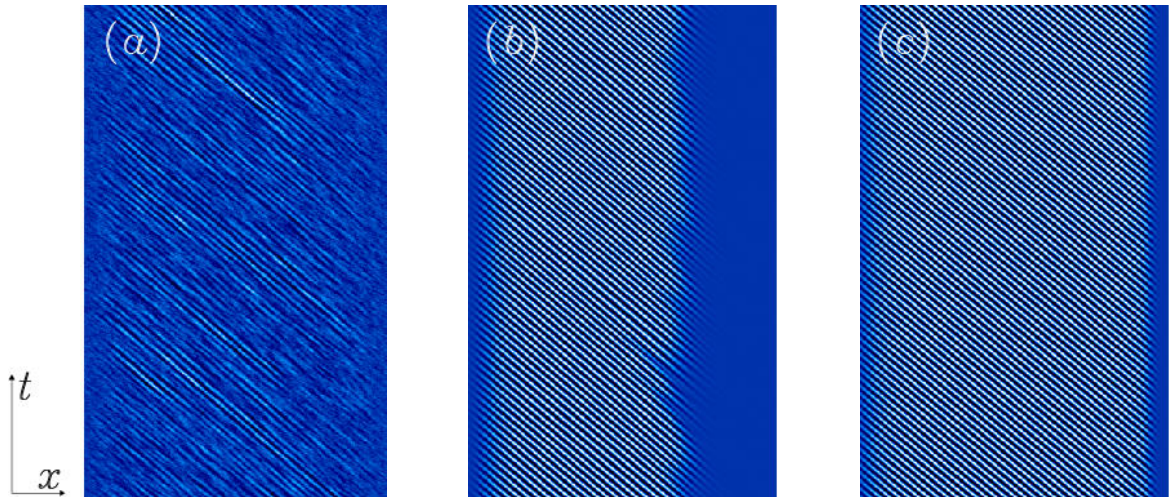
Figure 4.2:   Evolution of the near field of the real part of the signal $Re(\alpha_1(x, t))$ for: (a) $F = 0.999$, (b) $F = 1.025$, (c) $F = 1.1$, in 2500 time units. Parameters are: $\Delta_0 = 0, \Delta_1 = -0.25, v = 0.42$, system size $= 1.7678 \cdot 512$ pixels $\simeq 900$ space units. Only the regions in which the signal is excited are shown, that is the region of the plateau of the supergaussian pump. The expression of supergaussian pump in all simulations is $E_0(x) = e^{-\frac{1}{2}(x/317)^{10}}$, with x varying in the interval $[-453; 453]$. This produces a profile that is everywhere smooth but has a flat central plateau.
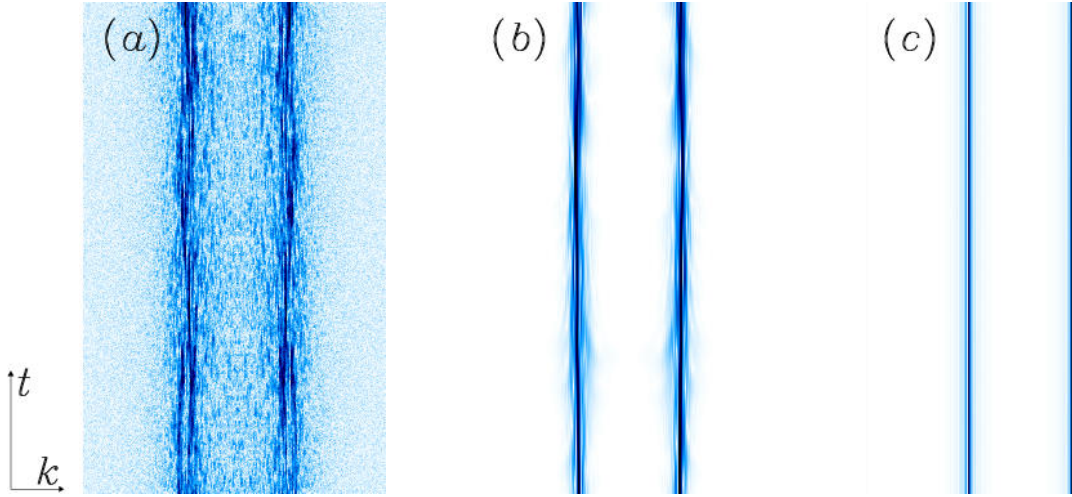
Figure 4.3: Evolution of the far field $|\alpha_1(k,t)|$ for: (a) $F = 0.999$, (b) $F = 1.025$, (c) $F = 1.1$. Same parameters as in Fig.4.2

following we discuss the different properties of these trajectories and how they are reflected in the associated Wigner distribution.

4.3.1.a   Below threshold

Below but close to threshold we find weakly damped fluctuations which are a precursor to the traveling pattern that appears at threshold. The fluctuations impose a degree of spatial self-organization in those regions in which the pump is sufficiently strong to bring the OPO close to threshold. In Fig.4.2(a) we plot the real part of the stochastic variable $\alpha_1(x,t)$ for a single trajectory. This is a realization of these fluctuations for a pump with a supergaussian profile. These quantum images have been described in OPO without walk-off [Gatti & Lugiato, Lugiato & al. (97), Marzoli & al., Lugiato & al. (95), Lugiato & al. (99), Gatti & al. (97)1]. Due to the transverse walk-off these noisy patterns are traveling. Not too close to threshold, the damped fluctuations can be analyzed with linearization procedures [Gatti & al. (97)1] in the limit of small fluctuations. Our nonlinear quantum equations enable us to study also the regime closer to threshold, where large critical fluctuations are expected to occur. Note, in particular, that the results in Fig.4.2(a) were obtained for $F = 0.999$.

The selection of a preferred wave-number in the stochastic pattern of Fig.4.2(a) becomes more evident in the far field shown in Fig.4.3(a). It is clear that there are preferred values of the wave-number but that a broad distribution of weakly damped modes around these preferred k_c and $-k_c$ modes is apparent. An interesting characterization of the stochastic dynamics in the far field, Fig.4.3(a), is obtained by looking at the time evolution of the stochastic amplitudes for the most intense modes $\alpha_1(k_c,t)$. We first recall that the linear stability analysis of Sect. 4.1.1 identifies the existence of a non-vanishing frequency $(\omega(k) = vk)$ at threshold caused by the walk-off. This implies that a traveling pattern will emerge above threshold and that the corresponding Fourier modes will oscillate at this
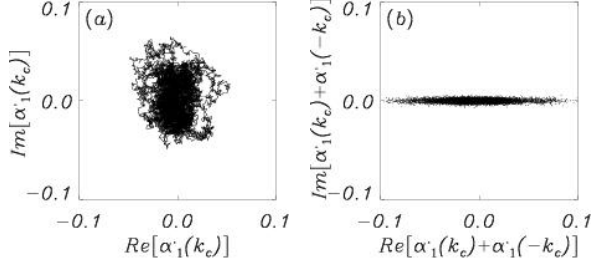
Figure 4.4: (a) trajectory of the slowly varying amplitude $\alpha'_1(+k_c)$ during 20.000 time units. (b) trajectory of $[\alpha'_1(+k_c) + \alpha'_1(-k_c)]$ during 20.000 time units. $F = 0.999$, other parameters are as in Fig.4.2, except for $dx = 51\lambda_c/512 \simeq 1.7702$, where $\lambda_c = 2\pi/k_c$, 512 is the number of grid points.
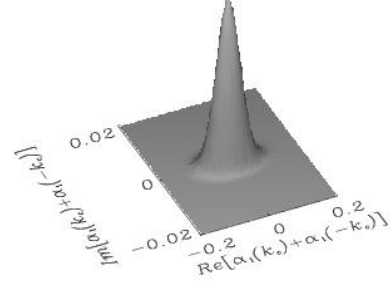
Figure 4.5: Wigner distribution for the superposition of modes $\alpha_1(+k_c) + \alpha_1(-k_c)$. Parameters of Fig.4.4. Total time 2.000.000 units. Note the factor 10 difference in the scale of the two axes.

frequency. We can remove this time-dependence by working in a frame rotating at this frequency. This corresponds to factoring out a time factor $e^{i\omega(k)t}$ to obtaining the slowly varying amplitude $\alpha'_1(k,t) = \alpha_1(k,t)e^{-i\omega(k)t}$. A phase space trajectory for the slowly varying amplitude of the dominating Fourier component, $\alpha'_1(k_c,t)$, is shown in Fig.4.4(a).

The linear stability analysis of Sect. 4.1.1 also identified the direction of instability V_+. In particular, in the case of a real pump, and for the critical mode k_c, this direction is given by $[\alpha_1(+k_c) + \alpha_1^*(-k_c)]$. As a consequence the superposition of modes $[\alpha_1(+k_c) + \alpha_1(-k_c)]$ can be decomposed in two quadratures, one corresponding to the direction of instability that becomes undamped at threshold $(Re[\alpha_1(+k_c)+\alpha_1(-k_c)])$, and the orthogonal quadrature $(Im[\alpha_1(+k_c)+\alpha_1(-k_c)])$ that remains damped. We observe that the superposition of slowly varying modes $\alpha'_1(\pm k_c, t)$ can be decomposed into damped and undamped quadrature in the same way. In fact due to the symmetry $\omega(k) = -\omega(-k)$ we have $V_\pm(\vec{k}, -\vec{k}) = e^{i\omega(k)t}[e^{i\Phi\pm}\delta A'_1(\vec{k}) \pm \delta A_1'^*(-\vec{k})]$, so that the relative phase $e^{i\Phi\pm}$ between the slowly varying modes is the same as that in the equation (4.12). Hence, we can also identify the real and imaginary quadratures of the superposition of modes $[\alpha'_1(+k_c) + \alpha'_1(-k_c)]$ as damped and undamped at threshold. The corresponding time trajectory of this superposition of modes displays very clearly the expected reduction of fluctuations in the damped imaginary quadrature (see Fig.4.4(b)).

From the stochastic trajectories that randomly visit the different points of phase space it is easy to construct a relative histogram giving a probability density in this phase space. This density is identified with the Wigner distribution. As with all Wigner functions, the marginal distributions, obtained for one field quadrature by integrating over the orthogonal quadrature, are true probability distributions for the remaining quadrature. At a finite distance from threshold the Wigner distribution $W(\alpha_1(k))$ for the field $\alpha_1(k)$ obtained in this way has a Gaussian shape consistent with a linearized analysis of fluctuations. Such a Gaussian Wigner distribution is a solution of the FPE for the Wigner representation of *linear* signal fluctuations. If we consider the Wigner distribution for the superposition of modes discussed above $W(\alpha_1(+k_c) + \alpha_1(-k_c))$, then we obtain a Gaussian centered on the origin but with a variance

that depends on the orientation in phase space [3]. There is an axis with a reduced variance ('squeezed') and the orthogonal one with a larger variance ('anti-squeezed') (see Fig.4.5). These features reflect the asymmetry or phase-sensitivity of the fluctuations already visualized in the stochastic trajectory.

4.3.1.b   Convective regime

Differences between the regime below threshold and the convective regime are clearly seen both in the near and far signal fields. We observe a macroscopic traveling pattern in the near field (Fig.4.2(b)). This is clearly associated with wave-numbers distributed around the value of the selected one (k_M) in the far field (Fig.4.3(b)). The spectrum of excited wave-numbers is clearly narrower in the convective regime than below threshold. This is reflected in the more regular pattern appearing in the near field. Our simulations display the typical features associated with the convective regime [Santagiustina & al. (98)a]:

- The noise sustained pattern does not fill the whole region in which the pump has a value above threshold. This is because the pattern grows while traveling in the walk-off direction. Note that the space point at which the pattern reaches a macroscopic observable value changes randomly from time to time. This reflects the origin of the pattern in (quantum) noise.

- The far field shows the predominance of different wave-numbers at different times resulting in a spatial spectrum that is broader than that found in the absence of walk-off or in the absolutely unstable regime. There is competition between the modes within this broad spectrum and hence it is not possible to define, in this regime, a *single* wave-number k_M corresponding to the most excited modes. Modes with different wave-numbers compete to form the pattern, switching on and off as the pattern evolves. The significative temporal scales are given by the time that the perturbation needs to cross the system.

Phase space trajectories for this regime are shown in Fig. 4.6. We find that there are random changes in the phase and amplitude of the slowly varying signal $\alpha_1'(+k_c)$ around a zero mean value (Fig.4.6(a)). This is similar to the behavior depicted in Fig.4.4(a) below threshold. The difference is that in the convective regime macroscopic intensities are reached, with the signal amplitude taking values comparable to those reached in the absolutely unstable regime (compare scales of Figs. 4.4(a), 4.6(a), and 4.10). The continuous changes in intensity from zero to macroscopic values originate in the fact that, in the convective regime, a given mode is not constantly switched-on (see Fig.4.3(b)). The pattern is sustained by noise and is subject to a continuous renovation: different stripe patterns (with different wave-numbers) grow, travel in the system starting from noise and die out. This has an important consequence in the time scales of the far field dynamics: below threshold these scales are determined by noise, while in the convective regime they are determined by the time needed for a perturbation to travel through the system. Another indication of the nonlinear dynamics of fluctuations that occur in this regime is that the quadrature displaying reduced fluctuations is no longer the one determined by

---

[3]If the pump is flat, equations for $\alpha_1(k,t)$ are invariant under the change $\alpha_1(k,t) \rightarrow e^{i\phi}\alpha_1(k,t)$, so that it is equivalent to construct the W distribution considering trajectories $\alpha_1(k,t)$ or $\alpha_1'(k,t)$. For non flat pump this symmetry property is generally lost. In the pictures we represent the W distribution for the amplitudes α_1.
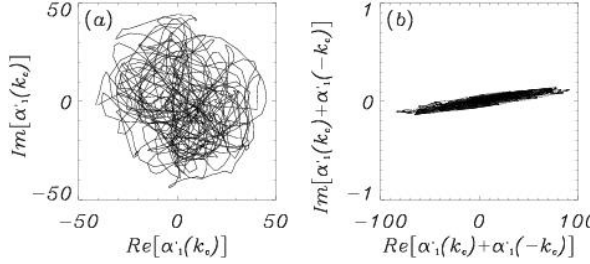
Figure 4.6: (a) Trajectory of slowly varying amplitude of $\alpha_1'(+k_c)$ during 100.000 time units. (b) Trajectory of $[\alpha_1'(+k_c)+\alpha_1'(-k_c)]$. Parameters $F=1.025$, $\Delta_0=0, \Delta_1=-0.25, v=0.42, dx \simeq 1.7702$.
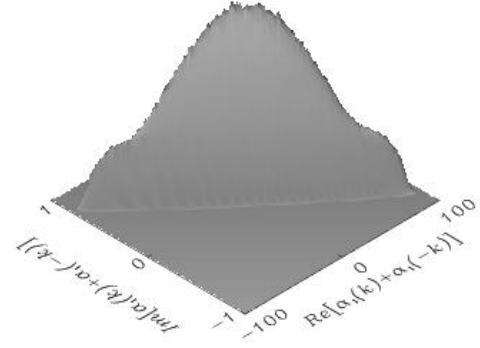
Figure 4.7: $W(\alpha_1(+k) + \alpha_1(-k))$, for an excited mode $k = 1.04k_c$, obtained from a trajectory during 10.000.000 time units. Other parameters as in Fig. 4.6.

the linear analysis. This is seen in Fig.4.6(b) where the ellipse of fluctuations is tilted with respect to the corresponding one below threshold Fig.4.4(b).

The probability distributions obtained from the trajectories of Fig.4.6 also reflect the nonlinear nature of the fluctuations in this regime. In Fig.4.7 we show the W distribution for the superposition of modes $[\alpha_1(+k) + \alpha_1(-k)]$ for one of the most excited wave-numbers, namely $k = 1.04k_c$. A most noticeable feature is the non-Gaussian shape of the distribution for large values of the amplitude in the direction of undamped fluctuations. The wings of the distribution originate in the macroscopic fluctuations of the mode under consideration when it switches-on. Its most probable value is still zero, reflecting the fact that most of the time the mode remains switched-off. We can view these nongaussian features in the wings of our Wigner functions as precursors of the pair of peaks appearing in the absolutely unstable regime. These wings become more pronounced as we approach the absolutely unstable regime, as shown in Fig.4.8 for $F = 1.04$.

Finally, we note that the modes that become excited and contribute to the dynamics seem to reach a common maximum amplitude. This is probably fixed by the maximum value of the energy exchanged with the pump mode in the nonlinear interaction. This is shown in Fig.4.9 where the possible values of different modes are seen to be cut-off at essentially the same amplitude. The nongaussian form of these distributions is also clear and this again demonstrates that we are dealing with nonlinear effects associated with the quantum fluctuations.

4.3.1.c Absolutely unstable regime

In the absolutely unstable regime we observe from the near field plot, Fig.4.2(c), that a macroscopic and stable traveling pattern fills the whole of the above threshold region. This behavior is reflected in the far field, Fig.4.3(c), which shows a well-defined and fixed dominant wave number and a narrow spatial spectrum. We should note that the dominant wave-number k_M does not coincide with the most unstable wave-number at threshold (k_c). This is a consequence of the interplay between nonlinearities
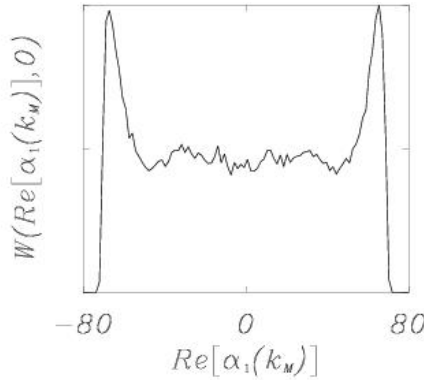
Figure 4.8: Cut of the Wigner distribution along the real axis, $W(Re(\alpha_1(+k_M)),0)$, for the most excited mode $k_M = 1.06k_c$, obtained from a trajectory during 6.000.000 time units. $F = 1.04$ and other parameters as in Fig. 4.6.
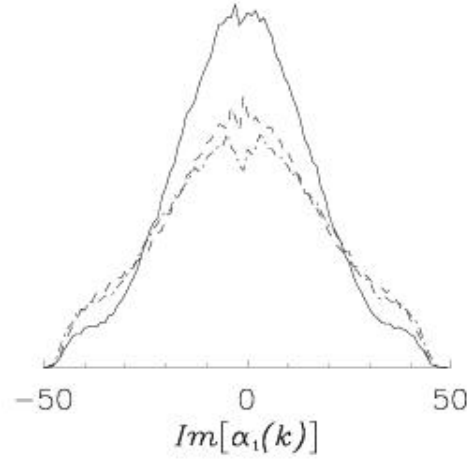
Figure 4.9: Section of the Wigner distribution along the imaginary axis $W(0, Im(\alpha_1(k)))$ for 3 excited modes: k_c (dashed line), $k' = 1.04k_c$ (dash dot line), $k'' = 1.06k_c$ (continuous line). Same parameters as Fig.4.6.

and walk-off. Phase space trajectories for the amplitudes of these two modes are shown in Fig.4.10. Even after elimination of the rapid frequency there remains a phase diffusion process, but macroscopic values of the intensity are maintained. Although there is essentially only the phase diffusion for k_M, the critical mode, with wave-number k_c, displays a second frequency superimposed on the phase diffusion process.

The phase space trajectory for the superposition of modes $[\alpha'_1(\vec{k}_M, t) + \alpha'_1(-\vec{k}_M, t)]$ is shown in Fig. 4.11. We observe that fluctuations are not uniformly distributed around a zero value as they were in the below threshold (Fig.4.4) and convective (Fig.4.6) regimes. Instead, they describe a closed curve around the origin. The associated W distributions display peaks at two values. These correspond to
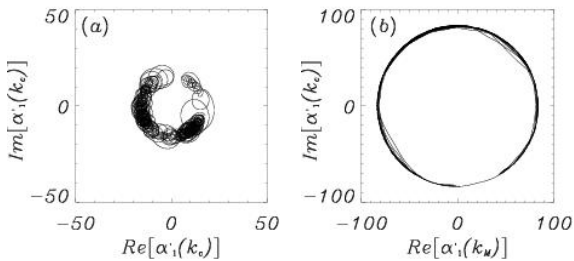
Figure 4.10: Trajectories of (a) $\alpha'_1(k_c)$ and (b) $\alpha'_1(k_M)$ during 100.000 time units, $F = 1.05$, other parameters as in Fig.4.6
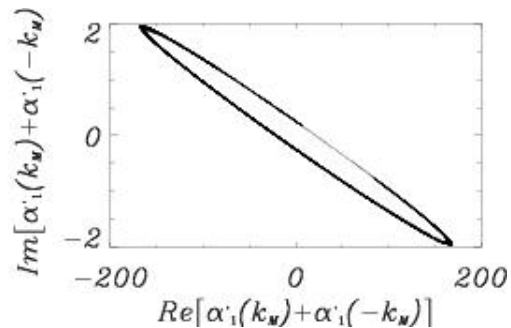
Figure 4.11: Trajectory of $[\alpha'_1(+k_M) + \alpha'_1(-k_M)]$ over 10.000.000 time units. Other parameters as in Fig.4.10.
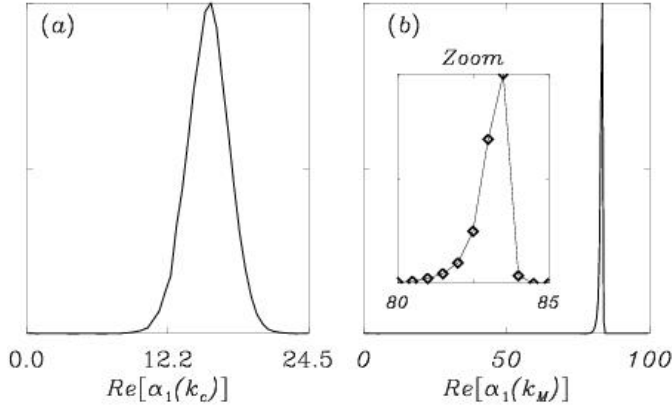
Figure 4.12: $W(Re(\alpha_1(k)), 0)$, for positive values of $Re[\alpha_1(k)]$, for (a): $k = k_c$, (b): $k = k_M$, obtained from a trajectory during 10.000.000 time units. Other parameters as in Fig.4.10. These figures are symmetric around 0.

the two points of maximum curvature of the elliptical ring.

The main characteristics of the trajectories in phase space are reflected in the associated Wigner distributions. For the less intense modes contributing to the dynamics we can approximate the associated Wigner function $W(\alpha_1(k))$ by a Gaussian, displaced from and orbiting about the origin in phase space. In Fig.4.12(a) we show a cut along the real direction of the Wigner distribution for the critical mode ($W(Re[\alpha_1(k_c)], 0)$). By contrast, the most intense mode (with wave-number k_M) displays some interesting new features. Fig.4.12(b) shows an asymmetry in the distribution of fluctuations around the mean amplitude in each of the peaks, with a sharp decay of the distribution at some maximum amplitude. These facts indicate the existence of nonlinear properties associated with the quantum fluctuations in the absolutely unstable regime. These features would necessarily be absent in any analysis based on a linearization about a deterministic macroscopic state.

4.3.2 Non-classical properties in the convective regime

The convective regime is characterized by amplified fluctuations and macroscopic noisy patterns. It is interesting to ask, therefore, if any of the low-noise quantum features found below threshold can survive in this noisy environment. Quantum effects in the OPO have been observed as sub-shot noise fluctuations both in the field quadratures and intensity differences associated with the down-converted light [Wu & al., Reynaud, Heidmann]. Examples of the noisy features associated with the real part of the signal field in this regime are plotted in Fig.4.13 for three different values of the driving field, all within the convective regime. Note the different scales on the vertical axes in these figures.

It is helpful, in looking for non-classical effects, to keep in mind the manner in which such effects appear below threshold. We will also restrict ourselves to the study of quantum correlations in the far field. Conditions for squeezing and associated non-classical effects are usually expressed in terms of normally ordered moments of operators (indicated by : :). These can be obtained from the symmetrically ordered moments (indicated by $S()$), that are associated with the Wigner function, by use of the
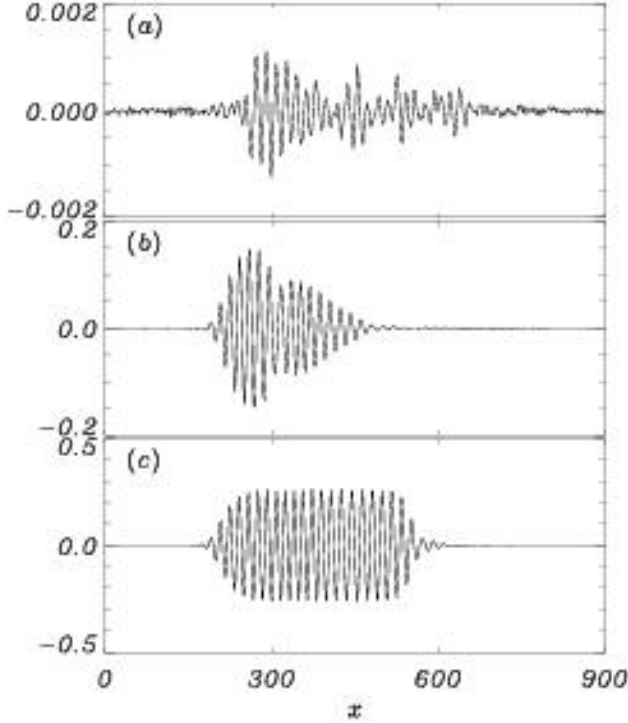
Figure 4.13: Snapshots of the real part signal $Re(\alpha_1(x))$ for different pump values:(a) $F = 1.001$, (b) $F = 1.01$, (c) $F = 1.025$. Other parameters are: $dx = 1.7678$, 512 grid points, $a_0 = 1$, $\Delta_0 = 0$, $\Delta_1 = -0.25$, $v = 0.42$. Note the different vertical scales in the figures.

commutation relations (4.17):

$$\langle : \hat{A}(k,t)\hat{A}(k',t) : \rangle = \langle S(\hat{A}(k,t)\hat{A}(k',t)) \rangle$$

$$\langle : \hat{A}(k,t)\hat{A}^\dagger(k',t) : \rangle = \langle S(\hat{A}(k,t)\hat{A}^\dagger(k',t)) \rangle - \frac{1}{2}\delta(k-k')$$

The δ function appearing in the second of these equations is a signature of the shot or vacuum noise. Our approximation scheme is based in the Wigner representation and gives results for correlations of symmetrically ordered operators for the intracavity fields. In order to obtain results for the corresponding normally ordered products and to test for the presence of non-classical effects, we need to establish a reference shot noise level. This level can be obtained for each quadrature correlation from the variance of the *linear* stochastic process associated with the empty cavity:

$$\partial_t s(x,t) = -\left[(1 + i\Delta_1) - 2i\nabla^2\right] s(x,t) + \frac{1}{a^{1/4}}\frac{g}{\gamma}\xi_1(x,t).$$

Here we have omitted the walk-off term as it does not affect the shot noise level. Squeezing in our simulations will be associated with a quadrature probability distribution that is narrower than the Gaussian associated with this linear process. In general we can consider a different quadrature for each wave-number k. It is useful to define a pair of (superposition mode) quadratures for each k parameterized by the angle θ. For the critical wave-number these take the form

$$\hat{X}_\pm(\theta) = \frac{1}{2}\left[\hat{A}_1(k_c,t) \pm \hat{A}_1(-k_c,t)\right]e^{i\theta} + h.c.. \tag{4.41}$$

We expect, in general, that the most strongly squeezed quadrature should depend on the value of θ [Jeffers & Oppo].
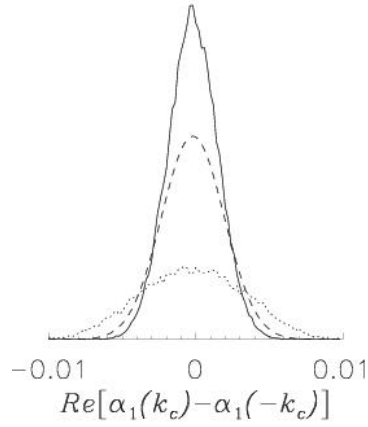
Figure 4.14: $W(Re(\alpha_1(k_c, t) - \alpha_1(-k_c, t)), 0)$. Continuous line is obtained for $F = 1.001$, and dotted line for $F = 1.01$. The dashed line represents the distribution for the vacuum state, corresponding to the shot noise level. The distributions are relative to trajectories of 2.000.000 time units. Other parameters as in Fig.4.13.

We begin our investigation of the convective regime at a point that is just above threshold with $F = 1.001$ (Fig.4.13(a)). Fluctuations associated with the pattern are in this case still relatively small and we find that the Wigner distribution has a Gaussian shape as shown in Fig.4.14. We find that there is quadrature squeezing, with the squeezed quadrature $\hat{X}_-(0)$ exhibiting the same level of squeezing as is found just below threshold. In particular, for $F = F_{thr} \pm 0.001$ we find that the intracavity field is squeezed by 50% below the shot noise limit for a flat pump and by 37% for a supergaussian pump. This indicates a smooth variation across threshold for the squeezed quadrature variance. For excited modes, other than the critical one, we also find squeezing below the shot noise level for the appropriate quadrature. It is also possible to evaluate the squeezing *outside* the cavity. The output field arises from the interference of the intracavity field transmitted and the input field reflected by the cavity input/output mirror [Collett & Gardiner]. In the previous Chapter we have shown that the evaluation of the dynamics of the output field requires the simulation of coupled stochastic processes [Zambrini & al. (00)].

Increasing the value of the pump, so as to move further into the convective regime, leads to a rapid increase in the magnitude of the signal field. Indeed, for ($F = 1.01$) we observe, in Fig.4.13(b) that the signal field has grown by two orders of magnitude. Fluctuations are still extremely phase sensitive and, as depicted in Fig.4.6(a) there is a strong reduction in the fluctuations for some quadratures. This reduction is insufficient, however, to reach below the shot noise level and there is no squeezing. In fact, we find residual fluctuations $+27\%$ *above* the shot noise level. This is comparable with the value associated with the coherent states. These enhanced fluctuations are associated with a much broader Wigner distribution as shown in Fig.4.14. It is remarkable, however, that this enhanced but still small level of fluctuation can coexist with the macroscopic fluctuations in orthogonal quadrature. If we move still further above threshold then we find, for $F = 1.025$ (Fig.4.13(c)), a variance which is 159 times the shot noise level and both quadratures display fluctuations that are well above the level usually associated with quantum effects. We note that for the parameter values used here, the threshold of absolute instability for an infinite system occurs at $F \sim 1.035$.

Figure 4.15: Variance of $(\hat{X}_-(\theta))$ at $F = 1.025$ for the critical wavenumber $k = k_c$. The minimum occurs for $\theta < 0$.
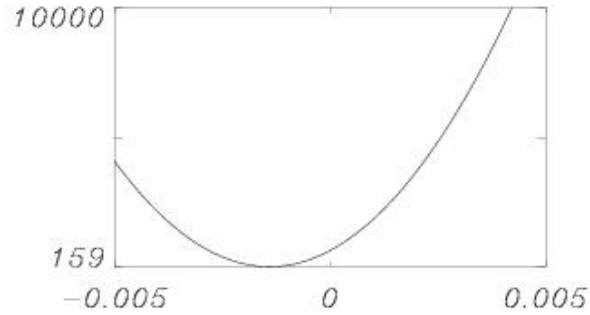
A further indication of the nonlinear nature of the fluctuations in the convective regime is given by the fact that the angle θ, for which there is the greatest reduction in the fluctuations, changes with the strength of the pump value. This has already been discussed in connection with Fig.4.6(a). In particular, for the critical wave-number, $\hat{X}_-(\theta)$ shows strongest squeezing for $\theta = 0$ in the linear regime below threshold. In the convective regime, however, the greatest reduction in the quadrature fluctuations occurs for a value of $\theta < 0$. This is shown in Fig.4.15 in which we plot the variance $\text{Var}(\hat{X}_-(\theta))$ in normal ordering and normalized to the shot noise level, for $F = 1.025$.

The OPO can also exhibit strong correlations between the far field intensities associated with opposite wave-numbers. We have calculated the fluctuations in the intensity difference for opposite wave-numbers associated with the normally ordered moment

$$\langle : \left(\hat{A_1}^\dagger(k)\hat{A}_1(k) - \hat{A_1}^\dagger(-k)\hat{A}_1(-k) \right)^2 : \rangle. \tag{4.42}$$

A negative value for this quantity indicates a non-classical effect sometimes referred to as twin beams or intensity-difference squeezing [Zambrini & San Miguel]. As in our discussion of quadrature squeezing, we find that this quantity is only negative very near to threshold ($F = 1.001$). Further into the convective regime we find that the macroscopic noise associated with the formation of a pattern increases the noise in the intensity difference. For $F = 1.01$ we find that the intensity-difference squeezing has been replaced by fluctuations in excess of the shot noise level.

In summary, we have shown that quantum effects can survive above threshold in the convective regime but only very near to threshold. On increasing the pump and entering further into the convective regime, we find that nonlinear effects associated with the fluctuations tend to distribute part of the macroscopic fluctuations into the observables that are squeezed nearer to threshold. This identifies walk-off as an effective mechanism of quantum decoherence in which the macroscopic nonlinear fluctuations present in the convective regime overwhelm quantum effects associated with noise reduction.

4.4   Symmetry breaking effects in OPO with walk-off

In the previous Section we have considered the OPO with a super-Gaussian transverse profile of the pump. The finite pump profile with transverse walk-off allows for the convectively unstable regime. In this Section we focus on the consequences of walk-off in the absolute regime where the **pattern is**

dynamically sustained. To this end, and for pedagogical reasons, we consider mainly an infinitely extended system in the transverse direction, obtained with a constant **plane wave pump**

$$E_0(\vec{x}) = E_0 \tag{4.43}$$

so that no convective regime exists. As discussed in Sect.4.1.2, a stable pattern appears in this situation above the threshold of signal generation. The walk-off term breaks the important **reflection** symmetry. In the following we investigate the effects of this symmetry breaking in the quantum correlations of the far field components. For completeness, at the end of this section, we generalize our numerical results considering a spatial dependent wide pump.

In Ch.1 we discussed the relation between nonlinear wave-mixing processes and non-classical states of light, in the context of twin and multi-photon processes. We mentioned that the down converted field (considering only the longitudinal modes) of the non-degenerate optical parametric oscillator (NDOPO) consists of two intense laser-like *twin beams*, distinguished by their polarization or frequency [Reynaud, Reynaud & al. (87)]. The inclusion of the transverse modes gives rise to a more complex scenario: in the simplest theoretical description, a stripe pattern emerges, caused by the interference of two *spatially* tilted signal beams with transverse wavevectors $\pm \vec{k}_c$. Within a three-mode approximation, these two beams have equal photon numbers and are entangled, i.e. their intensity difference is sub-Poissonian [Graham, Lugiato & Castelli, Grynberg & Lugiato]. The prediction of entanglement is linked to considerations of transverse momentum conservation.

In this Section we consider the question of entanglement between the two macroscopic tilted signal beams in the intense pattern that emerges above threshold, when *multi-photon interactions* are present (see Sect.1.4.1.b). In this regime two important aspects have to be taken into account. First, nonlinearity causes the emergence of **harmonics of the transverse mode k_c selected at threshold**, so that a three-mode approximation is no longer valid. Second, walk-off breaks the symmetry between the spatial beams and destroys the equivalence between the beams of wavevectors $\pm \vec{k}_c$.

Let us consider the **total transverse momentum**

$$\hat{\vec{P}} = \int \vec{k}(\hat{N}_0(\vec{k}) + \hat{N}_1(\vec{k}))d\vec{k} \tag{4.44}$$

where $\hat{N}_0$ and $\hat{N}_1$ are photon number operators for the pump and signal fields. The DOPO is described by the Hamiltonian (4.22) with pump Eq.(4.43). The invariance under continuous translations in the transverse plane, implies that the total transverse momentum $\hat{\vec{P}}$ is conserved in the Hamiltonian evolution

$$[\hat{H}, \hat{\vec{P}}] = 0 \tag{4.45}$$

and, in the presence of cavity losses, it has a zero steady state average

$$\langle \hat{\vec{P}} \rangle = 0. \tag{4.46}$$

The momentum conservation, which is at the root of entanglement properties of the spatial beams [Lugiato & Castelli, Grynberg & Lugiato] at threshold, is independent of the walk-off term. In addition,

this term appears only in the free Hamiltonian, and does not seem to affect the creation processes of twin photons governed by $\hat{H}_{int}$.

In order to clarify the role of walk-off in the photon number properties of different spatial modes, we consider in the following Sections different approximations which disclose when the combination of walk-off and nonlinearity becomes crucial.

4.4.1 Quadratic Hamiltonian model

Common approximations to study $\chi^{(2)}$ processes use quadratic Hamiltonians [Castelli & Lugiato, Gatti & al. (97)1, Zambrini & al. (00)]. We have seen that this is, in particular, a suitable approximation to study the DOPO below threshold ($E_0 < \sqrt{(1 + \Delta_0)}$). Neglecting pump depletion leads to the interaction PDC Hamiltonian

$$\hat{H}_{int}^L = i\frac{g}{2}A_0 \int d^2\vec{k} \left[\hat{A}_1^\dagger(\vec{k})\hat{A}_1^\dagger(-\vec{k}) - h.c. \right] \tag{4.47}$$

where A_0 is the homogeneous constant classical pump. The total transverse momentum in this approximation reduces to $\hat{\vec{P}}^L = \int \vec{k}\hat{N}_1(\vec{k})d\vec{k}$, and considering the total quadratic Hamiltonian $\hat{H}^L = \hat{H}_0^L + \hat{H}_{int}^L$ we have that

$$[\hat{H}^L, \hat{\vec{P}}^L] = 0. \tag{4.48}$$

In particular, the intensity difference between any two modes with opposite transverse wavevector, $\hat{N}_D = \hat{N}_1(\vec{k}) - \hat{N}_1(-\vec{k})$, commutes with $\hat{H}^L$. Therefore the properties of the intensity difference of twin beams below threshold are not modified by the consideration walk-off. This conclusion is consistent with the fact that in the undepleted pump approximation the walk-off term can be removed from the dynamical equations by a change of reference frame, since the signal field is not coupled to any other dynamical variable.

4.4.2 Three modes model

The assumption of undepleted pump is not appropriate above threshold. As mentioned in Sect.1.4.1.a suitable nonlinear approximation immediately at the threshold of signal generation takes into account the dominant role of the *three modes* with operators $\hat{a}_{0,\vec{0}}$ and $\hat{a}_{1,\pm\vec{k}_c}$, where $\vec{k}_c$ is given in Eq.(4.11). The fundamental interaction (Fig.4.16a) is the destruction of a photon of the homogeneous pump mode ($\vec{k}_\perp = 0$) and the creation of two tilted signal twin photons with transverse wavevector $\pm\vec{k}_c$, described by the *3-mode* Hamiltonian

$$\hat{H}_{int}^{(3)} = ig \left[\hat{a}_{0,\vec{0}}\hat{a}_{1,\vec{k}_c}^\dagger \hat{a}_{1,-\vec{k}_c}^\dagger - h.c. \right].. \tag{4.49}$$

where the operators $\hat{a}_{i,\vec{k}}$ ($i = 0, 1$) correspond to a discrete set of wave-vectors and differ from $\hat{A}_i(\vec{k})$ in normalization factors. In this approximation and in a given spontaneously selected direction for the pattern, the total momentum is

$$\hat{P}^{(3)} = k_c(\hat{a}^\dagger_{1,+\vec{k}_c}\hat{a}_{1,+\vec{k}_c} - \hat{a}^\dagger_{1,-\vec{k}_c}\hat{a}_{1,-\vec{k}_c}) = k_c\hat{N}_D. \tag{4.50}$$
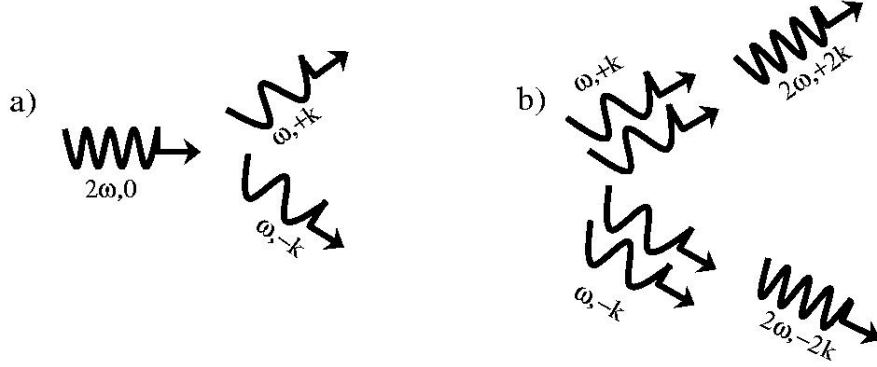
Figure 4.16: a) 3-mode interaction described by $\hat{H}_{int}^{(3)}$ Eq. (4.49). b) Secondary processes: 2 subharmonic photons with the same transverse wavevector generate a photon with double frequency and wave-vector.

Momentum conservation $[\hat{H}^{(3)}, \hat{P}^{(3)}] = 0$ implies that, independently of walk-off, the twin beams have the same mean intensity and they are entangled [Graham, Lugiato & Castelli]. Still, an effect of walk-off can be seen in the mean value of the Heisenberg equation

$$\partial_t \langle \hat{a}_{1,\vec{k}_c} \rangle = \gamma(-1 + ivk_c)\langle \hat{a}_{1,\vec{k}_c} \rangle + g\langle \hat{a}_{0,\vec{0}}\hat{a}_{1,-\vec{k}_c}^{\dagger} \rangle. \tag{4.51}$$

The walk-off term ivk_c breaks the *reflection* symmetry (between $\vec{k}_c$ and $-\vec{k}_c$) resulting in a different phase evolution for $\langle \hat{a}_{1,+\vec{k}_c} \rangle$ and $\langle \hat{a}_{1,-\vec{k}_c} \rangle$.

4.4.3   Five modes model

This *3-mode* model gives only a good description of the DOPO extremely close to threshold. Numerics indicate that increasing the pump intensity just one per cent above threshold there is significant feedback of the signal on the pump, and spatial harmonics come into play (multimode interaction). A nonlinear perturbative analysis of the process of pattern formation [Oppo & al. (94), Ward & al. (00)] shows that, at first order in the distance to threshold, the *3-mode* model is appropriate, but in second order also pump modes with transverse wavevector $\pm 2\vec{k}_c$ are excited. A natural next approximation is then to take into account *five modes* in the interaction process: $\hat{a}_{0,\vec{0}}$, $\hat{a}_{0,\pm 2\vec{k}_c}$, $\hat{a}_{1,\pm\vec{k}_c}$. The *5-mode* interaction Hamiltonian describes also the secondary processes of Fig.4.16b, namely the combination of two tilted signal photons giving a pump photon with double wave-vector:
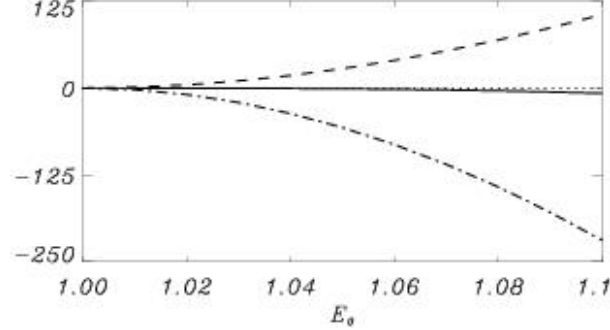
$$\hat{H}_{int}^{(5)} = \hat{H}_{int}^{(3)} + i\frac{g}{2}[\hat{a}_{0,2\vec{k}_c}\hat{a}_{1,\vec{k}_c}^{\dagger 2} + \hat{a}_{0,-2\vec{k}_c}\hat{a}_{1,-\vec{k}_c}^{\dagger 2} - h.c.]. \tag{4.52}$$

The conserved transverse momentum is

$$\hat{P}^{(5)} = k_c(\hat{N}_{1,\vec{k}_c} - \hat{N}_{1,-\vec{k}_c}) + 2k_c(\hat{N}_{0,2\vec{k}_c} - \hat{N}_{0,-2\vec{k}_c}) \tag{4.53}$$

The conservation law $[\hat{H}^{(5)}, \hat{P}^{(5)}] = 0$ only imposes the restriction that the intensity difference $\hat{N}_D$ in the two signal beams is minus twice the intensity difference of the two pump tilted beams. But $\hat{N}_D$ is

Figure 4.17: $N_1(k_c) - N_1(-k_c)$ (dash-dotted line), $N_0(2k_c) - N_0(-2k_c)$ (dashed line), and $P^{(5)}/k_c$ (continuous line) shown as a function of the pump E_0. Parameters: $v = 0.42$, system size $L = 512 \cdot \Delta x = 10\frac{2\pi}{k_c}$, $\Delta_0 = 0$, $\Delta_1 = -0.25$. Pump threshold value: $E_0^{thr} = 1$. The dotted line is the zero value of $N_1(k_c) - N_1(-k_c)$ for $v = 0$.

no longer a constant of motion and the commutator

$$[\hat{H}^{(5)}, \hat{N}_D] = ig[-\hat{a}_{0,2\vec{k}_c}\hat{a}^{\dagger 2}_{1,\vec{k}_c} + \hat{a}_{0,-2\vec{k}_c}\hat{a}^{\dagger 2}_{1,-\vec{k}_c} - h.c.] \tag{4.54}$$

is not fixed to take a zero value. Therefore, when a multimode nonlinear interaction is at work, the properties of the spatial beams $\hat{N}_1(\pm\vec{k}_c)$ might change: The photon number of a signal beam $\vec{k}_c$ might be larger than the photon number of the beam $-\vec{k}_c$, the difference compensating the difference in the photon number of the two pump tilted beams. This should not occur when there is no walk-off, because of symmetry considerations. However walk-off implies the breakdown of reflection symmetry, which suggests having $\langle\hat{N}_D\rangle \neq 0$ as a natural possibility. In fact, note that $[\hat{H}^{(5)}, \hat{N}_D]$ is phase sensitive and therefore dynamically modified by symmetry breaking caused by walk-off (see Eq. 4.51).

4.4.4 Numerical analysis

In order to substantiate the above ideas we investigate numerically a continuous nonlinear model without constraint in the number of coupled modes. We first consider the nonlinear *classical* equations of the DOPO, given by Eqs. (4.40) neglecting the noise source. When $v = 0$ a stationary pattern appears and in the far field $N_1(k_c) = N_1(-k_c)$, even if - as shown above - this does not follow from a conservation law when there is a multimode interaction. On the other hand, when walk-off is taken into account ($v \neq 0$), broken symmetry leads to a tilted signal beam more intense than the signal beam of opposite transverse wavevector, in an amount that compensates the difference between the two tilted pump beams: In Fig. (4.17) we show that $N_1(k_c) - N_1(-k_c) = 2(N_0(-2k_c) + N_0(2k_c))$, so that the conservation law $P^{(5)} = 0$ is fulfilled. However, this is only strictly true close enough to threshold, where the *5-mode* approximation is valid. Already for the pump values shown in Fig.4.17 we observe that $P^{(5)} \neq 0$. This indicates that a larger number of transverse modes are being excited and contribute to the conserved total transverse momentum P. A microscopic interpretation of our findings in Fig. (4.17) is as follows: At threshold there is a primary process of annihilation of a pump photon creating two tilted signal photons (*3-mode model*), generating two beams such that $\langle\hat{N}_1(+k_c)\rangle = \langle\hat{N}_1(-k_c)\rangle$. The secondary processes of Fig. (4.16b) can happen with a different rate depending on the walk-off direction. Then, multimode interaction combined with broken reflection symmetry leads to a stronger depletion of one of the two signal beams.

A natural question is then if quantum correlations are partially destroyed by the asymmetric deple-tion of the signal beams at k_c, as it happens in NDOPO (neglecting spatial dependence) when signal and idler have different losses [Lane & al., Lugiato & Grynberg]. To describe the quantum fields, we consider the **time dependent parametric approximation** presented in Sect4.2.2 and the 1D Langevin equations 4.40. Hence stochastic averages associated with α_1 give the symmetrically ordered aver-ages of corresponding operators in the signal field, driven by the "classical" pump field $\mathcal{A}_0$. This time approximation is interesting in this context because captures three fundamental features: first the non-linearity of the system, $i.e.$ the depletion of the pump (term α_1^2); second the dynamical coupling between pump and signal, which in particular does not allow the elimination of the relative walk-off term chang-ing the reference system; and third, the spatial multimode interaction allowing for the manifestation of symmetry breaking in the beam intensities.

To characterize the correlations of the signal beams at k_c we calculate from Eq. (4.40) the normal ordered variance normalized to the shot noise ($\mathcal{N}_N(k)$) value

$$\mathcal{V} = \frac{\langle : [\hat{N}_1(k_c) - \hat{N}_1(-k_c)]^2 : \rangle - \langle \hat{N}_1(k_c) - \hat{N}_1(-k_c) \rangle^2}{\mathcal{N}_N(k)}. \tag{4.55}$$

Negative values of $\mathcal{V}$ indicate a non-classical sub-Poissonian statistics for the intensity difference of the two signal beams at $\pm k_c$. Being $\mathcal{V}$ a normal ordered quantity, it is proportional to the output variance [Collett & Gardiner], indicating possible non-classical signatures in the output fields correlations. Out-side the cavity the quantity showing stronger quantum signatures is the spectral variance $V(\omega)$ (Eq. (19) in [Marzoli & al.]). The macroscopic entanglement, or total noise suppression, is reached at $\omega = 0$. The integral over all frequency of $V(\omega)$ corresponds to the equal times variance, proportional to the intracavity quantity $\mathcal{V}$ (Eq. 4.55) calculated here.

For the DOPO below threshold we find that the two opposite beams have the same variances (above the level of coherent states) and $\mathcal{V} = -0.5$ for $v = 0$ and $v \neq 0$. This is in agreement with analytical calculations for a continuous linear model which give -independently of the walk-off- a re-duction of 50% in the fluctuations of the intensity difference with respect to the level of the coherent states inside the cavity [Gatti & al. (97)1]. Also at threshold -where linearization fails due to undamped critical fluctuations but a *3-mode model* is suitable-, we obtain the same results, in agreement with Ref.[Graham]. Above threshold, and if $v = 0$, we still obtain $\langle \hat{N}_D \rangle = 0$ and sub-Poissonian statistics with $\mathcal{V} = -0.5$. As discussed previously, given the multimode interaction, this result does not follow from momentum conservation alone. In fact it is associated with the presence of a macroscopic spatial structure that dictates the spatial structure, symmetry properties and correlations of the fluctuations [Zambrini & al. (02)].

Considering the effect of walk-off above threshold ($v \neq 0$) we find that the variances of the two beams become different, the most intense beam fluctuating more strongly. We obtain

$$\langle \delta N_1(-k_c)^2 \rangle / \langle \delta N_1(k_c)^2 \rangle \simeq 1.005, 1.01, 1.02, 1.03, 1.04 \tag{4.56}$$

for pump values respectively $E_0/E_0^{thr} = 1.01, 1.03, 1.05, 1.07, 1.1$, where we have taken $L = 30\frac{2\pi}{k_c}$ and other parameters as in Fig.4.17.

However the correlation between these two non-equivalent beams is strong and macroscopic entanglement is preserved. In fact, within our accuracy, we get always the same value $\mathcal{V} \simeq -0.5$ obtained for $v = 0$. We finally point out that the different noise levels of the two beams, as caused by walk-off, is a general phenomenon that might explain experimental observations in other systems [Sharping & al.].

Our discussion so far has considered the ideal situation of a plane wave pump, but we have checked that our results are meaningful for a more physical spatial dependent wide pump profile. In this case the tilted beams have to be detected in a broad area of the size of the far field peaks [Marzoli & al.]. We have performed numerical simulations in the absolute regime of a DOPO with a broad pump

$$E_0(x) = E_{top} E_0^{thr} e^{-\frac{1}{2}(\frac{x}{317})^{10}} \tag{4.57}$$

and $E_{top} = 1.1$, taking $L = 51\frac{2\pi}{k_c}$ and other parameters as in Fig.4.17. In this situation we obtain $\mathcal{V} = 3$ for $k = k_c$ if $\Delta k = 2\pi/L$; increasing the integration area around k_c we find that $\mathcal{V} = -0.35$ for $3\Delta k$, $\mathcal{V} = -0.40$ for $5\Delta k$, $\mathcal{V} = -0.49$ for $7\Delta k$. In the convective regime ($E_{top} = 1.025$) at $k = k_c$ we obtain $\mathcal{V} \simeq 10^2$, and integrating over a broad area of $30\Delta k$ the variance decreases an order of magnitude, remaining always classical. In this regime the macroscopic entanglement is destroyed [Zambrini & al. (02)].

In conclusion, we predict quantum entanglement between the spatially tilted macroscopic signal beams of a DOPO above threshold when nonlinear multimode interaction is effective. Walk-off breaks the symmetry between the two beams, the more intense becoming more noisy, but quantum entanglement is preserved.

4.5   Quantum correlations for vanishing walk-off

In this Section we study the non-classical correlations that are present from below to above-threshold in the DOPO when the walk-off vanishes. The results shown on the following are obtained with the Langevin equations for the Q representation introduced in Sect.4.2.3. The choice of these equations is due to their *wide domain* of validity above threshold, allowing for the description of quantum fluctuations far from the threshold, where complex spatial structures appear. In Sect. 4.1.2 we briefly reviewed the relevant classical results concerning the instabilities to pattern formation and to homogeneous solutions well above threshold, when walk-off vanishes. Our aim is to study the quantum properties of the correlations in regimes that have not been previously studied. In order to check the results that follow from the nonlinear Langevin equations (4.35-4.35) we first present calculations of quantum correlations below threshold and at the critical point, comparing them with analytical results in the linear approximation (Sect.4.5.1). In In Sect. 4.5.2 we consider the regime above threshold, where complex patterns arise. We investigate the possibility of entanglement of tilted beams (twin-beams-like correlation) in the multimode process, behind stripe pattern formation involving higher order spatial harmonics (Sect. 4.5.2.a). We also investigate the possibility of entanglement in spatially disordered structures (Sect.4.5.2.b).

In the next sections show results obtained by numerical integration of Eq. (4.35) and Eq. (4.36) with the same integration method of Ref.[Zambrini & al. (00), Bache & al.]. In particular we consider
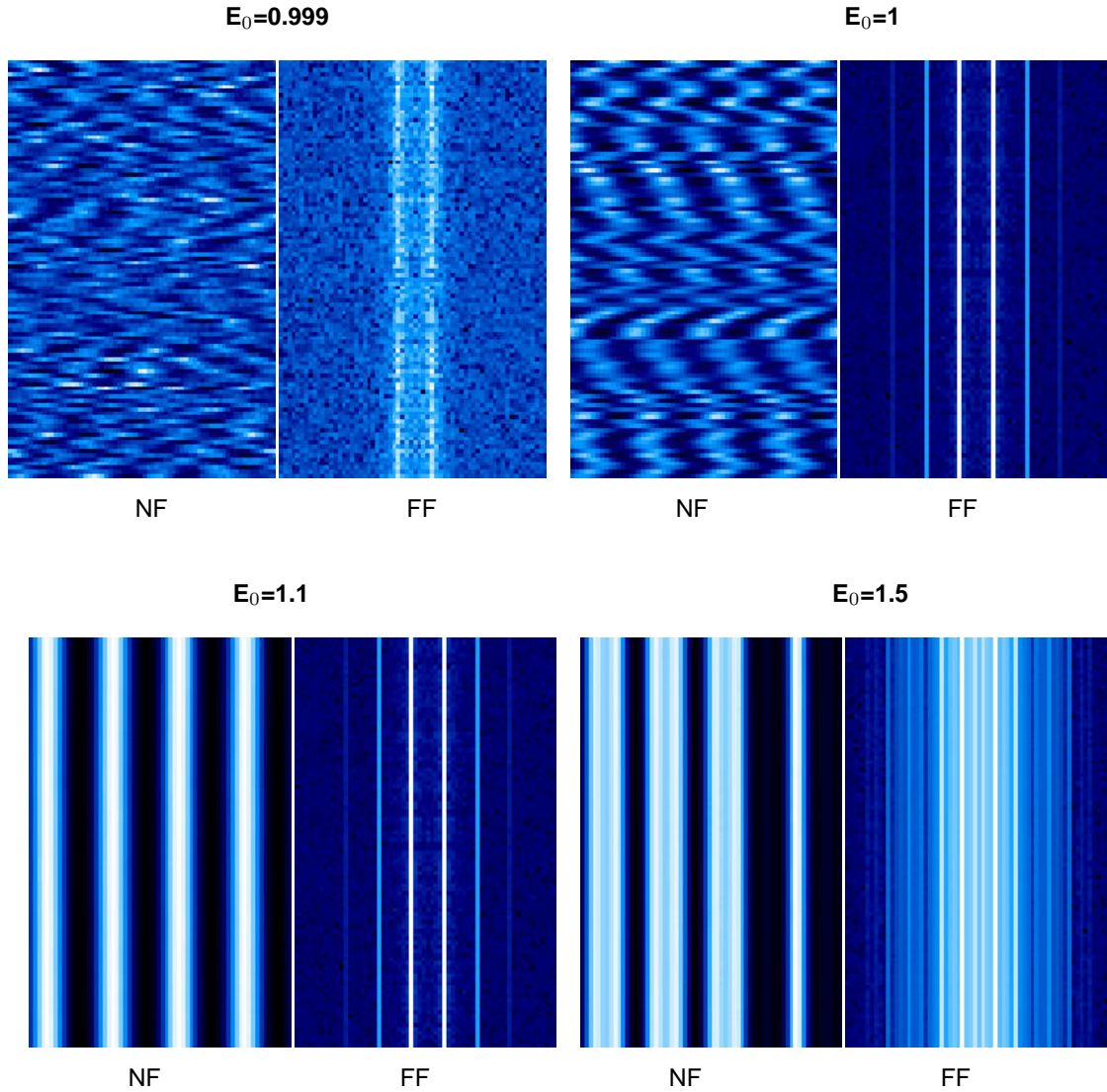
E$_0$=0.999

E$_0$=1

E$_0$=1.1

E$_0$=1.5

Figure 4.18: Spatio-temporal evolution of the real part of the near field (NF) and of the intensity of the far field (FF) (in log scale), for different values of the pump $E_0 = 0.999, 1, 1.1, 1.5$. The FF intensity is defined as $|\alpha_i(k)|^2$, where $\alpha_i(k)$ is the Fourier transform of the near field $\alpha_i(x)$. The horizontal coordinate is the transversal position (x in NF and k in FF) describes by 64 points, and the vertical one is the time interval 10^7 (in γ units), using a discretization time step of $\Delta t = 0.01$. The initial condition for the signal is $\alpha_1(x, 0) = 10^{-5}(\epsilon(x) + 10\sin(k_c x))$ with $\epsilon(x)$ Gaussian random numbers of variance one.

one transversal dimension ($D = 1$) and parameters:

$$\Delta_0 = 0, \quad \Delta_1 = -0.18, \quad \frac{g}{\sqrt{a}\gamma} = 10^{-4} \quad\quad\quad (4.58)$$

with a system size of four critical wavelengths $L = 4\lambda_c$, with $\lambda_c = \frac{2\pi}{k_c}$ (see Sect. 4.1.2).

4.5.1 Quantum correlations below and at threshold

The spatio-temporal dynamics of the signal field is shown in Fig.4.18 for two relevant values of the pump, below but near to threshold (quantum images regime), $E_0 = 0.999$ and at threshold ($E_0 = 1$). The far field (FF) shows strong fluctuations dominated by the critical wave-vector: in Sects. (4.5.1.a-4.5.1.b) we discuss the quadratures and intensity quantum correlations of these modes.

4.5.1.a Quadrature correlations

The direction in which quadrature squeezing appears is determined by the eigenfunction $V_\pm(k, -k)$ given in Eq.(4.12) [Zambrini & al. (02)]. The solution $V_+(k, -k)$ gives the direction of amplification of fluctuations, while fluctuations are damped for $V_-(k, -k)$, giving rise to quadrature squeezing. In particular, for the critical wave-vector k_c and for our choice of parameter (real A_0^{st}) we obtain $V_\pm(k_c, -k_c) = \delta A_1(k_c) \pm \delta A_1^*(-k_c)$. Therefore, the largest squeezing at threshold will be in the difference of real parts and the sum of imaginary parts of the field for wave-numbers k_c and $-k_c$.

We define the real quadrature operator:

$$\hat{X}(k) = \hat{A}_1(k) + \hat{A}_1^\dagger(k) \tag{4.59}$$

and the quadrature superpositions

$$\hat{X}_-(k) = \hat{X}(k) - \hat{X}(-k) \tag{4.60}$$

$$\hat{X}_+(k) = \hat{X}(k) + \hat{X}(-k), \tag{4.61}$$

corresponding, respectively, to damped and undamped quantities at threshold.

Below threshold, within a linearization approximation [Gatti & al. (97)1], the normal-ordered variances normalized to the shot noise ($\mathcal{N}_X$) [Zambrini & al. (02)] are:

$$\frac{<: (\hat{X}_-(k_c))^2 :>}{\mathcal{N}_X} = \frac{-E_0}{1 + E_0} \tag{4.62}$$

$$\frac{<: (\hat{X}_+(k_c))^2 :>}{\mathcal{N}_X} = \frac{E_0}{1 - E_0}. \tag{4.63}$$

These quantities coincide with the variances since the mean values are zero: $< \hat{X}_\pm(k) >= 0$. The normal ordering allows us to immediately identify non-classical features associated with squeezing such as negative variances. Eq. (4.62) shows an increasing degree of squeezing, approaching the value -0.5 at threshold. In Fig.4.19 theoretical predictions and numerical results are shown to be in good agreement, confirming the validity of Eqs. (4.35-4.36) below threshold. On the other hand Eq. (4.63) is always positive indicating that the the fluctuations in the direction of instability are essentially classical and larger than those found for a coherent state. In Fig.4.20 we show the agreement between theoretical predictions and numerical results for the undamped quadrature, even as close as 1 ‰to threshold. The limits of the linear treatment, discussed above, are now evident in the divergence of Eq. (4.63) for $E_0 \to 1$. In contrast, numerical simulation of the nonlinear Eqs. (4.35-4.36) gives the expected saturation at the critical point, at a value which depends on the noise level.
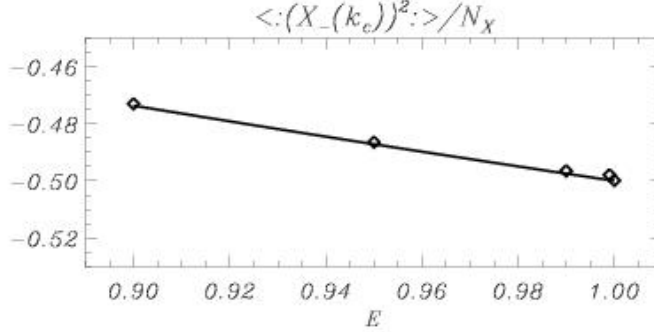
Figure 4.19: Normal ordered variance of the damped quadrature $\hat{X}_-(k_c)$ normalized to shot noise: diamonds are results obtained by numerical simulation, while the continuous line corresponds to the analytical expression Eq. (4.62). For any trajectory at given pump intensity, we average during a time of 10^7, integrating with a time discretization of 10^{-3} (with time scaled as in Eq. (4.4)).

4.5.1.b Intensity correlations

We can find non-classical features in the intensities of the twin beams by evaluating the normal-ordered variance in the difference of the two intensities, introduced in the previous Section (Eq.(4.55)):

$$\mathcal{V}(k) = \frac{\langle : [\delta\hat{N}_1(k) - \delta\hat{N}_1(-k)]^2 : \rangle}{\mathcal{N}_N(k)}, \tag{4.64}$$

with shot noise value $\mathcal{N}_N(k)$ proportional to the sum of the intensities of the two beams with wavevectors $\pm k$. We remind that in a linear analytical treatment below threshold $\mathcal{V}(k) = -0.5$, independently of the pump intensity and of the wave-vector [Gatti & al. (97)1, Zambrini & San Miguel]. This is in contrast with the behavior of the quadratures correlations Eqs. (4.62-4.63), that are stronger for the critical wave vector or at the critical point. Nevertheless, the critical conditions are of significant interest because of presence of higher intensities.

The numerical expression of $\mathcal{V}(k)$ for different spatial modes ($0 < k \leq 5k_c$) is compared, in Fig.4.21, with the analytical value -0.5 for pump $E_0 = 0.99$, showing good agreement. Small deviations for large wavevectors k can appear numerically due to the smallness of the shot noise to which the variance is normalized; $\mathcal{N}_N$ is proportional to the mean intensity of the field, shown also in Fig.4.21.

In Fig.4.22 we plot the variance $\mathcal{V}(k_c)$ at the critical wave-vector as a function of the pump E_0: We obtain good agreement with analytical predictions below threshold.

Figure 4.20: Variance of the undamped quadrature $\hat{X}_+(k_c)$: the diamonds are results obtained with numerical simulation, while the continuous line corresponds to the analytical expression Eq. (4.63). At the last point, corresponding to $E_0 = 1$, the linear treatment gives an infinite variance (the asymptotic behavior is represented by a dashed line), while our nonlinear treatment gives the expected saturation.
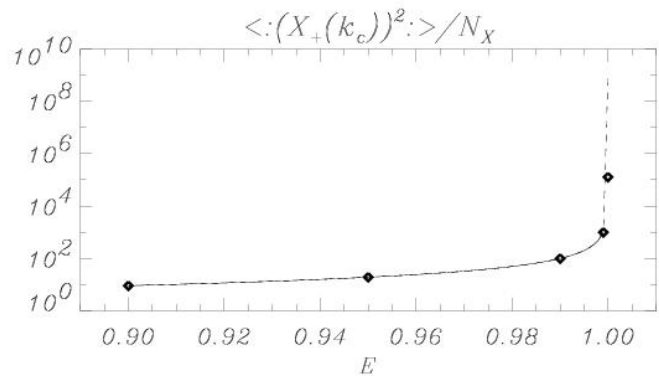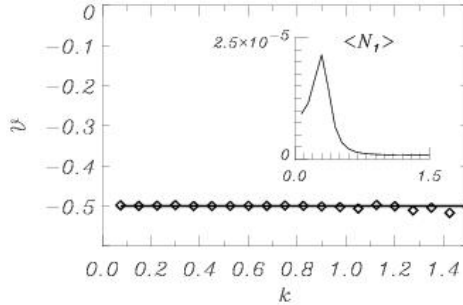
Figure 4.21: Analytical (continuous line) and numerical (diamonds) twin beams correlations $\mathcal{V}(k)$ (Eq. (4.55)) below threshold ($E_0 = 0.99$). The insert shows the mean intensity of the signal, with a maximum at $k_c = 0.3$.
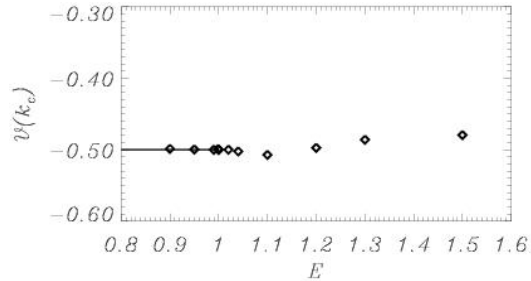
Figure 4.22: Variance $\mathcal{V}(k_c)$ at the critical wavevector ($k_c = 0.3$), increasing the pump intensity from below to above threshold ($E_c = 1$). The diamonds are numerical results and the continuous line is the analytical value obtained by linearizing below threshold.

4.5.2 Quantum correlations above threshold

The nonlinear equations in the Q representation are used here to study the regime of pattern formation above threshold. These equations improve the time dependent parametric approximation [Zambrini & al. (02)]: we have seen that the parametric approximation is well suited to study the convective regime (in presence of walk-off) or the instability point, because the pump fluctuations are disregarded with respect to the signal ones. On the other hand, Eqs.(4.35) and (4.36) are valid in a *wide region* above threshold, and give a complete description of the pump fluctuations.

Slightly above the threshold ($E_0 = 1.02$) the variance of the quadratures superposition Eq. (4.60) becomes classical. To understand how the mode dynamics changes when going above threshold, we recall that below threshold the trajectory $\alpha_1(k_c, t)$ occupies a circular region centered in zero, in the phase space given by its real and imaginary part. Above threshold the mean amplitude has a macroscopic value increasing with the pump intensity and the distribution of fluctuations in phase and intensity quadratures is rather different, as shown in Fig.4.23a. A trajectory for a mode during a larger time would describe a circle in phase space.

Figure 4.23: a) Trajectory in the phase space of $\alpha_1(k_c)$ during 10^7 scaled units for $E_0 = 1.02$. b) Phase sum $< \theta_+ + \theta_- >$ (in radians) increasing the pump intensity.
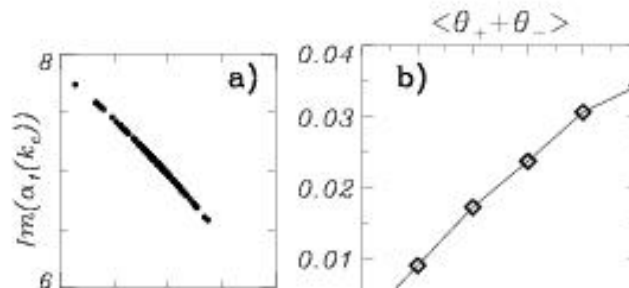
The origin of these large fluctuations in the phase quadrature is well known in the theory of single transverse-mode NDOPO [Reid & Drummond (88), Reid & Drummond (89)]. Due to the diffusion of the difference of the signal and idler phases, the above threshold solution is not stable, and "cannot be analyzed correctly by the assumption of small fluctuations and methods of linearization" [Reid & Drummond (88), Reid & Drummond (89)]. The situation is similar to that of the laser above threshold, for which a correct analysis is performed using intensity and phase variables and *not* linearizing in the diffusing (phase) variable. In Ref.[Kheruntsyan & Petrosyan] an exact steady-state Wigner function is calculated in the single transverse-mode NDOPO by adiabatically eliminating the pump. The phase diffusion in a mode is evident in the radial symmetry of this distribution.

The single transverse-mode NDOPO is equivalent to a three mode model, describing the extended DOPO near threshold [Castelli & Lugiato] through the relevant fields $\alpha_1(\pm k_c)$ and $\alpha_0(0)$. The stationary signal is

$$
\begin{aligned}
\alpha_1(x,t) &= \alpha_1(k_c)e^{ik_cx} + \alpha_1(-k_c)e^{-ik_cx} \\
&= 2|\alpha_1(k_c)|e^{i\frac{\theta_+ + \theta_-}{2}}\cos\left(k_cx + \frac{\theta_+ - \theta_-}{2}\right),
\end{aligned}
\tag{4.65}
$$

with $\alpha_1(\pm k_c) = |\alpha_1(\pm k_c)|e^{i\theta_\pm}$, and $|\alpha_1(k_c)| = |\alpha_1(-k_c)|$. We recognize the effect of the phases $\theta_\pm$ in the near field. The sum of these phases fixes the global phase of the signal, locked to the pump, while the arbitrary phase difference fixes the spatial position of the stripe pattern. In continuous systems, where all modes are taken into account, the diffusion of the phase difference can be interpreted as the action of the Goldstone mode [Zambrini & al. (00)], that is neutrally stable, giving a continuous translation of the pattern. This is particularly evident in Fig.4.18 at threshold ($E_0 = 1$).

In a linear treatment below threshold, the fluctuations of $\langle\theta_+ + \theta_-\rangle$ have zero average and are damped (with $\Delta_0 = 0$). Increasing the pump we always observe small fluctuations, but the average changes. Fig.4.23b shows that the mean value $\langle\theta_+ + \theta_-\rangle$ increases from its zero value with the distance above threshold. This is a nonlinear effect due to the feedback of the signal on the pump. Above threshold the average of the nonlinear term in the pump equation is not zero, so the pump is no longer real and this induces a phase rotation in the signal. Therefore it should be expected that the strongest quadrature squeezing will be eventually found for a local oscillator phase that depends on this phase rotation. Here, however, we will restrict our attention to the non-classical features associated with intensity correlations. In fact this corresponds to a measure of quadrature squeezing as they result from the interference of a local oscillator given by the mean signal field with the squeezed fluctuations of the same mode.

4.5.2.a   Intensity correlations in stripe patterns

The stripe pattern formed above threshold is due to the interference of signal beams with opposite critical wavevectors. Momentum conservation leads to the entanglement between these signal beams [Graham, Castelli & Lugiato, Zambrini & San Miguel]. This gives non-classical intensity correlations characterized by $\mathcal{V} = -0.5$.
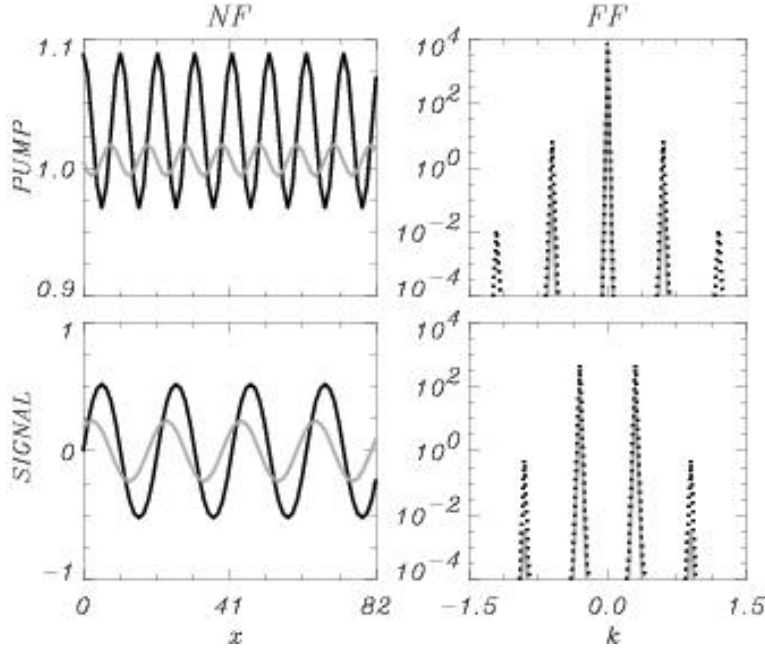
Figure 4.24: Snapshots of the real part of the near fields (NF) and intensity (log scale) of the far fields (FF) for both the pump and the signal. The grey plots are obtained for a pump value $E_0 = 1.02$ and the black ones (in continuous or dotted lines) for $E_0 = 1.1$.

Increasing the pump intensity we observe excitation of harmonics of the critical wavenumber (compare **far field (FF)** in Fig. 4.18 for $E_0 = 1$ and for $E_0 = 1.1$). In Fig. 4.24 we show the real part of the **near field (NF)** pattern in the pump and in the signal and the corresponding FF intensities for pumps $E_0 = 1.02$ and $E_0 = 1.1$. We observe that the odd harmonics are excited in the signal and the even ones in the pump mode, with an exponential decay of energy at higher wavevector modes. The presence of a multimode interaction means that the momentum conservation no longer constrains the intensities of the twin beams, as it does below and at threshold. However, as shown in Ref.[Zambrini & San Miguel], we do observe in this regime the symmetry

$$\langle N_1(k) \rangle = \langle N_1(-k) \rangle \tag{4.66}$$

in intensity averages and quantum correlations between the critical modes survive, as shown in Fig.4.22 for $1 < E_0 < 1.1$. The secondary process of up-conversion of pairs of signal photons $+k_c$ (or equivalently $-k_c$) to form pump photons $+2k_c$ ($-2k_c$) does not seem to destroy the quantum correlations between the signal "twin" photons ($+k_c$ and $-k_c$). In principle this process gives an incoherent depletion of the "twin" beams, but probably due to the smallness of this secondary effect, the quantum correlations associated with the fundamental process survives. Therefore this system shows twin-beams-like correlations in a multiphoton process, as in the case of SHG presented in Sect.1.4.1.b.

The spatial spectrum of the intensity variance $\mathcal{V}$ is plotted in Fig.4.25. We observe that at 2% above threshold the spectrum is similar to the spectrum below threshold (compare with Fig. 4.21). A reduction of the squeezing is observed (peak at $k = 3k_c = 0.9$ in Fig.4.25), however, corresponding to the appearance of the third harmonic. Increasing the pump to 10% above threshold we observe an enhancement of the spectral bandwidth in which this reduction of squeezing appears. The third harmonic in the signal is involved in at least two important processes: the down-conversion of the ho-
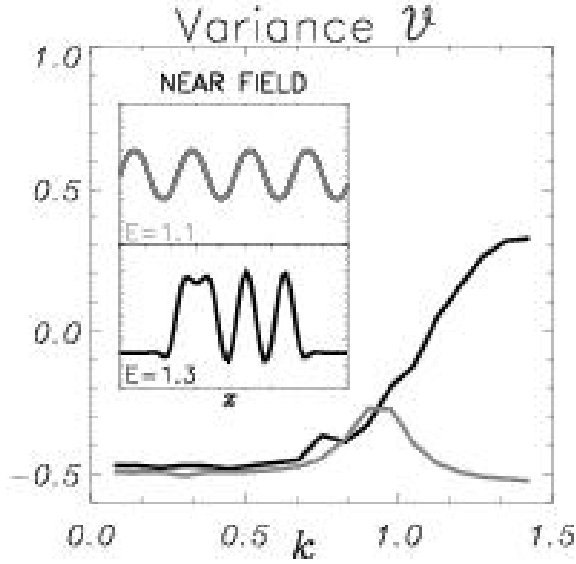
Figure 4.25: Twin beams correlations $\mathcal{V}(k)$ above threshold, for $E_0 = 1.02$ (grey) and for $E_0 = 1.1$ (black).

mogeneous pump into twin photons $+3k_c$ and $-3k_c$ and the secondary process of down-conversion of the second harmonics $\pm 2k_c$ of the pump into opposite signal photons $\pm 3k_c$ and $\mp k_c$. We note that as the Hamiltonian operator is Hermitian, the opposite (up-conversion) processes are also allowed. The observed reduction of squeezing can be interpreted as a signature of the mentioned secondary process, in which the pairs signal $+3k_c$ and $-3k_c$ photons are incoherently (not simultaneously) generated and destroyed. In other words, signal modes are depleted independently, taking part in different cascading processes and generating harmonics. The entanglement should be preserved in opposite signal modes for which the fundamental down-conversion process prevails. We have confirmed that opposite spatial modes in the pump field do not show quantum correlations.

We note that the variances $\mathcal{V}$ obtained with the Q-representation –after reordering– are in good agreement with the corresponding quantities calculated with the time dependent parametric approximation in the Wigner representation in Ref.[Zambrini & San Miguel].

4.5.2.b   Intensity correlations in spatially disordered structures

With increasing pump intensity, a transition from a modulated pattern to homogeneous solutions takes place. The transition depends effectively on the noise level. For example, for pump $E_0 = 1.1$, for which we have analyzed in Sect. 4.5.2.a fluctuations in stripe patterns, a high level of noise ($g/\gamma = 10^{-2}$) leads to a disordered structure. Due to the bistability in this regime, different homogeneous solutions can be selected in separated spatial domains (see Fig.4.18 for $E_0 = 1.5$). All solutions presented in Fig.4.18 are obtained starting from a modulated initial condition at k_c. Therefore we are *stimulating*, with a particular initial configuration, the shape of the final structure. In Fig.4.26a we show the stationary configuration for $E_0 = 1.5$, in which the most excited mode is k_c. The disordered character of the structure gives rise to a broad spectrum, in which the other dominant modes are not harmonics of k_c. The most intense signal modes combine to form pump modes: for example in Fig. 4.26a the signal
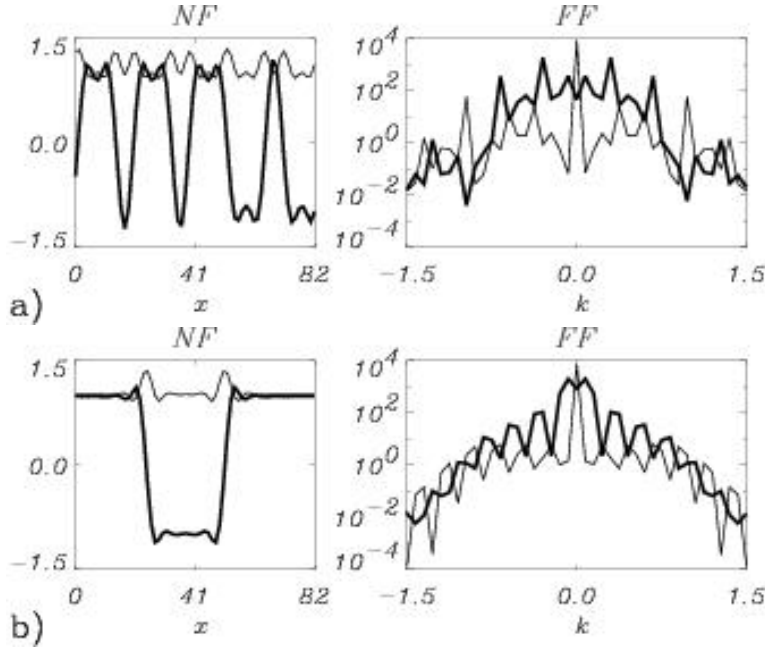
Figure 4.26: Snapshots of the real part of the NF and intensity (log scale) of the FF for the pump (thin line) and the signal (thick line), for $E_0 = 1.5$, starting from a rolls pattern (a) and from a step function with values -1 and $+1$(b).

modes $k_c = 4\Delta k = 0.3$ and $9\Delta k = 0.675$ give the pump mode $13\Delta k = 0.975$. With our choice of parameters $\Delta k = 0.075$, with Δk depending on the size of the system: $\Delta k = 2\pi/L = 2\pi/4\lambda_c$. The stationary disordered structure shows the same reflection symmetry $\langle N_1(k) \rangle = \langle N_1(-k) \rangle$, of the stripe pattern considered in Sect. 4.5.2.a.

Studying the properties of the quantum fluctuations in this regime, we observe non-classical correlations between the two signal "twin" beams with critical wave-vectors, also in these spatially disordered structures (see Fig.4.22 for $1.2 \leq E_0 \leq 1.5$). This result does not depend on momentum conservation or on the presence of a regular pattern. We have also considered the entanglement properties of modes different from the critical one. In Fig. 4.27 we show the spatial spectrum of the variance $\mathcal{V}$. As in the case of a regular stripe pattern, analyzed in the previous section, we continue to find quantum correlated twin beams. However there are some interesting differences. The peak in $\mathcal{V}$ now corresponds to a strongly depleted (*low* mean intensity) signal mode for $k = 0.975$. This contrasts with the previous case, where $k = 3k_c$ was an excited mode. The most interesting feature is the appearance of a bandwidth of "twin" beams, where the signal field is intense; the correlations become classical for big wave-vectors ($k \gtrsim 1$), where the signal is depleted more than the pump field, reaching asymptotically the level of coherent states (see dotted grey line in Fig.4.27). In conclusion, the "twin"-beams quantum correlations persist in disordered structures. This signature of the fundamental down-conversion process is preserved throughout the region of intense signal modes.

The demanding question is how the spectrum of the variance $\mathcal{V}$ is influenced by the shape of the selected spatial structure. In this regime no special character is associated with the critical wavelength periodicity. Therefore we consider a stationary state of two domains, obtained from an initial step condition (Fig. 4.26b). Also in this case, with a very different stationary state, we observe non-
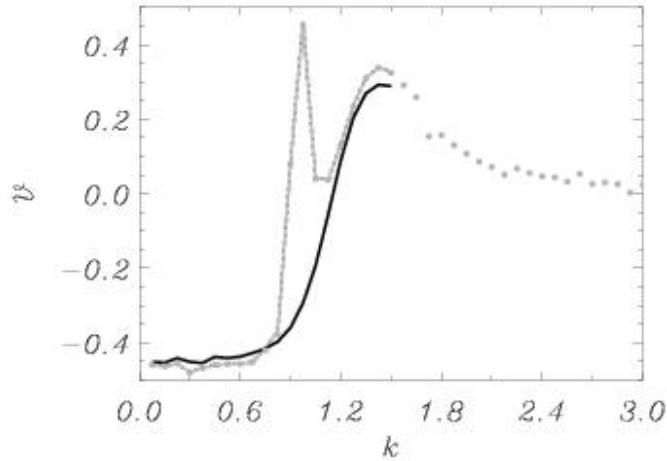
Figure 4.27: Twin beams correlations $\mathcal{V}(k)$ for pump $E_0 = 1.5$. The grey (black) line is the spectrum $\mathcal{V}(k)$ for the pattern shown in Fig.4.26a (Fig.4.26b). The grey dotted line is obtained considering a system with the same size ($L = 4\lambda_c$) but with a finer discretization (128 instead of 64 points), starting from a stripe configuration of critical wave-length. In this way we can see the asymptotic behavior of the spectrum for large wavevectors. For small wavevectors the results are in good agreement with the simulation using 64 points.

classical intensity correlations in the bandwidth $0 < k \lesssim 1$, as shown in Fig.4.27 (black line). In this case no peaks appear, suggesting that the presence of modes with reduced squeezing (as the peak for $k = 0.975$ observed in the previous structure) depends on the selected spatial structure.

The key point is the relative importance of the fundamental coherent process of twin photon down-conversion, and other incoherent cascading processes, which depends on the spatial configuration chosen by the system. To give more evidence of this statement, we study the variance $\mathcal{V}$ in three different spatial configurations, obtained for $E_0 = 1.3$, starting the simulations from noise, from rolls (as in Fig. 4.26a) and from a step function (as in Fig.4.26b). In Fig. 4.28 we show the spectral variances
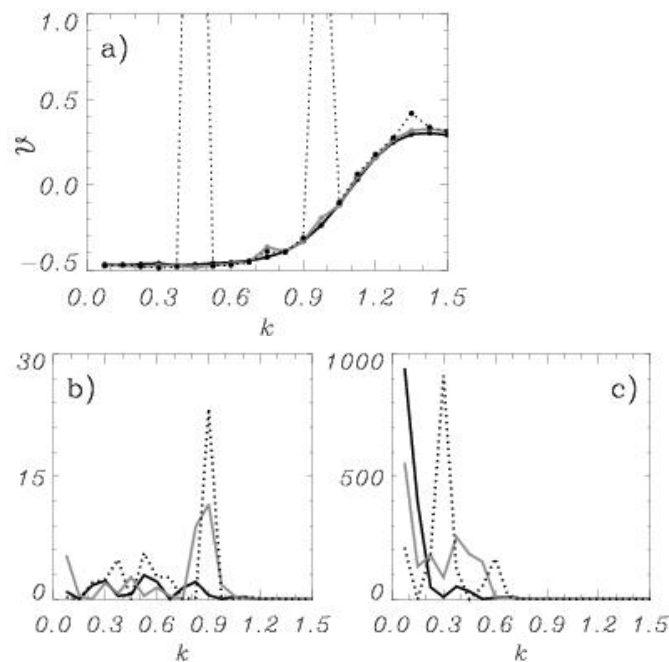

Figure 4.28: a) Twin beams correlations $\mathcal{V}(k)$ for pump $E_0 = 1.3$, corresponding to different spatial structures, obtained starting from a step function (black line), from noise (grey line) and from a stripe pattern with critical wave-length (dotted line). Mean FF intensity in the pump ($< N_0 >$) (b) and in the signal ($< N_1 >$) fields (c), for the same three spatial configurations.

(a) and the mean FF intensity (b). The domain configurations obtained staring from noise and from a step function give overlapping smooth variances, while two peaks appear when starting from rolls . Also in this case the peaks appear associated with strongly depleted signal modes with low intensities, and can be in different positions depending on the selected spatial structure. The bandwidth of non-classical variance $\mathcal{V}$ seems to be a general feature, almost independent of the structure selected. It corresponds to the FF region of intense tilted signal beams.

4.6   Summary and conclusions

In this Chapter we have discussed quantum features of a type I degenerate optical parametric oscillator above threshold. We have considered the DOPO when there is a transverse walk-off effect and also in the case in which it vanishes. The instabilities predicted in both cases are reviewed in Sect.4.1.

In order to describe the nonlinear interactions of a DOPO above threshold, we have proposed two approximated methods based on the use of the W and Q representations. We obtained two sets of **nonlinear Langevin equations**, describing the pump and the signal fields (Sect.4.2). Our initial motivation has been the study of noise sustained patterns, characterized by a broad far field spectrum with competition among many wave-numbers. Therefore few mode approximations are not adequate in this regime. Noise sustained patterns are the result of amplified quantum fluctuations around a unstable reference state. These two approximations can be extended to other interesting regimes.

The method based on the use of the W representation is a time dependent parametric approximation (Sect.4.2.2), in which vacuum fluctuations are neglected in the pump mode: the pump field is treated as a classical variable, but driven by the c-number representation of the quantum sub-harmonic signal field. The key point is that this formulation includes the effects of the fluctuations in the signal on the pump, which in turn act back on the signal. Correlation functions of quadratures and intensity of the signal field calculated in this representation correspond to symmetrically ordered correlations. This approximation is valid in regimes of macroscopic signal fluctuations, such as the convective regime or the instability region at the threshold for pattern generation.

The second method is based on the use of the Q representation (Sect.4.2.3), that for an OPO satisfies a pseudo FPE, in which the diffusion is not always positive definite. However, the diffusion matrix is positive definite unless the fluctuations are strong enough to push the pump field up to twice the threshold value. This never occurred in our simulations and we have not attempted to calculate the effects of such highly unlikely trajectories on our ensembles. This approximation is valid in a wide region of pump intensities, allowing for the description of quantum fields dynamics in several spatial structures above threshold.

In Sections 4.3, 4.4 and 4.5 we have studied different regimes of the DOPO above the threshold of pattern formation. Also, we have checked the validity of the proposed approximations *below* the threshold for pattern formation, comparing our results with known results obtained in a linear approximation, where pump depletion and fluctuations are neglected.

The main goal of Sect. 4.3 is the study of the quantum properties of macroscopic **patterns sus-**

tained by quantum fluctuations in the DOPO with *walk-off*. Using the time dependent parametric approximation, we have described the quantum fluctuations in type I OPO with walk-off in three regimes: below threshold, in the convective unstable regime and in the absolute unstable regime. To characterize the behavior of the quantum fields, we have calculated the Wigner distribution of the most intense modes (Sect.4.3.1) and evaluated the **squeezing** level reached in the quadratures fluctuations. Below threshold we find that the Wigner representation has a Gaussian shape centered at the origin. This is the result previously found in a OPO without walk-off [Gatti & al. (97)1] from a linearized analysis. We also find that walk-off does not destroy the existence of squeezing in suitable quadratures. In the convective regime the macroscopic character of the fluctuations is reflected in a extremely broad Wigner distribution where the probability is still centered at the origin but the nonlinear effects lead to the appearance of wings in the distribution which is no longer a Gaussian. These wings are in fact precursors of the pair of peaks appearing in the absolutely convective regime. We show that squeezing in the appropriate observables can be also obtained in this regime but only just above threshold (Sect.4.3.2). The walk-off and the nonlinearities act as quantum decoherence mechanism, distributing part of the macroscopic fluctuations into the observables that were squeezed below threshold. Another nonlinear effect appears in the selection of the quadrature displaying reduced fluctuations. This quadrature is no longer the one determined linearly. In the absolutely unstable regime there are also clear indications of nonlinear properties associated with quantum fluctuations. The interplay between walk-off and non-linearity results in a complex dynamics in which the frequencies of far-field modes are not constant, giving a complicated variation of the phases. Also, the most intense mode is not the critical mode. We find that while the Wigner distribution for the less intense modes can be approximated by a Gaussian (displaced from the origin and orbiting about it), this is not the case for the most intense modes for which the distribution of fluctuations is asymmetric around the mean amplitude with a sharp decay at some maximum amplitude.

In Sect.4.4 we have used the the time dependent parametric approximation to study another important effect of the transverse walk-off term, that is the breaking of the **reflection symmetry** for the opposite far field modes $\pm k$. We saw in Ch.3 that a multimode spatial treatment allows for the identification of symmetry breaking effects. In that case we studied the spatial distribution of the fluctuations and we discussed the role of the Goldstone mode. In this Chapter, we are interested in the effects of the breaking of a discrete reflection symmetry due to the walk-off term. For the sake of simplicity we discuss this problem for a flat transverse profile of the pump. In this case the pattern arising at threshold is absolutely stable. We studied the walk-off effects on spatial **twin beams correlations**. Our continuous analysis, which avoids few-mode approximations, shows that, neglecting walk-off effects, beam entanglement is preserved when more harmonics are excited in the stripe pattern. In this case twin-beams-like correlations appear in a multimode process (see Sect.1.4.1.b) and do not follow from momentum conservation. When walk-off is not negligible, we show that one beam is more intense and it fluctuates more than the opposite one. Unexpectedly, also for such imbalance between the "twin" beams, the entanglement in fluctuations remains unchanged in the domain of parameters explored. We also show that twin beams correlations can be calculated within the time dependent parametric approximation when large critical fluctuations appear, at the OPO threshold. The large fluctuations of the

signal in the critical point cannot be described by approximations based on linearization. Generalizing our results for a finite pump profile we have shown that the correlations between the intensities of opposite far field modes in the convective regime are classical. Therefore in this regime, for macroscopic fluctuations, neither squeezing nor intensity twin beams correlations survive.

In Sect.4.5 we have used the Q representation for studying quantum correlations in the DOPO, when transverse walk-off vanishes. Below threshold squeezing in quadratures and non-classical intensity correlations are obtained, in agreement with linear analytical results. At threshold, a pair of quantum correlated twin beams is generated. These beams have wavevectors $\pm k_c$, corresponding to the critical wavelength. As we move further above threshold the twin beams can recombine to generate new pump photons. The combination of a $+k_c$ and a $-k_c$ photon regenerates one of the original pump photons. The combination of a pair of $+k_c$ photons or a pair of $-k_c$ photons, however, is a new process and introduces higher harmonics in the pump and hence in the the signal (multiphoton process). Such processes can also degrade, but not completely suppress, the quantum correlations in some signal modes, as in the spatial harmonics $\pm 3k_c$. This is a signature of the incoherent depletion of those modes. The twin beams correlations between the intensities of the critical modes $\pm k_c$ are preserved when a multimode process is present, in agreement with the results obtained with the time dependent approximation in Sect.4.4.4. Yet further above threshold we enter a regime of spatially disordered structures. Remarkably, quantum correlations persist even in this regime, in the bandwidth of intense signal modes, where they take a form that depends on the spatial pattern that is generated.

Chapter 5

Type II Optical Parametric Oscillator

In this Chapter we study a type II Optical Parametric Oscillator below threshold. In this device the pump field is down converted in two orthogonally polarized fields. Therefore this device is a good candidate to examine new phenomena associated with the polarization degree of freedom in quantum phenomena occurring in macroscopic beams of light in transverse spatially extended systems. These quantum properties open the way to the use of the polarization in the quantum processing of images. Due to the birefringence of the crystal a transverse walk-off arises between the two orthogonally polarized fields. We study the effects of walk-off on the spatial distribution of the fluctuations and on quantum correlations.

Sect.5.1 describes our basic model, input-output relations and some characteristics of the far field. Sect.5.2 contains our calculations and results for spatial EPR entanglement between quadratures of the signal and idler fields in opposite points of the far field (see Sect.1.4.2). A precedent of macroscopic EPR experiments in OPO are those of Ref.[Ou & al., Zhang& al.], but they do not refer to spatial EPR, distinguishing signal and idler by their polarization. Spatial EPR was theoretically considered in Refs. [Gatti & al. (99)a, Gatti & al. (00)b] in type I-OPO. We build on these results by considering the polarization degree of freedom and including the walk-off effects in our treatment. Our main finding is that for the intersection points of the far field rings there is noise suppression much below the standard quantum limit in the proper quadratures combinations of any orthogonal polarization components of the critical modes.

In Sects.5.3 and 5.4 we describe our analysis of the question of macroscopic polarization entanglement in terms of Stokes operators. This question had not been previously considered taking into account the spatial transverse dependence. There is a recent experimental observation of polarization squeezing in three of the four Stokes parameters [Bowen & al.], but this does not consider correlations or entanglement properties. Macroscopic polarization entanglement in terms of Stokes parameters is considered in Ref. [Korolkova & al.], but in a situation that does not involve transverse spatial depen-

dence. As a main result we show that there exists macroscopic polarization entanglement between the states of the beams at the two spatial points of intersection of the far field rings: we find perfect quantum correlation at zero-frequency in all Stokes operators.

5.1 Input/output relations and far field characteristics

We consider a type II OPO below threshold, in the undepleted pump approximation. In this approximation the pump field is described by a fixed classical variable A_0. In the mean field approximation the signal ($\hat{A}_1$, ordinary x polarized) and the idler ($\hat{A}_2$, extraordinary y polarized) fields obey the following Heisenberg operator equations [Szwaj & al.]:

$$\partial_t \hat{A}_1 = -\gamma_1(1 + i\Delta_1 - ia_1\nabla^2 + \rho_1\partial_y)\hat{A}_1 + \sqrt{\gamma_1\gamma_2}A_0\hat{A}_2^\dagger + \sqrt{2\gamma_1}\hat{A}_1^{in} \tag{5.1}$$

$$\partial_t \hat{A}_2 = -\gamma_2(1 + i\Delta_2 - ia_2\nabla^2 + \rho_2\partial_y)\hat{A}_2 + \sqrt{\gamma_1\gamma_2}A_0\hat{A}_1^\dagger + \sqrt{2\gamma_2}\hat{A}_2^{in} \tag{5.2}$$

where γ_i are the cavity linewidths for the signal and idler fields, Δ_i are the cavity detunings, ∇^2 is the two dimensional transverse Laplacian that models the effect of diffraction in the paraxial approximation, and a_i are the diffraction strengths. As in the previous Chapter, we also consider the effects of the transverse walk-off. In type II phase matching the transverse walk-off arises between the signal and idler fields. It is described by the drift terms $\rho_i\partial_y\hat{A}_i$. $\hat{A}_i^{in}$ are the the input field operators, describing the fluctuations of the signal and idler modes entering for the partially transmitting mirror of the cavity.

From the Fourier transform:

$$\hat{A}(\vec{x}, t) = \int \frac{d^2\vec{k}}{2\pi} \int \frac{d\omega}{\sqrt{2\pi}} e^{i(\vec{k}\cdot\vec{x} - \omega t)} \hat{A}(\vec{k}, \omega) \tag{5.3}$$

$$\hat{A}^\dagger(\vec{x}, t) = \int \frac{d^2\vec{k}}{2\pi} \int \frac{d\omega}{\sqrt{2\pi}} e^{i(\vec{k}\cdot\vec{x} - \omega t)} \hat{A}^\dagger(-\vec{k}, -\omega) \tag{5.4}$$

we obtain the following algebraic linear relation, giving the intracavity mode operators $\hat{\nu}(\vec{k}, \omega)$ in terms of the input fields $\hat{\nu}^{in}(\vec{k}, \omega)$

$$\boldsymbol{L}\hat{\boldsymbol{\nu}} = \boldsymbol{\Gamma}\hat{\boldsymbol{\nu}}^{in}, \tag{5.5}$$

where we have introduced the operator vectors

$$\hat{\boldsymbol{\nu}} = \begin{pmatrix} \hat{A}_1(\vec{k}, \omega) \\ \hat{A}_2^\dagger(-\vec{k}, -\omega) \end{pmatrix}, \hat{\boldsymbol{\nu}}^{in} = \begin{pmatrix} \hat{A}_1^{in}(\vec{k}, \omega) \\ \hat{A}_2^{in\dagger}(-\vec{k}, -\omega) \end{pmatrix}, \tag{5.6}$$

and the matrices

$$\boldsymbol{L} = \begin{pmatrix} \gamma_1(1 + i\Delta_1(\vec{k}, \omega)) & -\sqrt{\gamma_1\gamma_2}A_0 \\ -\sqrt{\gamma_1\gamma_2}A_0^* & \gamma_2(1 - i\Delta_2(-\vec{k}, -\omega)) \end{pmatrix}, \boldsymbol{\Gamma} = \begin{pmatrix} \sqrt{2\gamma_1} & 0 \\ 0 & \sqrt{2\gamma_2} \end{pmatrix}, \tag{5.7}$$

with

$$\Delta_j(\vec{k}, \omega) = \Delta_j + a_j|\vec{k}|^2 + \rho_j k_y - \omega/\gamma_j. \tag{5.8}$$

Using the input/output relations $\hat{\nu}^{out} = \boldsymbol{\Gamma}\hat{\nu} - \hat{\nu}^{in}$ [Collett & Gardiner] introduced in Sect.1.2.3.a, we obtain the output fields:

$$\hat{A}_{1,2}^{out}(\vec{k},\omega) = U_{1,2}(\vec{k},\omega)\hat{A}_{1,2}^{in}(\vec{k},\omega) + V_{1,2}(\vec{k},\omega)\hat{A}_{2,1}^{in}(-\vec{k},-\omega). \tag{5.9}$$

The coefficients of the input/output transformation are:

$$U_1(\vec{k},\omega) = \frac{2[1 - i\Delta_2(-\vec{k},-\omega)]}{[1 + i\Delta_1(\vec{k},\omega)][1 - i\Delta_2(-\vec{k},-\omega)] - |A_0|^2} - 1 \tag{5.10}$$

$$V_1(\vec{k},\omega) = \frac{2A_0}{[1 + i\Delta_1(\vec{k},\omega)][1 - i\Delta_2(-\vec{k},-\omega)] - |A_0|^2} \tag{5.11}$$

and U_2, V_2 are obtained interchanging indexes 1 and 2 in Eqs. (5.10) and Eq. (5.11).

Assuming the input signal and idler fields in a vacuum state it is immediate to obtain the non-vanishing second order moments of the output fields

$$\langle \hat{A}_1^{out\,\dagger}(\vec{k},\omega)\hat{A}_1^{out}(\vec{k}',\omega')\rangle = |V_1(\vec{k},\omega)|^2\delta(\vec{k}-\vec{k}')\delta(\omega-\omega'), \tag{5.12}$$

$$\langle \hat{A}_2^{out\,\dagger}(\vec{k},\omega)\hat{A}_2^{out}(\vec{k}',\omega')\rangle = |V_2(\vec{k},\omega)|^2\delta(\vec{k}-\vec{k}')\delta(\omega-\omega'), \tag{5.13}$$

$$\langle \hat{A}_1^{out}(\vec{k},\omega)\hat{A}_2^{out}(\vec{k}',\omega')\rangle = U_1(\vec{k},\omega)V_2(-\vec{k},-\omega)\delta(\vec{k}+\vec{k}')\delta(\omega+\omega') \tag{5.14}$$

and the corresponding hermitian conjugate ones. From these moments, quadrature and intensity correlations can be analytically calculated for a transversally homogeneous pump A_0. These calculations are simplified considering the unitary conditions (see, for instance, Ref. [Szwaj & al.]) and the symmetries of the system. From Eqs.(5.12),(5.13) we obtain the local Far Field (FF) intensity. From Eq.(5.14) it is evident that correlations between signal and idler are non vanishing only between opposite points of the far field. Such two-mode correlations are due to the quadratic form of the Hamiltonian describing the OPO below threshold, within a linear approximation. In the following, and in order to avoid unphysical divergences [1], we consider the fields to be integrated over a detection region $R_{\vec{k}}$ of area σ:

$$\hat{A}^{out}(\vec{k}) \to \int_{R_{\vec{k}}} dk'\,\hat{A}^{out}(\vec{k}'). \tag{5.15}$$

At the threshold for signal generation ($A_0^{thr} = 1$), and for a negative total detuning ($\gamma_1\Delta_1 + \gamma_2\Delta_2 < 0$), an instability at finite wavenumber and with nonzero frequency appears, as extensively discussed in Ref. [Izús & al., Ward & al. (01)]. The modes that become unstable at threshold are determined by the relations $\Delta_1(\vec{k},\omega_H(\vec{k})) = 0$ and $\Delta_2(\vec{k},\omega_H(\vec{k})) = 0$, where

$$\omega_H(\vec{k}) = \frac{\gamma_1\gamma_2}{\gamma_1 + \gamma_2}[\Delta_1 - \Delta_2 + (a_1 - a_2)|\vec{k}|^2 + (\rho_1 + \rho_2)k_y] \tag{5.16}$$

is the frequency that becomes undamped at threshold (Hopf bifurcation).

The unstable critical modes lie on two rings of the far field given by:

$$\gamma_1\Delta_1 + \gamma_2\Delta_2 + (\gamma_1 a_1 + \gamma_2 a_2)|\vec{k}|^2 \pm (\gamma_1\rho_1 - \gamma_2\rho_2)k_y = 0. \tag{5.17}$$

If the relative walk-off $\gamma_1\rho_1 - \gamma_2\rho_2$ vanishes, Eq.(5.17) describes a single ring. Therefore in absence of walk-off the signal and the idler far field distributions are superimposed, and an intense ring is observed.
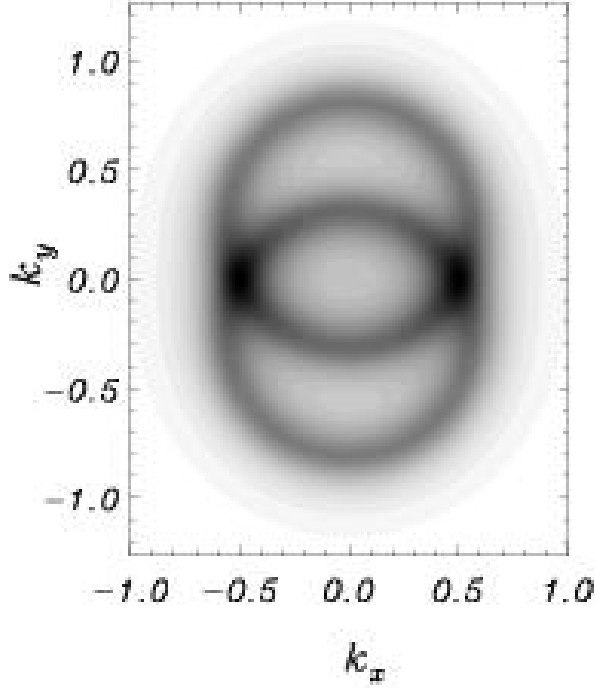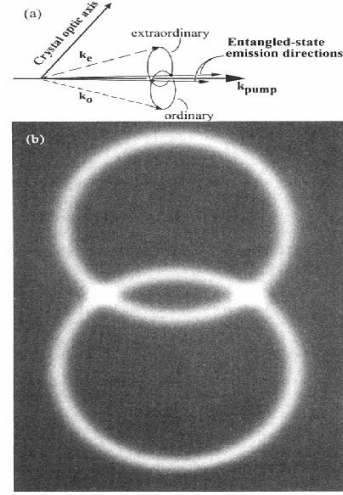
Figure 5.2: (a) Spontaneous down-conversion cones present with type II phase matching. Correlated photons lie on opposite sides of the pump beam. (b) A photograph of the down-conversion photons. Taken from Ref.[Kwiat & al.].

Figure 5.1: Far field intensity Eq. (5.18) for the choice of parameters $\Delta_1 = \Delta_2 = -0.25$, $a_1 = a_2 = 1$, $\rho_1 = 0$, $\rho_2 = 1$, $\gamma_1 = \gamma_2 = 1$ [Lane & al.], $A_0 = 0.99$. The same parameters will be used for all Figures, unless another choice is specified. The lower (upper) ring corresponds to the intensity of the field 1 (2).

The two rings of Eq.(5.17) are clearly identified in Fig.5.1, where we represent the stationary mean intensity close to threshold:

$$\langle \hat{A}_1^{out\,\dagger}(\vec{k},t)\hat{A}_1^{out}(\vec{k},t) + \hat{A}_2^{out\,\dagger}(\vec{k},t)\hat{A}_2^{out}(\vec{k},t)\rangle = \frac{\sigma}{2\pi}\int d\omega(|V_1(\vec{k},\omega)|^2 + |V_2(\vec{k},\omega)|^2). \tag{5.18}$$

This figure is similar to the well-known experimental image obtained when there is no cavity, in spontaneous parametric down conversion (see Fig.5.2 [Kwiat & al.]). We want to point out that the cavity introduces fundamental differences: in particular in this case there is a threshold above which a pattern appears in the transverse profile of the fields. As discussed in Sect.1.3.2, the modulus of the wave-vector of such pattern is identified in the noisy precursor below threshold. The existence of a selected wave-number is an effect of the optical cavity, its value being determined by the cavity detuning.

The main contribution to the integrals in Eq. (5.18) are the most intense frequencies components

---

[1]For further discussions about singularity problems in presence of a flat pump see Ref. [Szwaj & al.].

given by Eq. (5.16). Hence the intensity at the Hopf frequency

$$\langle \hat{A}_1^{out\,\dagger}(\vec{k}, \omega_H(\vec{k})) \hat{A}_1^{out}(\vec{k}, \omega_H(\vec{k})) + \hat{A}_2^{out\,\dagger}(\vec{k}, \omega_H(\vec{k})) \hat{A}_2^{out}(\vec{k}, \omega_H(\vec{k})) \rangle \tag{5.19}$$

is very similar to the one of Fig. 5.1. This image of the FF shows that the intensity reaches the highest value at the intersection points of the two rings, where ordinary and extraordinary fields are superimposed. From Eq.(5.17) it is immediate to obtain the coordinates of these crossing points:

$$\pm \vec{k}_H = (\pm k_x^c, 0), \text{ with } k_x^c = \sqrt{\frac{-\gamma_1 \Delta_1 - \gamma_2 \Delta_2}{\gamma_1 a_1 + \gamma_2 a_2}}. \tag{5.20}$$

In our calculations we will also consider the FF modes on the rings for which the influence of the walk-off is stronger. These are the four points of intersection of the two rings and the y axis, with ordinates:

$$\pm k_{y\pm}^c = \frac{\pm(\gamma_1 \rho_1 - \gamma_2 \rho_2) \pm \sqrt{(\gamma_1 \rho_1 - \gamma_2 \rho_2)^2 - 4(\gamma_1 \Delta_1 + \gamma_2 \Delta_2)(\gamma_1 a_1 + \gamma_2 a_2)}}{2(\gamma_1 a_1 + \gamma_2 a_2)}. \tag{5.21}$$

We define the two external points by $\pm \vec{k}_V = (0, \pm k_{y+}^c)$, with k_{y+}^c obtained from Eq. (5.21) with both $+$ signs.

In the following and for simplicity we omit the label out, indicating with $\hat{A}_{1,2}$ always the output fields, characterized by Eqs. (5.12-5.14).

5.2   Spatial EPR entanglement between quadrature-polarization field components

The vectorial field is a superposition of linearly polarized components:

$$\hat{\vec{A}} = \hat{A}_1 \vec{e}_x + \hat{A}_2 \vec{e}_y. \tag{5.22}$$

By means of a wave retarder

$$W = \begin{pmatrix} 1 & 0 \\ 0 & e^{i\Gamma} \end{pmatrix} \tag{5.23}$$

and a polarization rotator

$$P = \begin{pmatrix} \cos\Theta & \sin\Theta \\ -\sin\Theta & \cos\Theta \end{pmatrix}, \tag{5.24}$$

we obtain a field $\hat{\vec{A}}_{\Gamma\Theta} = WP\hat{\vec{A}}$ in any polarization state

$$\hat{\vec{A}}_{\Gamma\Theta} = (\hat{A}_1 \cos\Theta + \hat{A}_2 e^{i\Gamma} \sin\Theta) \vec{e}_x + (-\hat{A}_1 \sin\Theta + \hat{A}_2 e^{i\Gamma} \cos\Theta) \vec{e}_y. \tag{5.25}$$

With a linear polarizer

$$L = \begin{pmatrix} 1 & 0 \\ 0 & 0 \end{pmatrix}, \tag{5.26}$$

we can select a field polarization component, and, integrating over a detection region $R_{\vec{k}}$, we obtain

$$\hat{A}_{\Gamma\Theta}(\vec{k}, t) = \int_{R_{\vec{k}}} d\vec{k}'(\hat{A}_1(\vec{k}', t)\cos\Theta + \hat{A}_2(\vec{k}', t)e^{i\Gamma}\sin\Theta). \tag{5.27}$$

By homodyne detection we can select a quadrature component of this polarization component. We define the quadrature Ψ by

$$A_{\Gamma\Theta}^{\Psi}(t) = A_{\Gamma\Theta}(t)e^{i\Psi} + (A_{\Gamma\Theta})^{\dagger}(t)e^{-i\Psi}. \tag{5.28}$$

In any FF point, the arbitrary quadrature-polarization component (5.28) has vanishing mean value and a spectral variance which depends only on Θ, but it is independent of the choice of the phase factors Ψ and Γ: Integrating over the the detection region $R_{\pm\vec{k}}$ of area σ we obtain

$$\int dt e^{i\omega t}\langle\hat{A}_{\Gamma\Theta}^{\Psi}(\vec{k}, t)A_{\Gamma\Theta}^{\Psi}(\vec{k}, 0)\rangle = \tag{5.29}$$
$$\sigma[1 + \cos^2\Theta(|V_1(\vec{k}, \omega)|^2 + |V_1(\vec{k}, -\omega)|^2) + \sin^2\Theta(|V_2(\vec{k}, \omega)|^2 + |V_2(\vec{k}, -\omega)|^2],$$

where σ fixes the shot noise level. Therefore, in any far field point the variance of an arbitrary quadrature-polarization component is above the shot noise level σ. We observe that if we place the detectors in the FF line $k_y = 0$ the variance results independent of all angles, including Θ. We find

$$\int dt e^{i\omega t}\langle\hat{A}_{\Gamma\Theta}^{\Psi}((k_x, 0), t)A_{\Gamma\Theta}^{\Psi}((k_x, 0), 0)\rangle = \sigma[1 + |V_1((k_x, 0), \omega)|^2 + |V_1((k_x, 0), -\omega)|^2], \tag{5.30}$$

In other words, for $k_y = 0$, the level of fluctuations is independent of the choice of the polarization state and quadrature, depending only on the position k_x.

We next consider the correlations between the field component detected in two spatially separated FF points. Such correlations are not vanishing only for *opposite* FF points $\vec{k}$ and $-\vec{k}$. We will show that the correlations between quadratures in these two spatial points of the transverse field show EPR entanglement. A two mode state is here defined to be EPR entangled if for two orthogonal quadratures $\hat{X}_i$ and $\hat{Y}_i$ in each mode i ($i = 1, 2$) the conditional variances $V_{cond}^-(\hat{X}_1|\hat{X}_2)$ and $V_{cond}^+(\hat{Y}_1|\hat{Y}_2)$ are *both* less than 1, as discussed in Ref.[Leuchs & al.]. The conditional variance is defined by

$$V_{cond}^{\pm}(\hat{A}|\hat{B}) = \min_g \frac{V(\hat{A} \pm g\hat{B})}{V(\hat{A}_{SN})} \tag{5.31}$$

being $V(\hat{A})$ the variance, and $V(\hat{A}_{SN})$ the shot noise level. The factor g is introduced to optimize noise reduction and is experimentally obtained by an attenuator and a delay line [Gatti & al. (00)b]. We note that

$$V(\hat{X}_1 - \hat{X}_2) < V(\hat{X}_{1,SN}) \quad \text{and} \quad V(\hat{Y}_1 + \hat{Y}_2) < V(\hat{Y}_{1,SN}) \tag{5.32}$$

is a sufficient condition for EPR entanglement, corresponding to the choice $g = 1$. The definition of EPR entanglement used here [Leuchs & al.] provides a sufficient condition for the *inseparability* criterion recently discussed for continuous variables systems by [Duan & al.].

For a single-mode type II OPO below threshold, in which transverse effects are not considered, EPR correlations between signal and idler modes of different polarizations have been predicted [Reid & Drummond (90)] and experimentally demonstrated [Reid & Drummond (90)]. Recent investigations show the possibility of EPR entanglement between spatial regions of the transverse profile of the signal field of a degenerate optical parametric oscillator [Gatti & al. (99)a, Gatti & al. (00)b]. For type II phase matching we can consider two opposite far field modes with x and y polarizations, respectively. Neglecting walk-off effects we would then find results equivalent to the degenerate case in type I phase matching [Gatti & al. (99)a, Gatti & al. (00)b]. In addition of considering the effect of the walk-off, the novelty of our discussion here for type II OPO is that we can also consider how these correlations change with the polarization state.

As an indicator to look for EPR entanglement in our case, we introduce the spectral variance of the difference of quadratures

$$\mathcal{V}_g(\pm\vec{k},\omega;\vec{\Phi}) = \int dt e^{i\omega t} \langle (\hat{A}^{\Psi}_{\Gamma\Theta}(\vec{k},t) - g^* \hat{A}^{\Psi'}_{\Gamma'\Theta'}(-\vec{k},t))(\hat{A}^{\Psi}_{\Gamma\Theta}(\vec{k},0) - g\hat{A}^{\Psi'}_{\Gamma'\Theta'}(-\vec{k},0)) \rangle, \qquad (5.33)$$

where the vector $\vec{\Phi} = (\Gamma, \Theta, \Psi, \Gamma', \Theta', \Psi')$ is the set of parameters determining the polarizations (lower labels) and quadratures (upper labels) of the opposite FF modes under consideration. The value of g giving the minimum variance (5.33) is

$$\bar{g} = \frac{\int dt e^{i\omega t} \langle \hat{A}^{\Psi'}_{\Gamma'\Theta'}(-\vec{k},t) \hat{A}^{\Psi}_{\Gamma\Theta}(\vec{k},0) \rangle}{\int dt e^{i\omega t} \langle \hat{A}^{\Psi'}_{\Gamma'\Theta'}(-\vec{k},t) \hat{A}^{\Psi'}_{\Gamma'\Theta'}(-\vec{k},0) \rangle} \qquad (5.34)$$

From the output moments Eqs. (5.12-5.14) we obtain

$$\mathcal{V}_g(\pm\vec{k},\omega;\vec{\Phi}) = \sigma \quad \Big[\, |e^{i(\Psi+\Psi'+\Gamma')}\cos\Theta U_1(\vec{k},\omega) - g^*\sin\Theta' V_2^*(-\vec{k},-\omega)|^2 \qquad (5.35)$$

$$+ |e^{i(\Psi+\Psi'+\Gamma')}g^*\sin\Theta' U_1(\vec{k},-\omega) - \cos\Theta V_2^*(-\vec{k},\omega)|^2$$

$$+ |e^{i(\Psi+\Psi'+\Gamma)}\sin\Theta U_1(-\vec{k},-\omega) - g^*\cos\Theta' V_2^*(\vec{k},\omega)|^2$$

$$+ |e^{i(\Psi+\Psi'+\Gamma)}g^*\cos\Theta' U_1(-\vec{k},\omega) - \sin\Theta V_2^*(\vec{k},-\omega)|^2 \Big]$$

with shot noise level $\sigma(1 + |g|^2)$. A variance below this shot noise level is a signature of squeezing. We are looking for the more stringent conditions (5.31) discussed above: EPR entanglement imposes the requirement that $\mathcal{V}_g(\pm\vec{k},\omega;\vec{\Phi})$ goes below the shot noise level of $\hat{A}^{\Psi}_{\Gamma\Theta}$ (that is we should find $\mathcal{V}_g(\pm\vec{k},\omega;\vec{\Phi}) < \sigma$), simultaneously for two combinations of orthogonal quadratures [Leuchs & al.].

The general result (5.35) depends on many parameters. However it is important to note that $\mathcal{V}_g$ only depends on the phases $\Psi, \Psi', \Gamma, \Gamma'$ through the independent combinations $(\Psi+\Psi'+\Gamma)$ and $(\Psi+\Psi'+\Gamma')$. The dependence on the sum of quadratures angles Ψ and Ψ' is well known in other contexts. It is easily understood taking into account that measuring by a single homodyne detector the noise in a quadrature $\frac{\Psi+\Psi'}{2}$ of the difference of the spatial $\pm\vec{k}$ and polarization $(\Gamma, \Theta, \Gamma', \Theta')$ modes is equivalent to the noise measurement described by Eq.(5.33) [Reid & Drummond (90)]. The result that $\mathcal{V}_g$ depends on independent variations of Γ and Γ' only through their sum with the sum of the quadrature phases $\Psi + \Psi'$ means that it is equivalent to vary the selected quadrature changing the phase of the local oscillator or to shift both signal and idler fields by a proper phase with the phase retarders.
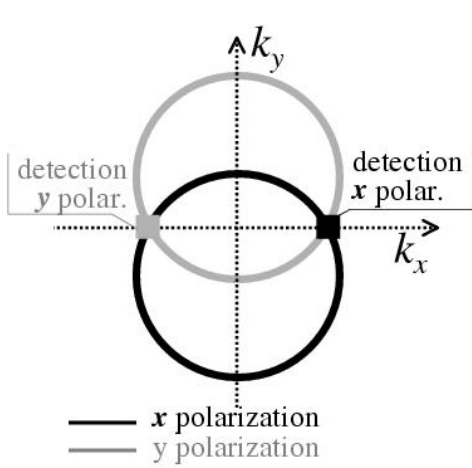
Figure 5.3: FF signal (black) and idler (grey) rings and detection scheme not influenced by the walk-off: The x and y polarizations are detected in the points $\pm\vec{k}_H$ where the rings cross (square symbols).
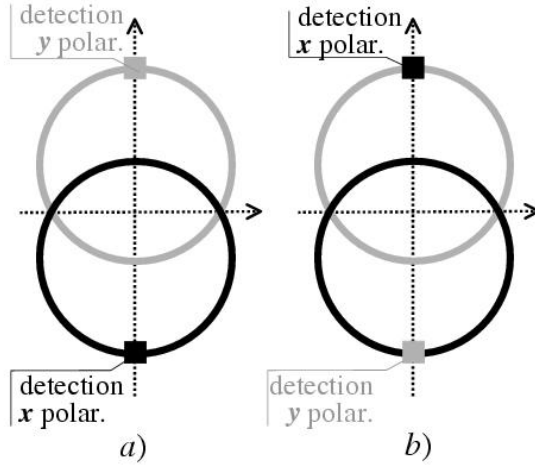
Figure 5.4: FF signal and idler rings and detection scheme influenced by the walk-off: a) The x and y polarized fields are detected in the points $\pm\vec{k}_V$ indicated by the square symbols, on the intense x polarized (black) and y polarized (grey) rings (bright detection). b) In the same points $\pm\vec{k}_V$ (square symbols) the orthogonal polarizations y and x are detected (dark detection).

In order to study how correlations change in different spatial points of the FF we consider two detection schemes, with detectors in opposite FF points, which represent possible extreme cases:

- In the first detection scheme the field is detected in the crossing points $\pm\vec{k}_H$ of the signal and idler rings in the FF, as represented in Fig. 5.3. Being these points in the line $k_y = 0$, they are not affected by the transverse walk-off. In Fig. 5.3 we indicate the case in which in one point the polarization component x is selected and in the opposite point the polarization y is selected. In Sect. 5.2.1 we will show that for these special points of the FF any change in the selection of the polarization does not influence the results given by Eq. (5.35).

- In the second arrangement, shown in Fig. 5.4, the detectors are located in a couple of opposite points $\pm\vec{k}_V$ on the line $k_x = 0$, where the walk-off effect is more pronounced. In Sect. 5.2.2 we will consider the effect of changing the polarization state selected. We can distinguish two extreme cases: Fig.5.4a shows the arrangement in which the most intense polarization components on the rings are detected. We name this scheme as "vertical bright scheme". Fig.5.4b shows the case in which the y (x) polarization component is selected on the intense lower (upper) circle x (y) polarized. We name this scheme as "vertical dark scheme".

5.2.1   EPR between far field modes unaffected by walk-off

In the line $k_y = 0$ there is no effect of the transverse walk-off and the coefficients given by Eqs.(5.8), (5.10) and (5.11) have the following reflection symmetry:

$$
\begin{aligned}
U_j(k_x, k_y = 0) &= U_j(-k_x, k_y = 0) \\
V_j(k_x, k_y = 0) &= V_j(-k_x, k_y = 0)
\end{aligned}
\tag{5.36}
$$

with $j = 1, 2$. The results presented in this section are strongly dependent on this symmetry, generally present also in previous treatments of spatial EPR correlations and squeezing.

Even with this symmetric form of the coefficients the variance given by Eq.(5.35) is a complicated function of many parameters. For the sake of simplicity we first consider Eq.(5.35) in the case of $g = 1$ (see Eq.(5.32)). The microscopic process of generation of twin photons with linear orthogonal polarization ($\Theta = 0$ and $\Theta' = \pi/2$) suggests a natural choice for the relative phases of the polarizers. Hence we consider a case in which the polarizers in the opposite points $\pm\vec{k}_H$ have a relative phase fixed by

$$
\Theta' = \Theta + \pi/2.
\tag{5.37}
$$

Using this relation between Θ' and Θ, Eq.(5.35) becomes independent of Θ for $g = 1$ when the additional choice

$$
\Gamma' = \Gamma + \pi
\tag{5.38}
$$

is also made. With these particular choice of parameters, Eq. (5.35) for the $\pm\vec{k}_H$ points (5.20) reduces to:

$$
\begin{aligned}
\mathcal{V}_{g=1}(\pm\vec{k}_H, \omega; [\Gamma, \Theta, \Psi, \Gamma + \pi, \Theta + \pi/2, \Psi']) &= \sigma \Big[\, |e^{i(\Psi+\Psi'+\Gamma)}U_1(\vec{k}_H, \omega) + V_2^*(\vec{k}_H, -\omega)|^2 \\
&+ \quad |e^{i(\Psi+\Psi'+\Gamma)}U_1(\vec{k}_H, -\omega) + V_2^*(\vec{k}_H, \omega)|^2 \Big].
\end{aligned}
\tag{5.39}
$$

Eq.(5.39) explicitly shows that the fluctuations in any quadrature of the difference of opposite spatial modes $\pm\vec{k}_H$, with relative polarizations fixed by Eqs.(5.37)-(5.38), are independent of the choice of the polarization reference Θ.

With the above motivation for the relations between phase parameters, we analyze the EPR correlations in the $\pm\vec{k}_H$ points (Fig. 5.3) fixing the parameters $\Theta = 0$, $\Gamma = \pi$, $\Theta' = \pi/2$, $\Gamma' = 2\pi$, so that $\hat{A}_{\Gamma\Theta}^{\Psi} = \hat{A}_1^{\Psi}$ and $\hat{A}_{\Gamma'\Theta'}^{\Psi'} = \hat{A}_2^{\Psi}$, and varying the quadrature angles Ψ, Ψ'. There is no loss of generality in this choice of Γ and Θ since Eq.(5.39) is independent of Θ, and the phase Γ can be absorbed in the quadrature angles $\Psi + \Psi'$. As discussed previously (see Eq.(5.32)), EPR entanglement is guaranteed – for some quadratures ($\Psi + \Psi'$) – if both the 'position' and 'momentum' operators

$$
\hat{A}_1^{\Psi}(\vec{k}_H) - \hat{A}_2^{\Psi'}(-\vec{k}_H) = [\hat{A}_1(\vec{k}_H)e^{i\Psi} + H.c.] - [\hat{A}_2(-\vec{k}_H)e^{i\Psi'} + H.c.]
\tag{5.40}
$$

$$
\hat{A}_1^{\Psi+\pi/2}(\vec{k}_H) + \hat{A}_2^{\Psi'+\pi/2}(-\vec{k}_H) = [i\hat{A}_1(\vec{k}_H)e^{i\Psi} + H.c.] + [i\hat{A}_2(-\vec{k}_H)e^{i\Psi'} + H.c.]
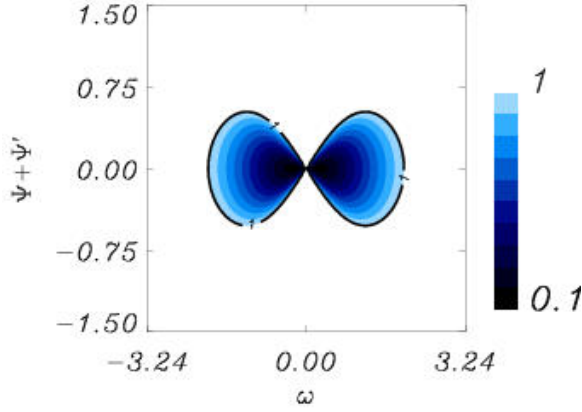\tag{5.41}
$$

Figure 5.5: $\mathcal{V}_{g=1}(\pm\vec{k}_H,\omega;\vec{\Phi})/\sigma$ for $\vec{\Phi} = (\pi,0,\Psi,0,\pi/2,\Psi')$ as a function of $\Psi + \Psi'$ (rad) and the frequency ω. EPR entanglement is obtained for values less than 1 (dark line). Values above 1 outside this line are not displayed.
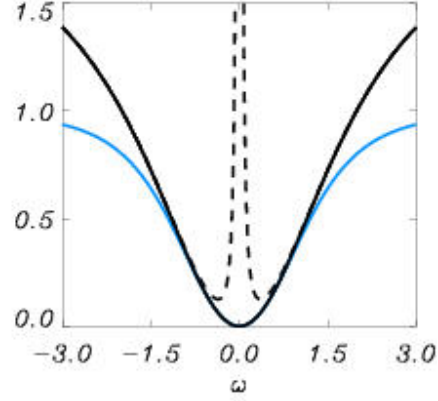
Figure 5.6: $\mathcal{V}_g(\pm\vec{k}_H,\omega;\vec{\Phi})/\sigma$ for $\Psi+\Psi' = 0$ and $g = 1$ (dark continuous line), for $\Psi + \Psi' = 0$ and $g = \bar{g}$ (light continuous line), and for $\Psi + \Psi' \simeq 0.06$rad and $g = 1$ (dashed line).

show simultaneously a variance below the reference value σ. This value corresponds to the shot noise level of both $\hat{A}_1^\Psi(\vec{k}_H)$ and $\hat{A}_1^{\Psi+\pi/2}(\vec{k}_H)$. Using Eq. (5.35) it turns out that (5.40) and (5.41) have the same spectral variance. Therefore, in the following we only consider Eq. (5.35) normalized to the shot noise level σ for the 'position' operator Eq. (5.40), which is identified by the angles $\vec{\Phi} = (\pi,0,\Psi,0,\pi/2,\Psi')$.

In Fig. 5.5 we represent the normalized variance $\mathcal{V}_{g=1}(\pm\vec{k}_H,\omega;\vec{\Phi})/\sigma$ for the points $\pm\vec{k}_H$. When this normalized variance is less than 1, we find EPR entanglement. We see a maximum noise reduction for $\Psi + \Psi' = 0$, and for $\omega = 0$. Fig.5.6 shows a cut of Fig.5.5 for $\Psi + \Psi' = 0$ (continuous black line). A variation in the quadrature angle results in a mixing of squeezed and unsqueezed quadratures degrading the entanglement: strongest degrading effects are evident at small frequency (dashed black in Fig.5.6).

The fact that there is maximum noise reduction for $\Psi+\Psi' = 0$ can be understood by analogy with the result for the single-mode non-degenerate OPO of Ref.[Reid & Drummond (90)]. In fact, for the case of vanishing detunings of the signal and idler and for real pump, which was the one considered in Ref. [Reid & Drummond (90)], the squeezing direction corresponds to the real quadratures ($\Psi = \Psi' = 0$). In our case we find an analogous result because we are also considering a real pump, and the effective detunings, given by (5.8), also vanish: $\Delta_j(\vec{k} = \pm\vec{k}_H,\omega = 0) = 0$.

Our calculations allows us to search for EPR entanglement considering any couple of opposite FF modes (distinguished by their transversal wavevector) and selecting *any* polarization. We have found EPR entanglement for the modes $\pm\vec{k}_H$ for any choice of the polarization component in $-\vec{k}_H$ (varying Θ), if in $+\vec{k}_H$ we select the orthogonal polarization ($\Theta' = \Theta + \pi/2$). In these far field points $\pm\vec{k}_H$, which are not affected by the walk-off, any mixing of the the signal and idler fields detected in a point is entangled with the field in the symmetric point, if this is also properly mixed (Eqs.(5.37)-(5.38)).

So far we have considered the case $g = 1$ and we have found a sufficient condition to guarantee EPR entanglement between the modes $\pm\vec{k}_H$ is fulfilled (see Eq.5.32). If we now optimize the noise reduction considering $g = \bar{g}$ we obtain the results shown in Fig.5.7. Comparing the normalized variance $\mathcal{V}_{g=1}$ (Fig. 5.5) with $\mathcal{V}_{\bar{g}}$ (Fig. 5.7) we observe that with the choice $g = \bar{g}$, EPR entanglement is observed in a larger frequency bandwidth. For a more direct comparison of the variances obtained for $g = \bar{g}$ and $g = 1$, both quantities are plotted for

Figure 5.7: Same as in Fig.5.5, but for the choice $g = \bar{g}$.

$\Psi + \Psi' = 0$ in Fig.5.6: for small frequencies the results are very similar, while for increasing values of the frequencies the choice $g = \bar{g}$ allows to observe EPR entanglement even when this effect is lost for $g = 1$.

Our strong EPR correlations have been obtained for $\Theta' = \Theta + \pi/2$. As already mentioned, this phase relation corresponds to the underlying process governing the creation of twin photons with orthogonal polarizations. In addition, for $g = 1$ we have obtained that the EPR correlations are independent of Θ. If we decrease the relative angle between Θ and Θ', we observe a progressive reduction of the entanglement. In the limit case $\Theta = \Theta'$ the correlation between opposite spatial modes is vanishing and $\mathcal{V}_g > \sigma$. In fact in this case no twin photons are detected.

5.2.2   EPR between far field modes in the walk-off direction

In this section we study possible EPR entanglement for opposite points of the far field along the walk-off direction (y), in the arrangements shown in Fig.5.4. An important effect of the transverse walk-off is breaking a reflection symmetry in the far field. This symmetry is generally broken for $k_y \neq 0$. For the points shown in Fig.5.4

$$U_j(k_x = 0, k_y) \quad \neq \quad U_j(k_x = 0, -k_y) \qquad j = 1, 2 \tag{5.42}$$

$$V_j(k_x = 0, k_y) \quad \neq \quad V_j(k_x = 0, -k_y) \qquad j = 1, 2. \tag{5.43}$$

Following the considerations in the previous Section, we will also consider here the case of phase polarizations $\Theta, \Theta', \Gamma, \Gamma'$ fixed by Eqs.(5.37)-(5.38). For this special choice of phase relations, the variance (5.35) for arbitrary g reduces to:

$$\mathcal{V}_g(\pm\vec{k}, \omega; \vec{\Phi}) = \tag{5.44}$$

$$\sigma\{\cos^2\Theta[|e^{i(\Psi+\Psi'+\Gamma)}U_1(\vec{k},\omega) + g^*V_2^*(-\vec{k},-\omega)|^2 + |e^{i(\Psi+\Psi'+\Gamma)}g^*U_1(\vec{k},-\omega) + V_2^*(-\vec{k},\omega)|^2]$$

$$+ \sin^2\Theta[|e^{i(\Psi+\Psi'+\Gamma)}U_1(-\vec{k},-\omega) + g^*V_2^*(\vec{k},\omega)|^2 + |e^{i(\Psi+\Psi'+\Gamma)}g^*U_1(-\vec{k},\omega) + V_2^*(\vec{k},-\omega)|^2]\}.$$
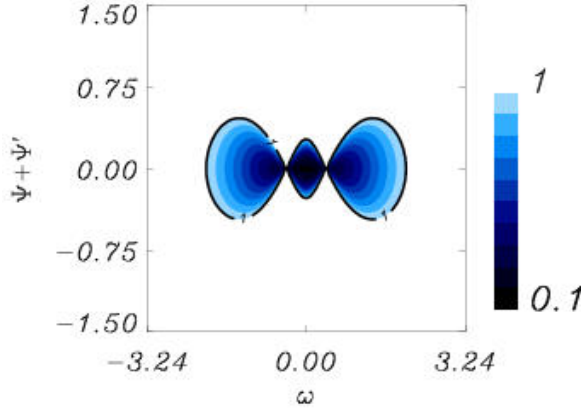
Figure 5.8: $\mathcal{V}_{g=1}(\pm\vec{k}_V, \omega; \vec{\Phi})/\sigma$ for $\vec{\Phi} = (\pi, \pi/2, \Psi, 0, \pi, \Psi')$ as a function of $\Psi + \Psi'$ (rad) and the frequency ω. The detection scheme is the one shown in Fig.5.4a. EPR entanglement is obtained for values less than 1 (dark line). Values above 1 outside this line are not displayed.
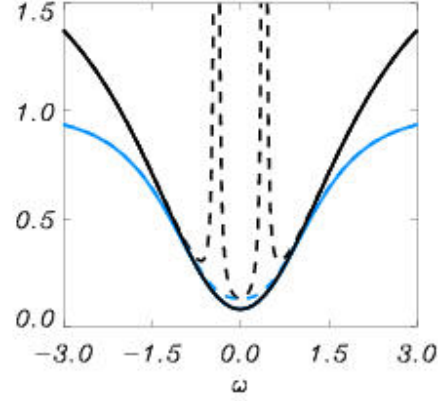
Figure 5.9: Dependence of $\mathcal{V}_g(\pm\vec{k}_V, \omega; \vec{\Phi})/\sigma$ on the frequency ω, for $\Psi + \Psi' = 0$ and $g = 1$ (dark continuous line), for $\Psi + \Psi' = 0$ and $g = \bar{g}$ (light continuous line), for $\Psi + \Psi' \simeq 0.06$rad and $g = 1$ (dark dashed line), and for $\Psi + \Psi' \simeq 0.06$rad and $g = \bar{g}$ (light dashed line).

The lack of reflection symmetry implies that the variance $\mathcal{V}_g(\pm\vec{k}, \omega; \vec{\Phi})$ depends now on the angle Θ and a simple result analogous to Eq.(5.39) cannot be obtained when $k_y \neq 0$. Eq.(5.44) depends on the sum $\Psi + \Psi' + \Gamma$: therefore, without loss of generality, we can absorb the effect of the wave retarder in the phase of the local oscillator, fixing the angle $\Gamma = \pi$ as in Sect.5.2.1. In the following we consider the dependence of Eq.(5.44) on the angle Θ. Varying Θ different polarization components are selected locally. We will see that the selection of different values of Θ can improve or degrade EPR entanglement. In particular we consider two values for the angle Θ ($= 0, \pi/2$) leading to very different situations.

First we consider the case represented in Fig.5.4a, in which the polarizer is oriented in such a way that the most intense linear polarization component is selected locally. We are selecting two critical spatial modes $\hat{A}_1(-\vec{k}_V)$ and $\hat{A}_2(\vec{k}_V)$, whose quantum fluctuations are weakly damped. This is the "vertical bright" detection scheme. In order to detect the intense polarization components at $\pm\vec{k}_V$ the phase Θ must be fixed at

$$\Theta = \pi/2 \tag{5.45}$$

and, given Eq.(5.37), $\Theta' = \pi$. Therefore the phases to be considered are $\vec{\Phi} = (\pi, \pi/2, \Psi, 0, \pi, \Psi')$. We first consider the case $g = 1$. We look for EPR entanglement between the 'position' and 'momentum' quadratures

$$\hat{A}_1^{\Psi'}(-\vec{k}_V) - \hat{A}_2^{\Psi}(\vec{k}_V), \qquad \hat{A}_1^{\Psi'+\pi/2}(-\vec{k}_V) + \hat{A}_2^{\Psi+\pi/2}(\vec{k}_V). \tag{5.46}$$

We will only show the variance of the 'position' quadrature, the orthogonal one being equivalent. We obtain EPR entanglement, as shown in Fig.5.8. Maximum noise reduction is obtained for for $\Psi + \Psi' = 0$. The variance $\mathcal{V}_{g=1}$ normalized to σ and for $\Psi + \Psi' = 0$ is represented as a function of the frequency ω

in Fig.5.9: the best entanglement is observed for $\omega = 0$. Also in this case a variation in the quadrature angle $\Psi + \Psi'$ results in a mixing of squeezed and unsqueezed quadratures degrading the entanglement (Fig.5.9). We note an important difference with respect to the case for $\pm \vec{k}_H$: in Fig.5.6 the largest degradation of entanglement for $\Psi + \Psi' \neq 0$ was observed for vanishing frequency ($\omega \simeq 0$), while in Fig.5.9 we see that for vanishing frequency the entanglement is only partially degraded. The largest degradation occurs now for $\omega \simeq \pm 0.4045$ (two peaks in Fig.5.9). This is the value of the Hopf frequency ω_H for the mode $\vec{k}_V$, as can be easily checked by Eq.(5.16).

In Fig. 5.10 we show the optimized ($g = \bar{g}$) variance $\mathcal{V}_{g=\bar{g}}$ (5.44) normalized to the shot noise σ. We obtain EPR maximum entanglement for $\Psi + \Psi' = 0$ and for small frequencies. Both the minimum and maximum fluctuations are obtained in a bandwidth of frequencies centered in zero, as in the case for the points $\pm \vec{k}_H$. The effects of the Hopf frequency found for $g = 1$ disappear for $g = \bar{g}$. A clear difference with respect to the variance $\mathcal{V}_{g=\bar{g}}$ obtained in Sect.5.2.1 is the level of maximum noise suppression reached. Even if in both cases we observe strong EPR entanglement, in this "vertical bright" arrangement the quadratures corre-

Figure 5.10: $\mathcal{V}_{g=\bar{g}}(\pm \vec{k}_V, \omega; \vec{\Phi})/\sigma$ as in Fig.5.8, but for the choice $g = \bar{g}$.

lations are reduced, as can be seen comparing Fig.5.6 and Fig.5.9. This reduction is caused by the walk-off. The fields in the critical modes $\pm \vec{k}_H$ –not affected by walk-off– have vanishing effective detunings (5.8) for the threshold frequency $\omega_H(\vec{k}_H) = 0$; while the fields in the critical modes $\pm \vec{k}_V$ –in the walk-off direction– have vanishing effective detunings (5.8) for the threshold frequency $\omega_H(\pm \vec{k}_V) \neq 0$. The fact that the detunings do not vanish for $\omega = 0$ seems to be the mechanism responsible for the reduction of squeezing at $\omega = 0$ for the modes $\pm \vec{k}_V$. On the other hand, also the unsqueezed quadrature is influenced by this effect, showing a reduced amplification with respect to the values obtained for the points $\pm \vec{k}_H$. Comparing Figs.5.7 and 5.10, we see that in this "vertical bright" arrangement the variance is less sensible to deviations of the quadrature phases selected, with respect the optimum choice $\Psi + \Psi' = 0$. In Fig.5.10 we observe a broad interval of phases $\Psi + \Psi'$ giving EPR entanglement for $\omega = 0$.

Next we consider the detection scheme of Fig.5.4b. In this case the phase of the polarizer at $+\vec{k}_V$ is fixed at

$$\Theta = 0, \tag{5.47}$$

and $\vec{\Phi} = (\pi, 0, \Psi, 0, \pi/2, \Psi')$. With this selection of the phases of the polarizers the intense field component are filtered out. In this "vertical dark" detection scheme, the detected modes ($\hat{A}_1(\vec{k}_V)$ and $\hat{A}_2(-\vec{k}_V)$) have low intensities. The main point is that now we are considering **non critical modes**
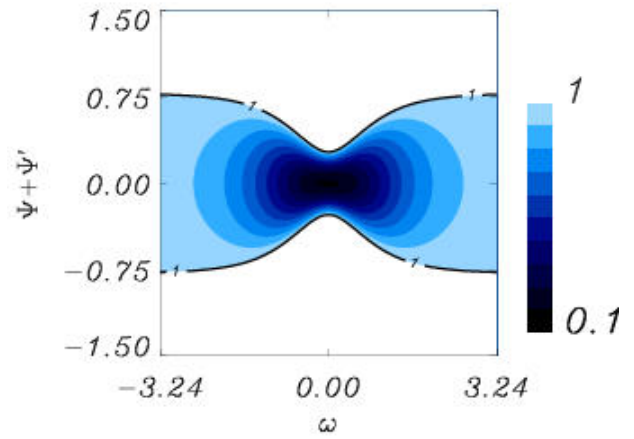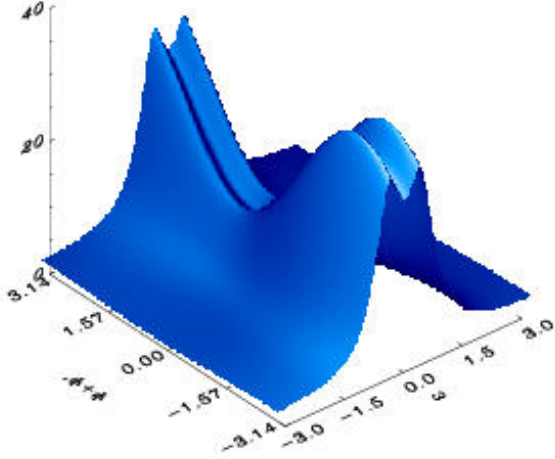
Figure 5.11: $\mathcal{V}_{g=1}(\pm\vec{k}_V,\omega;\vec{\Phi})/\sigma$ for $\vec{\Phi} = (\pi,0,\Psi,0,\pi/2,\Psi')$, as a function of $\Psi + \Psi'$ (rad) and frequency ω. The detection scheme is the one shown in Fig.5.4b.
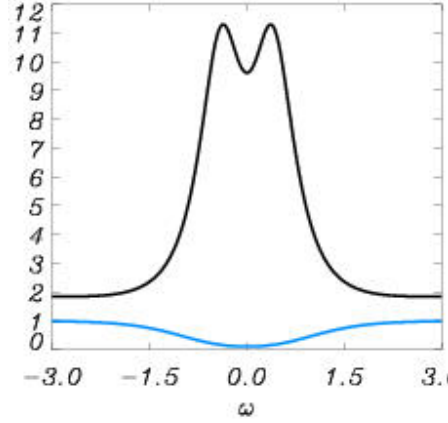
Figure 5.12: Dependence of $\mathcal{V}_g(\pm\vec{k}_V,\omega;\vec{\Phi})/\sigma$ on the frequency ω, for $\Psi + \Psi' = \bar{\Psi}$ and $g = 1$ (dark continuous line), for $\Psi + \Psi' = \bar{\Psi}$ and $g = \bar{g}$ (light continuous line). $\bar{\Psi} \simeq 0.81$rad.

that are strongly damped at any frequency (see Sect.5.1). We evaluate again the spectral variances of the position and momentum quadratures. In this case the results obtained for $g = 1$ and $g = \bar{g}$ are completely different. We start considering Eq.(5.44) for $g = 1$. We obtain that $\mathcal{V}_{g=1}$ is always larger than σ, therefore no EPR entanglement is observed (see Fig.5.11). In the same way that in the vertical bright scheme, the largest fluctuations are observed at $\omega \neq 0$. Fig.5.12 shows a cut of Fig.5.11 for the quadrature $\bar{\Psi}$, for which there is a minimum in the direction $\Psi + \Psi'$.

We now consider the variance (5.44) for the best choice $g = \bar{g}$. We find that $\mathcal{V}_{\bar{g}}$, represented in Fig.5.13, is reduced below the shot noise level σ for a large region of parameters. Therefore, with a proper choice of g, EPR entanglement is obtained also in this case. From Fig.5.13 we also see that for $\Psi + \Psi' = 0$ only small entanglement would be observed, and in the region of large frequencies. In fact, the quadrature at which strong EPR effects are observed is $\Psi + \Psi' = \bar{\Psi} \neq 0$. Fig.5.12 shows $\mathcal{V}_{\bar{g}}$ for this choice of $\Psi + \Psi'$. Changing the walk-off parameter we have found that $\bar{\Psi}$ increases
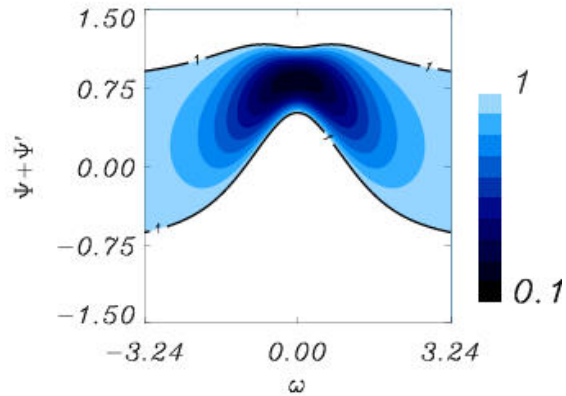

Figure 5.13: Same as in Fig.5.11, but for the choice of $g = \bar{g}$. EPR entanglement is obtained for values less than 1 (dark line). Values above 1 outside this line are not displayed.
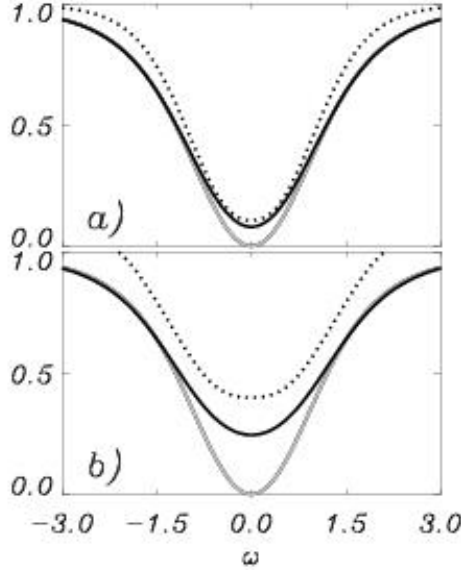
Figure 5.14: Spectral variance $\mathcal{V}_{\bar{g}}$ as a function of frequency, for the detection schemes represented in Fig.5.3 (light line), Fig.5.4a (dark continuous line), and Fig.5.4b (dark dotted line). The angles $\Psi + \Psi' = 0, 0, 0.81$ rad are selected respectively for each detection scheme. a) walk-off $\rho_2 = 1$; b) walk-off $\rho_2 = 1.5$.

with the walk-off.

In Fig.5.14 we show a comparison of the best EPR entanglement ($g = \bar{g}$, optimum $\Psi + \Psi'$) found for the three detection schemes considered, namely Fig.5.3, Fig.5.4a and Fig.5.4b. We observe that the correlations are less important when we move from the detection scheme of Fig.5.3 to the the "vertical bright" and "vertical dark" schemes of Fig.5.4a and Fig.5.4b. We also show the effects of increasing the walk-off: we can see that EPR entanglement in the "vertical dark" and "bright" schemes get worst increasing the walk-off strength. Obviously the results for the detection scheme of Fig. 5.3 are not influenced by walk-off.

5.3 Stokes operators: Far field local properties

In the previous Section we have seen how the selection of different polarization components in the far field influences the quadratures EPR entanglement between opposite FF points. The results we have obtained also show the effects of the transverse walk-off. In this Section our aim is to characterize the polarization properties of a type II OPO, when transverse walk-off is taken into account. The polarization state of the field in any point of the transverse plane can be characterized in terms of the Stokes parameters [Born & Wolf]. An operational definition of the Stokes parameters is given by use of polarizers and retarders [Born & Wolf, Hecht]. In the quantum formalism there are different ways to describe the polarization giving the same classical limit [Hakioglu, Tsegaye & al.]. Here we consider the quantum Stokes operators $\hat{S}_j(\vec{k}, t)$ ($j = 0, 1, 2, 3$), for each FF mode $\vec{k}$, obtained replacing by creation and annihilation operators the corresponding observables in the classical definitions (see Ref. [Usachev & al.] and references therein):

$$\hat{S}_0(\vec{k}, t) = \hat{A}_1^\dagger(\vec{k}, t)\hat{A}_1(\vec{k}, t) + \hat{A}_2^\dagger(\vec{k}, t)\hat{A}_2(\vec{k}, t) \tag{5.48}$$

Figure 5.15: (a) Classical and (b) quantum Stokes vectors mapped on a Poincaré sphere; the ball at the end of the quantum vector visualizes the quantum noise in $\hat{S}_1$, $\hat{S}_2$, and $\hat{S}_3$; and the quantum sphere thickness visualizes the quantum noise in $\hat{S}_0$. Taken from [Bowen & al.]
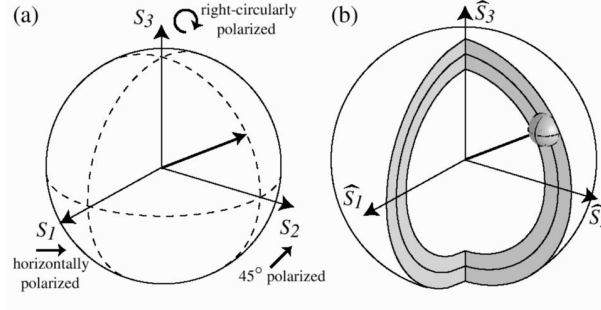
is the total intensity operator,

$$\hat{S}_1(\vec{k},t) = \hat{A}_1^\dagger(\vec{k},t)\hat{A}_1(\vec{k},t) - \hat{A}_2^\dagger(\vec{k},t)\hat{A}_2(\vec{k},t) \tag{5.49}$$

gives the difference between the x and y linear polarizations,

$$\hat{S}_2(\vec{k},t) = \hat{A}_1^\dagger(\vec{k},t)\hat{A}_2(\vec{k},t) + \hat{A}_2^\dagger(\vec{k},t)\hat{A}_1(\vec{k},t) \tag{5.50}$$

gives the difference between the $45°$ and $135°$ linear polarizations, and

$$\hat{S}_3(\vec{k},t) = -i(\hat{A}_1^\dagger(\vec{k},t)\hat{A}_2(\vec{k},t) - \hat{A}_2^\dagger(\vec{k},t)\hat{A}_1(\vec{k},t)) \tag{5.51}$$

gives the difference between the right-handed and the left handed circular polarizations components [2]. The definitions (5.48)-(5.51) correspond, except for a constant, to the the Schwinger transformation of the modes $\hat{A}_1(\vec{k},t)$ and $\hat{A}_2(\vec{k},t)$ giving operators satisfying angular momentum commutation relations [Söderholm & al.]:

$$\left[\hat{S}_0(\vec{k},t), \hat{S}_j(\vec{k}',t')\right] = 0 \tag{5.52}$$

$$\left[\hat{S}_j(\vec{k},t), \hat{S}_k(\vec{k}',t')\right] = 2i\epsilon_{jkl}\hat{S}_l(\vec{k},t)\delta(t-t')\sigma\delta_{\vec{k}\vec{k}'} \tag{5.53}$$

with $j,k,l = 1,2,3$ [3]. The precision of simultaneous measurements of the Stokes operators is limited by the Heisenberg principle. For instance we have

$$\Delta^2\hat{S}_1(\vec{k},t)\Delta^2\hat{S}_2(\vec{k},t') \geq \frac{1}{4}|\langle[\hat{S}_1(\vec{k},t), \hat{S}_2(\vec{k},t')]\rangle|^2 = |\langle\hat{S}_3(\vec{k},t)\rangle|^2\delta(t-t'). \tag{5.54}$$

The Stokes vector $\hat{\mathbf{S}} = (\hat{S}_1, \hat{S}_2, \hat{S}_3)$ can be represented in a quantum Poincaré sphere, with a radius defined by $\langle\hat{S}_0\rangle$ (see for instance Ref.[Korolkova & al.]). Given the fluctuations of $\hat{S}_i$, the quantum states are not defined by points on the surface of this sphere, but rather they are defined by different volumes, such as spheres (coherent states) or ellipsoids (squeezed states), as shown in Fig.5.15. These quantum uncertainty volumes on the Poincaré sphere have been confirmed by recent experiments [Bowen & al.]. The transformations Eqs.(5.23) and (5.24) introduced in the previous Section can be

---

[2] These Stokes parameters are function of the discretized FF modes introduced in Eq. 5.15.

[3] The factor $\sigma\delta_{\vec{k}\vec{k}'}$ appears due to the discretization introduced for the fields and is nonvanishing for Stokes parameters measured on overlapping regions.
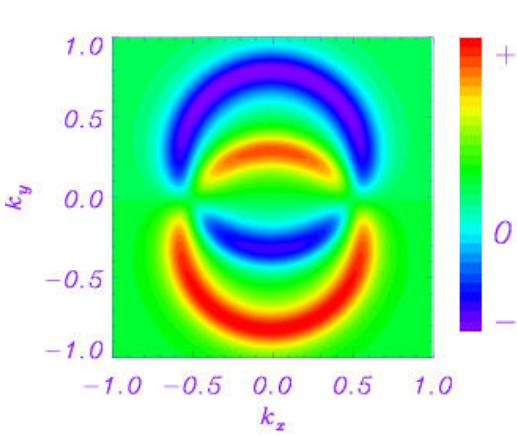
Figure 5.16: Stationary average of the Stokes operator $\langle \hat{S}_1(\vec{k}) \rangle$ in the FF (Eq.(5.55)).
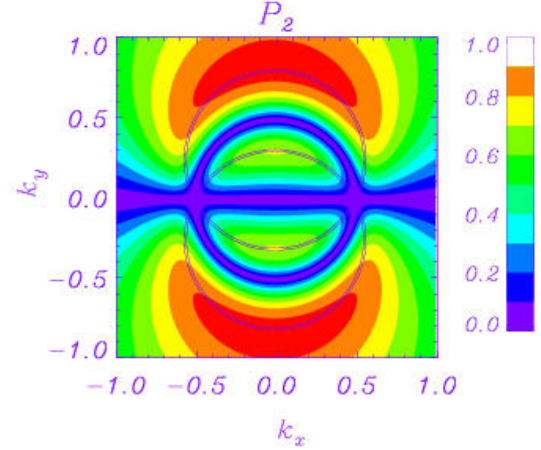
Figure 5.17: Second order polarization degree $P_2(\vec{k}, t)$ defined in Eq. (5.57). The two circles of double continuous line show the signal and idler maxima intensities.

also visualized in the Poincaré Sphere. In fact they correspond to a rotation in the Poincaré Sphere of an angle 2Θ around the S_3 axis and of $-\Gamma$ around the S_1 axis.

Given Eqs. (5.12-5.14) we obtain the stationary value of the average of the Stokes parameters in the FF points. The average of $\hat{S}_0$ is given in Eq. (5.18) and for the others Stokes parameters we find:

$$\langle \hat{S}_1(\vec{k}, t) \rangle = \frac{\sigma}{2\pi} \int d\omega (|V_1(\vec{k}, \omega)|^2 - |V_2(\vec{k}, \omega)|^2) \tag{5.55}$$

$$\langle \hat{S}_2(\vec{k}, t) \rangle = \langle \hat{S}_3(\vec{k}, t) \rangle = 0. \tag{5.56}$$

The average of $\hat{S}_2$ and $\hat{S}_3$ vanishes in any point of the far field, because any signal or idler photon has the same probability to be measured along the $45°$ and $135°$ polarizations directions. The same is true for the left and right circular polarizations. The equal average intensities at the output of the beam splitters are subtracted, giving vanishing values of $\langle \hat{S}_2 \rangle$ and $\langle \hat{S}_3 \rangle$ independently of the relative intensity of the signal and the idler. In Fig. 5.16 we show the far field spatial profile of $\langle \hat{S}_1 \rangle$: the lower ring is dominated by the linear polarization x while the upper one is dominated by the y polarization. If there was no walk-off, $\langle \hat{S}_1 \rangle$ would vanish in all the FF, while in our case ($\rho_1, \rho_2 \neq 0$) it only vanishes along the direction $k_y = 0$. Therefore, in the $\pm \vec{k}_H$ points we have an intense field (see $\hat{S}_0$ in Fig. 5.1) with vanishing average of the Stokes vector $\hat{\mathbf{S}}$ and with variances of $\hat{S}_i$ *not* limited by the Heisenberg principle, since from Eq. (5.54) $|\langle [\hat{S}_i(\vec{k}, t), \hat{S}_j(\vec{k}', t')] \rangle| = 0$, $i \neq j$.

The parameter that corresponds to the classical characterization of the polarization state of a quasi-monochromatic field, is the second order polarization degree

$$P_2(\vec{k}, t) = \frac{\sqrt{\sum_{j=1}^{3} \langle \hat{S}_j(\vec{k}, t) \rangle^2}}{\langle \hat{S}_0(\vec{k}, t) \rangle} \tag{5.57}$$

varying from $P_2 = 0$ for unpolarized light, to $P_2 = 1$ for completely polarized light. In Fig. 5.17 we observe how the polarization degree, that reduces to

$$P_2 = \frac{|\langle \hat{S}_1 \rangle|}{\langle \hat{S}_0 \rangle}, \tag{5.58}$$

varies in the FF: In particular, the intense FF rings are always polarized except around the line $k_y = 0$, where P_2 vanishes. Therefore, the field in the points $\pm \vec{k}_H$ is unpolarized in the ordinary sense. However the concept of polarized and unpolarized light needs to be generalized in quantum optics [Klyshko (97), Usachev & al., Söderholm & al., Prakash & Chandra, Luis]. The fact that $\langle \hat{S}_j \rangle = 0$ ($j = 1, 2, 3$), so that P_2 vanishes, does not guarantee to have an unpolarized state from a quantum point of view. Rather one has to consider the values of the higher order input moments of $\hat{S}_j$. [Klyshko (97)] showed that in the single-mode type II PDC, the squeezed vacuum is unpolarized in the ordinary sense ($P_2 = 0$) due to the diffusion in the difference of the signal and idler phases. On the other hand, due to the twin photon creation, there is complete noise suppression in the intensity difference of the two linearly polarized modes, i.e. in $\hat{S}_1$, leading to polarization squeezing [Chirkin & al.]. Due to this anisotropic distribution of the fluctuations in the Stokes vector $\hat{\mathbf{S}}$ there is a *"hidden polarization"* [Klyshko (97)], which has been observed experimentally recently [Usachev & al.]. We note that similar hidden polarization should be observed locally in the transverse near field plane of a type II OPO. Our interest here is in the far field plane, where twin photons are spatially separated.

In order to characterize the far field polarization properties, we proceed to evaluate the variance of the Stokes parameters. We define the spectral correlation function

$$\Gamma_i(\vec{k}, \vec{k}', \Omega) = \int dt e^{i\Omega t} [\langle \hat{S}_i(\vec{k}, t) \hat{S}_i(\vec{k}', 0) \rangle - \langle \hat{S}_i(\vec{k}, t) \rangle \langle \hat{S}_i(\vec{k}', 0) \rangle]. \tag{5.59}$$

Given the moments (5.12-5.14) and using the moments theorem [Goodman], we obtain non vanishing contributions only for $\vec{k}' = \vec{k}$ (self correlation) and for $\vec{k}' = -\vec{k}$ (twin photons correlation). For $\Omega = 0$, corresponding to integrating over a time interval long enough with respect to the cavity lifetime, the self correlation of $\hat{S}_1$ is

$$\Gamma_1(\vec{k}, \vec{k}, 0) = \sigma^2 \int \frac{d\omega}{2\pi} [|U_1(\vec{k}, \omega)|^2 |V_1(\vec{k}, \omega)|^2 + |U_2(\vec{k}, \omega)|^2 |V_2(\vec{k}, \omega)|^2] \tag{5.60}$$

while the twin photons correlation for opposite FF points is

$$\Gamma_1(\vec{k}, -\vec{k}, 0) = -\Gamma_1(\vec{k}, \vec{k}, 0). \tag{5.61}$$

It can be easily shown that the second and the third Stokes operators have equivalent variances:

$$\Gamma_2(\vec{k}, \vec{k}', \omega) = \Gamma_3(\vec{k}, \vec{k}', \omega). \tag{5.62}$$

For the self correlations we obtain

$$\Gamma_{2,3}(\vec{k}, \vec{k}, 0) = \sigma^2 \int \frac{d\omega}{2\pi} [|U_2(\vec{k}, \omega)|^2 |V_1(\vec{k}, \omega)|^2 + |U_1(\vec{k}, \omega)|^2 |V_2(\vec{k}, \omega)|^2] \tag{5.63}$$

and for the twin correlations

$$\Gamma_{2,3}(\vec{k}, -\vec{k}, 0) = \sigma^2 \int \frac{d\omega}{2\pi} [U_1^*(\vec{k}, \omega) U_1(-\vec{k}, -\omega) V_2^*(-\vec{k}, -\omega) V_2(\vec{k}, \omega) + c.c.] \tag{5.64}$$
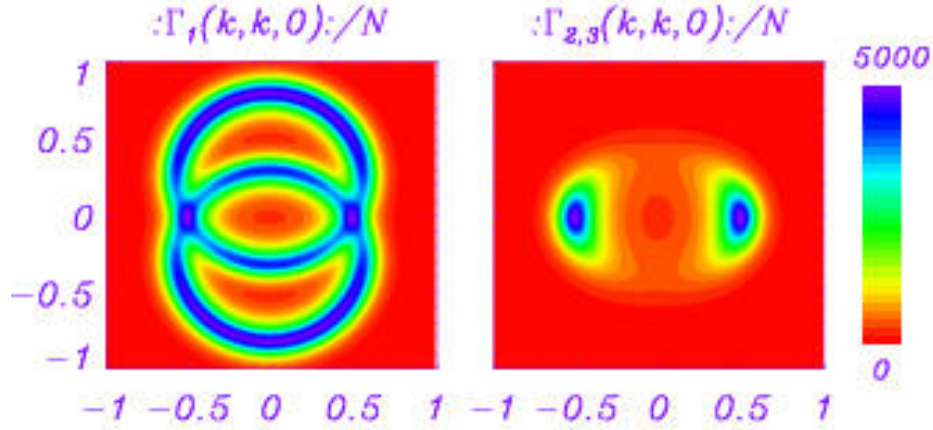
Figure 5.18: Normal ordered variances $\Gamma_1(\vec{k}, \vec{k}, 0)$ and $\Gamma_{2,3}(\vec{k}, \vec{k}, 0)$ normalized to the shot noise $N = \langle \hat{S}_0(\vec{k}, t) \rangle \sigma$.

For symmetry reasons Eq.(5.60) and Eq.(5.63) give identical results in the crossing points of the rings $\vec{k} = \vec{k_H}$ (see Fig. 5.18). Since the fluctuations are isotropically distributed in $\hat{S}$ no "hidden polarization" is observed in these points. Let us now consider the possibility of quantum effects. First, the shot noise level for all the Stokes parameters (i.e. $\Gamma_i(\vec{k}, \vec{k}, 0)$ evaluated on coherent states) is given by the average total intensity $\langle \hat{S}_0(\vec{k}, t) \rangle \sigma$ (see Eq. (5.18))[Korolkova & al., Klyshko (97)]. Inspection of Eq.(5.60) and Eq.(5.63) shows that all the Stokes operators have *classical* statistics in any FF point, as shown in Fig. 5.18. In these diagrams we represent the normal ordered variances. These are obtained from the variances Eq.(5.60) and Eq.(5.63) after subtraction of the corresponding shot noise. We see that these are positive quantities in all the far field, i.e. no polarization squeezing appears [Chirkin & al.]. The physical reason is that twin photons are emitted with opposite wave-vectors (opposite FF points), while locally no correlations between orthogonal polarizations are observed. This motivates us to consider in the next Section the correlations between the Stokes operators of twin beams.

In conclusion, when there is walk-off the polarization state (P_2) varies in the FF, the fluctuations in the Stokes parameters are above the classical level in all the far field and no polarization squeezing is observed. For $k_y = 0$ and in particular for $\pm \vec{k_H}$, $P_2 = 0$ and fluctuations are isotropically distributed in all Stokes parameters so that the field is completely *unpolarized*. This result would apply to all the FF plane if there was no walk-off.

5.4 Stokes operators: Far field correlations

From Eq. (5.61) and Eq. (5.64) we see that $\hat{S}_1$ for opposite FF modes is *anticorrelated*, while $\hat{S}_2$ and equivalently $\hat{S}_3$ are positively *correlated*. The physical reason for the sign of these correlations is always the underlying twin photon process which creates pairs of photons with opposite wave-vector and orthogonal polarizations x and y, leading to a positive correlation of the corresponding beam

intensities.

These considerations suggest to look for noise suppression in the following superpositions of Stokes operators

$$D_1(\vec{k}, \vec{k}', \omega) = \int dt e^{i\omega t} \{\langle [\hat{S}_1(\vec{k}, t) + \hat{S}_1(-\vec{k}', t)][\hat{S}_1(\vec{k}, 0) + \hat{S}_1(-\vec{k}', 0)]\rangle\} \tag{5.65}$$

and

$$D_i(\vec{k}, \vec{k}', \omega) = \int dt e^{i\omega t} \{\langle [\hat{S}_i(\vec{k}, t) - \hat{S}_i(\vec{k}', t)][\hat{S}_i(\vec{k}, 0) - \hat{S}_i(\vec{k}', 0)]\rangle\} \tag{5.66}$$

with $i = 0, 2, 3$. We note that $D_1(\vec{k}, \vec{k}', \omega) = D_0(\vec{k}, \vec{k}', \omega)$ (see the definitions Eq. (5.48) and (5.49)). In addition, it follows from Eqs.(5.63)-(5.64) that $D_2 = D_3$. These quantities are non-vanishing for opposite points $\vec{k}' = -\vec{k}$. From the unitarity of the transformation (5.9) we know that $|U_1(\vec{k}, \omega)|^2 = |U_2(-\vec{k}, -\omega)|^2$ and $|V_1(\vec{k}, \omega)|^2 = |V_2(-\vec{k}, -\omega)|^2$, so that from Eqs. (5.55) and (5.56) we obtain that

$$\langle \hat{S}_1(\vec{k}, t) + \hat{S}_1(\vec{k}', t)\rangle = \langle \hat{S}_i(\vec{k}, t) - \hat{S}_i(\vec{k}', t)\rangle = 0 \tag{5.67}$$

($i = 0, 2, 3$). Therefore Eqs.(5.65) and (5.66) actually define variances.

From Eq. (5.60-5.61) we obtain

$$D_1(\vec{k}, -\vec{k}, 0) = \Gamma_1(\vec{k}, \vec{k}, 0) + \Gamma_1(-\vec{k}, -\vec{k}, 0) + \Gamma_1(-\vec{k}, \vec{k}, 0) + \Gamma_1(\vec{k}, -\vec{k}, 0) = 0 \tag{5.68}$$

for any $\vec{k}$: There is complete noise suppression in the sum of the Stokes parameters $\hat{S}_1$ evaluated in opposite regions of the transversal field. Therefore the normal ordered variance is equal to minus the shot noise taking nonclassical negative values. In conclusion, due to the twin beams intensity correlations, we find entanglement for $\hat{S}_1$ evaluated in any opposite FF points and for any pump intensity.

The Stokes operators generally cannot be simultaneously measured with infinite precision (see Eq. (5.54)). Also the superpositions of Stokes operators involved in (5.65) and (5.66) are in principle limited by the Heisenberg relations. However we have that

$$\langle [\hat{S}_1(\vec{k}, t) + \hat{S}_1(-\vec{k}, t), \hat{S}_2(\vec{k}, t') - \hat{S}_2(-\vec{k}, t')]\rangle = 2i\sigma \langle \hat{S}_3(\vec{k}, t) - \hat{S}_3(-\vec{k}, t)\rangle \delta(t - t') = 0 \tag{5.69}$$

as follows from Eq. (5.67). Therefore there are superpositions of the Stokes operators whose measurement is not limited by Heisenberg relations because the average of their commutator vanishes. In the same way, also the other superpositions of Stokes operators for any couple of opposite points can be simultaneously measured with total precision. This result opens the possibility to observe noise suppression not only in the first Stokes operator superposition (5.68), but also in the other superpositions Eqs. (5.66). However, we obtain that

$$D_2(\vec{k}, -\vec{k}, 0) = \Gamma_2(\vec{k}, \vec{k}, 0) + \Gamma_2(-\vec{k}, -\vec{k}, 0) - \Gamma_2(-\vec{k}, \vec{k}, 0) - \Gamma_2(\vec{k}, -\vec{k}, 0) \neq 0, \tag{5.70}$$

so that $D_2(\vec{k}, -\vec{k}, 0)$ generally does not vanish for arbitrary $\vec{k}$. The profile of the normal ordered $D_2(\vec{k}, -\vec{k}, 0)$ is represented in Fig. 5.19: we observe that in most part of the far field where there is large light intensity this quantity is positive, giving classical statistics. However there is a bandwidth
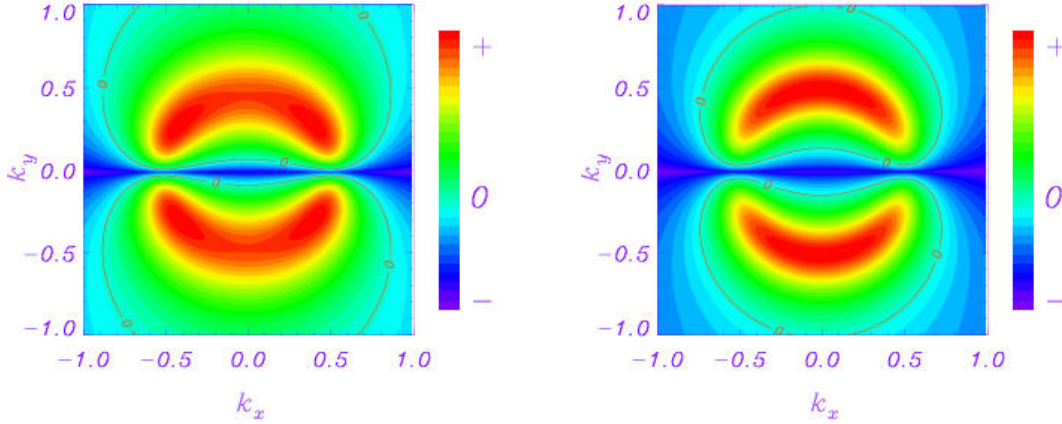
Figure 5.19: $D_2(\vec{k}, -\vec{k}, 0)$ normal ordered normalized to the shot noise. The white contour line shows the boundaries between classical and quantum statistics.

Figure 5.20: The same as in Fig. 5.19, but with walk-off $\rho_2 = 0.5$.

of small wave-vectors $k_y \sim 0$ for which the normal ordered D_2 is negative and therefore quantum effects are observed. This small bandwidth becomes smaller when increasing the walk-off, as can be seen comparing Fig. 5.19 –obtained with $\rho_2 = 1$– with Fig. 5.20 –obtained with $\rho_2 = 0.5$–.

In particular, along the $k_y = 0$ line, we obtain that $D_2(k_x, -k_x, 0) = 0$. This result easily follows from the symmetry Eq. (5.36). Therefore, along the $k_y = 0$ line we have $D_1 = D_2 = D_3 = 0$ which indicates perfect polarization entanglement between opposite FF modes. In summary, in the direction orthogonal to the walk-off ($k_y = 0$), we show complete noise suppression in properly chosen opposite modes superpositions of **all** the Stokes parameters. Along this line the two points $\pm\vec{k}_H$ are of special interest because they have a large photon number.

We finally point out that, the situation studied here is different from the case of bright squeezed light considered in Ref. [Korolkova & al.] and that the perfect correlations obtained between Stokes parameters cannot be used here to obtain an EPR paradox: in fact from Eq. (5.54) and Eqs. (5.55-5.56) we obtain that no limits in the local variances of the Stokes parameters are imposed by the Heisenberg principle.

5.5 Summary and Conclusions

We have investigated the EPR entanglement between quadrature-polarization components of the signal and idler fields in opposite FF points of a type II OPO blow threshold, paying special attention to the effects of walk-off. We have analyzed the effects of selecting different polarization components: when walk-off vanishes or in the far field region not affected by walk-off ($k_y = 0$), there is an almost complete suppression of noise in the proper quadratures difference of *any* orthogonal polarization components of

the critical modes (Sect. 5.2.1). Selecting non-orthogonal polarization components the correlations are reduced, vanishing for parallel polarizations. Walk-off strongly influences the strength of correlations. First, the variance of the quadratures difference of orthogonal polarization components depends on the reference polarization: the best EPR entanglement conditions are fulfilled when the most intense polarization components are locally selected ("vertical bright" scheme). If the selected polarizations are not the most intense ("vertical dark" scheme) we still find EPR entanglement, but correlations are reduced and there is also a rotation of the quadrature angle giving the best squeezing (Sect.5.2.2).

Our study of EPR quadrature correlations identifies how these correlations depend on the polarization state. We have further investigated non classical polarization properties in terms of the Stokes operators. The properties of the Stokes parameters in a single point of the far field do not show any non classical behavior (Sect.5.3). For $k_y = 0$, where there are no walk-off effects, we have shown that the average of the Stokes vector vanishes, and all the Stokes operators can be measured with perfect precision. All Stokes operators are very noisy (above the level of coherent states) and the fluctuations are not sensitive to polarization optical elements: in fact the field is completely unpolarized, i.e. there is no 'hidden' polarization. Quantum effects are observed when considering polarization correlations between two opposite points of the far field (Sect.5.4). Still in the direction orthogonal to the walk-off ($k_y = 0$) we show *perfect* entanglement of *all* the Stokes operators measured in opposite FF regions. This result is independent on the distance to the threshold. These results for $k_y = 0$ would apply in all the FF for vanishing walk-off. When there is walk-off and for $k_y \neq 0$ the entanglement in the second and third Stokes operators is lost, but for $\hat{S}_0$ and $\hat{S}_1$ there is still perfect correlation between two opposite points of the FF, reflecting the twin photon process emission.

Chapter 6

Summary and conclusions

In this work we have studied spatial quantum fluctuations in the transverse self-organized spatial structures (*quantum structures*) that arise when light interacts with a nonlinear medium in an optical cavity. We have considered devices such as the OPO and the Kerr resonator in several regimes of operation, with emphasis on those in which there is interaction among many macroscopically populated modes of the electric field. The quantum analysis of these regimes has been performed with different analytical and numerical methods. In fact, there do not exist methods of general validity to describe quantum nonlinear optical systems. Methodological aspects arising in the description of such systems have been constantly addressed in this work. In particular we have investigated the possibility offered by phase space methods in different representations.

In Ch.2 we have discussed the possibility to use a method proposed by Yuen and Tombesi in 1986 in a highly nonlinear problem. This method is based on a doubling phase space technique and allows to map a pseudo Fokker-Planck equation with negative diffusion for the evolution of the Q representation, into a set of stochastic equations for complex variables describing the fields. We have applied this method to the analytically soluble problem of the single-mode anharmonic oscillator: in this way it has been possible to compare the expectation value of the field operators with the averages calculated from the stochastic equations obtained in the Yuen-Tombesi approach. We have shown that the exact value for the moments of the field can be obtained from the stochastic differential equations in the doubled phase space. We have also identified a subtle problem of this approach. In fact the results are highly sensitive to the order in which averages are performed: averaging over initial conditions before performing the stochastic average gives the correct result. In the future it would be interesting to study if dissipation effects improve the range of applicability of the method. Future work on this subject should also allow for a direct comparison between this approach and the more popular P_+ representation.

In Ch.3 we have studied the spatial distribution and the quantum correlations of the field interacting with a Kerr medium in an optical resonator. Immediately above the threshold for pattern formation a stable stripe structure appears in the transverse profile of the field. The instability takes place in the polarization component of the field orthogonal to that of the pump (polarization instability). This

model was previously studied in a few modes approximation by [Hoyuelos & al. (99)]. In this work we have characterized the quantum structures arising above threshold using a continuous model, i.e. including the whole set of wave-vectors in the transverse plane. The method used is based on a linearization approximation: in the W representation we obtain a set of linear Langevin equations with spatial dependent coefficients, that can be numerically solved. These equations describe the spatio-temporal evolution of the fluctuations of the field around the stable stripe solution. This continuous model offers the possibility of studying single stochastic realizations of the dynamics of the fluctuations in the transverse plane. In this way we have reached a deep understanding of the spatial behavior of the quantum fluctuations.

We have identified the role played by the excitation of the Goldstone mode that tends to restore the translational symmetry broken by the appearance of the stripe structure. This mode is marginally stable and continuously excited by noise, giving a diffusion of the phase which fixes the position of the pattern. This Goldstone mode dominates the quantum fluctuations above threshold in any translational invariant systems. In general, moments involving such large (linearly undamped) fluctuations cannot be correctly described within a linearized approximation in the field amplitudes. In fact, such an approach leads to *unphysically divergent quadrature correlations*, although correct results can be obtained for the intensity correlations [Zambrini & al. (00), Gomila & Colet]. Increasing the transverse size of our system we have observed that quantum noise excites also long wavelength modes, that are weakly damped (soft modes). These soft modes are responsible for the local deformations of the fluctuating pattern.

In order to obtain the output correlations, we have formulated a general stochastic description of the spatial configuration of the output field immediately beyond the input/output mirror. We have shown that the spatial configuration of the output field is closely similar to that of the intracavity field, provided that it is averaged over a time window of the order of the cavity linewidth. The output fluctuations have been used to study spatial correlations. We have calculated the quantum correlation between the x-polarized homogeneous mode and the y-polarized tilted wave modes in the output field, as well as the correlation between the two tilted twin beams. The correlations between x and y polarization components of the field can be used to perform a quantum non-demolition (QND) measurement, inferring information about the x-polarized pump by looking at the y-polarized field. We have compared the prediction of the three-mode model [Hoyuelos & al. (99)] for the correlation functions, with those of our complete multimode model, finding good agreement close enough to threshold.

In Ch.4 we have studied spatial quantum fluctuations in a type I OPO in different regimes. Using a continuous model it has been possible to give the first description of the quantum effects associated with transverse walk-off in this device. Due to the interplay of the nonlinearity and of the transverse walk-off term there appear noise sustained patterns which are a macroscopic manifestation of quantum noise. In order to describe quantum fluctuations in such patterns, we have proposed two nonlinear methods (Sect.4.2.1): a time dependent parametric approximation and a stochastic method in the Q representation. Both methods have been shown to be useful, not only for the OPO in the convectively unstable regime where noise sustained patterns occur, but also for other devices and regimes. In fact, the time dependent parametric approximation has also been used in this work to describe the traveling

stable pattern in the absolutely unstable regime just above threshold, as well as the critical fluctuations at threshold. On the other hand, the stochastic equations in the Q representation have been used in this work to study the quantum fluctuations far from threshold, in multimode patterns and disordered structures, as well as the critical fluctuations at threshold. In Ref.[Bache & al.] this approach has also been used to study quantum fluctuations in SHG.

In the convective regime macroscopic multimode quantum fluctuations occur: our aim has been to study quantum effects in these noise sustained spatial structures (Sect.4.3). We have found that the squeezing (Sect.4.3.2) and twin-beams correlations (Sect.4.4.4) between far field modes are present near threshold but they do not survive when the noise is amplified to macroscopic values. In fact, the walk-off and the nonlinearities act as quantum decoherence mechanism, distributing part of the macroscopic fluctuations into the observables that were squeezed below threshold. The characterization of this regime has also been completed by the analysis of the temporal trajectories of the most intense far field signal modes and by the reconstruction of the corresponding Wigner distribution. Below threshold we have found the well known Gaussian shape of the squeezed vacuum, but in the convective regime the macroscopic character of the fluctuations is reflected in a extremely broad and non-Gaussian Wigner distribution. Nonlinear effects lead to the appearance of wings in the Wigner distribution, which are precursors of the pair of peaks appearing in the absolutely unstable regime.

Considering an OPO with a flat pump profile, the traveling pattern appearing at threshold is absolutely stable. In this regime we have studied the symmetry breaking effects of walk-off in the energy distribution of opposite far field modes (Sect.4.4). We have found that walk-off causes one beam to be more intense and it fluctuates more than the opposite one. Unexpectedly, also for such imbalance between the "twin" beams, the entanglement in fluctuations remains unchanged. If walk-off effects are neglected, the reflection symmetry in the far field is restored. In this case we have studied how twin beams correlations behave in the instability region and in multi-photon processes (Sects.4.4–4.5). Our continuous analysis (using both nonlinear approximations mentioned above) has shown that beam entanglement is preserved both in the threshold region, for undamped critical fluctuations, and above threshold, where more harmonics are excited in the stripe pattern. Twin-beams-like correlations appear above threshold in a multimode process. Such correlations do not follow from momentum conservation. Further above threshold we have calculated these intensity correlations in a regime of spatially disordered structures. We have found that quantum correlations persist even in this regime, in the bandwidth of intense signal modes, where they take a form that depends on the spatial pattern that is generated.

In Ch.5 we have studied the type II OPO in the regime of quantum images, below the threshold of pattern formation. The aim of our study has been to characterize the effects of the walk-off term and to study the polarization properties of this system. The walk-off influences non uniformly the far field points: in particular walk-off effects vanish in the axis $k_y = 0$ when walk-off is assumed in the direction y. We have found spatial EPR entanglement between opposite far field modes in different quadratures and polarization components. We have shown how these spatial correlations vary in the transverse far field plane: the best results are found in the region not influenced by the walk-off, while walk-off in general causes a reduction of the EPR entanglement (Sect.5.2).

To characterize the polarization state of the transverse field in any point we have calculated the variances and the correlations of the Stokes operators (Sect.5.3). In the direction where no walk-off effects are present ($k_y = 0$) we have shown that the field is unpolarized, and that the Stokes operators are very noisy (above the level of the coherent states). Nevertheless, we have shown perfect entanglement of all the Stokes operators measured in opposite points ($(\pm k_x, 0)$). In the regions influenced by the walk-off ($k_y \neq 0$) either the extraordinary or the ordinary field is locally more intense: the field in these points is polarized. Perfect entanglement in this case is found only in two of the four Stokes operators ($\hat{S}_0$ and $\hat{S}_1$). The entanglement in these operators is a consequence of twin-beam like correlations between opposite spatial points.

In summary, we have contributed to the understanding of the behavior of the quantum fluctuations in self-organized structures in optical systems. We have used continuous models, considering the whole set of the spatial modes of the transverse profile of the field. In this way we have given a complete description of the spatial distribution of the fluctuations. In general the advantage of continuous models is the possibility to follow the evolution of the spatial profiles of the fields in different regimes above threshold, where different patterns involving many modes arise. Within this approach we have also described the effects of symmetry breaking on the quantum correlations, considering translational and reflection symmetries.

We have considered both linear and nonlinear evolutions of the quantum fluctuations of the fields. Linear methods are well-known and are generally useful to describe quantum images, leading to twin photons correlations. On the other hand, we have proposed also nonlinear methods within proper phase space descriptions, that allowed to describe highly nonlinear interactions between field modes. In these regimes complex photons interactions take place, giving multi-photon processes, and in general the behavior of the spatial correlations is not predictable a priori. Our calculations showed that even in multimode patterns, twin-beams like correlations survive. We have also obtained non classical correlations in disordered structures (frozen chaos).

All the regimes that we have considered are characterized by large photon numbers. We have shown several examples of entanglement properties that survive in these regimes, in presence of macroscopic fields. Here observables such as intensities are described by continuous operators. The present interest for the quantum properties of these macroscopic states is demonstrated by several proposals to use these continuous variables in quantum information processes [Lloyd & Braunstein, Hald & al., Furusawa & al., Leuchs & al.] and in fundamental tests of quantum mechanics [Ralph & al., Chen & al., Reid & al.].

Appendix A

FPE and Langevin equations

In this Appendix we present a brief discussion of the link between a given Fokker-Planck equation and an equivalent stochastic system (a more complete account can be found in [Gardiner, San Miguel & Toral]). As we have already noted, the Fokker-Planck equation does not correspond to a unique stochastic system and so it is natural to start with a stochastic system. Consider the pair of (Langevin) SDEs

$$\frac{\partial \alpha}{\partial t} = B_\alpha + C_{\alpha\alpha} f_\alpha(t) + C_{\alpha\alpha^*} f_{\alpha^*}(t) \tag{A.1}$$

$$\frac{\partial \alpha^*}{\partial t} = B_{\alpha^*} + C_{\alpha^*\alpha^*} f_{\alpha^*}(t) + C_{\alpha^*\alpha} f_\alpha(t), \tag{A.2}$$

with white Gaussian noise terms f_i, defined to have zero average and second moments of the form

$$\langle f_i(t) f_j(t') \rangle = \delta_{ij} \delta(t - t') \tag{A.3}$$

and the subscripts i, j denote α and α^*.

The formal solution of equations (A.1) and (A.2) is:

$$\alpha(t) = \alpha(0) + \int_0^t dt' B_\alpha(t') + \int_0^t C_{\alpha\alpha} dW(t') + \int_0^t C_{\alpha\alpha^*} dW_*(t') \tag{A.4}$$

$$\alpha^*(t) = \alpha^*(0) + \int_0^t dt' B_\alpha^*(t') + \int_0^t C_{\alpha^*\alpha} dW(t') + \int_0^t C_{\alpha^*\alpha^*} dW_*(t'), \tag{A.5}$$

where we have introduced the Wiener processes $dW(t) = f_\alpha(t)dt$ and $dW_*(t) = f_{\alpha^*}(t)dt$.

In order to use these stochastic processes, we need to give a prescription for carrying out the stochastic integrals over the Wiener processes. In this paper, we choose the Stratonovich interpretation of the stochastic integral in which

$$\int_0^t g(\alpha, \alpha^*) dW(t') = \sum_i [W(t_i) - W(t_{i-1})] \cdot g\left(\frac{\alpha(t_i) + \alpha(t_{i-1})}{2}, \frac{\alpha^*(t_i) + \alpha^*(t_{i-1})}{2} \right). \tag{A.6}$$

The reason of this choice, instead of the Itô interpretation, is that we will be constructing analytical averages over the stochastic process and the Stratonovich formalism allows us to use the familiar rules of calculus.

From the Langevin equations it is possible to obtain a *unique* Fokker-Planck equation for the probability distribution $\mathcal{W}(\alpha(t), \alpha^*(t), t)$. If we consider the trajectory obtained in a single realization of the stochastic process $\vec{f} = (f_\alpha, f_{\alpha^*})$ and start from the initial value $\vec{\alpha}(0) = (\alpha(0), \alpha^*(0))$, then the solution at time t is completely determined and the probability distribution for it is the δ-function $\delta\left(\alpha - \alpha(t; \vec{\alpha}(0); [\vec{f}(t)])\right) \delta\left(\alpha^* - \alpha^*(t; \vec{\alpha}(0); [\vec{f}(t)])\right)$. Considering a set of initial conditions $\vec{\alpha_0}$, distributed according some initial distribution $p_0 = p(\vec{\alpha}(0); 0)$, we can obtain the shape of the distribution at time t:

$$p(\vec{\alpha}, t; [\vec{f}(t)]) = \langle \delta\left(\alpha - \alpha(t; \vec{\alpha}(0); [\vec{f}(t)])\right) \delta\left(\alpha^* - \alpha^*(t; \vec{\alpha}(0); [\vec{f}(t)])\right)\rangle_{p_0}, \tag{A.7}$$

where the subscript p_0 denotes an average over the initial probability distribution. The quantity p satisfies the conservation equation

$$\frac{\partial}{\partial t}p + \frac{\partial}{\partial \alpha}(\dot{\alpha}p) + \frac{\partial}{\partial \alpha^*}(\dot{\alpha}^*p) = 0. \tag{A.8}$$

The complete probability distribution is obtained by also averaging over the stochastic trajectories obtained with different noise realizations, denoted by the subscript $[\vec{f}(t)]$:

$$\mathcal{W}(\alpha, \alpha^*, t) = \langle p(\alpha, \alpha^*, t; [\vec{f}(t)])\rangle_{[\vec{f}(t)]}. \tag{A.9}$$

The time evolution for the distribution $\mathcal{W}$ can be obtained using the continuity equation and gives [Gardiner, Sancho & al.]:

$$\frac{\partial}{\partial t}\mathcal{W} = -\frac{\partial}{\partial \alpha}B_\alpha\mathcal{W} - \frac{\partial}{\partial \alpha^*}B_{\alpha^*}\mathcal{W} + \frac{1}{2}\sum_{ijl}\left[\partial_i C_{ij}\partial_l C_{lj}\right]\mathcal{W},$$

where the subscripts i, j, k again denote α and α^*. If compare this form of the Fokker-Planck equation with the Eq.(2.1) then we obtain the correspondences:

$$D_{\alpha\alpha} = C_{\alpha\alpha}^2 + C_{\alpha\alpha^*}^2 \tag{A.10}$$

$$D_{\alpha^*\alpha^*} = C_{\alpha^*\alpha^*}^2 + C_{\alpha^*\alpha}^2 \tag{A.11}$$

$$D_{\alpha\alpha^*} = C_{\alpha\alpha}C_{\alpha^*\alpha} + C_{\alpha^*\alpha^*}C_{\alpha\alpha^*} \tag{A.12}$$

$$A_\alpha = B_\alpha + \frac{1}{2}\left[\left(\frac{\partial}{\partial \alpha}C_{\alpha\alpha}\right)C_{\alpha\alpha} + \left(\frac{\partial}{\partial \alpha^*}C_{\alpha\alpha}\right)C_{\alpha^*\alpha} + \right.$$
$$\left. \left(\frac{\partial}{\partial \alpha}C_{\alpha\alpha^*}\right)C_{\alpha\alpha^*} + \left(\frac{\partial}{\partial \alpha^*}C_{\alpha\alpha^*}\right)C_{\alpha^*\alpha^*}\right] \tag{A.13}$$

$$A_{\alpha^*} = B_{\alpha^*} + \frac{1}{2}\left[\left(\frac{\partial}{\partial \alpha}C_{\alpha^*\alpha}\right)C_{\alpha\alpha} + \left(\frac{\partial}{\partial \alpha^*}C_{\alpha^*\alpha}\right)C_{\alpha^*\alpha} + \right.$$
$$\left. \left(\frac{\partial}{\partial \alpha}C_{\alpha^*\alpha^*}\right)C_{\alpha\alpha^*} + \left(\frac{\partial}{\partial \alpha^*}C_{\alpha^*\alpha^*}\right)C_{\alpha^*\alpha^*}\right]. \tag{A.14}$$

Note that these equations do not give unique forms for the B and C functions. This is a consequence of the lack of a unique stochastic representation for a given Fokker-Planck equation.

If our stochastic variables α and α^* are to be complex conjugate quantities, then it follows from equations (A.1) and (A.2) that $B_{\alpha^*}^* = B_\alpha$, $C_{\alpha\alpha}^* = C_{\alpha^*\alpha}$ and $C_{\alpha\alpha^*}^* = C_{\alpha^*\alpha^*}$. These conditions necessarily imply positive diffusion as, from (A.10) to (A.12), $D_{\alpha\alpha^*} > |D_{\alpha\alpha}|$. It follows that the stochastic variables cannot be complex conjugate quantities when we have negative diffusion. In order to avoid possible confusion, we replace the stochastic variable $\alpha^*(t)$ by $\alpha^+(t)$ whenever there is negative diffusion.

Appendix B

Phase matching in OPO's

Let us consider a three photon interaction in a quadratic nonlinear crystal ($\chi^{(2)}$ medium), with a polarization quadratic in the field. A pump photon at frequency ω_0 is converted into a signal and an idler photons at frequency ω_1 and ω_2, respectively. Conservation of energy and momentum require that

$$\hbar\omega_0 = \hbar\omega_1 + \hbar\omega_2 \tag{B.1}$$

$$\hbar\vec{k}_0 = \hbar\vec{k}_1 + \hbar\vec{k}_2, \tag{B.2}$$

where $\vec{k}$ is the wave-vector of the photon. These relations are the frequency and phase matching conditions. This three photon interaction is the fundamental process in OPO(see Ch.1). In this work we have considered frequency degenerate OPO's, such that $\omega_1 = \omega_2 = \omega$ and $\omega_0 = 2\omega$.

Given

$$k = |\vec{k}| = \frac{n\omega}{c}, \tag{B.3}$$

with n the refraction index, if the medium is non-dispersive and isotropic, once the energy conservation condition (B.1) is satisfied, the phase matching or momentum conservation condition (B.2) is automatically satisfied for collinear interaction

$$k_0 = k_1 + k_2 = 2k. \tag{B.4}$$

However, all optical materials are dispersive ($n = n(\omega)$), and, in general the energy and momentum conservation conditions cannot be satisfied simultaneously. In the normally dispersive region the index of refraction increases with the frequency. The possibility of phase matching the down-conversion process depends on the **birefringence** of the crystal. This is a property of some anisotropic crystal, for which in some coordinate system (three principal axes system) two of the three refraction indexes are

equal. These equal indexes define the ordinary refraction index, while the third index is the extraordinary refraction index. Therefore, such anisotropic media support two modes of differently refracted waves with two different directions and different polarizations, giving double refraction or birefringence, as represented in Fig.B.1. The birefringence provides a difference of refractive index for differently polarized fields, that can be used in order to compensate the effects of dispersion, by selecting the same index of refraction for the pump and signal $n_{2\omega} = n_\omega$. The two refracted waves that satisfy the phase matching conditions are the ordinary and extraordinary waves, and have orthogonal polarizations. There are two ways to satisfy the phase matching condition (see Fig.B.2):

- In type I phase matching the ordinary polarized pump photon is down-converted to produce pairs of extraordinary polarized photons that are degenerate both in frequency and in polarization. Therefore, their polarization is orthogonal to the one of the pump.

- In type II phase matching the signal photon is orthogonally polarized to the pump and the idler photons.

For a complete discussion about these questions see Refs. [Tang & Cheng, Saleh & Teich].

Due to the anisotropy of the media, rays do not necessarily travel in a direction perpendicular to their wavefronts. Indeed, they will only be perpendicular for propagation along or perpendicular to the optical axis. In general there is a misalignment between the Poynting vectors of ordinary and extraordinary waves. As a consequence, the extraordinary-polarized field will walk off, that is it will propagate in the transverse direction relative to the ordinarily polarized field. This transverse walk-off effect is described in the dynamical equations of the OPO in the mean field approximation by a transverse drift or walk-off term. In type I phase matching there is a walk-off of the down converted field relative to the pump. In type II phase matching there is a walk-off of the signal field relative to the pump and to the idler. For a derivation of the OPO equations including the effects of the transverse walk-off see Refs.[Ward & al. (98), Ward].
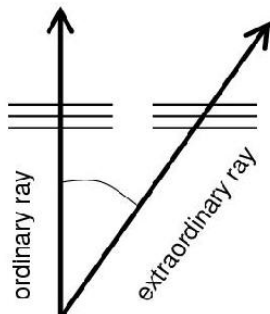

Figure B.1: Double refraction: the wave fronts of both refracted rays are parallel, but the Poynting vectors (arrows) of the ordinary and extraordinary waves are not parallel.
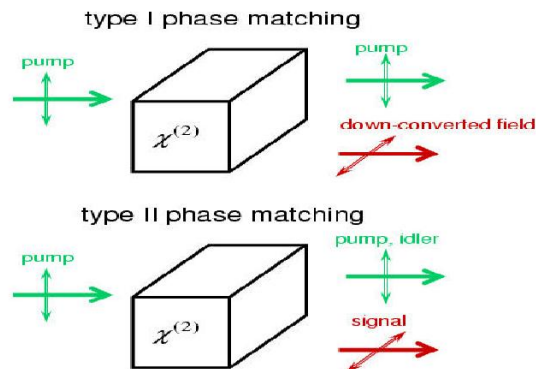

Figure B.2: Type I and type II phase matching.

Appendix C

Coefficients of the equation for the W distribution for the Kerr resonator

C.1 Drift, diffusion and third order terms of Eq.(3.7)

The drift terms of Eq.(3.7) are,

$$
\begin{aligned}
Q_1 &= \left[-(1 + i\eta\theta) + ig\eta(\alpha + \beta/2)(s - 1) + ia\nabla^2 \right] z_1 + E_o + i\eta g \left[\alpha z_1 z_2 + \beta z_3 z_4 \right] z_1 \\
Q_2 &= Q_1^* \\
Q_3 &= Q_3(z_1, z_2, z_3, z_4) = Q_1(z_3, z_4, z_1, z_2) \\
Q_4 &= Q_3^*.
\end{aligned}
$$

The diffusion terms are,

$$
D_{ij}(\vec{x}, \vec{x}') = \Gamma_{ij}\delta(\vec{x} - \vec{x}') \qquad
\Gamma = \begin{pmatrix}
c_s \alpha z_1^2 & 1 - s & c_s \beta z_1 z_3 & 0 \\
1 - s & -c_s \alpha z_2^2 & 0 & -c_s \beta z_2 z_4 \\
c_s \beta z_1 z_3 & 0 & c_s \alpha z_3^2 & 1 - s \\
0 & -c_s \beta z_2 z_4 & 1 - s & -c_s \alpha z_4^2
\end{pmatrix}, \qquad \text{(C.1)}
$$

with $c_s = i\eta gs$. The third order terms are,

$$
T_{ijl}(\vec{x}, \vec{x}', \vec{x}'') = \Theta_{ijl}\delta(\vec{x} - \vec{x}')\delta(\vec{x}' - \vec{x}'')
$$

(C.2)

where the non-zero terms of Θ_{ijl} are:

$$\Theta_{[112]} = i\frac{\alpha}{2}(1-s^2)\eta g z_1 \ , \ \ \Theta_{[334]} = i\frac{\alpha}{2}(1-s^2)\eta g z_3 \ , \tag{C.3}$$

$$\Theta_{[122]} = \Theta_{112}^* \ , \ \ \Theta_{[344]} = \Theta_{334}^*, \ \ \Theta_{[123]} = \frac{\beta}{2\alpha}\Theta_{334} \ ,$$

$$\Theta_{[124]} = \frac{\beta}{2\alpha}\Theta_{344} \ , \ \ \Theta_{[234]} = \frac{\beta}{2\alpha}\Theta_{122} \ , \ \ \Theta_{[134]} = \frac{\beta}{2\alpha}\Theta_{112} \ .$$

Square brackets [ ] indicate the possible permutations of indexes.

C.2 Drift and diffusion terms of Eq.(3.12)

For the drift terms we have,

$$
\begin{aligned}
Q_1 &= \left\{-(1+i\eta\theta) + i\nabla^2 + i\eta[2\alpha|F_+(\vec{x})|^2 + \beta|F_-(\vec{x})|^2]\right\} z_1(\vec{x},t) \\
&\quad + i\eta\left[\alpha F_+^2(\vec{x})z_2(\vec{x},t) + \beta F_+(\vec{x})F_-^*(\vec{x})z_3(\vec{x},t) + \beta F_+(\vec{x})F_-(\vec{x})z_4(\vec{x},t)\right] \\
Q_2 &= Q_1^* \\
Q_3 &= \left\{-(1+i\eta\theta) + i\nabla^2 + i\eta[2\alpha|F_-(\vec{x})|^2 + \beta|F_+(\vec{x})|^2]\right\} z_3(\vec{x},t) \\
&\quad + i\eta\left[\alpha F_-^2(\vec{x})z_4(\vec{x},t) + \beta F_-(\vec{x})F_+^*(\vec{x})z_1(\vec{x},t) + \beta F_-(\vec{x})F_+(\vec{x})z_2(\vec{x},t)\right] \\
Q_4 &= Q_3^*.
\end{aligned}
\tag{C.4}
$$

The diffusion terms are,

$$D_{ij}(\vec{x},\vec{x}') = \Gamma_{ij}\delta(\vec{x}-\vec{x}') \qquad \Gamma = \begin{pmatrix} 0 & 1 & 0 & 0 \\ 1 & 0 & 0 & 0 \\ 0 & 0 & 0 & 1 \\ 0 & 0 & 1 & 0 \end{pmatrix}. \tag{C.5}$$

List of Figures

Abbreviations

DOPO Degenerate Optical Parametric Oscillator

EPR Einstein-Podolsky-Rosen

FPE Fokker-Planck Equation

FF Far Field

NF Near Field

NDOPO Non Degenerate Optical Parametric Oscillator

OPA Optical Parametric Amplifier

OPO Optical Parametric Oscillator

PDC Parametric Down-Conversion

QND Quantum Non-Demolition

SHG Second Harmonic Generation

Bibliography

[Abraham & al.] *Instabilities and Chaos in Quantum Optics II*, edited by N. B. Abraham, F. T. Arecchi and L. A. Lugiato, NATO ASI Serie B: Physics, **177** (Plenum Press, New York, 1988).

[Abraham & Firth] Special issue on *Transverse Effects in Nonlinear Optical Systems*, edited by N. B. Abraham abd W. J. Firth, J. Opt. Soc. Am. B, **7**, no.6/7 (1990).

[Agarwal] G. S. Agarwal, Phys. Rev. A, **59**, 3071 (1999).

[Agez & al.] G. Agez, C. Szwaj, E. Louvergneaux, and P. Glorieux, Phys. Rev. A **66**, 063805 (2002).

[Aguado & al.] M. Aguado, R. F. Rodriguez, and M. San Miguel, Phys. Rev. A **39**, 5686 (1989).

[Arecchi & al.] F. T. Arecchi, S. Boccaletti and P. Ramazza, Phys. Rep. **318**, 1 (1999).

[Atature & al.] M. Atatüre, A. V. Sergienko, B. E. A. Saleh, and M. C. Teich, Phys. Rev. Lett. **86**, 4013 (2001).

[Aumann & al.] A. Aumann, E. Büthe, Y.A. Logvin, T. Ackemann and W. Lange, Phys. Rev. A **56**, R1709 (1997)

[Aytür & Kumar] O. Aytür and P. Kumar, Phys. Rev. Lett. **65**, 1551 (1990).

[Babcock & al.] K. L. Babcock, G. Ahlers, and D. S. Cannell, Phys. Rev. Lett. **67**, 3388 (1991); Phys. Rev. E **50**, 3670 (1994).

[Bache & al.] M. Bache, P. Scotto, R. Zambrini, M. San Miguel and M. Saffman, Phys. Rev. A **66**, 013809 (2002).

[Balle & al. (91)] S. Balle, F.De Pasquale, N.B. Abraham and M. San Miguel, Phys. Rev. A **45**, 1955 (1991).

[Balle & al. (93)] S. Balle, N.B. Abraham, P. Colet and M. San Miguel, IEEE J. Quantum Electron. **29**, 33 (1993).

[Banaszek & Wódkiewicz (96)] K. Banaszek and K. Wódkiewicz, Phys. Rev. Lett. **76**, 4344 (1996).

[Banaszek & Wódkiewicz (99)] K. Banaszek and K. Wódkiewicz, Phys. Rev. Lett. 82, 2009 (1999).

[Bardou & al.] F. Bardou, J.-P. Bouchaud, A. Aspect and C. Cohen-Tannoudji, *Lévy Statistics and Laser Cooling*, (Cambridge University Press, Cambridge, 2002).

[Barnett & al.] S. M. Barnett, C. R. Gilson, B. Huttner, and N. Imoto, Phys. Rev. Lett. **77**, 1739 (1996).

[Barnett & Radmore] S. M. Barnett and P. Radmore, *Methods in Theoretical Quantum Optics*, (Oxford University Press, Oxford, England, 1997).

[Barnett & Knight] S. M. Barnett and P. L. Knight, J. Opt. Soc. Am. B **2**, 467 (1985).

[Bender & Orszag] C. M. Bender, S. A. Orszag, *Advanced Mathematical Methods for Scientist and Engineers*, New York (McGraw-Hill, 1978).

[Bennink & al.] R. S. Bennink, V. Wong, A. M. Marino, D. L. Aronstein, R. W. Boyd, C. R. S., Jr., S. Lukishova, and D. J. Gauthier, Phys. Rev. Lett. **88**, 113901 (2002).

[Bohr & Rosenfeld] N. Bohr and L. Rosenfeld, Phys. Rev. **78**, 794 (1950). This paper is reprinted in *Quantum Theory and Measurement*, Edited by J. A. Wheeler and W. H. Zurek, (Princeton University Press, 1983).

[Bonifacio & Lugiato] R. Bonifacio and L.A. Lugiato, Lett. Nuovo Cimento **21**, 505 (1978).

[Born & Wolf] M. Born and E. Wolf, *Principle of Optics* (Pergamon, Oxford, 1975).

[Bortolozzo & al.] U. Bortolozzo, P. Villoresi, and P. L. Ramazza, Phys. Rev. Lett. **87**, 274102 (2001).

[Bouwmeester & al.] *The physics of quantum information*, D. Bouwmeester, A. Ekert, and A. Zeilinger eds. (Springer, Germany, 2000).

[Bowen & al.] W. P. Bowen, R. Schnabel, H.-A. Bachor, and P. K. Lam Phys. Rev. Lett. **88**, 093601 (2002).

[Boyd] R.W. Boyd, *Nonlinear Optics*, Academic Press, San Diego (1992).

[Braginsky] V. B. Braginsky and F. Ya. Khalili, *Quantum measurement*, (Cambridge University Press, 1992).

[Breitenbach & al.] G. Breitenbach, S. Schiller, and J. Mlynek, Nature (London) **387**, 471 (1997).

[Briggs] R. J. Briggs, *Electron-Stream Interaction with Plasmas*, (M. I. T. Press, Cambridge, Massachussets, 1964).

[Burnham & Weinberg] D. C. Burnham and D. L. Weinberg, Phys. Rev. Lett. **25**, 84 (1970).

[Cahill & Glauber] K. E. Cahill and R. J. Glauber, Phys. Rev. 177, 1857 (1969); Phys. Rev. 177, 1882 (1969).

[Carmichael] H. Carmichael, *An Open Systems Approach to Quantum Optics*, Lecture Notes in Physics, Vol. **m18**, (Springer,Berlin, 1993).

[Carmichael & Walls] H. J. Carmichael and D. F. Walls, J. Phys. B **9**, 1199 (1976).

[Carusotto & al.] I. Carusotto, Y. Castin, and J. Dalibard, Phys. Rev. A **63**, 023606 (2001).

[Castelli & Lugiato] F. Castelli and L. A. Lugiato, J. Mod. Opt. **44**, 765 (1997).

[Chaturvedi & Drummond] S. Chaturvedi and P. D. Drummond, Phys. Rev. A **55**, 912 (1997).

[Chen & al.] Z.B. Chen, J.W. Pan, G. Hou, and Y.D. Zhang, Phys. Rev. Lett. **88**, 040406 (2002).

[Chirkin & al.] A. S. Chirkin, A. A. Orlov, and D. Y. Paraschuk, Quantum Electron. **23**, 870 (1993).

[Choi & al.] S-K. Choi, M. Vasilyev, and P. Kumar, Phys. Rev. Lett. **83**, 1938 (1999).

[Collett & Gardiner] M.J. Collett and C.W. Gardiner, Phys. Rev. A **30**, 1386 (1984).

[Coullet & al.] P. Coullet, C. Elphick and D. Rappaux, Phys. Rev. Lett. **65**, 1352 (1990).

[Cross & Hohenberg] M. C. Cross and P. C. Hohenberg, Rev. Mod. Phys. **65**, 851 (1993).

[Davidovich] L. Davidovich, Rev. Mod. Phys., **68**, 127 (1996).

[de Oliveira] F. A. M. de Oliveira, Phys. Rev. A **45**, 5104 (1992).

[Deissler] R. J. Deissler, J. Stat. Phys. **40**, 371 (1985); J. Stat. Phys. **54**, 1459 (1989).

[Drummond (83)] P. D. Drummond, Phys. Rev. Lett. **50**, 1407 (1983).

[Drummond (86)] P. D. Drummond, Phys. Rev. A **33**, 4462 (1986).

[Drummond & al. (80)] P. D. Drummond, K. J. McNeil, and D. F. Walls, Opt. Acta **27**, 321 (1980).

[Drummond & al. (81)] P.D. Drummond, C. W. Gardiner, and D. F. Walls, Phys. Rev. A **24**, 914 (1981).

[Drummond & al. (02)] P. D. Drummond, K. Dechoum, and S. Chaturvedi, Phys. Rev. A **65**, 033806 (2002).

[Drummond & Gardiner] P. D. Drummond and C. W. Gardiner, J. Phys. A: Math. Gen. **13**, 2353 (1980).

[Drummond & Kinsler] P. D. Drummond and P. Kinsler, Quant. Semiclass. Opt. **7**, 727 (1995).

[Duan & al.] Lu-Ming Duan, G. Giedke, J. I. Cirac, and P. Zoller, Phys. Rev. Lett. **84**, 2722 (2000).

[Ducci & al.] S. Ducci, N. Trêps, A. Maître, and C. Fabre, Phys. Rev. A **64**, 023803 (2001).

[Einstein & al.] A. Einstein, B. Podolsky, and N. Rosen, Phys. Rev. **47**, 777 (1935).

[El-Orany, Peřina & al.] Faisal A. A. El-Orany, J. Peřina, V. Peřinová and M. Sebawe Abdalla, J. Opt. B **4**, S153 (2002); Eur. Phys. J. D **22**, 141 (2003) .

[Etrich & al.] C. Etrich, D. Michaelis, and F. Lederer, J. Opt. Soc. Am. B **19**, 792 (2002).

[Fabre] C. Fabre, Phys. Rep., **219**, 215 (1992).

[Fabre & al.] C. Fabre, J. B. Fouet, and A. Maitre, Opt. Lett. **25**, 76 (2000).

[Fainman & al.] Y. Fainman, E. Klancnik, S. H. Lee, Opt. Eng. **25**, 228 (1986).

[Firester] A. H. Firester, J. Appl. Phys. **40**, 4842 (1969); **41**, 703 (1970).

[Foster] D. Foster *Hydrodynamic Fluctuations, Broken Symmetry, and Correlation Fluctuations*, Addison Wesley, Redwood City, Ca (1983).

[Franken & al.] P. A. Franken, A. E. Hill, C. W. Peters, and G. Weinreich, Phys. Rev. Lett. **7**, 118 (1961).

[Franken & Ward] P. A. Franken and J. F. Ward, Rev. Mod. Phys. **35**, 23 (1963).

[Friberg & al.] S. Friberg, C.K. Hong, and L. Mandel, Phys. Rev. Lett. **54**, 2011 (1985)

[Furusawa & al.] A. Furusawa et al., Science **282**, 706 (1998).

[Gallego & al.] R. Gallego, M. San Miguel, R. Toral, Phys. Rev. E, **61**, 2241 (2000).

[Gao & al.] J.R. Gao, F. Cui, C. Xue, C. Xie, K. Peng, Opt. Lett., **23**, 870 (1998).

[García-Ojalvo & Sancho] J. García-Ojalvo and J. M. Sancho, *Noise in spatially extended systems* (Springer, New York, 1999).

[Gardiner & Zoller] C. W. Gardiner and P. Zoller, *Quantum Noise* Second Edition (Springer-Verlag, Berlin, 2000).

[Gardiner] C. W. Gardiner, *Handbook of Stochastic Processes* (Springer-Verlag, Berlin, 1985).

[Gatti & al. (97)1] A. Gatti, H. Wiedemann, L. A. Lugiato, I. Marzoli, G. L. Oppo, and S. M. Barnett, Phys. Rev. A **56**, 877 (1997).

[Gatti & al. (97)2] A. Gatti, L. A. Lugiato, G. Oppo, R. Martin, P. Di Trapani, and A. Berzanskis, Opt. Express **1**, 21 (1997).

[Gatti & al. (99)a] A. Gatti, L. A. Lugiato, K.I. Petsas and I. Marzoli, Europhys. Lett. **46**, 461 (1999).

[Gatti & al. (99)b] A. Gatti, E. Brambilla, L. A. Lugiato, and M. Kolobov, Phys. Rev. Lett. **83**, 1763 (1999).

[Gatti & al. (00)a] A. Gatti, E. Brambilla, L. A. Lugiato, and M. Kolobov, J. Opt. B: Quantum Semiclass. Opt. **2**, 196 (2000).

[Gatti & al. (00)b] A. Gatti, K.I. Petsas, I. Marzoli and L.A. Lugiato, Opt. Comm. **179**, 591 (2000).

[Gatti & Lugiato] A. Gatti and L. A. Lugiato, Phys. Rev. A **52**, 1675 (1995).

[Gatti & Mancini] A. Gatti and S. Mancini, Phys. Rev. A 65, 013816 (2002).

[Geddes & al.] J. B. Geddes, J. V. Moloney, E. M. Wright and W. J. Firth, Opt. Comm. **111**, 623, (1994).

[Gilchrist & al.] A. Gilchrist, C. W. Gardiner and P. D. Drummond, Phys. Rev. A **55**, 3014 (1997).

[Giordmaine] J. A. Giordmaine, Phys. Rev. Lett.**8**, 19 (1962).

[Giulini & al.] D. Giulini et al., *Decoherence and the Appearance of a Classical World in Quantum Theory* (Springer, Berlin, 1996).

[Glauber] R. J. Glauber, Phys. Rev. **130**, 2529 (1963).

[Gollub & Langer] J. P. Gollub and J. S. Langer Rev. Mod. Phys., 71(1999)

[Gomila & Colet] D. Gomila, and P. Colet, Phys. Rev. E **66**, 046223 (2002).

[Gomila & al. (01)] D. Gomila, P. Colet, M. San Miguel and G.-L. Oppo, Phys. Rev. Lett **87**, 194101 (2001).

[Gomila & al. (02)] D. Gomila, P. Colet, M. San Miguel, A. Scroggie and G.-L. Oppo, IEEE J. Quantum Elect. **29**, 238 (2003).

[Goodman] J. W. Goodman, *Statistical optics* (Wiley, New York, 1985), pg. 39.

[Graham] R. Graham, Phys. Rev. Lett. **52**, 117 (1984).

[Grangier] P. Grangier, Phys. Rep. **219**, 121 (1992); P. Grangier, J. A. Levenson and J-P. Poizat, Nature **396**, 537 (1998).

[Grynberg & al.] G. Grynberg, E. Le Bihan, P. Verkerk, P. Simoneau, J. R. R. Leite, D. Bloch, S. Le Boiteux, and M. Ducloy, Opt. Commun. **67**, 363 (1988).

[Grynberg & Lugiato] G. Grynberg and L. A. Lugiato, Opt. Commun. **101**, 69 (1993).

[Haken] H. Haken, *Synergetics - an Introduction* (Springer, Berlin, 1974).

[Hakioglu] T. Hakioglu, Phys. Rev. A **59**, 1586 (1999).

[Hald & al.] J. Hald, J. L. Sørensen, C. Schori, and E. S. Polzik, Phys. Rev. Lett. **83**, 1319 (1999).

[Hanbury Brown & Twiss] R. Hanbury Brown and R. Q. Twiss, Nature (London) 177, **27** (1956).

[Hecht] E. Hecht, Am. J. of Phys. **38**, 1156 (1970).

[Heidmann] A. Heidmann, R. J. Horowicz, S. Reynaud, E. Giacobino, C. Fabre and G. Camy, Phys. Rev. Lett. **59**, 2555 (1987).

[Holland & al.] M. J. Holland, M. Collett, D. F. Walls, M. D. Levenson, Phys. Rev. A **42**, 2995 (1990).

[Hoyuelos & al. (98)] M. Hoyuelos, P. Colet, M. San Miguel and D. Walgraef, Phys. Rev. E **58**, 2992 (1998).

[Hoyuelos & al. (99)] M. Hoyuelos, A. Sinatra, P. Colet, L. Lugiato and M. San Miguel, Phys. Rev. A **59**, 1622 (1999).

[Hoyuelos-Colet-San Miguel] M. Hoyuelos, P. Colet and M. San Miguel, Phys. Rev. E **58**, 74 (1998).

[Hillery & al.] M. Hillery, R. F. O'Connell, M. O. Scully, E. P. Wigner, Phys. Rep. **106**, 121 (1984).

[Hillery & Mlodinow] M. Hillery and L. D. Mlodinow, Phys. Rev. A **30**, 1860 (1984).

[Huang] K. Huang, *Statistical mechanics*, 2nd ed. (John Wiley & Sons, New York, 1987)

[Husimi] K. Husimi, Proc. Phys. Math. Soc. Japan, **22**, 264 (1940).

[Kheruntsyan & Petrosyan] K. V. Kheruntsyan and K. G. Petrosyan Phys. Rev. A **62**, 015801 (2000)

[Kimble] H. J. Kimble, *Quantum fluctuations in quantum optics-squeezing and related phenomena*, Les Houches, session LIII, 1990, edited by J.Dalibard, S. Reynaud, and J. Zinn Justin (Elsevier Science Publ. 1992).

[Kimble & al.] H. J. Kimble, M. Dagenais and L. Mandel, Phys. Rev. Lett**39**, 691 (1977).

[Kinsler] P. Kinsler, Phys. Rev. A **53**, 2000 (1996).

[Kinsler & Drummond] P. Kinsler, and P. D. Drummond, Phys. Rev. A **52**, 783 (1995)

[Klyshko (88)] D. M. Klyshko, *Photons and nonlinear optics*, (Gordon and Breach, New York, 1988).

[Klyshko (97)] D. M. Klyshko, JEPT **84**, 1065 (1997)

[Kolobov] M. I. Kolobov, Rev. Mod. Phys., **71**, 1539 (1999).

[Kolobov & Fabre] M.I. Kolobov and C. Fabre, Phys. Rev. Lett. **85**, 3789 (2000).

[Kolobov & Kumar] M. I. Kolobov and P. Kumar, Opt. Lett. **18**, 849 (1993).

[Kolobov & Lugiato] M. I. Kolobov and L. A. Lugiato, Phys. Rev. A **52**, 4930 (1995).

[Kolobov & Sokolov] M. I. Kolobov and I. V. Sokolov, Phys. Lett. A **140**, 101 (1989); M. I. Kolobov and I. V. Sokolov, Europhys. Lett. **15**, 271 (1991).

[Korolkova & al.] N. Korolkova, G. Leuchs, R. Loudon, T. C. Ralph, and C. Silberhorn, Phys. Rev. A **65**, 052306 (2002).

[Kumar & Mehta] S. Kumar and C. L. Mehta, Phys. Rev. A **21**, 1573 (1980); *ibid.* **24**, 1460 (1981).

[Kuzmich & al.] A. Kuzmich, I. A. Walmsley, and L. Mandel, Phys. Rev. Lett. **85**, 1349 (2000); Phys. Rev. A **64**, 063804 (2001).

[Kwiat & al.] P.G. Kwiat, K. Mattle, H. Weinfurter, A. Zeilinger, A. V. Sergienko, and Y.H. Shih, Phys. Rev. Lett. **75**, 4337 (1995).

[Infeld & Rowlands] E. Infeld, G. Rowlands, *Nonlinear waves, solitons, and chaos*, England (Cambridge University Press, 1990).

[Izús & al.] G. Izús, M. Santagiustina, M. San Miguel, and P. Colet, J. Opt. Soc. Am. **16**, 1592 (1999).

[Jeffers & Oppo] J. Jeffers and G-L. Oppo, Phys. Rev. A **60**, 2393 (1999).

[Jeffries & Weisenfeld] C. Jeffries and K. Weisenfeld, Phys. Rev. A **31**, 1077 (1985).

[Lamas-Linares & al.] A. Lamas-Linares, J. C. Howell, and D. Bowmeester, Nature **412**, 887 (2001).

[Lamb & al.] W. E. Lamb, W. P. Schleich, M. O. Scully, and C. H. Townes, Rev. Mod. Phys. **71**, S263 (1999).

[Lane & al.] A. S. Lane, M. D. Reid, and D. F. Walls, Phys. Rev. A **38**, 788 (1988).

[Lantz & Devaux] E. Lantz and F. Devaux, Quantum Semiclassic. Opt. **9**, 279 (1997).

[Le Berre & al.(79)] M. Le Berre-Rousseau, E. Ressayre, and A. Tallet, Phys. Rev. Lett. **43**, 1314 (1979).

[Le Berre & al.(99)] M. Le Berre, D. Leduc, S. Patrascu, E. Ressayre, and A. Tallet, Chaos, Solitons and Fractals **10**, 627 (1999).

[Leonhardt] U. Leonhardt, *Measuring the Quantum State of Light*, Cambridge University Press (Cambridge, UK, 1997).

[Leuchs & al.] G. Leuchs, Ch. Silberhorn, F. König, A. Sizmann, and N. Korolkova:*Quantum solitons in optical fibres: basic requisites for experimental quantum communication*, in *Quantum Information Theory with Continuous Variables*, S.L. Braunstein and A.K. Pati eds. (Kluwer Academic Publishers, Dodrecht 2002).

[Lloyd & Braunstein] S. Lloyd, S.L. Braunstein, Phys. Rev. Lett. **82**, 1784 (1999).

[Lodahl & Saffman] P. Lodahl and M. Saffman, Opt. Comm. **27**, 110 (2002).

[Loudon (80)] R. Loudon, Reports on Progress physics **43**, 913 (1980). This paper is included in Ref. [Selected papers (Mandel & Wolf)].

[Loudon (83)] R. Loudon, *The quantum theory of light*, Clarendon Press (Oxford, 1983).

[Louisell & al.] W. H. Louisell, A. Yariv and A. E. Siegman, Phys. Rev. **124**, 1646 (1961).

[Lugiato] *Special issue: Nonlinear Optical Structures, Pattern, Chaos*, in Chaos Solitons & Fractals **4**, no.8/9 (1994). Guest editor: L. A. Lugiato.

[Lugiato & al. (95)] L. A. Lugiato, A. Gatti, and H. Wiedemann, *Quantum fluctuations and nonlinear optical patterns*, Les Houches, session LVIII, 1995, edited by S. Reynaud, E. Giacobino, and J. Zinn Justin (Elsevier-North-Holland, Amsterdam, 1997).

[Lugiato & al. (96)] L. A. Lugiato, S. M. Barnett, A. Gatti, I. Marzoli, G. L. Oppo, and H. Wiedemann, pg. 5, in *Coherence and Quantum Optics VII*, edited by Eberly, Mandel, and Wolf, Plenum Press (New York, 1996).

[Lugiato & al. (97)] L. A. Lugiato, A. Gatti, H. Ritsch, I. Marzoli, and G. L. Oppo, J. Mod. Opt. **44**, 1899 (1997).

[Lugiato & al. (99)] L. A. Lugiato, M. Brambilla, and A. Gatti, "Optical Pattern formation", in *Advances in Atomic Molecular and Optical Physics* **40**, 229, B. Bederson and H. Walther eds. (Academic Press, New York, 1999).

[Lugiato & al. (02)] L. A. Lugiato, A. Gatti, and M. Brambilla, J. Opt. B **4**, S1 (2002).

[Lugiato & Castelli] L.A. Lugiato and F. Castelli, Phys. Rev. Lett. **68**, 3284 (1992).

[Lugiato & Grynberg] L. A. Lugiato and G. Grynberg, Europhys. Lett. **29**, 675 (1995).

[Lugiato & Lefever] L. A. Lugiato and L. Lefever, Phys. Rev. Lett. **58**, 2209 (1987).

[Lugiato & Oppo] L. A. Lugiato and G. Oppo, pg.60 in Ref.[Quantum Structures (98)].

[Luis] A. Luis, Phys. Rev. A **66**, 013806 (2002).

[Ma] S. K. Ma, *Statistical Mechanics*, Chapter 29, World Scientific (1985).

[Mandel(79)] L. Mandel, Opt. Lett. **4**, 205 (1979).

[Mandel(82)] L. Mandel, Phys. Rev. Lett. **49**, 136 (1982).

[Mandel & Wolf] L. Mandel and E. Wolf, *Optical coherence and quantum optics* (Cambridge University Press, Cambridge, 1995).

[Manley & Rowe] J. M. Manley and H. E. Rowe, Proc. IRE **44**, 904 (1956).

[Marshall] T. W. Marshall, Proc. R. Soc. London, Ser. A, **276**, 475 (1963).

[Marzoli & al.] I. Marzoli, A. Gatti, and L. A. Lugiato, Phys. Rev. Lett. **78**, 2092 (1997).

[McNeil & Gardiner] K. J. McNeil, and C. W. Gardiner, Phys. Rev. A **28**, 1560 (1983)

[Mertz & al.] J. Mertz, A. Heidmann, and C. Fabre, Phys. Rev. A **44**, 3229 (1991); J. Mertz, *et al.*, Opt. Lett. **16**, 1234 (1991).

[Milburn] G. J. Milburn, Phys. Rev. A **33**, 674 (1986).

[Midwinter] J. E. Midwinter, Appl. Phys. Lett. **12**, 68 (1968).

[Milburn & Wolf] G. J. Milburn, D. F. Walls, Opt. Comm. **39**, 401 (1981).

[Montagne & al.] R. Montagne, E. Hernández- García, A. Amengual and M. San Miguel, Phys. Rev. E **56**, 151 (1997).

[Nagasako & al.] E. M. Nagasako, R. W. Boyd, and G. S. Agarwal, Phys. Rev. A **55**, 1412 (1997).

[Nicolis & Prigogine] G. Nicolis, I. Prigogine, *Self-organization in nonequilibrium systems: from dissipative structures to order through fluctuations*, (New York, Wiley, 1977).

[Nogueira & al.] W. A. T. Nogueira, S. P. Walborn, S. Pádua, and C. H. Monken, Phys. Rev. Lett. **86**, 4009 (2001); Phys. Rev. A **66**, 053810 (2002).

[Olsen & Plimak] M. K. Olsen, L. I. Plimak, and M. Fleischhauer, Phys. Rev. A **65**, 053806 (2002).

[Oppo & al. (94)] G-L. Oppo, M. Brambilla, L. A. Lugiato, Phys. Rev. A **49**, 2028 (1994); G.-L. Oppo, M. Brambilla, D. Camesasca, A. Gatti, and L.A. Lugiato, J. Mod. Opt. **41**, 1151 (1994).

[Oppo & al. (01)] G-L. Oppo, A. J. Scroggie, W. J. Firth, Phys. Rev. E **63**, 066209 (2001).

[Orszag] M. Orszag, *Quantum optics: including noise reduction, trapped ions, quantum trajectories, and decoherence*, (Springer-Verlag Berlin, 2000).

[Ou & al.] Z.Y. Ou, S.F. Pereira, H.J. Kimble, and K.C. Peng, Phys. Rev. Lett. 68, 3663 (1992).

[Paul] H. Paul, Rev. Mod. Phys. **54**, 1061 (1982).

[Pawula] R. F. Pawula, Phys. Rev. **162**, 186 (1967).

[Pettiaux & al.] N.B. Pettiaux, R.D. Li and P. Mandel, Opt. Commun. **72**, 256 (1989).

[Plimak & al.] L. I. Plimak, M. K. Olsen and M. J. Collett, Phys. Rev. A **64**, 025801 (2001).

[Pope & al.] D. T. Pope, P. D. Drummond, and W. J. Munro Phys. Rev. A **62**, 042108 (2000).

[Porzio & al.] A. Porzio, F. Sciarrino, A. Chiummo, M. Fiorentino, S. Solimeno, Opt. Comm. **194**, 373 (2001).

[Prakash & Chandra] H. Prakash and N. Chandra, Phys. Rev. A **4**, 796 (1971).

[Quantum Structures (98)] *Quantum Structures in nonlinear Optics and Atomic Physics*, Focus Issue, Opt. Expr. **3**, No. 2 (1998).

[Quantum Structures (03)] *Quantum fluctuations and coherence in optical and atomic structures*, Special Issue, E. Phys. J. D **22**, No. 3 (2003).

[Ralph & al.] T. C. Ralph, W. J. Munro, and R. E. S. Polkinghorne, Phys. Rev. Lett. **85**, 2035 (2000); E. H. Huntington and T. C. Ralph, Phys. Rev. A **65**, 012306 (2002).

[Ramazza & al.] P. L. Ramazza, S. Ducci, and F. T. Arecchi, Phys. Rev. Lett. **81**, 4128 (1998).

[Reid & al.] M. D. Reid, W. J. Munro, and F. De Martini, Phys. Rev. A **66**, 033801 (2002).

[Reid & Drummond (88)] M. D. Reid and P. D. Drummond, Phys. Rev. Lett. **60**, 2731 (1988).

[Reid & Drummond (89)] D. Reid and P. D. Drummond, Phys. Rev. A **40**, 4493 (1989).

[Reid & Drummond (90)] M. D. Reid and P. D. Drummond, Phys. Rev. A **41**, 3930 (1990).

[Reid & Walls] M. D. Reid and D. F. Walls, Phys. Rev. A **34**, 1260 (1986).

[Reynaud] S. Reynaud, Europhys. Lett. **4**, 427, (1987).

[Reynaud & al. (87)] S. Reynaud, C. Fabre, and E. Giacobino, J. Opt. Soc. Am. B **4**, 1520 (1987).

[Reynaud & al. (92)] S. Reynaud, A. Heidmann, E. Giacobino and C. Fabre, in *Progress in Optics* **XXX**, 1 (1992).

[Ruelle] D. Ruelle, Nature **414**, 263 (2001).

[Risken] H. Risken, *The Fokker-Planck equation: methods of solution and applications* Berlin (Springer-Verlag, 1989).

[Royer] A. Royer, Phys. Rev. A 15, 449 (1977).

[Rowe & al.] M. A. Rowe, D. Kielpinski, V. Meyer, C. A. Sackett, W. M. Itano, C. Monroe, and D.J. Wineland, Nature (London) **409**, 791 (2001).

[Saleh & Teich] B. E. A. Saleh and M. C. Teich, *Fundametals of Photonics*, (Wiley, New York, 1991).

[San Miguel & Toral] M. San Miguel, R. Toral, "Stochastic Effects in Physical Systems", in *Instabilities and Nonequilibrium Structures VI*, eds. E. Tirapegui, J. Martinez, and R. Tiemann, Kluwer Academic Publishers, 35 (2000).

[Sancho & al.] J. M. Sancho, M. San Miguel, S. L. Katz, J. D. Gunton, Phys. Rev. A **26**, 1589 (1982)

[Santagiustina & al. (97)] M. Santagiustina, P. Colet, M. San Miguel, and D. Walgraef, Phys. Rev. Lett. **79**, 3633 (1997).

[Santagiustina & al. (98)a] M. Santagiustina, P. Colet, M. San Miguel, and D. Walgraef, Phys. Rev. E **58**, 3843 (1998).

[Santagiustina & al. (98)b] M. Santagiustina, P. Colet, M. San Miguel, and D. Walgraef, Opt. Lett. **23** 1167 (1998).

[Santagiustina & al. (99)] M. Santagiustina, P. Colet, M. San Miguel, and D. Walgraef, J. Opt. B **1**, 191 (1999).

[Sharping & al.] J. E. Sharping, M. Fiorentino, P. Kumar, Opt. Lett. **26**, 367 (2001).

[Schleich] W. S. Schleich, *Quantum Optics in Phase Space*, Berlin (Wiley-VCH,1997).

[Scroggie & al.] A. J. Scroggie, W. J. Firth, G. S. McDonald, M. Tlidi, R. Lefever, L. A. Lugiato , Pattern Formation in a Passive Kerr Cavity, in [Lugiato].

[Selected papers (Mandel & Wolf)] *Selected papers on coherence and fluctuations of light*, L. Mandel, E. Wolf, editors (Bellingham, Wash., USA, 1990).

[Shelby & al.] R. M. Shelby, M. D. Levenson, S. H. Perlmutter, R. F. DeVoe, and D. F. Walls, Phys. Rev. Lett. **57**, 691 (1986).

[Short & Mandel] R. Short and L. Mandel, Phys. Rev. Lett. **61**, 2921 (1983).

[Sinatra & al.] A. Sinatra, J.F. Roch, K. Vigneron, Ph. Grelu, J.Ph. Poizat, K. Wang and P. Grangier, Phys. Rev. A **57**, 2980 (1998).

[Slusher & al.] R. E. Slusher, L. W. Hollberg, B. Yurke, J. C. Mertz and J. F. Valley, Phys. Rev. Lett. **55**, 2489 (1985).

[Söderholm & al.] J. Söderholm, G. Björk, A. Trifonov, Opt. Spectrosc. **91**, 532 (2001).

[Staliunas & Sánchez-Morcillo] K. Staliunas and V. Sánchez-Morcillo, Opt. Comm. **177**, 389 (2000).

[Stoler] D. Stoler, Phys. Rev. D **1**, 3217 (1970); **4**, 1925 (1971).

[Sudarshan] E. C. G. Sudarshan, Phys. Rev. Lett. **10**, 277 (1963).

[Szwaj & al.] C. Szwaj, G.-L. Oppo, A. Gatti, L. A. Lugiato, E. Phys. J. D **10**, 433 (2000).

[Taki & al.] M. Taki, M. San Miguel and M. Santagiustina, Phys. Rev. E **61**, 2133 (2000).

[Tanas & al.] R. Tanás, A. Miranowicz and S. Kielich, Phys. Rev. A **43**, 4014 (1991).

[Tang & Cheng] C. L. Tang and L. K. Cheng, *Fundamentals of optical parametric processes and oscillators*, Laser Science Technology Series (Harwood academic publishers, The Netherlands, 1995).

[Teich & Saleh] M. C. Teich and B. E. A. Saleh, *Squeezed states of light*, Quantum Opt. **1**, 152 (1989).

[Tlidi & al.] M. Tlidi, M. Le Berre, A. Ressayre, A. Tallet, and L. Di Menza, Phys. Rev. A **61**, 043806 (2000).

[Tombesi] P. Tombesi, Phys. Lett. A **132**, 241 (1988).

[Toral & al.] R. Toral, A. Chakrabarti, Comp. Phys. Comm. **74**, 327 (1993).

[Treps & al.] N. Treps, U. Andersen, B. Buchler, P. K. Lam, A. Maître, H.-A. Bachor, and C. Fabre, Phys. Rev. Lett. **88**, 203601 (2002).

[Trillo & al.] S. Trillo, M. Haelterman, and A. Sheppard, Opt. Lett. **22**, 970 (1997).

[Tsameret & Steinberg] A. Tsameret and V. Steinberg, Phys. Rev. Lett. **67**, 3392 (1991); Phys. Rev. E **49**, 1291 (1994).

[Tsegaye & al.] T. Tsegaye, J. Söderholm, M. Atatüre, A. Trifonov, G. Björk, A. V. Sergienko, B. E. A. Saleh, and M. C. Teich, Phys. Rev. Lett. **85**, 5013 (2000).

[Turing] A. M. Turing, Phil. Trans. R. Soc. London B **237**, 37 (1952).

[Usachev & al.] P. Usachev, J. Söderholm, G. Björk, and A. Trifonov, Opt. Commun. **193**, 161 (2001).

[Vaupel & al.] M. Vaupel, A. Maître, and C. Fabre, Phys. Rev. Lett. **83**, 5278 (1999).

[Viñals & al.] J. Viñals, E. Hernandez-Garcia, M. San Miguel and R. Toral, Phys. Rev. A **44**, 1123 (1991).

[Vogel & Risken (88)] K. Vogel and H. Risken, Phys. Rev. A **38**, 2409 (1988).

[Vogel & Risken (89)a] K. Vogel and H. Risken, Phys. Rev. A **39**, 4675 (1989).

[Vogel & Risken (89)b] K. Vogel and H. Risken, Phys. Rev. A 40, R2847 (1989).

[Walgraef] D.Walgraef, *Spatio-Temporal Pattern Formation*, Berlin (Springer,1997).

[Wallentowitz & Vogel] S. Wallentowitz and W. Vogel Phys. Rev. A **53**, 4528 (1996).

[Walls (79)] D. F. Walls, Nature, **280**, 451 (1979).

[Walls (83)] D. F. Walls, Nature, **306**, 141 (1983).

[Walls & Milburn] D. F. Walls, G. J. Milburn, *Quantum optics*, Berlin (Springer, 1994).

[Ward] H. Ward, *Instabilités spatio-temporelles des oscillateurs paramétriques optiques: couplage walk-off/diffraction*, PhD Thesis (Université de Lille, 2001)

[Ward & al. (98)] H. Ward, M. N. Ouarazi, M. Taki and P. Glorieux, Eur. Phys. J. D **3**, 275 (1998).

[Ward & al. (00)] H. Ward, M. N. Ouarzazi, M. Taki, and P. Glorieux, Phys. Rev. E **63**, 016604 (2000).

[Ward & al. (01)] H. Ward, M. N. Ouarzazi, M. Taki, and P. Glorieux, Phys. Rev. E 63, 016604 (2001).

[Weihs & al.] G. Weihs, T. Jennewein, C. Simon, H. Weinfurter, and A. Zeilinger, Phys. Rev. Lett. **81**, 5039 (1998).

[Wiesenfeld] K. Wiesenfeld, J. Stat. Phys. **38**, 1071 (1985).

[Wigner] E. Wigner, Phys. Rev. **40**, 7749 (1932).

[Wu & al.] L. A. Wu, H. J. Kimble, J. L. Hall, and H. Wu, Phys. Rev. Lett. **57**, 2520 (1986).

[Yuen] H. P. Yuen, Phys. Rev. A **13**, 2226 (1976).

[Yuen & Chan] H. P. Yuen and V. W. S. Chan Opt. Lett. **8** 177 (1983); ibid. **8** 345 (1983).

[Yuen & Tombesi] H. P. Yuen and P. Tombesi, Opt. Comm. **59**, 155 (1986).

[Yurke] B. Yurke and D. Stoler, Phys. Rev. Lett. **57**, 13 (1986).

[Zambrini & al. (00)] R. Zambrini, M. Hoyuelos, A. Gatti, P. Colet, L. Lugiato, and M. San Miguel. Phys. Rev. A **62**, 63801 (2000).

[Zambrini & al. (02)] R. Zambrini, S. M. Barnett, P. Colet, and M. San Miguel, Phys. Rev. A **65**, 023813 (2002).

[Zambrini & al. (03)1] R. Zambrini, S. M. Barnett, P. Colet, and M. San Miguel, Eur. Phys. J. D **22**, 461 (2003).

[Zambrini & al. (03)2] R. Zambrini, A. Gatti, L. Lugiato, and M. San Miguel, "Nonclassical polarization properties of macroscopic light beams in Optical Parametric Oscillators below threshold", preprint.

[Zambrini & Barnett] R. Zambrini and S. M. Barnett, Phys. Rev. A **65**, 053810 (2002).

[Zambrini & San Miguel] R. Zambrini and M. San Miguel, Phys. Rev. A **66**, 023807 (2002).

[Zeilinger] A. Zeilinger, Rev. Mod. Phys. **71**, S288 (1999).

[Zhang] J. Zhang, *Optical parametric generation and amplification*, Laser Science Technology Series (Harwood academic publishers, The Netherlands, 1995).

[Zhang& al.] Y. Zhang, H. Wang, X. Li, J. Jing, C. Xie, and K. Peng, Phys. Rev. A **62**, 023813 (2000).

[Zou & Mandel] X. T. Zou and L. Mandel, Phys. Rev. A **41**, 475 (1990).

[Zurek] W. H. Zurek, Physics Today **44**, 36 (1991).

Curriculum vitae

• PERSONAL DATA

Name: Zambrini, Roberta

Place of birth: Milan, Italy.

Date of birth: 19th June, 1973.

Nationality: Italian.

Place of work: IMEDEA, Universitat de les Illes Balears (UIB), 07122. Palma de Mallorca, Spain. Tel: +34-971-172536; Fax: +34-971-173426

E-mail: roberta@imedea.uib.es

• EDUCATION AND FELLOWSHIPS

Master degree in Physics (February 1999) Università degli Studi di Milano, Italy.
Master Thesis: *Kerr nonlinear optical systems: study of noise in spatial structures*.
Supervisor: Prof. L. A. Lugiato.

PhD in Physics (1999-2003) Universitat de les Illes Balears, Palma de Mallorca, Spain.
PhD Thesis: *Quantum fluctuations in nonlinear optical systems*.
Supervisor: Maxi San Miguel.

Spoken languages: Italian, Spanish, English, French.

Computer experience: Use of UNIX and WINDOWS systems. Fortran program language.

Referee for Physical Review A

Fellowships (1993-2002)

1. Scholarship of the ISU, Università degli Studi di Milano, Italy (1993-94).
2. Erasmus Fellowship, Universitat de les Illes Balears (1998).
3. Fellowship of the European Commission through the TMR network QSTRUCT (1999).
4. PhD fellowship of the Spanish Government, Universitat de les Illes Balears (2000-2003).

- ## PUBLICATIONS

Publications in refereed journals

1. *Quantum fluctuations in a continuous vectorial Kerr medium model*,
   Roberta Zambrini, Miguel Hoyuelos, Alessandra Gatti, Pere Colet, Luigi Lugiato and Maxi San Miguel, Phys. Rev. A **62**, 063801 (2000).

2. *Macroscopic quantum fluctuations in noise-sustained optical patterns*,
   Roberta Zambrini, Stephen M. Barnett, Pere Colet and Maxi San Miguel, Phys. Rev. A **65**, 023813 (2002); Erratum: Phys. Rev. A 65, 049901 (2002).

3. *Analytic stochastic treatment of a nonlinear quantum model with negative diffusion*,
   Roberta Zambrini and Stephen M. Barnett, Phys. Rev. A 65, 053810 (2002).

4. *Quantum properties of transverse pattern formation in second-harmonic generation*,
   Morten Bache, Pierre Scotto, Roberta Zambrini, Maxi San Miguel and Mark Saffman, Phys. Rev. A 66, 013809 (2002).

5. *Twin beams, non linearity and walk-off in Optical Parametric Oscillators*,
   Roberta Zambrini and Maxi San Miguel, Phys. Rev. A 66, 023807 (2002).

6. *Non-classical behavior in multimode and disordered transverse structures in OPO. Use of the Q representation*,
   Roberta Zambrini, Stephen M. Barnett, Pere Colet, and Maxi San Miguel Eur. Phys. J. D 22, 461 (2003).

7. *Nonclassical polarization properties of macroscopic light beams in Optical Parametric Oscillators below threshold*,
   Roberta Zambrini, Alessadra Gatti, Maxi San Miguel, and Luigi Lugiato, (submitted).

8. *Multi-photon, multi-mode polarization entanglement in parametric down-conversion*,
   Alessadra Gatti, Roberta Zambrini, Maxi San Miguel, and Luigi Lugiato (submitted).

In preparation

1. *Walk-off breaking symmetry effects in type I OPO*,
   Majid Taki, Roberta Zambrini, Maxi San Miguel.

- ## CONFERENCE COMMUNICATIONS

- **QSTRUCT 1998 Meeting** (european TMR, Training and Mobility of Researchers, network to investigate quantum features of self-organized systems and trapped ions). Kinlochard (Aberfoyle), Scotland, United Kingdom, September 18-21, 1998.
  Talk presented by M. Hoyuelos: *"Classical and quantum correlations in patterns of a Kerr medium"*, M. Hoyuelos, P. Colet, M. San Miguel, D. Walgraef, A. Sinatra, R. Zambrini, A. Gatti and L. Lugiato.

– **QSTRUCT 1999 Meeting**. Innsbruck, Austria, January 15-17, 1999.

Talk presented by M. Hoyuelos: *"Quantum correlations in Kerr media"*, M. Hoyuelos, A. Sinatra, R. Zambrini, A. Gatti, L. Lugiato, P. Colet, and M. San Miguel.

– **Quantum Optics X**. Cala Viñas, Mallorca, Spain, Octuber 2-7, 1999.

Poster presented by R. Zambrini: *"Quantum correlations in vectorial patterns in a Kerr cavity"*, R. Zambrini, M. Hoyuelos, A. Gatti, L. Lugiato, P. Colet, M. San Miguel, A. Sinatra.

– **8th International Workshop on Instabilities and Nonequilibrium Structures**. Viña del Mar, Chile, December 13-17, 1999.

Poster presented by M. Hoyuelos: *"Fluctuation correlations in patterns of a Kerr medium"*, M. Hoyuelos, P. Colet, A. Sinatra, R. Zambrini, M. San Miguel y L. Lugiato.

– **QSTRUCT 2000 Meeting** (european TMR). Les Houches, France, March 15-19, 2000.

Talks presented by R. Zambrini: *"Quantum fluctuations in a continuous vectorial Kerr cavity model"*, R. Zambrini, M. Hoyuelos, A. Gatti, L. Lugiato, P. Colet, M. San Miguel; *"Quantum treatment of OPO's in convective regime"*, S. Barnett, R. Zambrini, G. Izús, M. San Miguel, P. Colet.

– **7th Central European Workshop in Quantum Optics**. Balatonfüred, Hungary, April 28-May 1, 2000.

Poster presented by R. Zambrini: *"Quantum correlations in vectorial patterns in a Kerr cavity"*, R. Zambrini, M. Hoyuelos, A. Gatti, L. Lugiato, P. Colet, M. San Miguel, A. Sinatra.

– **CLEO/Europe-IQEC 2000**. Nice Acropolis, Nice, France, September 10-15, 2000.

Talk of P. Colet: *"Quantum fluctuations in a continuous vectorial Kerr cavity model"*, R. Zambrini, M. Hoyuelos, A. Gatti, L. Lugiato, P. Colet, M. San Miguel.

Talk of R. Zambrini: *"Quantum correlations in noise-sustained optical patterns"*, S. Barnett, R. Zambrini, G. Izús, M. San Miguel, P. Colet.

– **Quantum Optics XI**. Cala Viñas, Mallorca, Spain, October 14-19, 2000.

Poster presented by R. Zambrini: *"Quantum correlations in noise-sustained optical patterns"*, S. Barnett, R. Zambrini, G. Izús, M. San Miguel, P. Colet.

– **QSTRUCT 2000 Young-researchers Meeting** (european TMR). Garching, Germany, November 23-25, 2000.

Talk presented by R. Zambrini: *"Quantum fluctuations in optical patterns: an introduction"*.

– **QSTRUCT 2000 Meeting** (european TMR). Munich, Germany, November 26-29, 2000.

Talk presented by R. Zambrini: *"Optical patterns sustained by quantum noise"*, S. Barnett, R . Zambrini, M. San Miguel, P. Colet.

– **International Workshop Coherent Evolution in Noisy Environment**. Dresden Germany, May 21-25, 2001.

Poster presented by R. Zambrini: *"Patterns sustained by quantum noise"*, R. Zambrini, S. Barnett, M. San Miguel, P. Colet.

– **QUANTIM 2001 Meeting**. Paris, France, May 14-16, 2001

Talks presented by R. Zambrini: *"Patterns sustained by quantum noise"*, R. Zambrini, S. Barnett, M. San Miguel, P. Colet.

"Quantum fluctuations in SHG", M. Bache, R. Zambrini, P. Scotto, M. San Miguel.

– **Eighth Rochester Conference on Coherence and Quantum Optics** (CQO8). Rochester, New York (USA), June, 13-16 2001

Poster presented by R. Zambrini: *"Optical patterns sustained by quantum noise"*, R. Zambrini, S. Barnett, M. San Miguel, P. Colet.

– **Workshop on dynamics of Lasers and OPO's** (PICS Franco-Catalan). Les Houches, France, September 24-28, 2001

Talk presented by R. Zambrini: *"Patterns sustained by quantum noise in OPO's"*, R. Zambrini, S. Barnett, M. San Miguel, P. Colet.

– **QUANTIM 2002 Meeting**. Besançon, France, May 29-31, 2002

Talk presented by R. Zambrini: *" Polarization entanglement in type II opo below threshold"*, R. Zambrini, M. San Miguel, A. Gatti, L. Lugiato

– **Workshop on Dynamics of Nonlinear Optical Systems (PICS Franco-Catalan)**. Playa de Aro (Gerona), Spain, September 2-6, 2002.

Talk presented by R. Zambrini: *"Polarization entanglement in type II OPO below threshold"*, R. Zambrini, M. San Miguel, A. Gatti, L. Lugiato.

– **EuroConference on Quantum Atom Optics**. San Feliu de Guixols, Spain, 21-26 September, 2002.

Poster presented by R. Zambrini: *"Macroscopic polarization entanglement in OPO"*, R. Zambrini, M. San Miguel, A. Gatti, L. Lugiato.

– **QUANTIM 2003 Meeting**. Como, Italy, March 4-8, 2003

Talk presented by R. Zambrini: *"Nonclassical polarization properties of macroscopic light beams in Optical Parametric Oscillators below threshold"*, R. Zambrini, M. San Miguel, A. Gatti, L. Lugiato.

• SEMINARS

– *"Quantum correlations in noise sustained optical patterns"*.

Department of Physics, University of Strathclyde (Glasgow, UK).
July 2000.

– *"Quantum correlations in noise sustained optical patterns"*.

Instituto Mediterraneo de Estudios Avanzados, IMEDEA (Palma de Mallorca, Spain).
November 16, 2000.

    – *"How to treat negative diffusion problems: the anharmonic oscillator in the Q-representation"*.
      Instituto Mediterraneo de Estudios Avanzados, IMEDEA (Palma de Mallorca, Spain).
      February 26, 2001.

    – *"Quantum fluctuations in optical patterns"*.
      Max-Planck-Institut für Physik komplexer Systeme (Dresden, Germany).
      May 8, 2001.

    – *"Non-linearity and quantum correlations in Optical Parametric Oscillators with walk-off"*.
      Department of Physics, Universitá dell'Insubria (Como, Italy).
      January 16, 2002.

• VISITS TO OTHER INSTITUTIONS

    – Department of Physics, University of Strathclyde (Glasgow, UK).
      1 June - 31 August 2000.

    – Department of Physics, Universitá dell'Insubria (Como, Italy).
      7 - 19 January 2002.

• SCHOOLS ATTENDED

    – Seminar/School **Coherent Evolution in Noisy Environment**.
      Max-Planck-Institut für Physik komplexer Systeme.
      Dresden, Germany, 30 April-12 May 2001.

    – **NATO-ASI Quantum Communication and Information Technologies**,
      Bilkent University.
      Ankara, Turkey, June 3-14, 2002.